University of Oviedo
Energy Department

Doctoral Thesis

ELLIPTIC AEROFOIL AERODYNAMICS IN A DEVELOPED PIV FACILITY

Author: María Rodríguez Lastra
Supervisors: Dr. Carlos Santolaria Morros
Dr. Eduardo Blanco Marigorta

Gijón, May 2014

RESUMEN DEL CONTENIDO DE TESIS DOCTORAL

1.- Título de la Tesis	
Español/Otro Idioma: Elliptic Aerofoil Aerodynamics in a Developed PIV Facility	Inglés: Elliptic Aerofoil Aerodynamics in a Developed PIV Facility

2.- Autor	
Nombre: María Rodríguez Lastra	DNI/Pasaporte/NIE:
Programa de Doctorado: Tecnología, diversificación, calidad y ahorro energético	
Órgano responsable: Universidad de Oviedo	

RESUMEN (en español)

El presente trabajo evalúa el comportamiento aerodinámico de un perfil elíptico de bajo espesor a números de Reynolds bajos por medio de las técnicas velocimetría por imágenes de partículas (PIV) y anemometría de hilo caliente (HWA). Esta investigación requirió el diseño u construcción de un túnel de viento de baja velocidad para llevar a cabo la campaña de medidas, en particular las realizadas con PIV.

El desarrollo de la instalación experimental para obtener una descripción física del comportamiento del flujo alrededor y detrás del álabe fue uno de los hitos más importantes a lo largo de esta investigación. Se diseñó una nueva geometría de tobera para este propósito específico, y se realizó un extenso estudio que verificase su buen comportamiento. Los resultados obtenidos con CFD mostraron los efectos favorables del perfil sobre el flujo, en comparación con los ofrecidos por otros tres perfiles extraídos de la bibliografía. Medidas hechas con hilo caliente corroboraron estos resultados. El trabajo metodológico incluyó también el desarrollo de procedimientos para las pedidas de PIV, además de software para el análisis de los datos y la estimación de incertidumbres experimentales.

Los efectos del ángulo de ataque sobre el flujo han sido analizados mediante medidas con PIV del flujo alrededor del álabe y en la estela para 0º, 5º, 10º and 15º. Debido a que estudios previos mostraron la autosimilitud de las distribuciones normalizadas de velocidad para distintas velocidades y rugosidades superficiales, solamente se estudió en profundidad un número Reynolds (calculado en base a la cuerda del perfil). La base de datos experimental adquirida con PIV permitió el estudio de campos de velocidades comprendiendo las componentes vertical y horizontal, obtenidas directamente de las medidas, así como distintas variables derivadas como la vorticidad y la turbulencia. También se acometió la visualización del flujo, lo que permitió obtener una visión en profundidad de los fenómenos que tenían lugar como son las estructuras coherentes, las capas límite y las burbujas laminares.

Por último se realizó una campaña intensiva de medidas con hilo caliente en la estela del álabe, con más de 2000 medidas en 380 posiciones. Los resultados obtenidos se emplearon para aportar información adicional sobre las escalas de turbulencia, las características de la estela y la generación de estructuras verticales, además de para verificar la exactitud de los datos de PIV. Asimismo, se ha elaborado un breve cálculo del coeficiente de arrastre y del ángulo de entrada en pérdida del álabe.

RESUMEN (en Inglés)

The present work assesses the aerodynamic performance at low-Reynolds number of a slender elliptic aerofoil by means of particle image velocimetry (PIV) and hot-wire anemometry (HWA) techniques. This investigation required the design and construction of a low-speed wind tunnel to perform the measurement campaign, in particular with PIV.

The development of the experimental facility to obtain a physical description of the flow behaviour around and behind the aerofoil was one of the main milestones throughout this research. A new nozzle profile was designed for this specific purpose and an extensive study that verified its good performance was conducted. CFD results showed favourable effects of the profile over the flow, compared to other three profiles extracted from the literature. Hot-wire measurements has corroborated these results. The methodology work included also the development of the procedures for the PIV measurements, together with the software for the analysis of the data, and the estimation of the experimental uncertainties.

The effects of the angle of attack on the flow have been analysed with PIV measurements of the flow around the aerofoil and in the wake at 0º, 5º, 10º and 15º. Only one chord-based Reynolds number was extensively studied because previous tests confirmed the self-similarity of the normalized velocity distributions with different velocities and surface roughness. The experimental database acquired with PIV have enabled the study of velocity fields comprising the streamwise and the vertical component, obtained directly from the measurements, as well as different derived variables as the vorticity and the turbulence. Flow visualization was carried out giving and in-depth vision of the flow phenomena such as coherent structures, boundary layers and laminar bubbles.

An intensive hot-wire test campaign was performed in the aerofoil wake, with more than 2000 measurements on 380 positions. Results were used to give extra information about turbulent scales, wake characteristics and generation of vortical structures, as well as to verify the accuracy of the PIV data. In addition, a brief calculation has been made of the drag coefficient and the stall angle of the aerofoil.

SR. DIRECTOR DE DEPARTAMENTO DE_____ ____ _____/
SR. PRESIDENTE DE LA COMISIÓN ACADÉMICA DEL PROGRAMA DE DOCTORADO EN _____

Agradecimientos

Me gustaría dedicar estas líneas de agradecimiento a todas aquellas personas que han hecho posible en mayor o menor medida la realización de esta tesis. En primer lugar, a mis dos directores los Dres. Carlos Santolaria Morros y Eduardo Blanco Marigorta, por sus inestimables consejos y dedicación durante estos cuatro años de trabajo.

Especialmente quiero citar a los profesores Dres. Jesús Fernández Oro y Mónica Galdo Vega por haber estado siempre dispuestos a ayudarme con la mejor de las sonrisas. Las horas de laboratorio se han hecho mucho más divertidas junto a vosotros. A todos mis compañeros en el Área de Mecánica de Fluidos, en particular a Israel Guerras Colón, quien caminó a mi lado durante los primeros años ofreciéndome toda su colaboración.

También debo agradecer a los Dres. Guillermo Paniagua y Tom Povey por haberme brindado la oportunidad de trabajar con ellos durante mis dos estancias de investigación en el Instituto Von Karman de Dinámica de Fluidos (Bélgica) y la Universidad de Oxford (Reino Unido). El conocimiento prestado por ambos ha sido tremendamente valioso.

Al Ministerio de Economía y Competitividad de España, que me ha permitido trabajar en un proyecto de investigación bajo el subprograma de Becas Predoctorales de Investigación, dentro del cual se ha desarrollado esta tesis.

Y por último deseo agradecer a mis padres, José y Maite, su cariño y apoyo incondicional a lo largo de mi vida. Vuestra dedicación ha hecho posible todos mis logros. Entre vuestros brazos siempre estará mi hogar. Y por supuesto, a mi prometido Pablo, por su eterno amor, paciencia y ayuda entregados sin reservas. Siempre has sido y serás una inspiración para mí. Te quiero.

María Rodríguez Lastra

Abstract

The present work assesses the aerodynamic performance at low-Reynolds number of a slender elliptic aerofoil by means of particle image velocimetry (PIV) and hot-wire anemometry (HWA) techniques. This investigation required the design and construction of a low-speed wind tunnel to perform the measurement campaign, in particular with PIV.

The development of the experimental facility to obtain a physical description of the flow behaviour around and behind the aerofoil was one of the main milestones throughout this research. A new nozzle profile was designed for this specific purpose and an extensive study that verified its good performance was conducted. CFD results showed favourable effects of the profile over the flow, compared to other three profiles extracted from the literature. Hot-wire measurements has corroborated these results. The methodology work included also the development of the procedures for the PIV measurements, together with the software for the analysis of the data, and the estimation of the experimental uncertainties.

The effects of the angle of attack on the flow were analysed with PIV measurements of the flow around the aerofoil and in the wake at 0°, 5°, 10° and 15°. Only one chord-based Reynolds number was extensively studied because previous tests confirmed the self-similarity of the normalized velocity distributions with different velocities and surface roughness. The experimental database acquired with PIV enabled the study of velocity fields comprising the streamwise and the vertical component, obtained directly from the measurements, as well as different derived variables as the vorticity and the turbulence. Flow visualization was carried out giving and in-depth vision of the flow phenomena such as coherent structures, boundary layers and laminar bubbles.

An intensive hot-wire test campaign was performed in the aerofoil wake, with more than 2000 measurements on 380 positions. Results were used to give extra information about turbulent scales, wake characteristics and generation of vortical structures, as well as to verify the accuracy of the PIV data. In addition, it was made a brief calculation of the drag coefficient and the stall angle of the aerofoil.

Resumen

El presente trabajo evalúa el comportamiento aerodinámico a números de Reynolds bajos de un perfil elíptico de poco espesor, por medio de las técnicas velocimetría por imágenes de partículas (PIV) y anemometría de hilo caliente (HWA). Esta investigación requirió el diseño y construcción de un túnel de viento de baja velocidad para llevar a cabo la campaña de medidas, en particular las realizadas con PIV.

El desarrollo de la instalación experimental para obtener una descripción física del comportamiento del flujo alrededor y detrás del álabe, fue uno de los hitos más importantes a lo largo de esta investigación. Se diseñó una nueva geometría de tobera para este propósito específico, y se realizó un extenso estudio que verificase su buen comportamiento. Los resultados obtenidos empleando la técnica CFD mostraron los efectos favorables del perfil sobre el flujo, en comparación con los ofrecidos por otros tres perfiles extraídos de la bibliografía. Medidas hechas con hilo caliente corroboraron estos resultados. El trabajo metodológico incluyó también el desarrollo de procedimientos para las pedidas de PIV, además de software para el análisis de los datos y la estimación de incertidumbres experimentales.

Los efectos del ángulo de ataque sobre el flujo fueron analizados mediante medidas con PIV del flujo alrededor del álabe y en la estela para 0°, 5°, 10° and 15°. Debido a que estudios previos mostraron la autosimilitud de las distribuciones normalizadas de velocidad para distintas velocidades y rugosidades superficiales, solamente se estudió en profundidad un número Reynolds (calculado en base a la cuerda del perfil). La base de datos experimental adquirida con PIV permitió el estudio de campos de velocidades comprendiendo las componentes vertical y horizontal, obtenidas directamente de las medidas, así como distintas variables derivadas como la vorticidad y la turbulencia. También se realizó una visualización del flujo, lo que permitió obtener una visión en profundidad de los fenómenos que tenían lugar, como son las estructuras coherentes, las capas límite y las burbujas laminares.

Por último, se realizó una campaña intensiva de medidas con hilo caliente en la estela del álabe, con más de 2000 medidas en 380 posiciones. Los resultados obtenidos se emplearon para aportar información adicional sobre las escalas de turbulencia, las características de la estela y la generación de estructuras vorticales, además de para verificar la exactitud de los datos de PIV. Asimismo, se elaboró un breve cálculo del coeficiente de arrastre y del ángulo de entrada en pérdida del álabe.

Contents

List of Figures

List of Tables

Symbols list

Acronyms

CCA Constant Current Anemometer

CCD Charge Couple Device

CRW Canard Rotor Wing

CTA Constant Temperature Anemometer

FFT Fast Fourier Transform

HWA Hot Wire Anemometry

LDV Laser Doppler Velocimetry

LSV Laser Speckle Velocimetry

MDF Medium-density fibreboard

PIV Particle Image Velocimetry

UAV Unmanned Aerial Vehicles

Subscripts

f Fluid

n Number of snapshots

p Particle

rms Root mean square

w Wire

Greek Letters

α	Angle of attack
χ	Electrical resistivity (Ω m)
ν	Kinematic viscosity (m^2/s)
ε	Turbulent dissipation rate (m^2/s^3)
λ	Wavelength (m)
λ_L	Taylor lengt scale (m)
ω	Vorticity (1/s)
σ	Standard deviation
τ_s	Relaxation time (s)
$\triangle M$	Scale uncertainty (mm/px)
$\triangle \tau$	Timing uncertainty (µs)
$\triangle X$	Displacement uncertainty (mm)

Lowercase symbols

$\triangle t$	Time inverval between two laser pulses (s)
d	Diameter (m)
d_I	Size of an interrogation window (pixel)
f_c	Cut-off frequency (Hz)
k	Turbulent kinetic energy (m^2/s^2)
l	Lenght (m)
r	Separation distance between two correlated points (m)
u	Streamwise velocity (m/s)
$\overline{u}$	Mean streamwise velocity (m/s)
u_{ef}	Effective velocity given by a single wire (m/s)
u_j	Velocity of the air jet (m/s)
u'	Streamwise velocity fluctuation (m/s)
v	Vertical velocity (m/s)
$\overline{v}$	Mean vertical velocity (m/s)
v'	Vertical velocity fluctuation (m/s)

Uppercase symbols

A	Cross-sectional area (m^2)
I	Electrical current (A)
C	Correlation coefficient
C_D	Drag coefficient
C_L	Lift coefficient
C_p	Pressure coefficient
F_{tot}	Total force (N)
L	Integral lengt scale (m)
M	Magnification factor (mm/px)
PSD	Power spectral density ($(m/s)^2 Hz^{-1}$)
$\dot{Q}_c$	Conductive heat-transfer rate (W)
$\dot{Q}_e$	Electrical heat-generation rate (W)
$\dot{Q_{fc}}$	Forced-convective heat-transfer rate (W)
$\dot{Q}_r$	Radiation heat-transfer rate (W)
$\dot{Q}_e$	Heat storage rate (W)
R	Resistance (Ω)
Re_c	Chord based Reynolds number
R_{uu}	Velocity correlation function
T	Temperature (K)
TI	Turbulent intensity
U_0	Free stream velocity (m/s)
U'	Convective velocity fluctuations(m/s)
X	Particle displacement (px)

CHAPTER 1

Introduction

In this doctoral thesis, the aerodynamic performance at low-Reynolds numbers of an elliptic aerofoil has been comprehensively investigated using PIV and HWA techniques. In order to perform the measurements, a low-speed wind tunnel has been developed, with an in depth study of a new contraction geometry. This chapter contains a description of elliptic aerofoils and its applications, as well as a general description of aerofoil aerodynamics and turbulence. It has been included the state of the art concerning wind tunnels, the measurement techniques used and aerodynamics of elliptic aerofoils. Finally, the general objectives of the thesis have been detailed.

1.1 Scope of the research

The work carried through is not only a research about the aerodynamics of an slender elliptic aerofoil, with a thickness ratio of $t/c = 0.09$ higher than any other profile studied in bibliography, but also a methodological study that provides the basis for future investigations. The main measurements have been carried out using a technique never utilized before by the Fluid Mechanics research group of the University of Oviedo: particle image velocimetry (PIV). Hot-wire anemometry was also used to validate the obtained results and give extra information about turbulence. Concerning the methodological study, some fundamental tasks were addressed to allow subsequent aerodynamic measurements over an elliptic aerofoil, namely a great effort was made not only to design a PIV wind tunnel but to construct the facility meeting all the needs. This included a previous survey to find the optimal contraction profile comparing a new design specifically developed for this purpose with other designs found in literature. The contraction was afterwards build up in an already existent wind tunnel and fully characterized using hot-wire anemometry before including it in the PIV wind tunnel's design. The establishment of the PIV technique also required considerable amount of time because previous studies needed to be done to identify the correct parameters.

The interest of the Fluid Mechanics group in elliptic profiles comes from the line of research regarding aerodynamic, mechanic and acoustic performance of axial fans, and more specifically jet fans used in road tunnel ventilation. Thus, the development of the new PIV

wind tunnel, the implementation of the PIV measurement technique, as well as the obtained results regarding PIV and HWA, constitute the basis for future in depth researches of the elliptic aerofoil such as aeroacoustic studies.

The research work that constitutes this thesis was funded by the Spanish Ministry of Economy and Competitiveness under the subprogram Predoctoral Research Grants, as a part of the project *Characterization of the aeroacoustic behaviour of elliptic aerofoils in turbulent flows* (DPI2009-13613).

1.2 Elliptic aerofoils

An aerofoil is the shape of a wing, blade or sail that, in case of experimenting a relative movement respect to a fluid, produces an aerodynamic force perpendicular to the velocity direction (lift). As it is shown in Figure 1.1, there are three types of aerofoils: cambered, symmetric and elliptic.

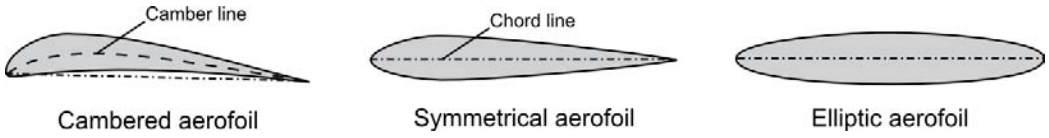

Figure 1.1: Types of aerofoils

Cambered aerofoils are designed for giving lift when moving towards a specific direction (forward). Their curvature provides very good performance with positive angles of attack but not with negative ones.

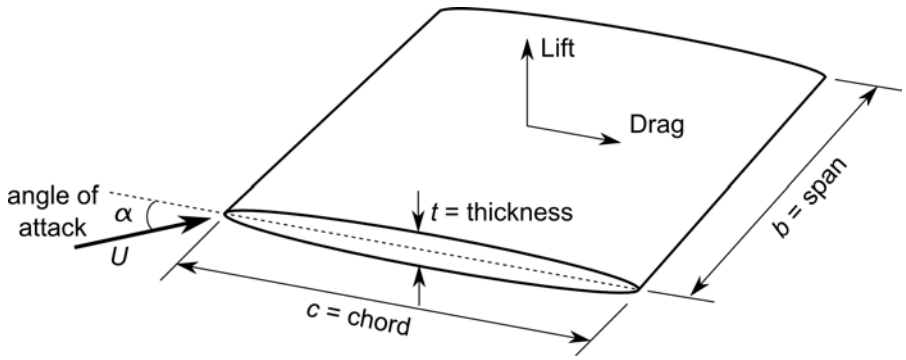

Figure 1.2: Elliptic aerofoil

Symmetric aerofoils also give lift when moving forward. They are prepared to work with positive and negative angles of attack equally due to their horizontal symmetry. As a consequence of not having curvature, the maximum lift obtained with these aerofoils is lower than with the previous ones.

Elliptic aerofoils are a type of aerofoils symmetric with respect to the vertical and horizontal axis (Figure 1.2). They can give lift working with positive and negative angles and, also, moving in both directions. Nevertheless, their performance is worse than the cambered or symmetrical ones, not only because of their lack of curvature but for their non-sharpened

trailing edge. These characteristics reduce lift and increase drag. Elliptic aerofoils are mainly used in applications requiring turbomachineries able to rotate in both directions, such as jet fan blades, unmanned aerial vehicles and small turbines.

Jet fans

Jet fans (see Figure 1.3) have been used since the early 1960's in road tunnels with longitudinal ventilation. This is a kind of forced ventilation where air comes through one of the tunnel entrances and exits at the opposite one. Usually the flow direction of a jet fan can be reversed, so that the ventilation direction coincides with the predominant movement of the vehicles inside the tunnel. To achieve the inversion of the flow, fan blades are designed to be reversible, i.e. the impeller can rotate clockwise and counter clockwise. To allow this feature, fan blades must be symmetrical. The reversibility requirement prohibits the fans to have stator, and the performance of the machine is entirely that of the rotor stage. The pressure difference between the inlet and the outlet in this type of fans is practically non-existent. All the provided energy to the flow is kinetic energy. The noise produced is an important factor to take into consideration due to the discomfort caused to the drivers. This is the reason why jet fans are partially intubated with a muffler both before and after the rotor.

Figure 1.3: Jet fans in a tunnel

Unmanned aerial vehicles

Unmanned Aerial Vehicles (UAV) have gained interest due to increased reliance on remotely piloted and autonomous air vehicles in military and homeland security applications. Specifically, the Canard Rotor Wing (CRW) is a vertical take off and landing flight demonstration aircraft built via a joint DARPA/Boeing effort, that uses a symmetric rotor

with an elliptic aerofoil section. The rotor uses conventional cyclic and collective control for rotary wing flight. The rotor can also be locked into a fixed position for use as a main wing for high speed forward flight. Figure 1.4 shows the Canard Rotor Wing.

Figure 1.4: Canard rotor/wing

Helical cross-flow (Gorlov) turbines

Figure 1.5: Gorlov helical turbine

The Gorlov helical turbine was presented by Alexander Gorlov in the 1990's as an important improvement on the Darrieus turbine. Both designs are vertical axis devices, which means the axis is positioned perpendicular to flow direction, whereas the more extended turbines are horizontal axis which means the axis is positioned parallel to the flow. The helical rotor design, with blades curved around the axis, reduces or eliminates the torque ripple encountered in traditional two-blade Darrieus turbines. This is due to the evenly distribution of the aerofoils throughout the rotation cycle, assuring a foil section at every possible angle of attack. Thus, the sum of the lift and drag forces on each blade do not change abruptly with rotation angle.

The aerofoil sections of this turbine are elliptic, i.e. symmetrical both top-to-bottom and from the leading-to-trailing edge. Thereby, the Gorlov turbine can spin equally well in either direction. A sample of a helical cross-flow turbine is depicted in Figure 1.5.

1.3 Aerodynamics of aerofoils

1.3.1 Drag and lift

An aerofoil is an aerodynamic shape designed to generate a mechanical force, F_{tot}, mainly perpendicular to the velocity direction, as a result of its relative motion with respect to a fluid. The sources of this force are shear stresses (viscous effects) and normal stresses (pressure effects) on the surface of the object. The distribution of pressure and shear stress on the surface of an aerofoil is schematically shown in Figure 1.6, in which negative pressures mean negative respect to atmospheric pressure. The total force on the aerofoil is the sum of the pressure and viscous forces integration over its surface, A, i.e.,

$$F_{tot} = \int_A p \, \mathrm{d}A + \int_A \tau \, \mathrm{d}A \tag{1.1}$$

The total force can be divided into two components: *a)* lift force which is normal to the free stream velocity, and *b)* drag force which is parallel to the free stream.

The lift is produced by the changing direction of the flow around the aerofoil. When lift occurs, so does lift-induced drag as a result of the creation of vortices (vortex drag) and the presence of additional viscous drag.

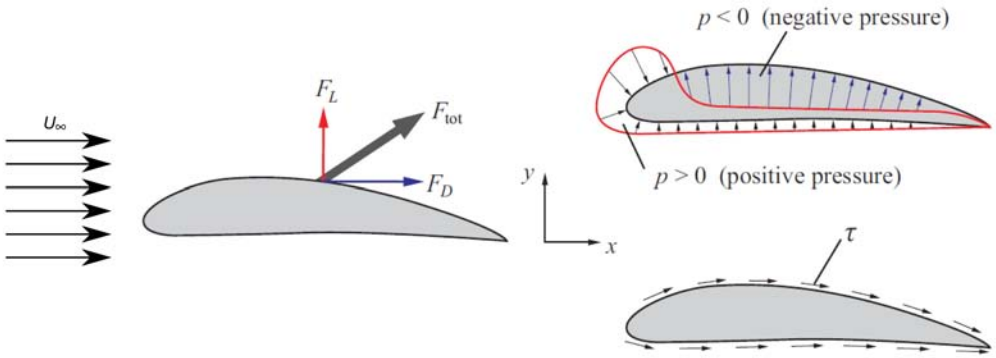

Figure 1.6: Schematic distribution of normal stress (pressure effects) and shear stress (viscosity effects) for an aerofoil

Lift and drag coefficients are dimensionless quantities defined as,

$$C_D = \frac{\text{drag force}}{\text{dynamic pressure} \times \text{Area}} = \frac{D}{\frac{1}{2}\rho U^2 A} \tag{1.2}$$

$$C_L = \frac{\text{lift force}}{\text{dynamic pressure} \times \text{Area}} = \frac{L}{\frac{1}{2}\rho U^2 A} \tag{1.3}$$

The coefficients C_D and C_L strongly depend on the geometry of the object, hence are usually determined by experimental studies or numerical simulations.

An aerofoil can be tilted with respect to the flow direction defining the angle of attack, α, (see Figure 1.7). Both C_D and C_L depend on the angle of attack and the design of the aerofoil, which generally is done to maximize C_L and minimize C_D. A symmetrical aerofoil will generate zero lift at zero angle of attack. But as the angle increases, the air is deflected through a larger angle and the vertical component of the airstream velocity increases, resulting in more lift and lift-induced drag. The lift reaches a maximum at a certain angle (critical angle of attack) and increasing the angle beyond this point causes the air to separate from the aerofoil and a reduction of lift. At the onset of stall, lift and lift-induced drag decrease abruptly. Nevertheless, viscous drag increases due to the formation of turbulent unattached flow on the surface of the body.

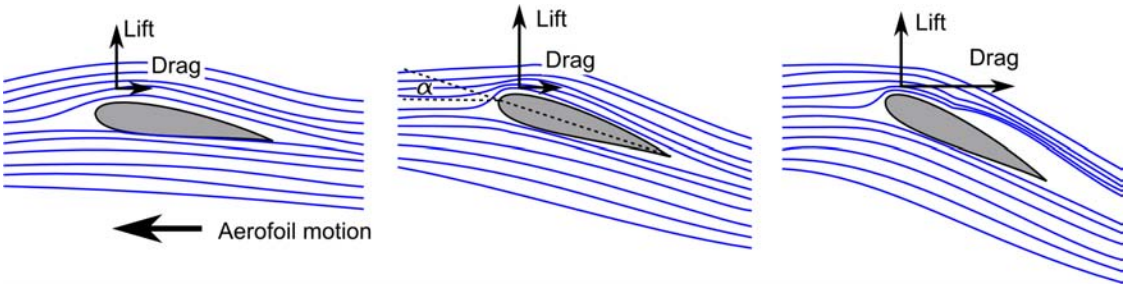

Figure 1.7: Flow streamlines and forces on an aerofoil

For thin air foils and small angles of attack (-10°$\leq \alpha \leq$10°) the lift is directly proportional to the angle, while the drag is nearly constant at smaller angles (-5°$\leq \alpha \leq$5°). As the angle increases above those values, the drag quickly rises because of increased frontal area and increased boundary layer thickness. It is known that the boundary layer affects the aerodynamic of the object by changing its shape. The flow reacts to the edge of the boundary layer just as it would to the physical surface of the object. Figure 1.8 shows typical variations of lift and drag coefficients with the angle of attack for a standard aerodynamic profile.

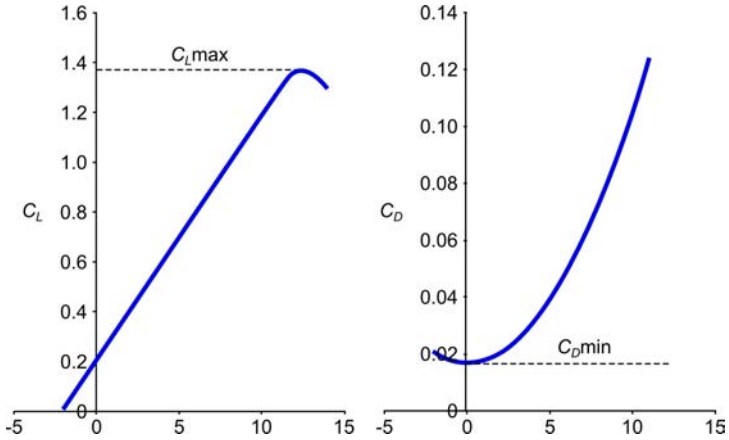

Figure 1.8: Typical variations of the lift and drag coefficients with the angle of attack

Because both the lift coefficient and drag coefficient are functions of the angle of attack, the drag coefficient can be interpreted as depending on the lift coefficient. Figure 1.9 shows the drag polar, which is the drag coefficient as a function of the lift coefficient.

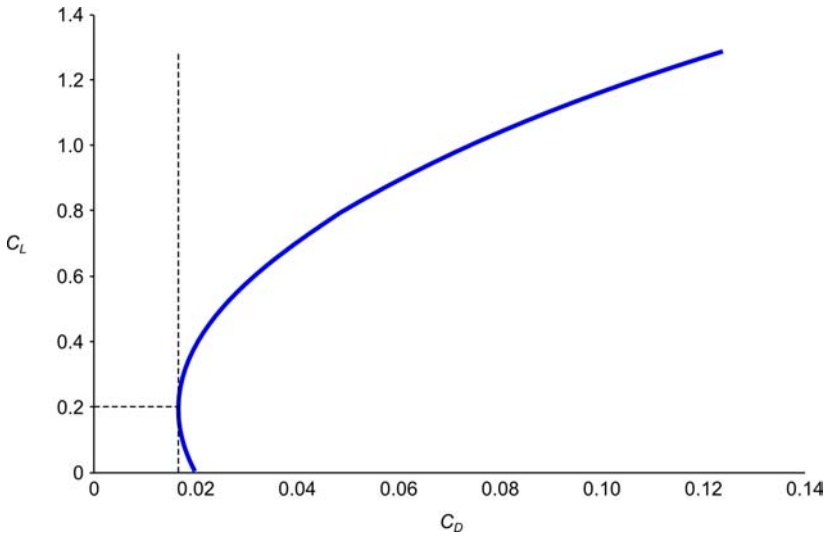

Figure 1.9: Drag polar

1.3.2 Theory of flow structure around an aerofoil

1.3.2.1 Flow around an immersed body

When a flow is suddenly accelerated to speed U_∞ at $t = 0$ towards a held fixed aerofoil, the streamlines near the body will behave as the ones depicted in Figure 1.10 (a). These streamlines appear right after the fluid has started moving but before boundary layer have developed on either sides -pressure and suction-. At this stage, there is a near discontinuity adjacent to the body's surface. As the fluid on the upper side goes around the trailing edge with a very high velocity, it has to overcome an abrupt deceleration and pressure rise from the trailing edge to the rear stagnation point B. This particular situation induces a counter clockwise movement of the fluid from the pressure side around the sharp trailing edge towards the stagnation point. The flow is able to turn the sharp trailing edge corner because the vorticity on the aerofoil's surface at that instant is nearly singular. Overall at this time, the flow is irrotational away from the body's surface, the aerofoil's net circulation is zero, it generates no lift, the stagnation point A is very close to the leading edge and the rear stagnation point at B resides on the aerofoil's suction face.

A short time later, in a hypothetical situation where the aerofoil's pressure-side boundary layer has developed first, the flow lines will be as shown in Figure 1.10 (b). The stagnation points A and B have not moved much, however, the pressure-side boundary layer separates at the trailing edge . This is produced because the fluid near the surface does not have sufficient kinetic energy to face the abrupt pressure rise near the stagnation point B nor can it turn the sharp-trailing edge corner. Furthermore, the near singularity of vorticity that initially resided on the aerofoil's surface trailing edge has been carried into the near wake as a concentrated vortex. Two phenomena near the trailing edge now act to eliminate the zone of separated flow: (1) The stagnation pressure at B is higher than the pressure in the moving fluid that is leaving the trailing edge from the pressure side, as it is verified by the Bernoulli equation. Thus, the resulting pressure gradient between B and the trailing edge pushes the stationary fluid near B toward the aerofoil's trailing edge. (2) The induced velocities from the vorticity in the separated pressure-side boundary layer and from the

near-wake concentrated vortex, both induce the stationary fluid near B to move toward the aerofoil's trailing edge.

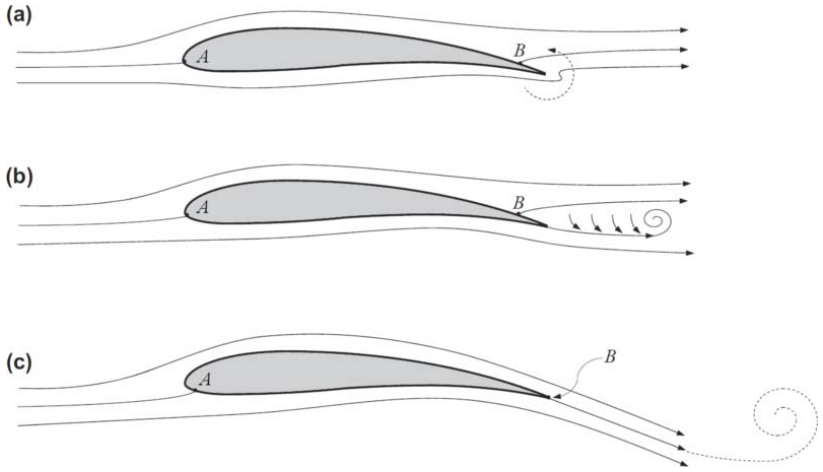

Figure 1.10: Flow patterns over a stationary aerofoil at a low angle of attack in an impulsively started horizontal flow

Figure 1.10 (c) shoes the final condition after the flow has travelled a chord length or two past the aerofoil. The leading-edge stagnation point has travelled under the nose of the foil and onto the foil's pressure side., and the suction-surface separation point B has been drawn to the trailing edge. Once the flow is established, the aerofoil now carries more vorticity in its suction-side boundary layer than it does in its pressure side-boundary layer. This difference causes the flow to sweep upward ahead of the aerofoil and downward behind it.

The final circulation magnitude bound to the aerofoil and that in the starting vortex is illustrated in Figure 1.11.The aerofoil is left with a circulation (clockwise) equal and opposite to the circulation of the starting vortex (counter clockwise). This circulation explains the velocity magnitude differences between the pressure and the suction sides of an aerofoil and, as a consequence, the induced lift.

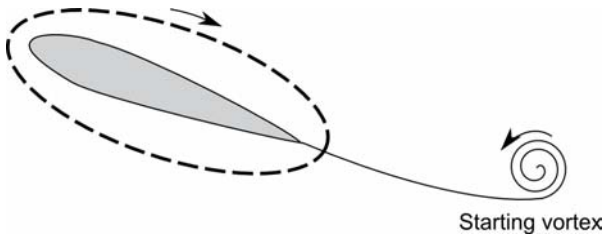

Figure 1.11: Starting vortex

1.3.2.2 Flow separation

Frequently in the upper surface, the flow does not reach the trailing edge but separates at an earlier spot on the aerofoil surface creating a wake. This boundary layer separation

results in negative effects such as drag increase, lift decrease, pressure recovery losses, etc.

Aerofoils usually have high velocity, low-pressure regions on the upper surface. At the trailing edge the flow has to return to the free-stream conditions, which means achieving higher pressure. Thus, particles moving from the aerofoil leading edge towards the trailing edge are subjected to an adverse pressure gradient. Those particles closest to the body are continually losing their kinetic energy due to viscous losses and, in some cases, they lack sufficient energy to overcome the adverse pressure gradient. This results in a backward movement of the particles and flow detachment. This separation is different and subtle than the geometrical based separation caused by a drastic geometry change, where the flow is unable to remain attached to the solid surface due to its inertia. The two types of flow separation are illustrated in Figure 1.12, pressure based separation (a) and geometrically based separation (b).

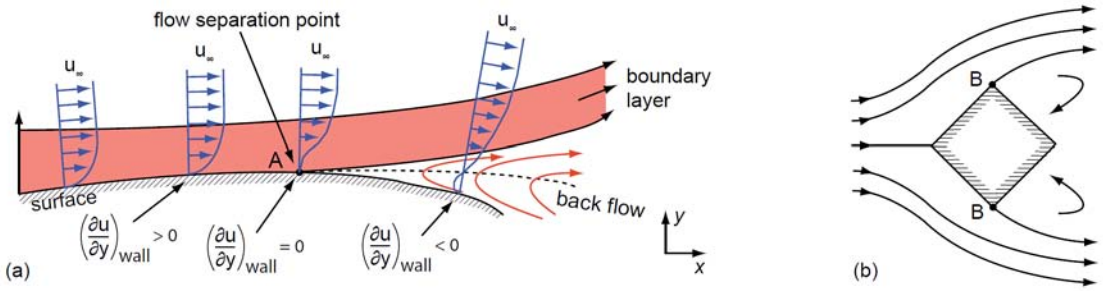

Figure 1.12: Pressure-based (a) and geometrically-based (b) flow separation. Adapted from Sturm et al. (2012)

Under stationary conditions, the flow separation can be described by the Navier-Stokes equation,

$$(\vec{v} \cdot \nabla) \cdot \vec{v} + \frac{\partial \vec{v}}{\partial t} = \frac{1}{\rho}\vec{F} - \frac{1}{\rho}\nabla p + \nu \Delta \vec{v} \tag{1.4}$$

where $\vec{v} = (u, v, w)$ is the velocity vector, ρ is the density ν is the kinematic viscosity, $\vec{F}$ is the external force per unit of volume, ∇p is the pressure force per unit of volume and $\nu \Delta \vec{v}$ represents the influence of friction within the equation.

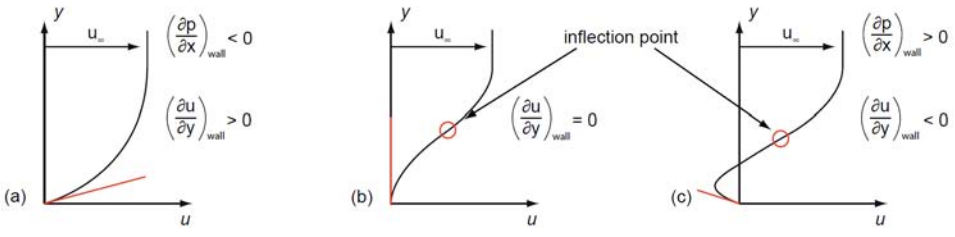

Figure 1.13: Flow profiles before (a), while (b) and after (c) boundary layer separation. Adapted from Sturm et al. (2012)

Considering only a bi-dimensional flow, z and w can be neglected. In addition, at the wall $y = 0$ and $\vec{v} = 0$ ($u = 0$, $v = 0$), in a stationary case where $\frac{\partial \vec{v}}{\partial t} = 0$ and without external forces $\vec{F} = 0$, Equation 1.4 can be simplified to

$$0 = -\frac{1}{\rho}\frac{\partial p}{\partial x} + \nu\frac{\partial^2 u}{\partial y^2} \tag{1.5}$$

Depending if $\frac{\partial p}{\partial x} < 0$ or $\frac{\partial p}{\partial x} > 0$, it results in different flow profiles (see Figure 1.13).

1.3.2.3 Wake

The wake is the region of disturbed flow immediately behind a stationary or moving body. Figure 1.14 shows different wakes behind and aerofoil as a function of the angle of attack.

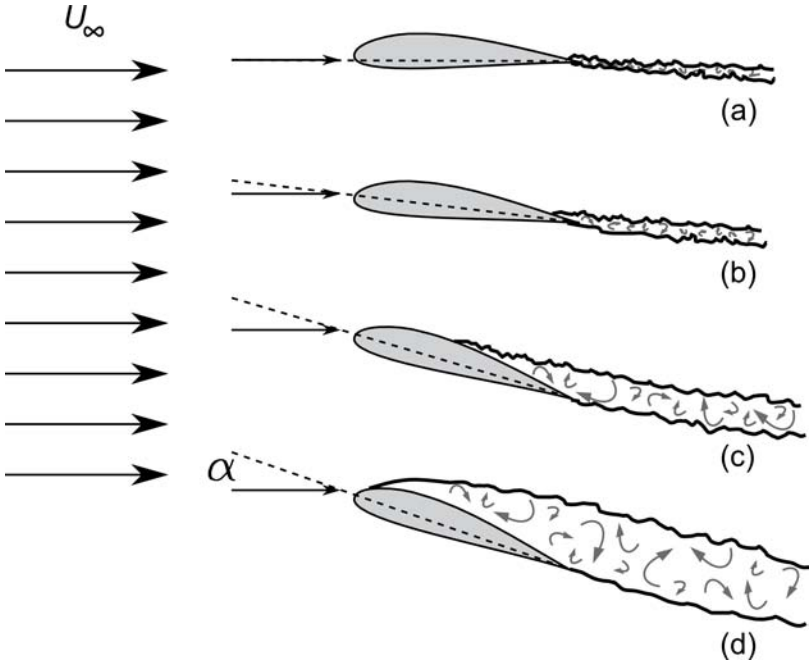

Figure 1.14: Wake behind an aerofoil for different angles of attack

As it has been stated before, the angle of attack is one of the factors that influence the boundary layer separation on an aerofoil. For α =0° (Figure 1.14 (a)), the turbulent flow starts at the very end of the trailing edge leading to a thin wake that propagates downstream. A slight increase of the angle of attack results in a displacement of the detachment of the boundary layer towards the leading edge (Figure 1.14 (b)). If the aerofoil continues being tilted, it will reach the angle of maximum lift. At this position the boundary layer will separate at some point in the middle of the upper surface causing the widening of the wake (Figure 1.14 (c)). At higher angles of attack the boundary layer will be detached near the leading edge (Figure 1.14 (d)) causing a wide turbulent wake right behind the aerofoil (stall).

1.3.2.4 Separation bubble

The boundary layer detachment on the aerofoil surface can be laminar or turbulent depending on the transition point being reached after or before the separation. The laminar boundary layer tends to separate easier and nearer the leading edge than the turbulent one. Usually a complete detachment is produced in both cases. However, in some cases,

when the laminar boundary layer separates near the leading edge but the angle of attack is not very high, a turbulent boundary layer might reattach to the aerofoil surface again. At this point, a separation bubble has been formed, and a recirculating zone with a *Reverse Flow Vortex* appears. (Figure 1.15).

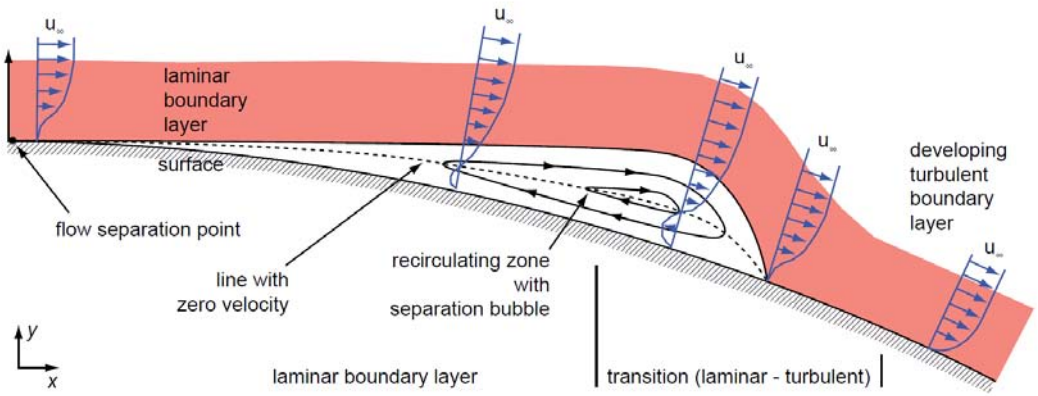

Figure 1.15: Aerofoil separation bubble adapted from Sturm et al. (2012)

Immediately following separation, a laminar shear layer -usually unstable- is created (Mueller and DeLaurier (2003)). Inside of the bubble there is an area called *Dead Air Region* which is characteristic of the separated laminar flow. Because the air in this region is not able to mix efficiently with the free stream flow, it is very close to being stationary. At a certain point in the separation bubble (see Figure 1.15), begins the fast transition from laminar to turbulent flow. The turbulent flow is not self-sustainable, however, it exchanges momentum with the mean flow, providing the near wall region with a source of energy from the free stream. If enough energy is gained by the turbulent flow, the boundary layer will be able to withstand the adverse pressure gradient and subsequently reattach.

The location and size of the bubble is a function of aerofoil shape, angle of attack, environmental disturbances and Reynolds number (Tani (1964); Mueller and DeLaurier (2003)).

1.3.3 Turbulence

Turbulent motion is the natural state of most fluids and in daily life almost all flows are turbulent. Flow around aeroplanes, cars, buildings or inside fans and turbines are typical examples. The motion of a very viscous or slow moving fluid tends to be smooth and regular, i.e. laminar flow. However, if the fluid viscosity is low, or the characteristic speed is moderate to large, then the movement of the fluid becomes irregular and chaotic, i.e. turbulent.

Certain authors sustain that there is no definition of turbulent flow, but it has a number of definite characteristics (Pope (2001) and Tennekes and Lumley (1972)):

1. **Irregularity**. Turbulent flow is chaotic and irregular, being governed always by Navier-Stokes equation. The flow consist of a spectrum of different eddy sizes (scales) that exist in a certain region in space for a certain time and then are subsequently destroyed. They have characteristic speed and dimension called velocity and length scale.

2. **Diffusivity**. In turbulent flows the diffusivity is increased because turbulence increases the exchange of momentum.

3. **Large Reynolds numbers**. Turbulent flow occurs at high Reynolds number. In case of boundary layers it happens at $Re_x \approx 5 \times 10^5$.

4. **Three-dimensional**. Turbulent flow is always three-dimensional and unsteady. However, when the equations are time averaged, it can be treated as two-dimensional if the geometry allows it.

5. **Dissipation**. Turbulent flow is dissipative, which means that kinetic energy in the small eddies is transformed into thermal energy. The small eddies receive the kinetic energy from slightly larger eddies. The slightly larger eddies extract their energy from even larger eddies and so on. The largest eddies extract their energy from the mean flow. This process of transferring energy from the largest turbulent scales to the smallest ones is called the cascade process.

6. **Continuum**. Even though there are turbulent scales in the flow, they are much larger than the molecular scales, so it can be treated as a continuum.

Apart from high velocities and low viscosities, turbulence can also arise from other factors as sharp velocity differences inside the flow or shear flows. In this category, there are two big groups: free flows, far from the influence of solid contours, and wall flows, developed by the effect of near walls. The scope of this thesis includes both types: the wake (free flow) and the flow around the aerofoil surface (wall flow). These shear flows are depicted in Figure 1.16. The rolling irregularities in the shear layer drag the surrounding flow allowing the layer to expand towards the movement perpendicular direction. Also, in the wake, as the downstream distance from the trailing edge increases, the biggest eddies break down into smaller ones dissipating their turbulent energy and increasing the flow velocity until the main flow conditions are restored.

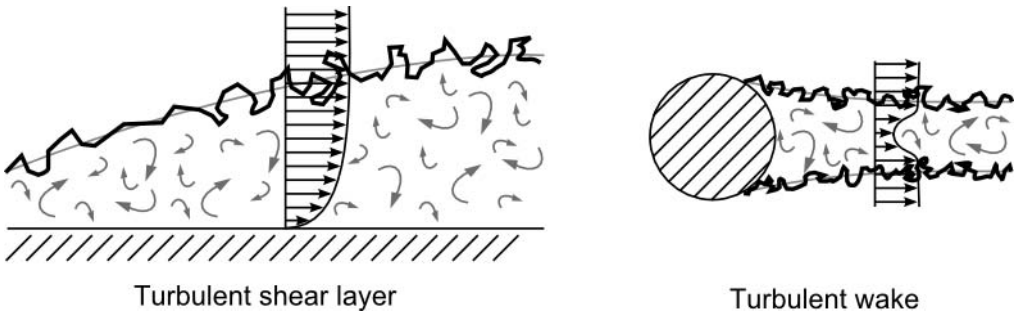

Figure 1.16: Examples of shear flows adapted from Oro (2012)

Turbulent scales

Turbulence has a wide range of spatial and temporal scales, the biggest scales extract energy from the mean flow while the smallest put an end to the dissipation phenomenon. Richardson (1922) was the first one to introduce the concept of *energy cascade* in which the largest eddies that are created by instabilities in the mean flow, are themselves subject to inertial instabilities and rapidly break-up or evolve into yet smaller vortices. At each instant, there is a continual cascade of energy from the large scale down to the small

(Figure 1.17). Viscosity plays no part in this cascade; since the Reynolds number is large, the viscous stresses acting on the large eddies are negligible. The whole process is mainly driven by inertial forces. However, when the eddy size turns so small that the Reynolds number is of order unity, viscous forces become significant and dissipation starts to be important.

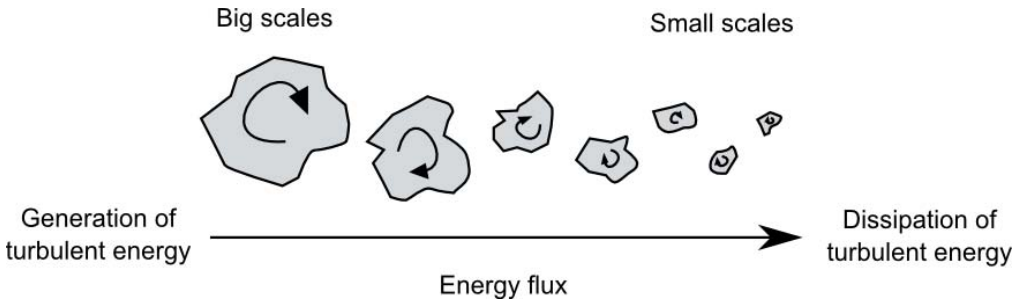

Figure 1.17: Turbulent scales

The energy cascade is often divided in three sub-domains:

- **Macroscale**. Associated with the largest vortices, it has characteristic velocity, length and time usually denoted as U, L and T. Also L is usually called *integral length scale*. The Reynolds number that corresponds to this scale is of the order of the main flow: $Re_0 \approx Re_L = UL/\nu$. These eddies depend on the boundary conditions and are clearly anisotropic.

- **Inertial subrange**. Concerns the medium scales where energy is progressively transferred to dissipative scales. Typically for the inertial subrange, the scales between macro and microscales are defined as length, l, velocity, u_l, and time, t. This subrange is wider as the Reynolds number increases.

- **Microscale**. Is the smallest scale and the Reynolds number is on the order of unity. The length is denoted as η, velocity as u_η and time as τ. This scale is also known as *Kolmogorov scale*.

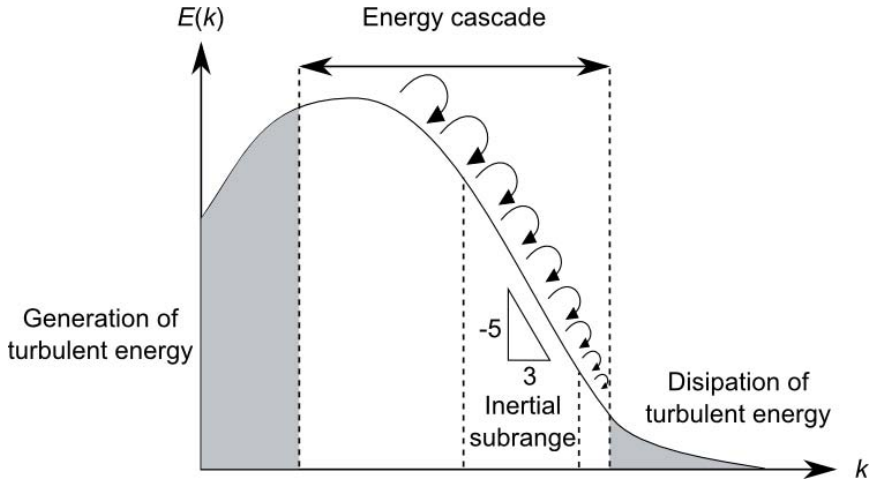

Figure 1.18: Turbulent energy spectra adapted from Oro (2012)

If velocity $u(x,t)$ is measured for some considerable period of time and the signal obtained is plotted in the frequency domain, a graph similar to that on Figure 1.18 will be obtained. Since the energy spectra, $E(k)$, depending on the wave number, k, is approximately the mathematical representation of the energy cascade, its distribution can be divided into three cascade sub-domains. The intermediate zone -inertial subrange- is characterized by a lineal evolution with a -5/3 slope (logarithmic scale).

1.4 Measurement techniques for flow characterization

There are many measurement techniques available nowadays, however it is useful to remark that not all of them are capable of measure the intrinsic fluctuations of the flow. The time response of the sensors is the key factor to distinguish between all different measurement techniques. Based on this feature it can be established two types of techniques for: (a) stationary measurements; (b) non-stationary measurements. Throughout the progress of this thesis several measurement techniques have been used. Even though pressure transducers and Pitot tubes were utilized occasionally, the study was focused mainly on the use of hot-wire anemometry and particle image velocimetry to obtain the velocity field around an elliptic aerofoil.

1.4.1 Stationary measurements

Local stationary variables can be obtained using classic measurement methods. There are many well known techniques; some of them are used in relative large domains such as gauge for pressure measurements and cup and windmill anemometers for velocity ones. Others can be used in more restricted geometries and are widely used for research purposes, like pressure transducers, manometers and Pitot tubes. Transducers and manometers are capable of measuring pressure at a certain position, while Pitot tubes allow velocity values to be obtained as an indirect measurement of static and stagnation pressure.

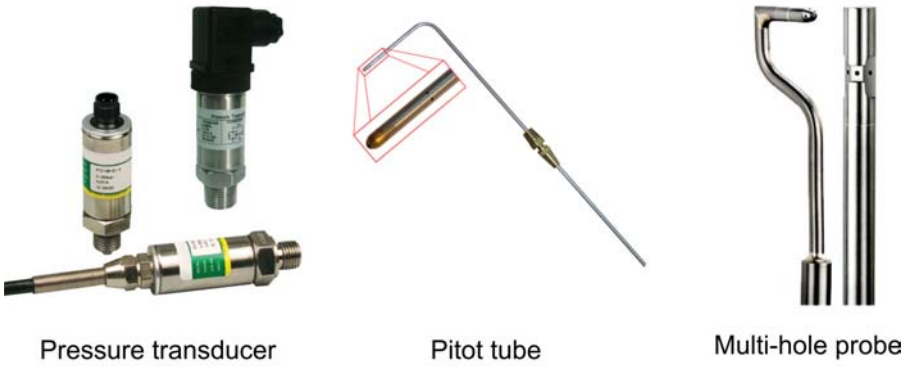

Figure 1.19: Stationary measurement instruments

When the flow is three-dimensional, a technique capable of measuring the three velocity components is required. The multi-hole probe is an instrument which measures the flow

pressure from its multiple holes and permits to obtain the velocity components from them. They are used in a wide range of applications such as velocity measurement in wind tunnels, hydrodynamic channels, flow in ducts, wake behind bodies and rigs for teaching purposes because its low costs. The multi-hole probe is characterized by its small size, wide velocity range from 5 m/s to 325 m/s ($0.02 < Ma < 0.95$), high resolution for high velocity angles (up to 70°) and not to require constant re-calibration of the probe.

1.4.2 Non-stationary measurements

Almost all real flows are turbulent, and their velocity fluctuations are conditioned by a characteristic frequency associated to the origin of the fluctuations. In order to record and study those variations, it is essential to use a measurement device with a good frequency response and a sample rate higher than the expected frequency of the fluctuations. There are several measurement techniques that allow non-stationary measurements, being the most known: multi-hole probes with pressure transducers in their head, hot-wire Anemometry (HWA), Laser Doppler Velocimetry (LDV) and Particle Image Velocimetry (PIV).

Figure 1.20: hot-wire anemometer

Hot-wire anemometry (Figure 1.20) is an intrusive technique ideal for measurement of velocity fluctuations in time domain. It has a good frequency response; measurements up to several tens of kHz are possible. Moreover, it allows obtaining the three velocity components with a low signal-to-noise ratio. The hot-wire anemometer uses up to three very fine tungsten or platinum wires of about 1 mm long and 5 µm diameter that is electrically heated to a temperature in the order of 250°C. The air passing through the wire dissipates part of the heat, thus it is possible to relate the heat flux changes in the wire with the flow velocity. Small dimensions of the wire are preferred even though they have less strength because they maximize the time response due to low thermal inertia, maximize spatial resolution, improve signal-to-noise ratio at high frequencies and eliminate output noise.

Despite of the high number of advantages of the HWA, this technique also has some drawbacks. Because of being an intrusive technique, it modifies the local flow field. It is insensitive to reversal of flow direction. The wire is fragile, which imply probe breakage and burn out; and the deposition of flow impurities on it alters the calibration characteristics and reduces frequency response. It is unable to fully map velocity fields that strongly

depend on space coordinates and time simultaneously and fails in hostile environments such as combustion.

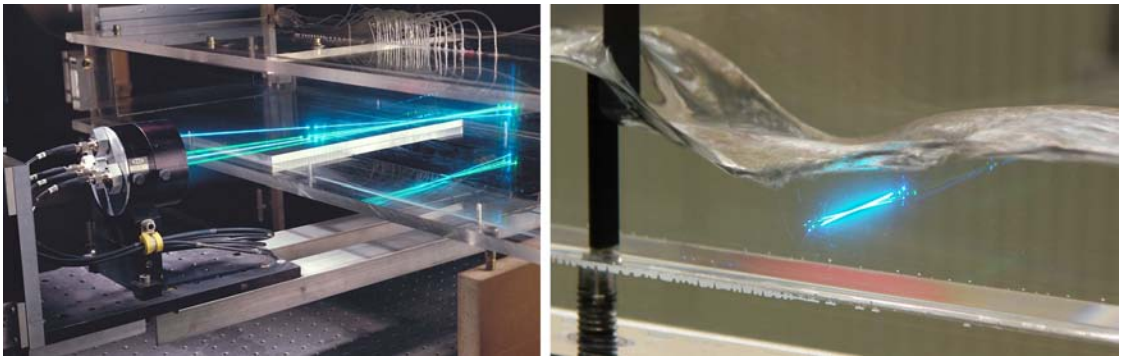

Figure 1.21: Laser Doppler velocimetry

Laser Doppler velocimetry (Figure 1.21) is a non-intrusive technique for flow measurement, developed at the 70's decade. The great advantage of this technique is that it can measure the flow velocity whatever it is (from mm/s to supersonic velocities). LDV uses the Doppler shift in a laser beam to measure the velocity in transparent or semi-transparent fluid flows. Two laser beams of collimated, monochromatic and coherent light (He-Ne, Argon ion or laser diode) passing through an optic lens are focused to intersect at their focal point (waist of the beam), where they interfere and generate a set of straight fringes. The particles, naturally present or induced in the flow, pass through the fringes reflecting light that is collected by a receiving optics. The wave frequency of the reflected light differ from the emitted one, being the Doppler shift between the incident and scattered light proportional to the particle velocity.

Laser Doppler velocimetry allows measuring velocities in both liquid and gases. Whereas liquids contain enough pollutants, gases need seeding of some kind. If three velocity components need to be obtained, three pairs of laser beams are required on the measurement area. The main drawback of this technique is that the studied zone needs to have full optical access.

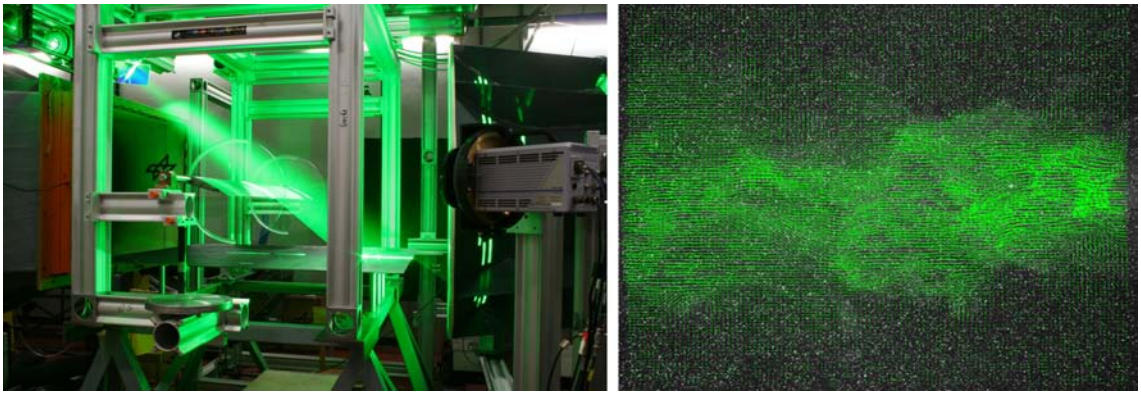

Figure 1.22: Particle image velocimetry

In the mid 80's appeared the first applications of particle image velocimetry (Figure 1.22) in flow characterization. This non-intrusive technique uses two laser sheets delayed one from another a time interval, Δt, and a synchronized high speed camera to measure the flow velocity. The particles present in the seeded flow are illuminated by the laser sheets, and the

scattered light is recorded by the camera. Images are processed to determine the distance travelled by particles, Δx, allowing to calculate the particle velocity ($u = \Delta x/\Delta t$) and, hence, the flow velocity. The image processing requires algorithms such as autocorrelation or cross-correlation, which suppose the main limitation of the method in addition of the optical access. The main advantage of this technique respect to the LDV and HW is that it measures the velocity in a whole plane instead of a single point. Three-dimensional fields could also be obtained using stereoscopic techniques with two cameras.

A brief comparison of the revised non-stationary measurement techniques is presented in Table 1.1.

	HWA	**LDV**	**PIV**
Frequency response	High (100 kHz)	Medium (30 kHz)	Limited (1-10 kHz)
Measurement process	Give velocity at a single spot	Give velocity a single spot	Give velocity maps
Calibration	Required	Not required	Not required
Optical access	Not required	Required	Required
Intrusivity	Intrusive	Non-intrusive	Non-intrusive
Seeding	Particles not required	Particles required	Particles required
Cost	Moderate (60 k€)	High (100 – 250 k€)	High (100 – 250 k€)

Table 1.1: Comparison of non-stationary measurement techniques

1.5 State of the art

This thesis comprises not only the aerodynamic characterization of an elliptic aerofoil but the design and development of an adequate facility and the tune-up of hot-wire anemometers and particle image velocimetry devices. Thus, the state of art comprehends briefly the existent bibliography concerning wind tunnels, WHA and PIV before addressing elliptic profiles and aerodynamic phenomena (flow separation, bubbles and wake).

1.5.1 Aerodynamic wind tunnels and measurement techniques

1.5.1.1 Wind tunnels

Wind tunnels represent a useful tool for investigating flow phenomena under controlled circumstances. They have been used widely to conduct fundamental research concerning flow behaviour related to flight for over a century (Prandt and Tietjens (1934); Baals and Corliss (1981)). The first wind tunnel was designed and operated by Frank H. Wenham in 1871 (Baals and Corliss (1981)). He measured the lift and drag forces created by the air rushing by, which represented a breakthrough in aeronautics. Wenham and his colleagues tested the effects of low angles of incidence, as well as the effect of the aspect ratio (narrow wings provided much more lift than stubby wings with the same areas). In 1901, The Wright brothers used a simple wind tunnel to study the effects of airflow over various shapes (Dodson (2005)). They developed their early wing designs using sub-scale tests in a small, low-cost tunnel. The use of wind tunnels subsequently proliferated as the science of

aerodynamics and discipline of aeronautical engineering. In 1930's the effects of free-stream turbulence on shear layers became apparent and it laid emphasis on wind tunnels with low levels of turbulence and unsteadiness. Mehta and Bradshaw (1979) published the design procedure of small blower tunnels establishing that most of the presented information was applicable to wind tunnels in general. More books and articles have been written about this topic, e.g. Bradshaw and Pankhurst (1964); Rae and Pope (1984) are other useful references when designing and constructing low-speed wind-tunnels.

Wind tunnel testing has become more recently an integral part of the automobile design and development process (Hucho and Sovran (1993)). Moreover, they have been used in diverse applications such as the study of atmospheric wind erosive effects and building-wind interactions. Some of the largest and most complex wind tunnel facilities operated by government, universities and industry are catalogued by Penaranda and Freda (1985), while list of some larger low-speed facilities is provided by Rae and Pope (1984).

1.5.1.2 Wind tunnel contractions

The design of the optimal contraction section in a wind tunnel is critical to obtain valuable data from the facility. A good choice is a crucial milestone to assure high-quality flow characteristics and, therefore, it deserves special attention. Typically, converging nozzles have been constructed using a pair of cubic polynomials where, for a fixed length and contraction ratio, the location of the joining point has been found to be determinant in the optimization of the designs (Bell and Mehta (1989); Morel (1975, 1977); Ramaeshan and Ramaswamy (2002). Figure 1.23 shows a typical example of the wall velocity distributions given by a three-dimensional potential flow code (VSAERO) (Bell and Mehta (1989)).

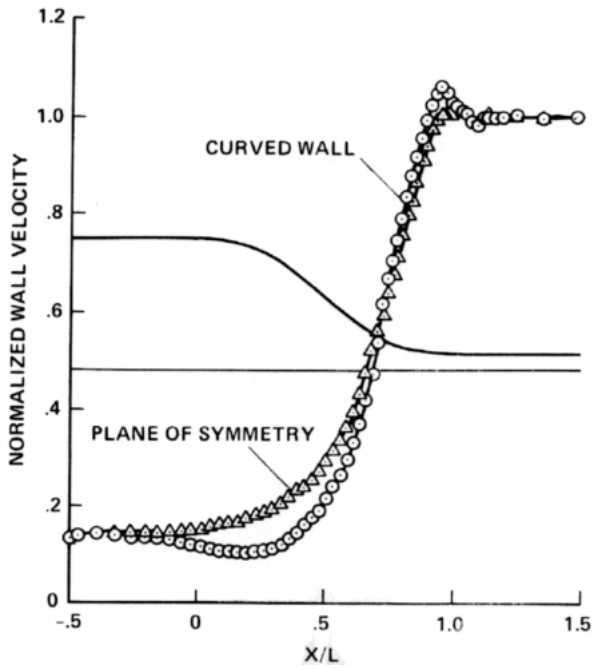

Figure 1.23: Typical calculated wall velocities (Bell and Mehta (1989))

Years ago, the analytical resolution of inviscid flow equations to study the flow field, required a lot of time. For that reason, design charts for nozzles were developed, and recurrent calculations were avoided (Bell and Mehta (1989); Fang (1997); Fang et al. (2001); Morel

(1975, 1977); Ramaeshan and Ramaswamy (2002)). However, due to the great computational advances and the development of more efficient codes, CFD has currently become an essential tool to optimize wind tunnel contractions. It is an accurate way to analyse the flow behaviour within the nozzle and, moreover, allows geometric parameters to be optimized. Because of the smooth transition of the side walls and the high Reynolds number reached within the nozzle, boundary layer growth is controlled and viscous computations are expected to be reasonably simple (no swirl flow, without separation and unsteadiness, first order turbulence modelling...).

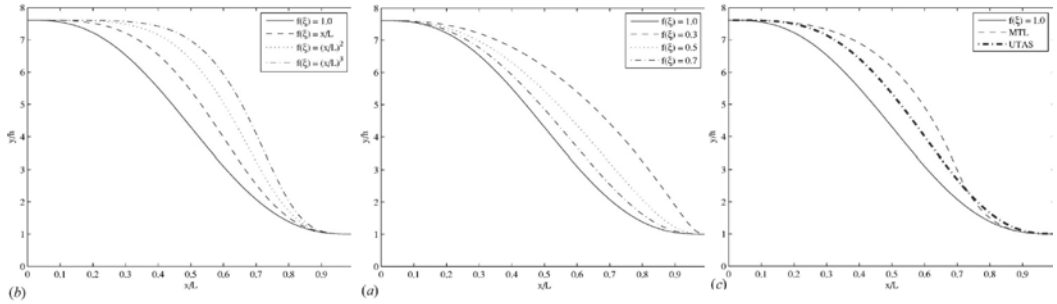

Figure 1.24: Contemporary contraction shapes investigated by Doolan (2007)

When designing a shape for a nozzle, one must keep in mind the most significant characteristics of a good design: prevent flow separation along the walls, reduction of mean and fluctuating velocity variations at the outlet, and increase of the flow mean velocity (Mehta and Bradshaw (1979)). A popular choice for wind tunnel contraction shapes has been the fifth-order polynomial introduced by Bell and Mehta (1988), however, other profiles have been studied throughout the years (Lindgren and Johansson (2002); Sargison et al. (2004); Brassard and Ferchichi (2005)). Figure 1.24 and Table 1.2 show a comparison of contraction shapes gathered by Doolan (2007).

Contraction shape	Separation	Re_θ	Exit plane uniformity
Fifth-order polynomial $f(\xi)=1.0$	No	344.49	0.004
Fifth-order polynomial $f(\xi)=0.3$	Yes	—	—
Fifth-order polynomial $f(\xi)=0.5$	No	277.15	0.017
Fifth-order polynomial $f(\xi)=0.7$	No	309.21	0.007
Fifth-order polynomial $f(\xi)=x/L$	No	332.18	0.004
Fifth-order polynomial $f(\xi)=(x/L)^2$	Yes	—	—
Fifth-order polynomial $f(\xi)=(x/L)^3$	Yes	—	—
MTL	No	354.29	0.004
UTAS	No	309.46	0.008

Table 1.2: Comparison of contraction shapes, 9m/s (Doolan (2007))

1.5.1.3 Hot-wire anemometry

According to Comte-Bellot (1977), the precise origin of hot-wire anemometry cannot be accurately determined. Boussinesq (1905) conducted one of the earlier studies of heat transfer from a heated wire. Afterwards, Boussinesq (1914) extended his results, attempting to

experimentally verify the theoretical results. These first studies of hot-wire anemometry only took into account the mean heat transfer characteristics from heated wires. Dryden and Kuethe (1929) were the first researchers in made quantitative measurements of fluctuations in subsonic incompressible flows using constant current anemometry, where the frequency response of the wire was extended by the use of a compensating amplifier. A constant temperature anemometer for measuring fluctuations by using a feedback amplifier to maintain a constant wire temperature up to a given frequency was developed by Ziegler (1934). This measurement technique was extended to compressible flows by Kovasznay (1950, 1953) but, due to their complexity, in which the heat transfer from a wire is a function of velocity, density, total temperature and wire temperature, these flow regimes were abandoned until the 70's and 80's (Rose and McDaid (1976)). Thanks to great technology advances in electronics and data acquisition, hot-wire anemometry has experienced an important development and, nowadays, it is a consolidated measurement technique used in a large number of investigations worldwide. A sample of published work conducted using hot-wire anemometry is Sandborn (1974); Baldwin et al. (1960); Vagt (1979); Kovasznay (1959); Owen and Foire (1986); Laufer (1975); Olivari (1980); Comte-Bellot et al. (1981). In addition, several books have been written about WHA (Sandborn (1972); Perry et al. (1982); Lomas (1986); Goldstein (1983); Bruun (1995)), and chapters have been included in books where the general subject was related with anemometry (Hinze (1975); Smol'yakov and Tkachenko (1983); Bradshaw (1971)).

1.5.1.4 Particle image velocimetry

A hundred years ago appeared the first concept of particle image velocimetry when Ludwig Prandtl designed and used flow measurements techniques with a suspension of mica particles in a water channel (Raffel et al. (2007)). Even though this first step only provided a qualitative description of the flow field, advances in measurement techniques have made possible to extract quantitative values of complex flows. The feasibility of Laser Speckle Velocimetry (LSV) was demonstrated in 1977 using a laminar tube flow (Barker (1997); Dudderar and Meynart (1997); Grousson and Mallic (1997)). Practical measurements of laser speckle velocimetry were applied to analyse the flow of liquids and gases (Meynart (1992, 1993)). The first time that the name *particle image velocimetry* was used was in 1984 by Adrian (1984). He introduced the concept in a scientific paper which stated that the low seeding density mode of LSV should be more appropriately classified as PIV (Pickering and Halliwell (1984)). This measurement technique became popular since it offered a new highly promising way to study the structure of the fluid flow. Many researchers have studied how to improve performance of optical and digital methods in the evaluation of PIV recordings (e.g. Adrian and Yao (1985); Adrian (1986)). According to Keane and Adrian (1992), the major milestone for the PIV technique was the use of a CCD camera in synchronization with a double oscillator Nd:YAG laser source. At the beginning of the 90's several papers presented the principle and fundamentals of digital PIV (Willert and Gharib (1991); Westerweel (1993)). Nowadays the PIV technique is still being continuously developed. Recent progresses in cross-correlation digital PIV methodologies have made possible to deliver higher accuracy referred to sub-pixel velocity measurements (Lourenco and Krothapalli (1995); Westerweel et al. (1997); Nogueira et al. (1999); Hart (2000); Werely and Meinhart (2001); McKenna and McGillis (2002)).

1.5.2 Flow structure around an aerofoil

1.5.2.1 Flow separation

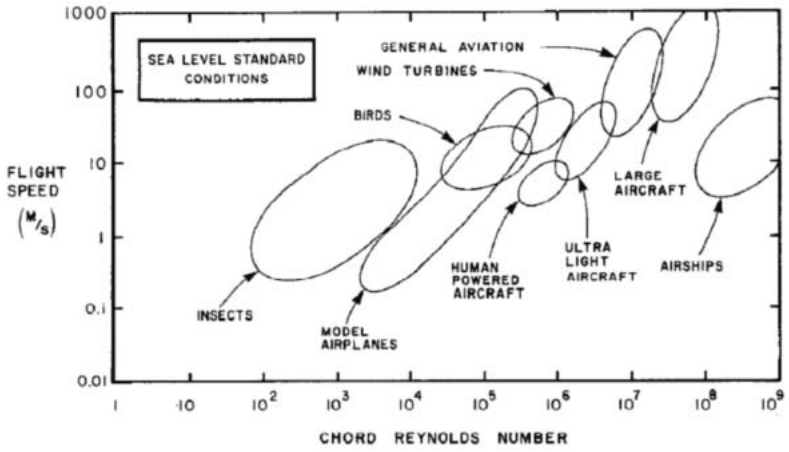

Figure 1.25: Chord Reynolds number for various classes of devices (Lissaman (1983))

A growing number of new mechanical systems such as small-scale turbines and unmanned aerial vehicles, lifting surfaces operate at relatively low chord Reynolds numbers, i.e. $Re_c \leq 5 \times 10^5$. Figure 1.25 by Lissaman (1983) shows the range of Reynolds numbers in which general classes of natural and man-made flying objects operate. At low Reynolds numbers, the operation of the aerofoil differs significantly from that for high Reynolds number flows (e.g. Tani (1964); Charmichael (1981); Mueller and DeLaurier (2003)). In particular, the laminar boundary layer on the upper surface of the aerofoil often separates and forms a separated shear layer. It is well known that, for low Re_c flows, viscous effects play a much more important role than in high Re_c flows, in which viscous effects are either neglected or restricted to a thin region near the body surface. Figure 1.26 shows that a significant change in the lift to drag ratio of typical smooth aerofoils occurs at a Reynolds number of approximately 10^5.

During 1980s most of published literature on low Re_c aerodynamics of aerofoils were focused on surface flow behaviours including boundary layer separation, reattachment and separation bubble, which have a significant influence on aerodynamic forces (e.g. Arena and Mueller (1980); Roberts (1980); Batill and Mueller (1981); Mueller and Batill (1982); Pohlen and Mueller (1984)) as reviewed by Lissaman (1983) and Marchman (1987). The separation of the boundary layer, also known as stall, over surfaces is a common and mostly undesired effect in fluid mechanics caused by a severe adverse pressure gradient (e.g. Simpson (1989) and Simpson (1996)), a geometrical aberration (e.g. Bradshaw and Wong (1972) and Kim et al. (1980)) or by other means. The detachment is often accompanied by significant thickening of the rotational flow region adjacent to the surface and an increase in the velocity component that is normal to the surface. The effects of this phenomenon in aerofoils are always losses of some kind, including loss of lift, drag increase, pressure recovery losses, etc. As a consequence, big efforts have been made by engineers to alter its location or avoid it entirely.

The mechanism of flow separation and stall has been reported widely in literature (e. g.

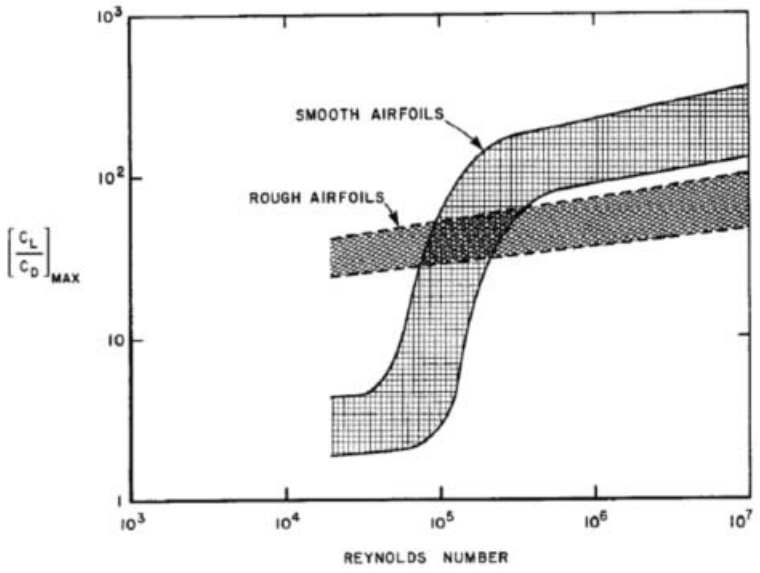

Figure 1.26: Lift to drag ratio as a function of Reynolds number (Lissaman (1983))

Devinant et al. (2002); Mueller and DeLaurier (2003); Larsen et al. (2007); Yang et al. (2008)). When the aerofoil angle of attack is increased from zero to stall, a number of phenomena can be observed: (i) the separation point on the suction side moves towards the leading edge; (ii) the separated boundary layer is laminar, though transition to turbulence in the shear layer occurs initially at the tail of the separated boundary layer and shifts towards the separation point; (iii) both lift and drag grow. When it is approached the angle of stall, transition to turbulence takes place near the separation point. In this situation the separated boundary layer reattaches forming a separation bubble. This bubble may suddenly burst resulting in the stall. At a sufficiently low chord Reynolds number, the transition to turbulence does not occur near the separation. Instead, the separated boundary layer remains laminar for a rather long downstream distance and does not reattach. According to Zhou et al. (2011), the stall will not occur without the separation bubble generated.

1.5.2.2 Separation bubble formation at low Re

At certain Reynolds numbers and angles of attack, the laminar boundary layer may separate from the leading edge since the flow energy at this region is not enough to overcome the developed adverse pressure gradient. Then, if the separated shear layer experiments a fast transition to a turbulent flow, a reattachment as a turbulent boundary layer could be induced. At this point, a laminar separation bubble is formed (Jones (1938); Diwan and Ramesh (2007)). These bubbles are typically observed close to the leading edge of thin aerofoils, on gas turbine blades and on low Reynolds number micro-aero-vehicle wings according to Diwan and Ramesh (2007). If the Reynolds number is sufficiently high, transition from laminar to turbulent flow will take place ahead of the theoretical laminar separation point, namely that point at which separation would have occurred if the boundary layer had remained laminar. Under these circumstances, the bubble formation will be precluded. On the other hand, if the Reynolds number is sufficiently low, the separated flow will not reattach to the surface and no bubble will be formed. Therefore, the bubble formation is possible only for a certain range of Reynolds numbers that will depend on the

pressure distribution, the surface curvature, the surface roughness and the turbulence of the free-stream. According to Mueller and DeLaurier (2003), the upper limit of the Reynolds range at which the creation of the laminar separation bubble takes place is $Re_c \leq 5 \times 10^5$. Huang and Lin (1995) established the lower limit at which the shear layer does not have enough energy to reattach and the bubble is not produced as $Re_c < 1 \times 10^4$. These values should be taken as estimations since the real flow conditions depend on aerofoils shape, roughness, pressure distribution and further factors (Crabtree (1959) and Aubertine et al. (2004)).

The presence of bubbles has a negative effect on the performance of the device because it modifies the effective shape of the aerofoil. Thus, the understanding of the physics of the laminar separation bubble and the determination of possible ways to control it are essential for efficient design of the aerofoils. Tani (1964) study in this matter was one of the earliest. He investigated the flows involving the separation bubbles and their effect on several types of stall, leading edge stall, trailing edge stall and thin aerofoil stall. He observed that the presence and characteristics of the stall were directly related to the presence and type of separation bubbles. Depending on the size of bubble, laminar separation bubbles were categorized as either short or long bubbles. A long bubble occupies a significant portion of the aerofoil surface and affects the inviscid pressure and velocity distributions over much of the aerofoil, whereas a short bubble covers only a small portion of aerofoil surface and does not affect the pressure and velocity distributions. Figure 1.27 (a) depicts a long laminar separation bubble at a small angle of attack (Mueller (1985)). In this situation the boundary layer thickness is increased, the lifting forces deteriorate and the pressure drag increases. If the Reynolds number increases or the angle of attack increases at a fixed Re, turbulent reattachment happens rapidly and the pressure gradient is virtually unaffected. Figure 1.27 (b) illustrates a short laminar separation bubble with the turbulent boundary layer separating near the trailing edge. As Re or angle of attack is increased even further, this unstable short bubble may take the shape of a long bubble or separate without reattaching, and it is said to have burst (Lissaman (1983); Mueller (1985)) accompanied by the characteristic decrease in lift and increase in drag. Figure 1.27 (c) shows the bursting of the short laminar separation bubble which remains detached over a stalled aerofoil.

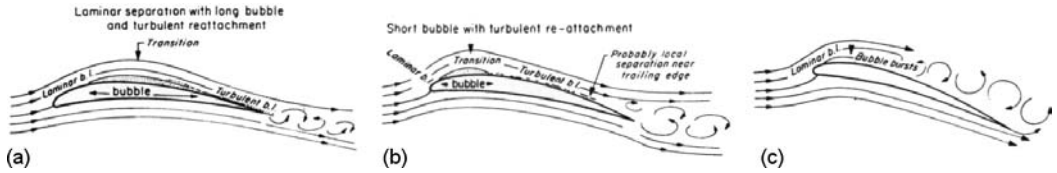

Figure 1.27: (a) Long laminar separation bubble. (b) Short laminar separation bubble with turbulent separation downstream. (c) Bursting of the short laminar separation bubble without reattachment. Mueller (1985)

Gaster (1967) was the first to study the stability characteristics associated with transition of laminar separation bubbles. The study was made of laminar separation bubbles formed over a wide range of Reynolds numbers and in a variety of pressure distributions. His final conclusion was that the structure of the bubble depended on the value of the Reynolds number of the separating boundary layer and a parameter based on the pressure rise over the region occupied by the bubble. Later on, Lissaman (1983) provided a general review of low Reynolds number flow and details on the formation and size of the laminar separation bubble concluding that the bubble size significantly impacted the drag and the stall of the aerofoil. Lin and Pauley (1996) conducted an unsteady simulation of an 2D aerofoil to

study the effects of the Reynolds number and angle of attack on the laminar separation bubble. They compared their results with low-turbulence wind tunnel tests and found favourable comparison between the two. They concluded that two dimensional vortex structures shed after laminar separation control the laminar separation bubble and can be regarded as reattachment mechanism. Recently, a number of studies have been done towards exploring the dynamics of separation bubbles which constitute at the same time laminar separation, transition to turbulence and aspects of both the attached and free shear layer (Watmuff (1999); Pauley et al. (1990); Marxen et al. (2003)).

1.5.2.3 Wake behind an aerofoil

The development of coherent structures in the aerofoil wake at low Reynolds numbers is of interest since it affects to their performance and governs the flow around downstream objects. These structures can result in undesirable structural vibrations and noise generation.

The structure and characteristics of two-dimensional bluff-bodies wakes have been the subject of active research over the past decades (e.g. Gerrard (1966); Perry et al. (1982); Cimbala and Krein (1990); Roshko (1993); Williamson (1996)). They offer information about the wake of an aerofoil at post-stall angles of attack because it can be expected to behave similar to that of a bluff body according to Huang et al. (2001). Of the few other investigations of wake turbulence structures produced by aerofoils, the experiments of Cambell (1957) provide information of the wake turbulence downstream of a two-dimensional aerofoil at low speeds. The study includes turbulence intensity distributions and power spectra of the velocity fluctuations as well. An experimental investigation of the near wake of a thin aerofoil (NACA 0012) at various angles of attack was reported by Hah and Lakshminarayana (1982). The mean-velocity, turbulence intensity and Reynolds-stress components showed the complex nature of the wake and its asymmetrical behaviour.

More recently, Akbari and Price (2003) simulated the flow over a pitching NACA 0012 aerofoil at $\alpha < 18°$ using a vortex method to solve the two-dimensional Navier-Stokes equations in vorticity/stream-function form. They noticed that the pitching oscillations of the aerofoil delayed the flow separation to higher angles compared to a static stall case. The lift force was observed to increase well beyond that at the static stall α. Kelvin–Helmholtz (K–H) vortices were observed on the suction surface following the release of the Karman vortex. Yarusevych et al. (2006) studied the boundary layer and turbulent wake of a NACA 0025 aerofoil at three Reynolds numbers ($Re_c = 5.5\times10^4$, 1.0×10^5 and 1.5×10^5) and three angles of attack (0°, 5° and 10°). Laminar boundary layer separation occurred on suction surface for all the cases. At $Re_c = 1.5 \times 10^5$ the separated boundary layer underwent transition to turbulence and reattached on the aerofoil surface, while at $Re_c = 5.5 \times 10^4$ and 1.0×10^5 failed to reattach. Transition was stimulated by the K–H vortices in the shear layer at the higher Re_c and broke down during the transition process, resulting in immediate reattachment. On the other hand, at the lower Re_c (i.e., 5.5×10^4 and 1.0×10^5) the vortices propagated further downstream, influencing Karman vortex shedding. Alam et al. (2010) studied the lift force and the near wake of a NACA 0012 aerofoil over the range of angles of attack of 0°-90° and ultra-low Reynolds numbers ($Re_c = 5.3\times10^3$ - 5.1×10^4). They examined the near-wake characteristics including the vortex formation length, wake width, span-wise vorticity, wake bubble size, wavelength of K-H vortices, Strouhal numbers and their dependence on the angle of attack and Reynolds numbers.

1.5.3 Elliptic aerofoils: experimental studies

The characterization of the wake, vortex shedding and trailing edge noise are some of the milestones in the study and improvement of elliptic aerofoil applications. The specific bibliography regarding the aerodynamic characteristics of elliptic aerofoils is limited, while more information has been published about elliptic cylinders, which thickness ratios are higher. One of the first studies has been published almost a century ago by Zahn et al. (1929). They studied the drag and pressures over the surface of four elliptic cylinders with four thickness ratios ($t/c = 0.40$, 0.33, 0.29 and 0.25) and various yaw angles. They found that, for low Re numbers, optimal drag characteristics took place when the elliptic cylinder had a thickness ratio of 0.25, whereas for high Re numbers, improved characteristics were obtained for thickness ratios smaller than 0.25. A decade after, Shubauer (1939) reported the influence of the free-stream turbulence on the boundary layer transition for a 0.33 thickness ratio elliptic cylinder at zero angle of attack. A conventional hot-wire anemometer was used to measure magnitude and frequency of speed fluctuations in the boundary layer finding that the transition location depended on both the turbulence scale and the free-stream turbulence intensity. Later on, Hoerner and Borst (1975) published the lift coefficient of elliptic aerofoils with several thickness ratios and a range of Reynolds numbers $2 \times 10^6 < Re < 7 \times 10^6$. White (1986) described the effect of laminar and turbulent flow conditions on the drag coefficients of some elliptic cylinders with various thickness's at zero angle of attack. Ota et al. (1987) studied the flow around an elliptic cylinder of thickness ratio 0.33 in the critical Reynolds number regime, $8.5 \times 10^4 < Re < 31.2 \times 10^4$. Their research included mean static pressure measurements along the surface and hot-wire anemometry measurements in the near wake. Nair and Sengupta (1997) studied the unsteady flow past two elliptic cylinders with $c/t = 4$ and 10 via the solution of the 2-D Navier-Stokes equations for two Reynolds numbers, $Re = 3 \times 10^3$ and 1×10^4 at different angles of attack. . They observed that ellipses developed asymmetry much earlier than circular cylinders.

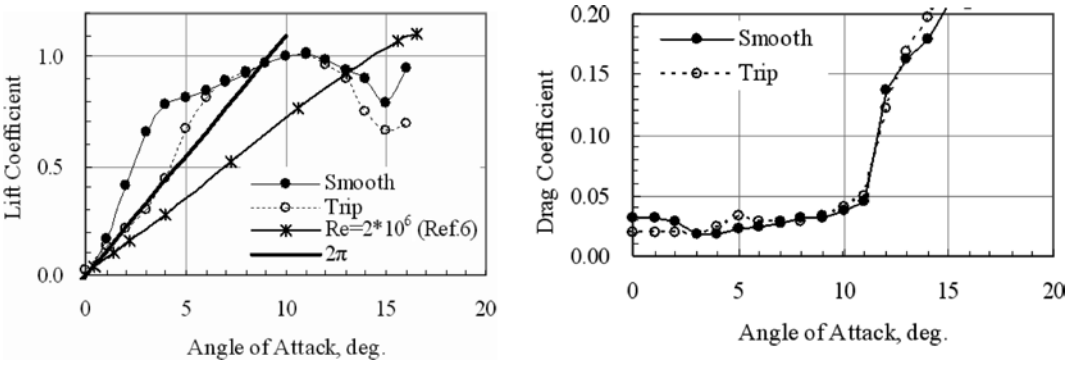

Figure 1.28: Drag and lift coefficients by Kwon and Park (2005)

Most recently, Moon-Sang and Sengupta (2005) simulated the unsteady viscous flow physics over two-dimensional ellipses with different thickness ratios $t/c = 0.62$, 0.80, 1 and 1.25 and various Reynolds numbers 200, 400 and 1×10^3. They observed that the Re and the cylinder thickness affected significantly the frequencies of force oscillations as well as the mean and amplitude values of the drag and lift forces. Kwon and Park (2005), studied the aerodynamic characteristics of a $t/c = 0.16$ thickness elliptic aerofoil at a $Re = 3 \times 10^5$. They performed wind tunnel tests measuring aerodynamic forces and moments for that aerofoil (see Figure 1.28), with and without a boundary layer transition trip and with low

free stream turbulence intensity (0.12%). Trip devices were attached on both the pressure and suction surfaces of the aerofoil at about 10% chord length to induce turbulent flow over the majority of the surface. The boundary layer trip technique is generally used in wind tunnel tests to simulate full scale or high Re flows in low Re aerofoil test conditions in a laboratory to enforce transition locations and to eliminate laminar separation bubbles (Kwon et al. (2006)). It was found that the lift curve of the elliptic aerofoil varied as function of the Reynolds number and lift did not linearly increase with angle of attack, in contrast to the behaviour of conventional aerofoils. In the experiment, C_L curves for both smooth and tripped cases behaved similarly when the angle of attack exceeded 6 °. Kwon also found that the asymmetric flow separation behaviour around the smooth aerofoil trailing edge caused a lift curve slope much greater than 2π at low angles of attack which differs from the behaviour of conventional aerofoils.

Kwon et al. (2006) extended the previous research on elliptic aerofoils to study in detail the boundary layer transition process using a particle image velocimetry (PIV) technique. Tests were conducted on the same elliptic aerofoil as in Kwon and Park (2005) for the same flow conditions. Velocity profiles were measured and shape factors were calculated from PIV measurements. Intermittent factors were computed from surface mounted hot film sensor measurements. The authors concluded that the unusual aerodynamic characteristics of elliptic aerofoils, such as a high lift curve slope and high drag coefficient at low angle of attack, were a consequence of the different flow regimes, i.e. laminar or turbulent, between the suction and pressure surfaces as angle of attack increases.

1.6 Objectives

The main objective of this thesis is to perform an aerodynamic study of a low-thickness elliptic aerofoil ($c/t = 11$) at low Reynolds numbers with various angles of attack. The study is focused on the use of two specific measurement techniques available; hot-wire anemometry and particle image velocimetry. The utilization of those techniques implies the development of appropriate facilities and needed procedures. The outcomes of this thesis will be the starting point for future aeroacoustic investigations. In addition, the experimental data obtained about velocity and turbulence will become valuable information for checking computational fluid dynamic results.

The general objective described before can be divided into a set of specific tasks as follows:

1. Design and construction of a low-speed wind tunnel with optical access for PIV measurements and suitable to recirculate tracer particles, maintaining the required concentration.

2. Implementation of PIV, a measurement technique never used before at the Fluid Mechanics Area of the University of Oviedo.

3. Study of possible tracer particles, determining which one offers best results for the experimental work.

4. Experimental analysis of the flow around the aerofoil using PIV.

5. Development of new codes using MATLAB for estimating turbulent statistics from PIV experimental data.

6. Experimental analysis of the downstream wake flow using HWA.

7. Development of new codes using MATLAB for estimating turbulent statistics from HWA experimental data, taking advantage of the frequency domain information that provides such technique.

8. Calculation of the drag force over the aerofoil using the velocity measurements available.

In conclusion, the aim of this work is not only to investigate the aerodynamics of a slender elliptic aerofoil but also to perform a methodological study that that provides the basis for future investigations in the Fluid Mechanics Area of the University of Oviedo.

CHAPTER 2

Fundamentals of HW anemometry and PIV

Both hot-wire anemometry and particle image velocimetry, have been used in this thesis to perform the experimental campaign. This chapter includes the fundamentals of these two measurement techniques without going into great depth on the most complex theoretical aspects. The basics of the techniques are explained only to give the reader an overview of the subject matter.

2.1 Hot-wire anemometry

2.1.1 Introduction

Hot-wire anemometry is a measurement technique that obtains indirectly the velocity of the flow at a specific position. This type of probes consists of a short length fine wire of tungsten, platinum or platinum alloys (usually platinum-rhodium 90-10 percent or platinum-iridium 80-20 percent) attached to two prongs made of stainless steel or nickel. A scheme of a single hot-wire anemometer is shown in Figure 2.1. It is possible to measure the three velocity components using a three-wires probe. To determine the air speed, the probe measures the heat exchange variations of each heated wire. Since the air passing through dissipates part of the heat, it is possible to relate heat flux changes in the wire with the flow velocity. To maximize the spatial resolution, the time response and improve signal-to-noise ratio at high frequencies the wire length must be small. A typical wire is 1 mm length and 5 µm diameter.

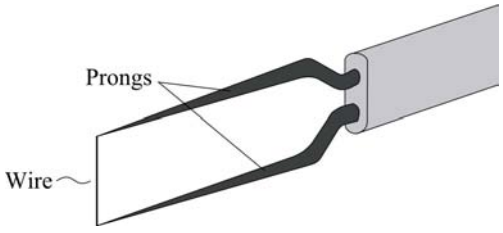

Figure 2.1: Single wire probe

The heat transfer from a heated wire placed in a fluid depend of both the properties of the fluid (density, ρ, viscosity, μ, thermal conductivity, k, specific heat, c_p, etc.) and the parameters of the flow (velocity vector, V, fluid temperature, T, pressure, p, etc.). The wire can be heated operating at constant current mode (CCA) or at constant temperature mode (CTA). The anemometer most used is the CTA and is the HWA employed in this thesis.

The basic operation of the HW probes is presented in the following sections. Hot-wire anemometry is a widely known technique, and all the concepts explained here can be expanded using existent bibliography (e.g. Bruun (1995)).

2.1.2 Heat transfer in the wire

Temperature distribution can be determined from the heat-rate balance equation from an incremental wire element, dx:

$$d\dot{Q}_e = d\dot{Q}_{fc} + d\dot{Q}_c + d\dot{Q}_r + d\dot{Q}_s \tag{2.1}$$

where $d\dot{Q}_e$ is the electrical heat-generation rate, $d\dot{Q}_{fc}$is the forced-convective heat-transfer rate, $d\dot{Q}_c$ is the conductive heat-transfer rate, $d\dot{Q}_r$ is the radiation heat-transfer rate, and $d\dot{Q}_s$ is the heat storage rate.

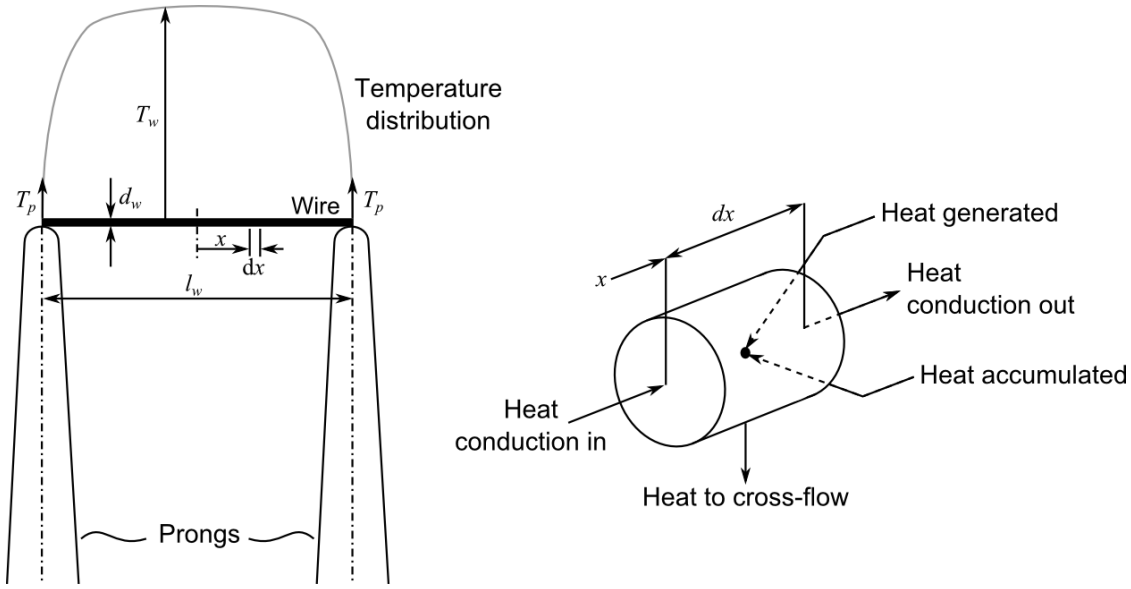

Figure 2.2: Hot-wire geometry and temperature distribution

The terms of Equation 2.1 can be expressed as:

$$d\dot{Q}_e = \frac{I^2 \chi_w}{A_w} dx \tag{2.2}$$

being I the electrical current, χ_w the electrical resistivity of the wire material at the local wire temperature T_w and A_w the cross-sectional area of the wire.

$$d\dot{Q}_{fc} = \pi d_w h (T_w - T_a) dx \tag{2.3}$$

where d_w is the diameter of the wire, h is the heat-transfer coefficient and T_a is the air temperature.

$$d\dot{Q}_c = -k_w A_w \frac{\partial^2 T_w}{\partial x^2} dx \tag{2.4}$$

being k_w the thermal conductivity of the wire material at the temperature T_w.

$$d\dot{Q}_r = \pi d_w \sigma \varepsilon (T_w^4 - T_s^4) dx \tag{2.5}$$

where σ is the Stefan-Boltzmann constant, ε is the emissivity of the sensor and T_s is the temperature of the surroundings. In most HWA applications this term is very small.

$$d\dot{Q}_s = \rho_w c_w A_w \frac{\partial T_w}{\partial t} dx \tag{2.6}$$

where ρ_w is the wire density and c_w is the specific heat of the wire material per unit mass.

During the normal operation of the probe, the heat exchange is mostly convective ($d\dot{Q}_{cf} \gg d\dot{Q}_c, d\dot{Q}_r, d\dot{Q}_s$), the terms of conduction, radiation and heat storage can be neglected. Thus, Equation 2.1 can be integrated as:

$$I^2 R_w = \pi d_w l h (T_w - T_a) \tag{2.7}$$

where R_w is the wire resistance.

The Nusselt number ($Nu = hl/k_f$) is often used in forced-convective heat-transfer phenomena. Substituting in Equation 2.1, it is obtained:

$$I^2 R_w = \pi l k_f Nu (T_w - T_a) \tag{2.8}$$

being k_f the fluid thermal conductivity and l the wire length.

The difficulty rests in obtaining the relation between the Nusselt number and the thermodynamic properties of the fluid around the wire. The most used correlations are of the form $a + bU^n$. Multiplying the Equation 2.8 by the wire resistance results:

$$E^2 = [A + BU^n](T_w - T_a) \tag{2.9}$$

where A represents the natural convection term and BU^n the forced convection term. The parameters A B and n must be obtained during the probe calibration. This equation is known as King's Law.

2.1.3 Resistance of the wire

The resistance, R_w, of a wire at a uniform temperature is given by

$$R_w = \frac{\chi_w l_w}{A_w} \tag{2.10}$$

where l_w is the wire length. It is common that manufacturers give resistance values at room temperature (20°C).

In order to maintain the wire at a certain temperature, the control circuit increases the voltage, E, until the wire resistance reaches a certain value. The normal operating temperature of the wire is about 250°C. The wire resistance at that specific temperature can be obtained as:

$$R_w = R_0[1 + \alpha_0(T_w - T_0)] \tag{2.11}$$

where T_0 (0°C) is the reference temperature and R_0, α_0 are the resistance and thermal resistivity coefficient at the reference temperature.

2.1.4 Control circuit

An electronic control circuit is required to maintain constant the temperature of the sensing element. The most important feature of these sensors is their ability to detect rapid variations of the flow speed. Consequently the control circuit must have a fast frequency response. This is achieved by incorporating a Wheatstone bridge, a feedback differential amplifier and an electronic-testing sub-circuit like the one shown in Figure 2.3.

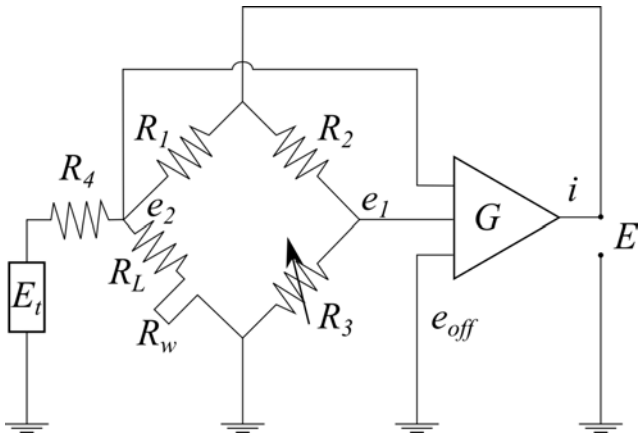

Figure 2.3: Control circuit for a CTA

The hot-wire probe is placed in the Wheatstone bridge, thus when the flow conditions vary, the error voltage $(e_2 - e_1)$ will be a measure of the corresponding change in the wire resistance. These voltages form the input to the operational amplifier. The amplifier has an output current, i, which is inversely proportional to the resistance change of the hot-wire sensor. Feeding this current back to the top of the bridge will restore the sensor's resistance to its original value.

Constant temperature anemometers have nowadays a low pass filter to reduce the signal-to-noise ratio, a sub-circuit to determine and establish the overheat ratio of the sensor and another sub-circuit to generate the square wave that allows frequency tests.

Frequency tests are performed introducing a small square wave in the bridge and observing the outlet voltage of the anemometer. The optimal frequency response is obtained adjusting the bridge parameters until an output signal similar to the one in Figure 2.4 is achieved. The cut-off frequency, f_c, is defined as

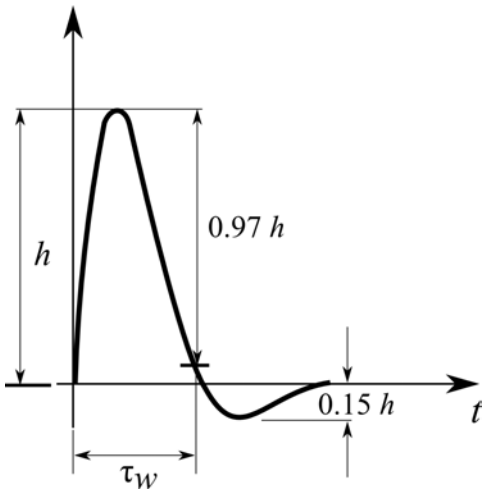

Figure 2.4: Sensor frequency response

$$f_c = \frac{1}{1.3\tau_w} \tag{2.12}$$

where τ_w is the time from the start of the pulse until the response signal has decayed to 3% of its maximum value.

2.1.5 HW probes manufacture

Due to the need to use HW probes of different geometries and configurations, in addition to the fragility and easy degradation of the wires, the Fluid Mechanics Laboratory of the University of Oviedo has a bench for manufacturing and repairing the probes. The members of the Fluid Mechanics Area have experience on design this type of probes; particularly they have worked recently on the development of new designs that avoid cross-wire interferences for a significant range of incident flow angles (Argüelles et al. (2012)).

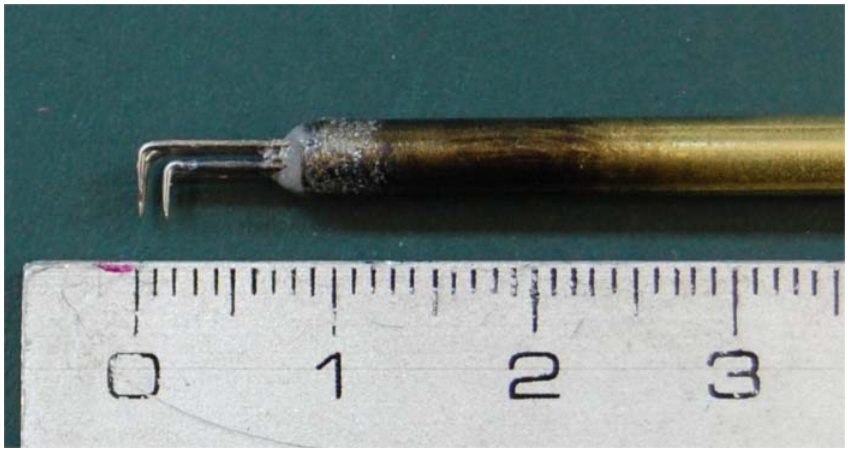

Figure 2.5: Image of a manufactured HW probe for this thesis

During the course of this thesis, two hot-wire X-probes (120°) have been manufactured to measure inside two different wind tunnels. The probe used for measuring velocity at the

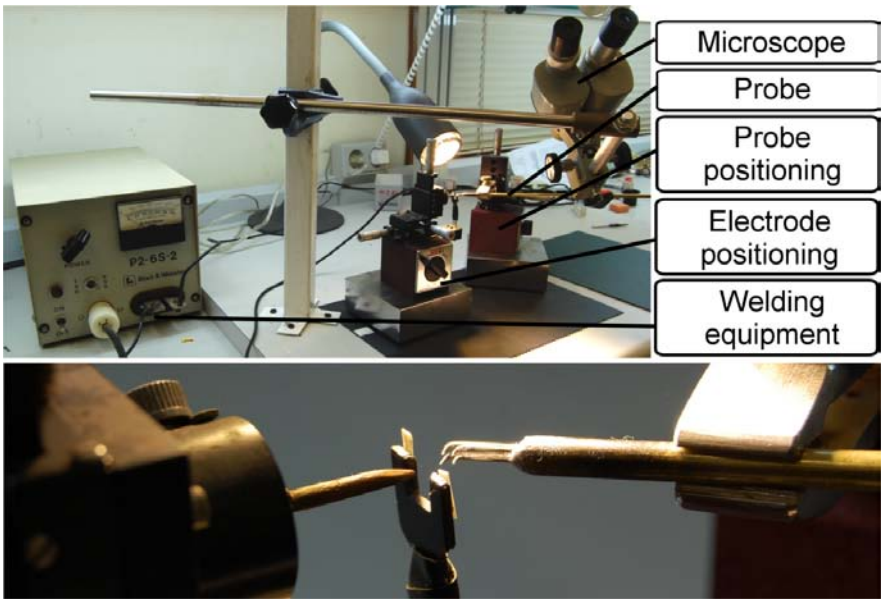

Figure 2.6: Bench for repairing HW probes and detail of HW welding process

aerofoil wake was the one with the more restrictive requirements because it needed shorter wire lengths. Figure 2.5 shows one of the manufactured HW probes. Both probes were made using tungsten wire of 5 µm diameter.

As it was stated before, the wires are extremely fragile and can degrade easily, losing its properties after several working hours. Moreover, the wires are broken or they come away from the prongs frequently. To address these drawbacks, a bench for repairing probes is available (Figure 2.6). The bench comprises a microscope for viewing the wire and prongs, a positioning element for the prong and electrode, and a welding equipment. As there is no specialized technicians to repair and weld the HW probes, it has been a requirement to learn the welding process in order to repair the damaged ones.

2.1.6 HW probes calibration

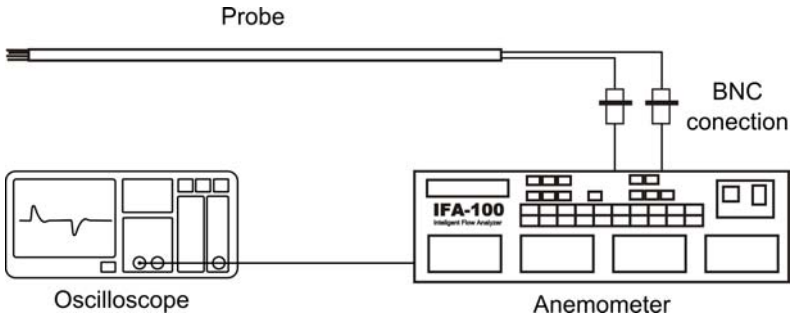

Figure 2.7: Frequency response adjustment of a HW probe

The calibration process is an essential part of the testing procedure with hot-wire anemometers because it obtains the law describing the wire behaviour. The probe is connected to a constant temperature anemometry unit, IFA-100 by TSI. This unit produces an output voltage-signal that can be conditioned. This signal relates the resistance of the wire with

the air velocity variations. It is important to adjust properly the frequency response of the signal, as it was stated in Subsection 2.1.4. The signal is adjusted using an oscilloscope to visualize the output voltage (Figure 2.7).

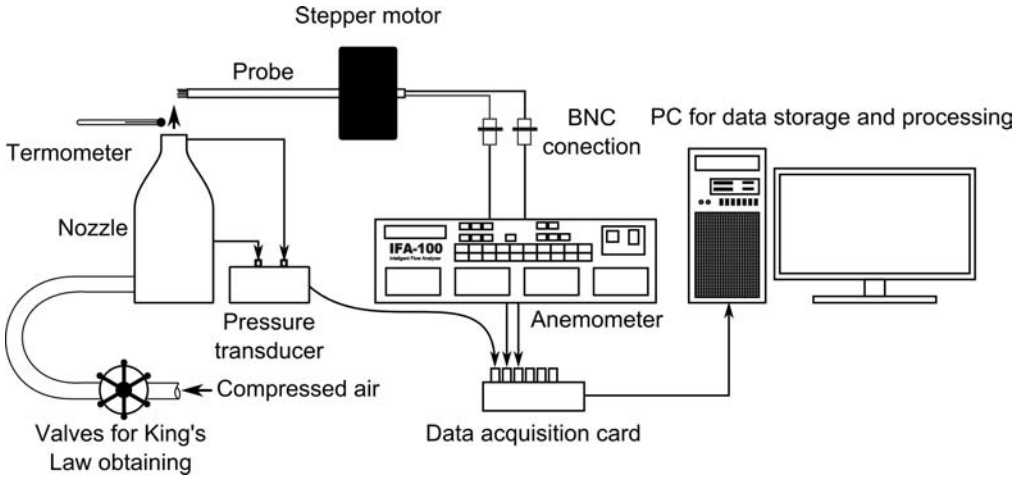

Figure 2.8: Calibration bench scheme

A calibration bench (Figure 2.8) is available to obtain the King's law for each wire. A sample of those obtained for a two-wire probe is shown in Figure 2.9. The calibration system consist of a nozzle which provides an air jet at a given speed, a gear system driven by a stepper motor to vary the incident air angle over the probe, a pressure transducer, a data acquisition system and a computer.

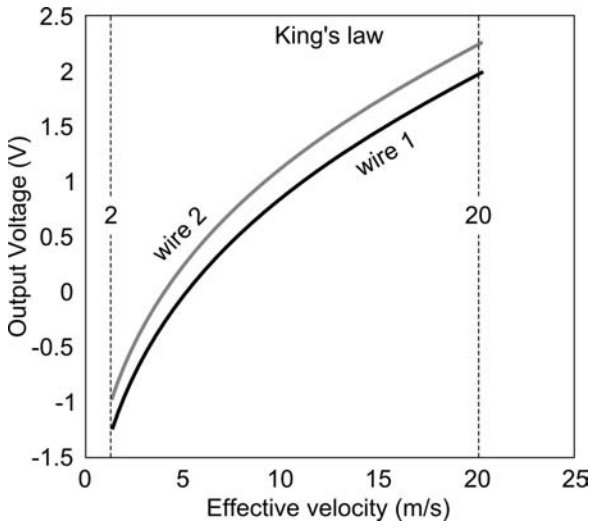

Figure 2.9: King's law sample of a two-wire probe

The air velocity coming out is determined by measuring the pressure in the settling chamber before the nozzle. The temperature is measured at the air jet. Several voltage values of the wire are recorded varying the air velocity. Those values are related with the air speed obtaining the required calibration curve. In addition, to determine the velocity components in bidimensional flows it is necessary to perform an angular calibration. The procedure consists on the variation of the incident air angle over the probe while the air velocity remains constant. Each wire gives an effective velocity used for defining a set of

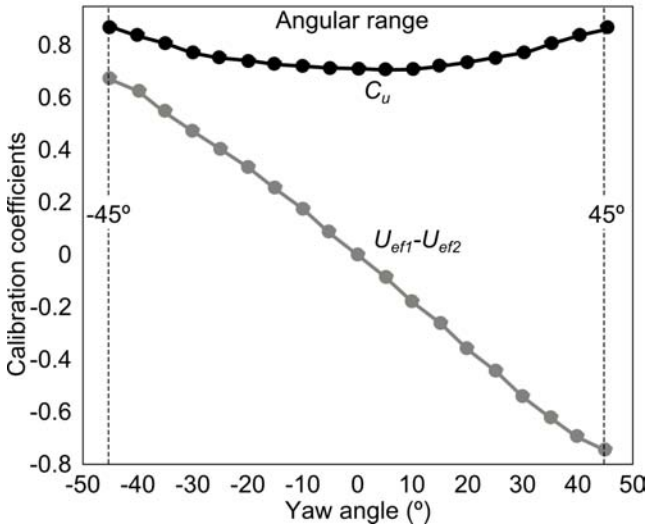

Figure 2.10: Angular calibration sample of a two-wire probe

coefficients.

$$Acf = u_{ef1} - u_{ef2} \qquad C_u = \frac{u_j}{\sqrt{u_{ef1} + u_{ef2}}} \tag{2.13}$$

where U_j is the velocity of the air jet and u_{ef1}, u_{ef2} are the effective velocities. Figure 2.10 show these coefficients as a function of yaw obtained during calibration of a two-wire probe.

2.1.7 Uncertainty of HW measurements

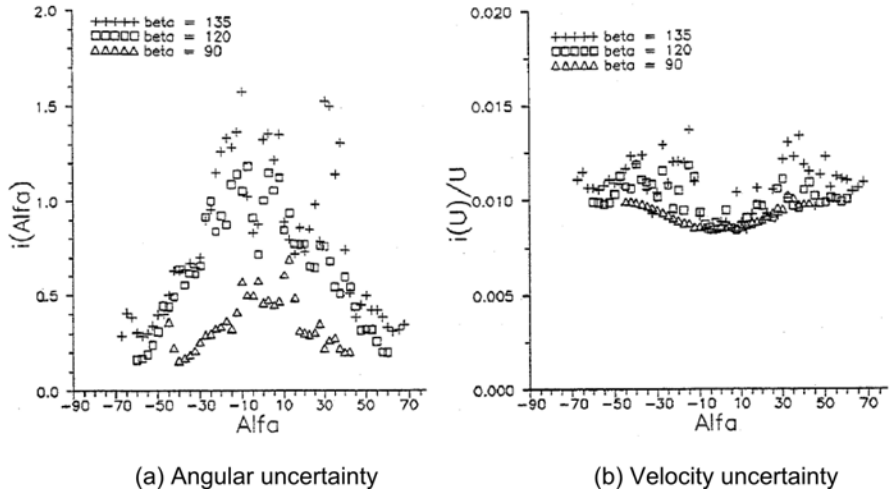

Figure 2.11: Typical error values obtained for 90°, 120° and 135° hot-wire probes (Blanco-Marigorta et al. (1998))

An analytical study of HW measurement uncertainties related to flow velocity and direction has been carried out. For the sake of brevity the process is not explained in this thesis and

the in depth uncertainty study can be read in Blanco-Marigorta et al. (1998); Argüelles et al. (2012).

It has been observed that the velocity uncertainty increase as the incident flow angles are closer to the angular calibration limits. The uncertainty of absolute velocity has been estimated to be 0.75% in the centre of the angular calibration range and up to 1.2% at the borders (±45°), while the angular uncertainty has been estimated to be 1° at the centre of the measurement range and 0.5° at the borders. Figure 2.11 shows typical error values obtained for 90°, 120° and 135° hot-wire probes.

2.2 Particle image velocimetry

2.2.1 Introduction

The particle image velocimetry is a measurement technique which allows obtaining instantaneous velocity field of a specific plane within a fluid. During the measurement process the laser sheet lights the seeded flow at two specific instants. Simultaneously, a CCD (*Charge Couple Device*) synchronized camera takes two images that are used to evaluate the particle displacement, magnitude related with the flow velocity. Figure 2.12 shows a typical PIV set-up in a wind tunnel. In order to evaluate the particle displacement, images are divided into small areas called *interrogation windows* and statistic methods are applied to them (see Figure 2.13). Knowing the time interval between the two recorded images, $\triangle t$, and the particle displacement, the velocity field can be obtained.

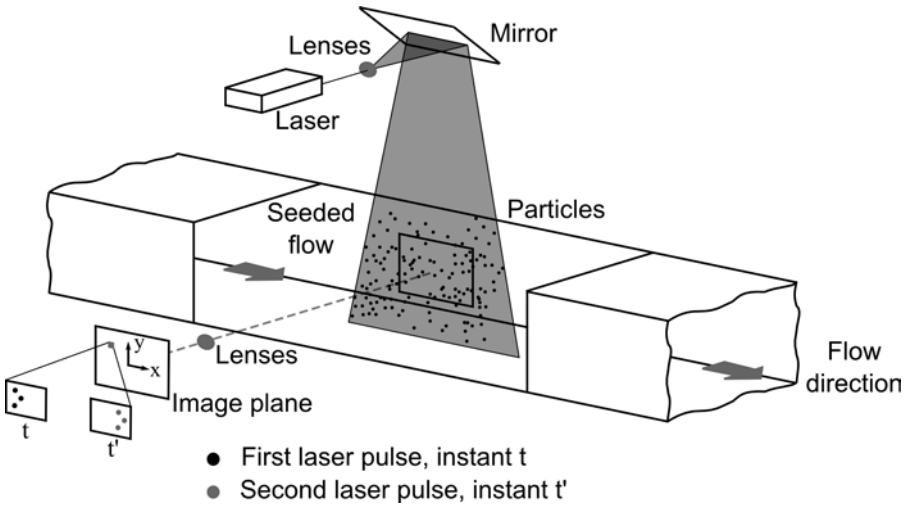

Figure 2.12: PIV experimental scheme

2.2.2 Seeding particles

The adequate selection of the seeding particles is one of the most important milestones in PIV. Because it is an indirect measurement technique -it obtains the velocity of the particles instead the velocity of the flow- ideally the fluid-mechanical properties of the

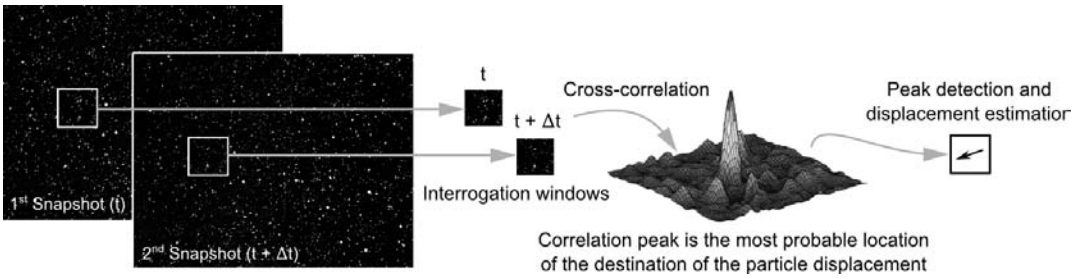

Figure 2.13: Cross-correlation procedure

particles must be similar to the ones of the flow. In addition, they must be able to scatter the light to allow the correct image acquisition.

Seeding

For proper flow tracking, is essential to generate a homogeneous particle seeding. A common-practice rule is that the particle distribution density, defined as the mean number of particles in a single interrogation window, should be at least 10. When gases are studied, the difference in density between the gaseous fluid and the particles is an important factor due the increment of velocity lag. Solid particles can agglomerate and are difficult to disperse, while liquid particles tend to evaporate quickly. Health considerations are crucial because researchers may inhale seeded air during testing. It is desirable that tracer particles should be non-toxic, non-corrosive, non-volatile, non-abrasive and chemically inert. The most common particles used for gases are listed in Table 2.1.

Type	Material	Mean diameter (µm)		
Solid	Polystyrene	0.5	-	10
	Alumina Al_2O_3	0.2	-	5
	Titania TiO_3	0.1	-	5
	Glass micro-spheres	0.2	-	3
	Glass micro-balloons	30	-	100
	Granules for synthetic coatings	10	-	50
	Dioctylphathalate	1	-	10
	Smoke		$<$	1
Liquid	Different oils	0.5	-	10
	Di-ethyl-hexyl-sebacate (DEHS)	0.5	-	1.5
	Helium-filled soap bubbles	1000	-	3000

Table 2.1: Seeding materials for gases (Raffel et al. (2007))

Particle size

The choice of particle size in gas flows is more critical than it is in liquids. If external forces (gravitational, centrifugal and electrostatic) can be considered negligible, the tracking capability of suspended particles is influenced only by the particle shape, the particle aerodynamically equivalent diameter d_p, the particle density ρ_p, the fluid density ρ_f, and fluid dynamic viscosityμ or kinematic viscosity, ν. Basset (1888) formulated the equation for unsteady motion of a suspended sphere relating the instantaneous relative velocity

$V = u_p - u_f$ between the particle and the fluid to the instantaneous velocities u_p and u_f of the particle and the fluid respectively (Figure 2.14).

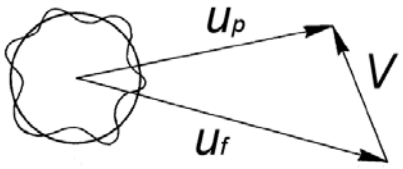

Figure 2.14: The relative motion of a suspended particle

$$\frac{\pi d_p^3}{6}\rho_p\frac{\mathrm{d}u_p}{\mathrm{d}t} = -3\pi d_p V + \frac{\pi d_p^3}{6}\rho_f\frac{\mathrm{d}u_f}{\mathrm{d}t} - \frac{1}{2}\frac{\pi d_p^3}{6}\rho_f\frac{\mathrm{d}V}{\mathrm{d}t} - \frac{3}{2}d_p^2(\pi\mu\rho_f)^{1/2}\int_{t_0}^{t}\frac{\mathrm{d}V}{\mathrm{d}\xi}\frac{\mathrm{d}\xi}{(1-\xi)^{1/2}} \quad (2.14)$$

The first two terms give the acceleration force and the viscous resistance according to Stokes' law. The acceleration of the fluid leads to a pressure gradient in the vicinity of the particle and hence to an additional force given by the third term. The fourth term represents the resistance of an inviscid fluid to the acceleration of the sphere, as given by potential theory. The final term is the *Basset history integral* which defines the resistance caused by the unsteadiness of the flow field.

For PIV gas flows, the density ratio of the seed material is much greater than the density of the fluid, and Equation 2.14 becomes dominated by the Stokes' terms, resulting the following expression:

$$\frac{du_p}{dt} = K(u_f - u_p) \quad (2.15)$$

where u_p and u_f are the velocity of the particle and the fluid respectively and K is a constant that depends on the particle and flow characteristics,

$$K = \frac{18\mu_f}{d_p^2\rho_f} \quad (2.16)$$

The gravitationally induced velocity U_g, that takes in consideration the gravitational forces when the fluid and particles densities are not the same, is determined in order to introduce how the particles behave under accelerations. This velocity is taken from Stokes' drag law, which assumptions are applicable when the particle is considered spherical and the particles Reynolds number is small. The gravitationally induced velocity is:

$$u_g = d_p^2\frac{(\rho_p - \rho_f)}{18\mu}g \quad (2.17)$$

Raffel et al. (2007) related the gravitational induced velocity equation to derive and estimate the velocity lag of a particle in a continuously accelerating fluid.

$$u_s = d_p^2\frac{(\rho_p - \rho_f)}{18\mu}a \quad (2.18)$$

They further determined that the step response of the particle typically follows an exponential law if the density of the particle is much greater than the fluid density, which is characteristic of using solid particles in gaseous flows. This resulted in the development of a relationship for a particle velocity:

$$u_p(t) = u_f(1 - e^{-\frac{1}{\tau}}) \tag{2.19}$$

being τ, the relaxation time (Hinsch (1993)),

$$\tau = \frac{d_p^2 \rho_f}{18\mu_f} \tag{2.20}$$

The relaxation time is an indicator of the ability of a certain size and density particle to respond to fluid acceleration. The particle velocity will lag behind the velocity of an accelerating fluid due to its inertia. The magnitude of this velocity lag for alumina particles was calculated using Equation 2.19. Figure 2.15 illustrates the particle response time of four different particle diameters in an air flow. The particle response time decreases with its diameter. In this research the alumina particles used have a mean diameter around 10 µm.

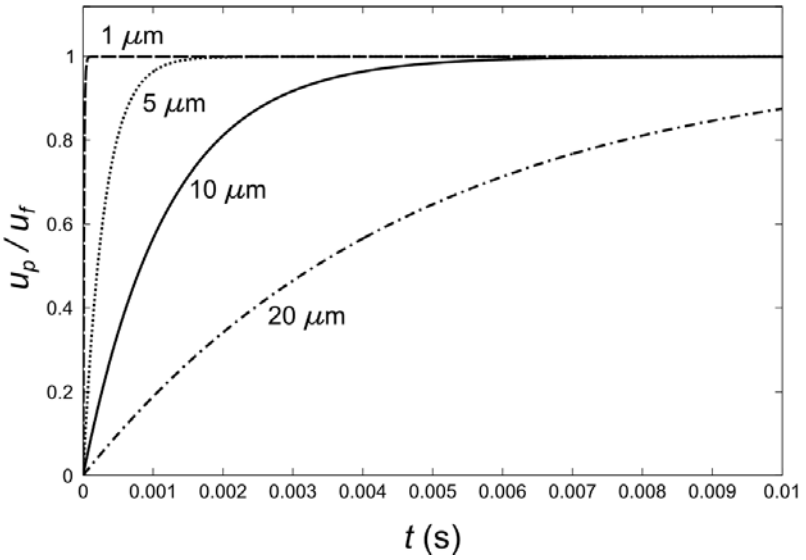

Figure 2.15: Alumina response time to fluid acceleration for four different particle diameters: 1 µm, 5 µm, 10 µm and 20 µm

Optical properties

The intensity of the particle images in the recordings is directly proportional to the scattered light power, thus it is an important factor to maximise. It is known that the light scattered by small particles is a function of the ratio of the refractive index of the particles to that of the surrounding medium (Raffel et al. (2007)). If the wavelength of the

incident light, λ, is smaller than the diameter, d_p, of spherical particles, Mie's scattering theory can be applied and the normalized diameter, q, is defined by:

$$q = \frac{\pi d_p}{\lambda} \tag{2.21}$$

The scattered light increases with q, hence, from this point of view, it is better to use bigger particles and low wavelength light. However, as it has been stated before, small particles are better to follow the flow, so a compromise between these two conditions must be found to achieve the best results.

Figure 2.16 shows the light scattering by a 1 µm oil particle in air. An increment of scattered light is observed on the direction of the laser beam, which is a disadvantage for its application in PIV because the recording takes place at an angle of 90°. The only way to overcome this drawback is to increase the laser power; however this condition is contrary to the low wavelength light required. So, again, a compromise between both necessities needs to be found.

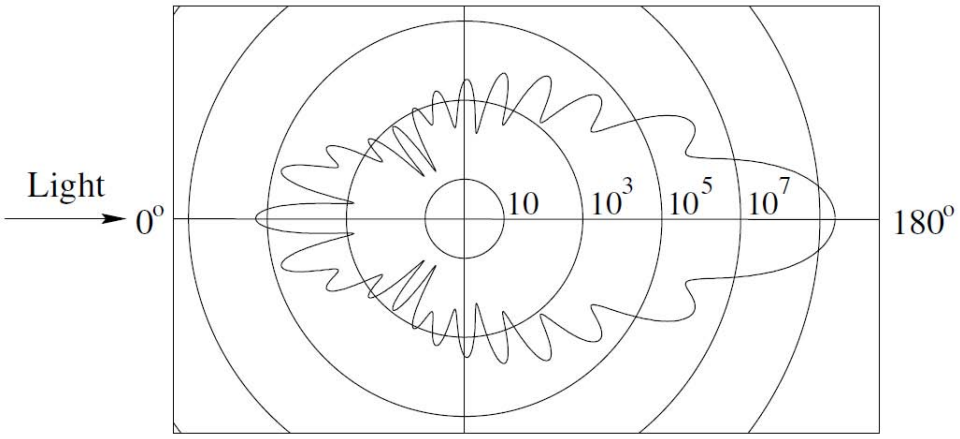

Figure 2.16: Light scattering by a 1 µm oil particle in air

2.2.3 Light source

The PIV technique uses lasers due to their ability to emit monochromatic light with high energy density. The Neodymium-doped YAG (Nd:YAG) is the most used laser because its mechanical and thermal properties. This type of lasers generates pulses of energy that can reach 400 mJ at a repetition rate of tens of Hz.

The advantage of pulsed lasers is the short duration of the laser pulse, typically a few to several nanoseconds. As a consequence, a particle travelling at even very high speeds is essentially *frozen* during the exposure with minimal blurring. Pulsed lasers operate by discharging energy stored in capacitor banks at a discrete time intervals to the flash-lamp, followed by the laser pulse. Pulsed lasers are ideally suited for PIV because they store and deliver all of the laser power at exactly the desired instant and at a constant repetition rate. In order to obtain a specific $\triangle t's$, two identical lasers firing in tandem

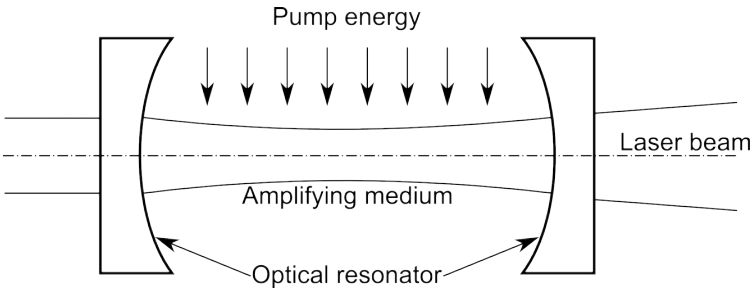

Figure 2.17: Simplified laser scheme

are required. The second laser can be suitably staggered in time with respect to the first laser to produce the desired interval between frames $\triangle t$. A synchronizer that produces the required trigger signals must be incorporated to ensure that the lasers, camera, computer and other hardware are properly synchronized.

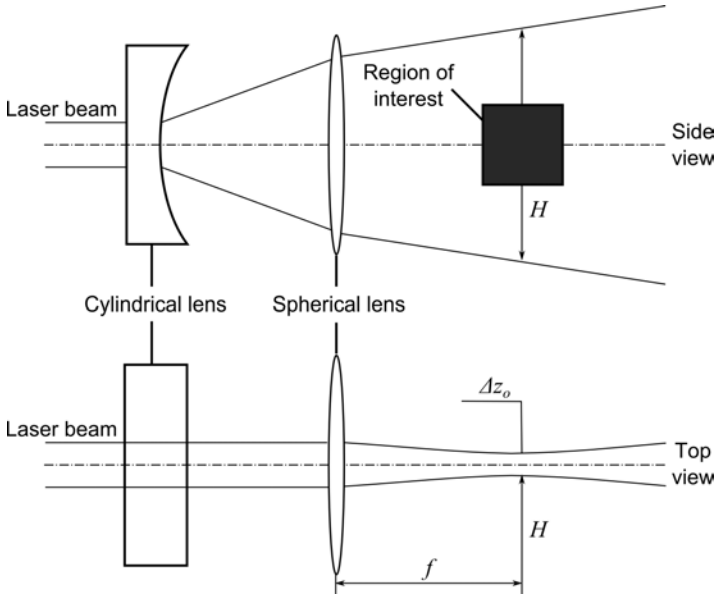

Figure 2.18: Schematic of a sheet-forming module

Figure 2.17 shows a simplified scheme of a laser with its main components:

- **Amplifying medium**: an atomic or molecular gas, semiconductor or solid material.
- **Pump source**: that excites the amplifying medium by the introduction of electromagnetic or chemical energy.
- **Optical resonator**: allows the oscillation within the amplifying medium.

The laser itself emits a collimated beam of light that needs to be treated in order to obtain the desired light sheet. The simplest method to generate that sheet is to use a cylindrical lens in combination with a spherical lens as shown in Figure 2.18. The cylindrical lens causes the laser beam to expand in one direction only. The spherical lens causes the expanding beam to focus along the perpendicular direction, at a distance of one focal length downstream to its beam waist. The intensity of light illuminating the particles depends on

the laser power and inversely on the height of the beam and the sheet thickness. Because the laser beams have a Gaussian intensity profile, the Gaussian variation is retained in both the in-plane and the thickness directions.

2.2.4 Recording hardware

The popular trend nowadays is to use CCD cameras for PIV recordings. Digital PIV results can be viewed in almost real-time with high-speed on-board computational hardware dedicated towards computing correlations. Another advantage of CCD sensors is that they are highly light-sensitive which enables experiments to be performed with less powerful lasers.

For certain applications, the delay between two laser pulses may be very small (micro-seconds), and it is not possible to read out 1 Mbyte of data to the computer memory in such a short time. Therefore, the first frame is stored very fast into a buffer located immediately adjacent to every sensor pixel. The second PIV frame is subsequently recorded and the two frames are read out sequentially to the computer memory, in time for the next double-frame capture. The cycle is completed in a time which is the period of laser pulsing or less.

CCD sensors have a discrete number of photoelectric cells (pixel) capable of perceive the light intensity, hence, the sensor translates the energy received from the photons into electric signals. The intensities of these signals depend on two factors: the wavelength of the incident radiation and the number of photons of each colour. Each current produced gives one tone (grey level) that is part of the tonal range (grey range) of the image. Usually the images are recorded with 8 bits or 16 bits, which means that each pixel can reach a discrete tone of a grey range which goes from 0 to 255 (2^8 tones), or to 65536 (2^{16} tones). Thus, the particles of two interrogation windows (with the same coordinates) can be identified comparing the pixel tones of those images taken at an instant t and $t + \triangle t$.

2.2.5 Velocity vectors calculation

In practice, instead of taking two totally-independent snapshots, combined methods are used. The calculation method described in this section is based on the recording of two images during one exposure (cross-correlation, Willert and Gharib (1991)) because it offers better results than double exposure in one image (auto-correlation, Adrian (1984) and Pickering and Halliwell (1984)).

Location and identification of particles

The aim of the cross-correlation technique is not to obtain the displacement of each particle, but the mean displacement of a group of particles using a statistical magnitude called *correlation coefficient*, C. This processing typically provides vectors on a uniform grid. Dividing a 1k $\times$ 1k pixel frame using 32 $\times$ 32 pixel interrogation windows will yield a 32 $\times$ 32 field of independent vectors. The term independent refers to the fact that the data contributing to a particular vector is not shared with any other vector. Nevertheless, very often the cross-correlation is performed with an overlap between adjacent windows. The commonly accepted value of overlap is 50%. Accordingly, the centre of each interrogation spot is displaced $d_I/2$ with respect to its neighbours, in both x and y directions, where d_I

is the size of an interrogation window. As a result, the total number of vectors is increased by a factor of 4. It should be noted that overlapped vectors are no longer independent, but share 50% of the contributing particle pairs with the neighbouring vectors.

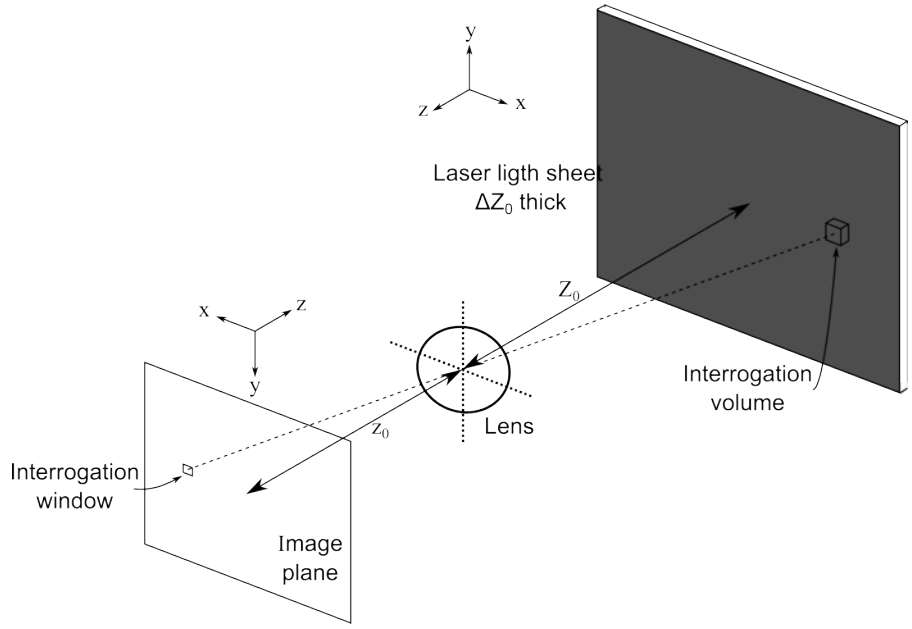

Figure 2.19: Scheme of image analysis in PIV

Whilst the small areas in a frame are called interrogation windows, the geometric projection of these areas on the laser light sheet is called *interrogation volume*. Figure 2.19 shows a scheme of the image analysis in PIV.

Fast Fourier Transform (FFT)

There are two ways to obtain the correlation coefficient: using a direct calculation or using an indirect calculation with the theorem of Wiener-Kinchin (Bracewell (1999) and Bendat and Piersol (2000)). Even though the first method could be the best from a mathematical point of view, results are needed to be obtained as fast as possible. Thus, the second method, which establishes that there is equivalence between the Fourier inverse transform of the power spectrum density and the correlation function of the considered signal (Raffel et al. (2007)), is the most used.

The working flow used with the FFT (Fast Fourier Transform) throughout this thesis is shown in Figure 2.20. Knowing the power spectrum density, the cross-correlation can be easily calculated formulating the Fourier inverse transform of that function.

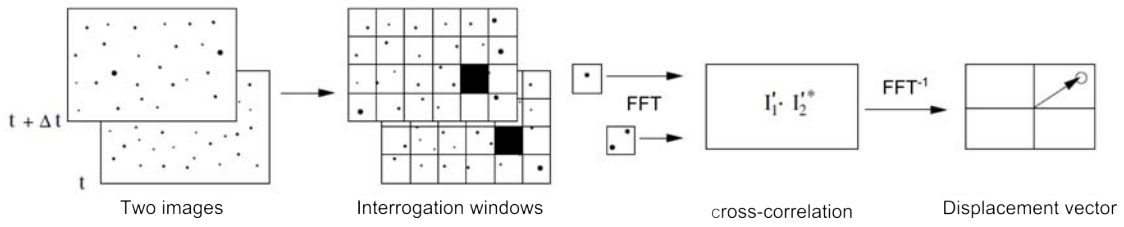

Figure 2.20: Used FFT method

Even when experimental conditions are ideal, a PIV vector map will contain "bad" vectors, also referred to as *false* or *spurious vectors*. These spurious vectors are readily identifiable when the vector field is replotted after subtracting the mean because they have magnitudes and/or directions which are substantially different from their neighbours. Spurious vectors result from interrogation windows in which the signal-to-noise ratio is less than the unity, i.e. a noise peak is higher than the signal peak. Typically less than 2% of vectors will be bad. The usual causes are the lack of particle pairs in the interrogation window due to inadequate seeding density or excessive out-of-plane motion so that the particle exits the light sheet between laser pulses. As an example two cross-correlation map are shown in Figure 2.21, corresponding to an interrogation window with high and low signal-to-noise ratio.

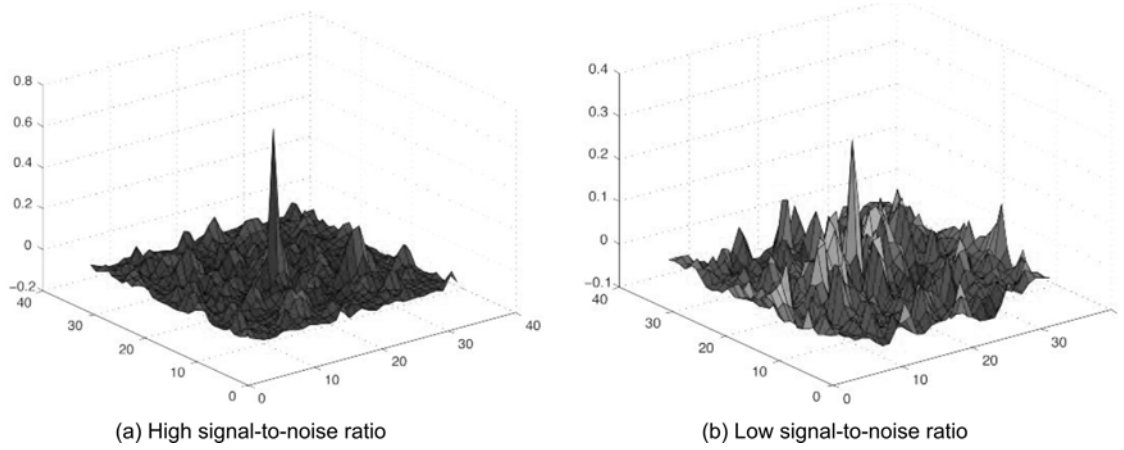

Figure 2.21: Examples of correlation maps

2.2.6 Uncertainty analysis of measurements

As it was described before, particle image velocimetry is a measurement method which obtains directly the velocity field of a particular area. In order to determine the uncertainties caused by the measurement system, it was necessary to define the average flow velocity for an interrogation area of a studied image at any instant. According to Bardera (2005), the velocity is computed using indirect measurements:

$$u = \frac{X}{M\Delta t} \tag{2.22}$$

where X is the displacement of the particle from the correlation algorithm measured in pixels (image plane), M is the magnification factor which relates the dimensions of the object plane with the dimensions of the CCD sensor (image plane), Δt is the interval between two laser pulses.

The total uncertainty of the measurement process is composed by a combination of systematic uncertainties and stochastic (or precision) uncertainties,

$$\left(\frac{\triangle u}{u}\right)_{tot} = \sqrt{\left(\frac{\triangle u}{u}\right)^2_{sys} + \left(\frac{\triangle u}{u}\right)^2_{sto}} \tag{2.23}$$

Taking into account the error propagation laws, Carter and Soria (2001) defined the systematic uncertainty of the velocity measurement as

$$\epsilon_u^2 = \left(\frac{\triangle u}{u}\right)^2_{sys} = \left(\frac{\triangle X}{X}\right)^2 + \left(\frac{\triangle M}{M}\right)^2 + \left(\frac{\triangle \tau}{\tau}\right)^2 \tag{2.24}$$

where $\triangle X$ is the displacement uncertainty, $\triangle M$ is the magnification uncertainty and $\triangle \tau$ is the timing uncertainty.

Scale uncertainty

The scale uncertainty is obtained from the calibration of the PIV measurements. The size of the images got from the PIV system is 1600 px×1192 px (width and height) being the magnification factor 25 mm / 278.7 px. Knowing that each pixel of the CCD sensor has a size of 9 µm, one can calculate the magnification as:

$$M = \frac{d_i}{d_o} = \frac{1600\,px \times 0.009\,mm/px}{143.5\,mm} = 0.1 \tag{2.25}$$

The minimum value that can be seen in the calibration target used is 0.5 mm, which means:

$$\left(\frac{\triangle M}{M}\right)^2 = \left(\frac{\triangle d_i}{d_i}\right)^2 + \left(\frac{\triangle d_o}{d_o}\right)^2 = 0 + \left(\frac{0.5\,mm}{143.5\,mm}\right)^2 \tag{2.26}$$

$$\left(\frac{\triangle M}{M}\right) = 0.0035$$

which leads to a scale uncertainty of $\triangle M = 0.00035 = 0.035\%$.

Timing uncertainty

The timing uncertainty was estimated with the smallest significant digit that can be selected in the PIV system used. In this case it is 0.1 µs, which is in a good agreement with the value proposed by Hallberg (2000). For the typical timing between two pulses established in the experiments (see section 2.2.8), 58 µs, the timing uncertainty is:

$$\left(\frac{\triangle \tau}{\tau}\right) = \frac{0.1\,\mu s}{58\,\mu s} = 0.0017 = 0.017\% \tag{2.27}$$

Displacement uncertainty

The displacement uncertainty encompasses all the errors produced from the acquisition of the image to the calculation of the velocity vectors. The displacement uncertainty considered in this thesis was the value calculated by Bardera (2005).

$$\left(\frac{\triangle x}{x}\right) = 0.002 = 0.2\% \tag{2.28}$$

Systematic uncertainty

Replacing the numerical values of each uncertainty in the Equation 2.24, the systematic uncertainty is obtained as

$$\epsilon_u^2 = \left(\frac{\triangle u}{u}\right)_{sys}^2 = (0.002)^2 + (0.00035)^2 + (0.0017)^2$$

$$\left(\frac{\triangle u}{u}\right)_{sys} = 0.0026 = 0.26\% \tag{2.29}$$

Stochastic uncertainty

To determine the stochastic uncertainty that comes from the nature of the measuring process itself, the expression given by Adeyinka and Naterer (2005) has been used.

$$P = \frac{t\sigma}{N} \tag{2.30}$$

where σ is the standard deviation of the N images used to obtain the flow field of each experiment (see section 2.2.9) and t is the confidence coefficient, which is 2 for a 95% confidence level (Student's t-distribution).

In order to calculate the stochastic uncertainty, the same experiment was repeated several times. The experiment consisted on calculating the velocity of a uniform field. The highest stochastic uncertainty calculated was 0.0017. It has the same order of magnitude than the systematic uncertainty.

Total uncertainty

Substituting the systematic uncertainty and the maximum stochastic uncertainty in Equation 2.23, the total uncertainty of the PIV measurement procedure is estimated as

$$\left(\frac{\triangle u}{u}\right)_{tot} = \sqrt{(0.0026)^2 + (0.0017)^2} = 0.0031 = 0.31\% \tag{2.31}$$

Even though the uncertainty of the procedure is very low, the errors of a specific measurement could be higher depending on factors such as the particles ability to follow the flow or the local intensity of turbulence. Some of these factors will be addressed later on in the measurement analysis.

2.2.7 Quality analysis of the tests images

One of the first steps when performing experiments with PIV technique is to analyse some test images to see if their qualities are good enough or certain parameters need to be adjusted. In the present research, the PIV experiments were performed using the software *Insight 3G*, provided by the manufacturer of the equipment. This software generates raw

images that have a size of 1600 px × 1192 px in a 16 bit grey level resolution. Parameters such as the laser power, the camera focus and the particle seeding were evaluated and adjusted in order to obtain the best outcomes possible given the available equipment and seeding materials.

The biggest effort was focused on checking that seeding density was appropriate for the desired application. As it was stated before, it is a common-practice rule to have at least 10 particles inside of an interrogation window to obtain a good signal, which means more accurate velocity vectors at each spot. Figure 2.22 shows the particle density reached inside the measurement plane for one particular image. As it can be observed, the number of particles that fall inside of an interrogation window is satisfactory.

Another factor to take into account when analysing an image is if there is any element that could cause distortion in the future processing process. The reason after the distortion is that there is no information of the particles moving behind those elements. In the studied case were all the aerofoil profile was focused, a circular shaped scratch was found out (see Figure 2.23). The emergence of this imperfection on the methacrylate window was caused by the friction with the alumina powder trapped between the aerofoil and the window when it was being tilted. It has to be noted that the colour levels of the image have been modified to clearly illustrate the scratch.

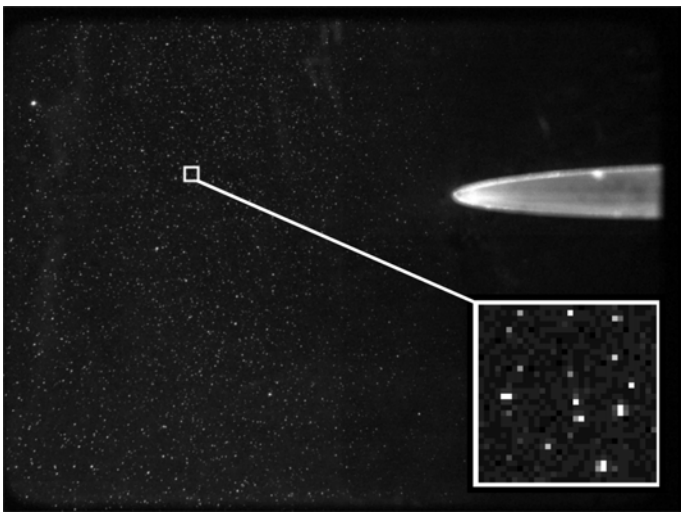

Figure 2.22: PIV image and interrogation window sample

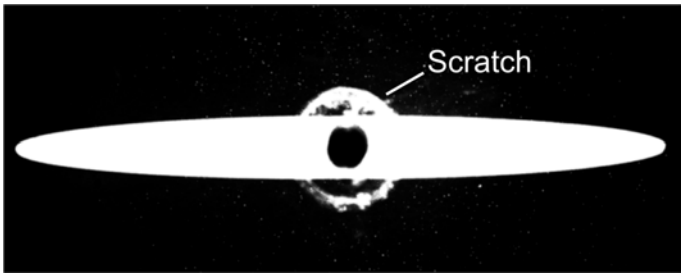

Figure 2.23: Illustration of the scratch reference location on a PIV image

2.2.8 Experimental parameters of the tests

One of the most important parameters to determine is the time delay between two laser pulses. This time interval must be selected so the particles displacement is less than $0.25 d_I$, being d_I the size of an interrogation window. All the PIV experiments were accomplished with a mean flow velocity (U) of 12 m/s inside the test chamber and an interrogation window size of 32 px $\times$ 32 px. Thus, the time delay is calculated as

$$\Delta t \leq 0{,}25 \frac{d_I M}{U} \tag{2.32}$$

where M is the magnification factor of the experiment, in this case M = 25 mm / 279 px. The time interval obtained with Eqn. 2.32 is 58 µs.

2.2.9 Convergence analysis of measurements

The stochastic convergence of the PIV measurements has been analysed in order to determine the optimum number of images per experiment to be acquired. The streamwise component of the velocity (U) has been used as control variable. Three different positions in the working area (inside and outside of the wake), and two aerofoil configurations (0° and 15° angles of attack) with different velocity gradients have been considered for this study. The variation of the average streamwise velocity with the increment of the number of processed images is shown in Figure 2.24.

It has been observed that the convergence of the control variable is seriously compromised in cases with less than 100 images per average. All the plots exhibit an unstable behaviour throughout that interval. In order to achieve good results, no less than 200 images should be used. However, to ensure the quality of the acquired data, a sample of 300 images was considered optimum. Thus, that was the number of snapshots used to perform the ensemble average of the PIV statistics.

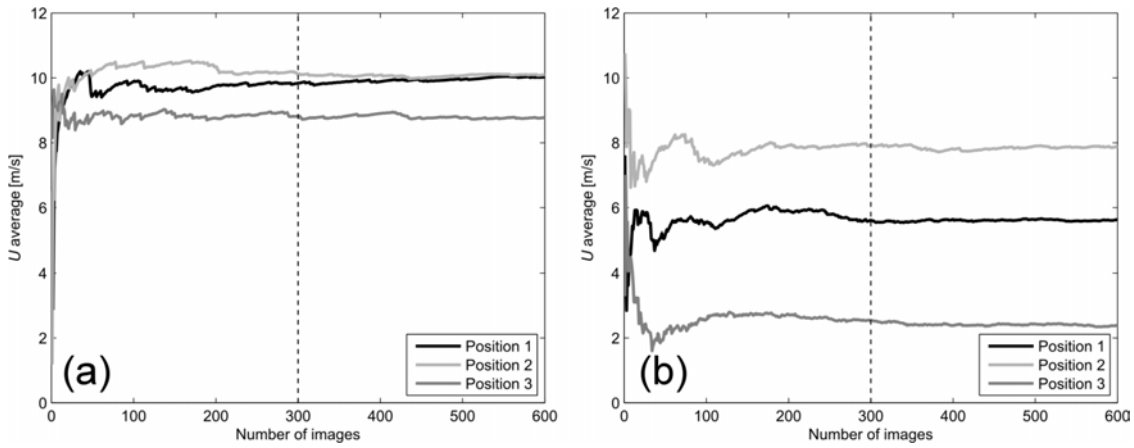

Figure 2.24: Velocity convergence as a function of the number of images for an angle of attack of (a) 0° and (b) 15°

CHAPTER 3

Experimental setup

The development of a new facility for PIV measurements was one of the main milestones throughout the process of this thesis. The Fluid Mechanics laboratory did not have a wind tunnel suitable for that task so the design and construction of a new one certainly meet a need. This chapter covers the development of the PIV wind tunnel including the previous study about the creation of a new nozzle profile. CFD results show the good performance of the contraction profile and hot-wire measurements corroborate it. It is also described in this chapter the different setups used for PIV and HW measurements, besides the configuration adopted for flow visualization.

3.1 Design of a two-dimensional contraction

One of the objectives of this thesis was to construct a new wind tunnel facility with the desired features for carrying out PIV and HW anemometry measurements. That task required to take special attention in one of the most important elements for guiding the flow inside the tunnel, the contraction. A previous investigation has been done to design an appropriate contraction for the PIV wind tunnel. The contraction was designed, constructed and characterized taking advantage of another necessity at the Fluid Dynamics Group of the University of Oviedo. The aeroacoustic wind tunnel in laboratory required a new nozzle, so it was presented as the perfect opportunity to study the goodness of the new design. After verifying the suitability of the contraction, it was included in the PIV wind tunnel scheme for its construction.

The facility where the new nozzle design was placed is a closed loop circuit wind tunnel arranged in a vertical layout, as shown in Figure 3.1. The total length of the tunnel is 24.6 m, with 8.3 m high and maximum operative velocities in the range of 20 m/s for the test section; i.e., a maximum Reynolds number of 1.7×10^6, based on the characteristic entrance length. The sections that compose the wind tunnel are described below. The test chamber is 4.2 m long and has a cross-sectional area of 4.45×2.80 m^2. The dimensions of the test section allow working inside with different equipment and without interference in the air free stream discharged from the nozzle. The settling chamber is the largest chamber of the wind tunnel, with a characteristic cross sectional area of 19 m^2. The chamber is composed of the following parts: the honey comb, the screens and the relaxation duct.

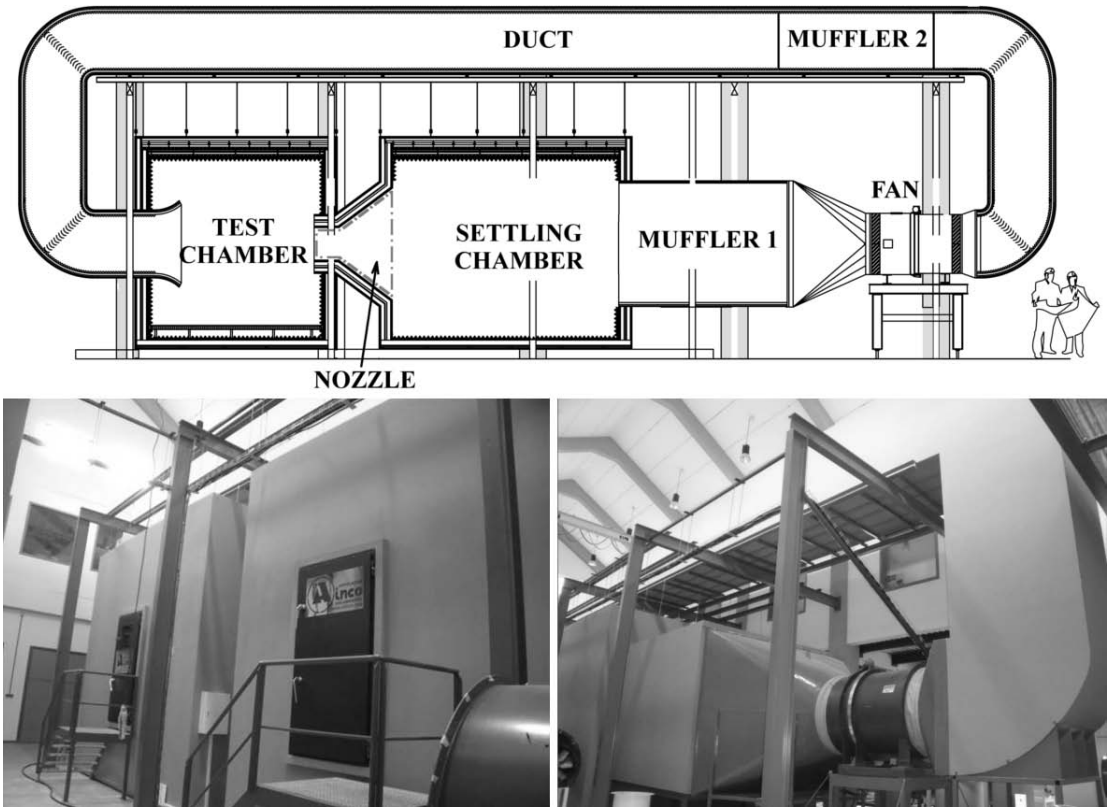

Figure 3.1: Wind tunnel for acoustic measurements

The combined effect of these components is to reduce the turbulence coming from the fan, by breaking down larger eddies into smaller ones. The screen holes present a characteristic size of 30 mm, which devises a typical length scale in the range of a tenth of centimetre for the inflow turbulence. Two mufflers, one between the settling chamber and the fan, and another in the longest duct, reduce the noise coming from the fan to the test section. This acoustic isolation makes possible to perform aeroacoustic measurements within the wind tunnel. The fan used is of axial anti-stall type, with the impeller mounted directly on the motor shaft. It provides a variable air flow modifying the pitch of the blades. The 30 kW driven motor establishes maximum flow rates in the range of 26 m^3/s (blades are full-opened) and a total-to-static pressure increment of 850 Pa. The new nozzle had to be placed between the settling chamber and the test section. Its length was determined by the separation between the chambers (1.505 m). Different contraction ratios were required to enable diverse experiments, so the nozzle was constructed with the possibility of modifying its lateral span. Thus, the distance between the two vertical faces had to be: 2.745 $\pm$ 0.2 m at the inlet and 1.000 $\pm$ 0.2 m at the outlet (Figure 3.2). As a consequence, the contraction ratio (in terms of crossed area) in the nozzle is variable, ranging from 9.5:1 to 6.25:1.

3.1.1 Nozzle contours studied

The most extended contraction profiles used for wind tunnels, which have been widely tested and recommended for this type of applications in the literature, are those based in a pair of two cubic polynomials (Bell and Mehta (1989); Morel (1975, 1977); Ramaeshan and Ramaswamy (2002)). This family of profiles could not be adapted in our case due to

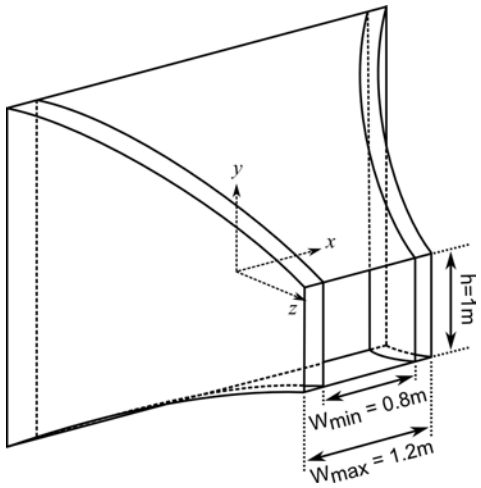

Figure 3.2: Scheme of the versatile nozzle

some unavoidable geometrical restrictions of the wind tunnel. In particular, the existent structure that connects both chambers limits the space in a way that a two cubic polynomial nozzle cannot be placed in it. To overcome this problem, a fourth order polynomial profile (FOP), given by Equation 3.1, and a logarithmic derivative profile (LDP), given by Equation 3.2, were explored as reasonable alternatives for the design.

$$y = a_0 + a_1 z + a_2 z^2 + a_3 z^3 + a_4 z^4 \tag{3.1}$$

$$y = b_1 + b_2 z \left(\ln\left(b_2 z\right) - b_3\right) \tag{3.2}$$

The LDP expression was obtained looking for a mathematical equation that was smoother and more gradual than the polynomial equations utilized normally and with less parameters as well. In addition it should be suitable for a reduced longitudinal dimension.

The polynomial in Equation 3.1 includes five coefficients (from a_0 to a_4) that must be fixed according to the following geometrical constraints: (i) Inlet and outlet height, (ii) zero acceleration of the air flow at the outlet, (iii) zero variation of acceleration of the air flow at the outlet, (iv) a particular inlet curvature. Mathematically, these conditions can be expressed as follows:

- $y(z = 0) = h_i$
- $y(z = l) = h_o$
- $a(z = l) = 0$
- $a'(z = l) = 0$
- $y'(z = 0) = \tan(\alpha)$

where h_i and h_o are half inlet and outlet height respectively, l is the nozzle length, z is the longitudinal coordinate in the nozzle, a is the flow acceleration and α is the inlet curvature. The angles chosen for α were 40, 50 and 60 degrees.

Equation 3.2 was obtained establishing that the nozzle profile follows a logarithmic derivative. This shape was chosen due to its smoothed curvature, with only three parameters defined as:

- $b_1 = h_i$
- $b_2 = \frac{h_i - h_o}{l}$
- $b_3 = \ln(h_i - h_o) + 1$

where b_1, b_2 and b_2 are a group of coefficients that adjust the offset and the slope of the logarithmic function.

A representation of the four contraction profiles is shown in Figure 3.3. In this plot, the non-dimensional length of the nozzle (z/L) and the non-dimensional vertical coordinate (y/h) are represented. The z coordinate increases in the downstream direction. The coordinate system is established with the origin at the centre line of the inlet plane. In the nozzle geometry, the remaining x coordinate is used for the span-wise direction.

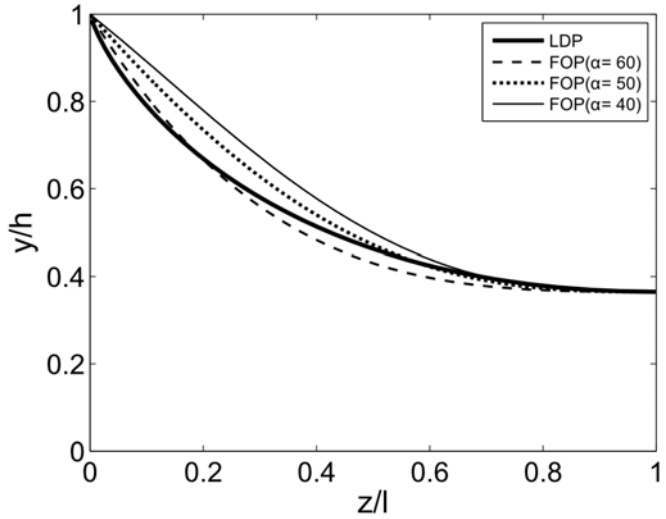

Figure 3.3: Contraction profiles

3.1.2 Numerical methodology and validation

The performance of all four contraction profiles was analysed using Computational Fluid Dynamics (CFD). The meshing procedure followed as well as the boundary conditions and models chosen for simulations are explained here.

Geometry and mesh

ANSYS ICEM CFD® meshing software was used for geometry and mesh generation (contraction outlet section = 1×1 m^2 and contraction inlet section = 2.745×2.745 m^2). Due to the symmetry presented, only one quarter of the nozzle was modelled in order to reduce the computational load. Part of the settling duct was also included in the geometry for accuracy purposes, as shown in Figure 3.4.

Every model was meshed using a structured mesh and avoiding highly skewed elements. A boundary layer grid dependence study, with five different density meshes, was performed using the velocity profiles along the vertical plane of the outlet as control variable. The

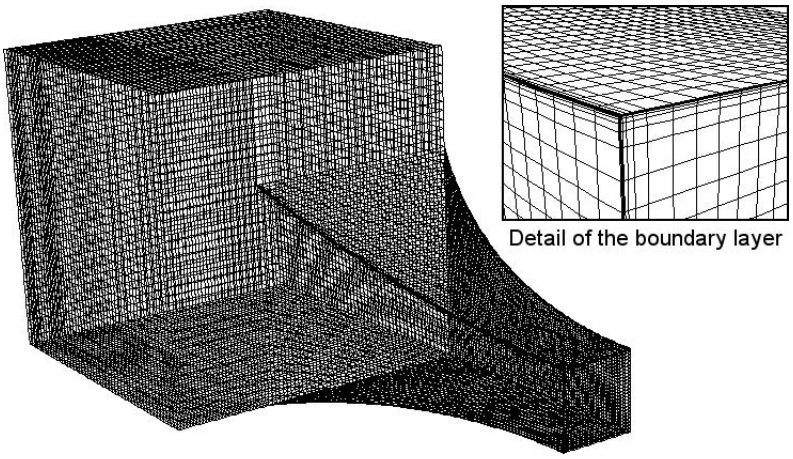

Figure 3.4: LDP model meshed

integral turbulent scales and turbulence intensities at the inlet, measured previously with a hot wire probe (detailed forward), were used for defining a high-density mesh. Further mesh refining was conducted towards the nozzle side-walls. The comparison of the numerical data obtained for each mesh is illustrated in Figure 3.5. The model with the coarser mesh (y^+ of 631.6) is the one that shows the biggest difference in the velocity profile. The velocity starts to drop off when y/h is 0.92, while for the rest of the models it occurs at y/h = 0.97. Results show that refining the mesh from a value of $y^+ = 0.297$ do not provide more accurate values of velocity at the boundary layer. The velocity values are slightly lower near the wall for the $y^+ = 82$ model than for the three finest mesh models. For them the results remain invariant. Taking into account these outcomes, the coarser mesh with the best results (y^+ of 0.297) was the chosen one for continuing the profile study, due to the staking strategy used in the contours (see Figure 3.4, detail).

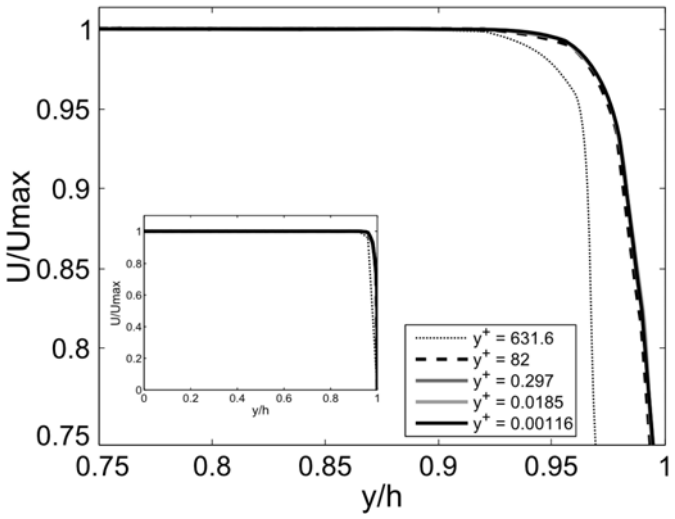

Figure 3.5: Numerical comparison of velocity profiles on vertical plane

Boundary conditions and models

The Computational Fluid Dynamics (CFD) package ANSYS-FLUENT® was used for solving the 3D steady Navier-Stokes equations in conjunction with the k-epsilon turbulence model and enhanced wall treatment on the structured meshes. This turbulence model was chosen because it obtains the production and dissipation of turbulence and allows predicting pressure gradients that leads to boundary layer separations. A SIMPLE pressure-velocity coupling algorithm was selected and second order discretization was applied for the equations to increase the accuracy of the results.

As boundary conditions, it was considered a gauge total pressure of 296.45 Pa at the beginning of the mesh (settling chamber inlet) with a turbulence intensity of 2.5% and a turbulent length scale of 0.25 m, both obtained with hot wire measurements at the inlet. An atmospheric (0 Pa) gauge pressure at the nozzle outlet was also imposed. Both are pressure conditions instead of velocity ones in order not to condition the simulation results.

3.1.3 Numerical results

The flow uniformity of each model at the outlet was studied and the results obtained are shown in Figure 3.6. Due to the geometrical resemblance of the contraction profiles, it was expected a close velocity tendency at the outlet of the nozzle. The flow velocity of all models remains greater than 99% of U_{max} until the 96% of the outlet height is reached, thus, providing a boundary layer size of 4% of the outlet height. In the detail of the velocity profiles at the boundary layer area, some differences can be observed. At this point the LDP profile presents slightly higher velocity values than the polynomial ones, achieving a better flow uniformity.

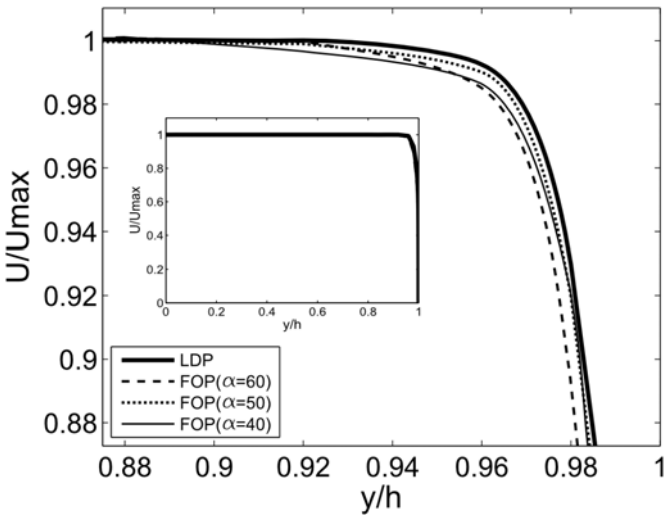

Figure 3.6: Velocity profiles at the outlet on vertical plane

The velocity contours of the LDP model at the middle plane are depicted in Figure 3.7. The flow coming from the settling chamber arrives at the contraction inlet with a mean velocity of 2.9 m/s; afterwards it is accelerated throughout the nozzle until its way out. At streamwise sections close to the nozzle inlet the flow velocity decreases as it nears the

wall. As long as the air advances towards the outlet this tendency diminish, being reversed near the outlet.

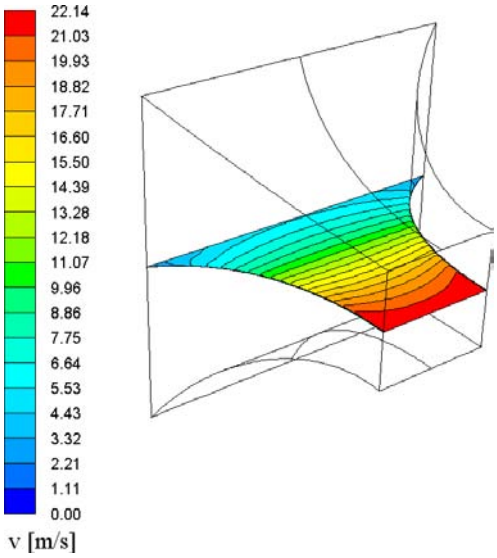

Figure 3.7: Velocity contours of LDP on middle plane

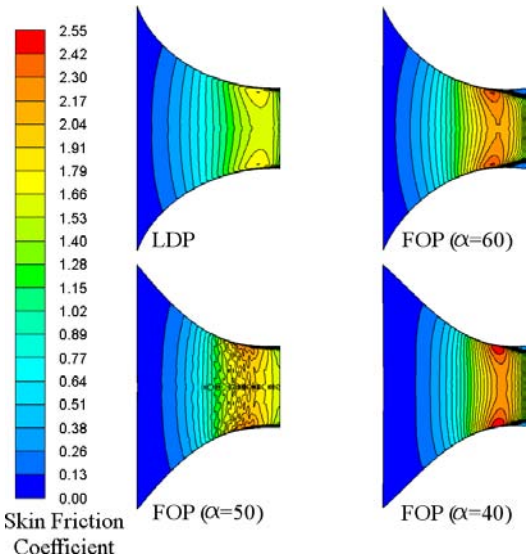

Figure 3.8: Skin friction coefficient contours at the nozzle upper wall

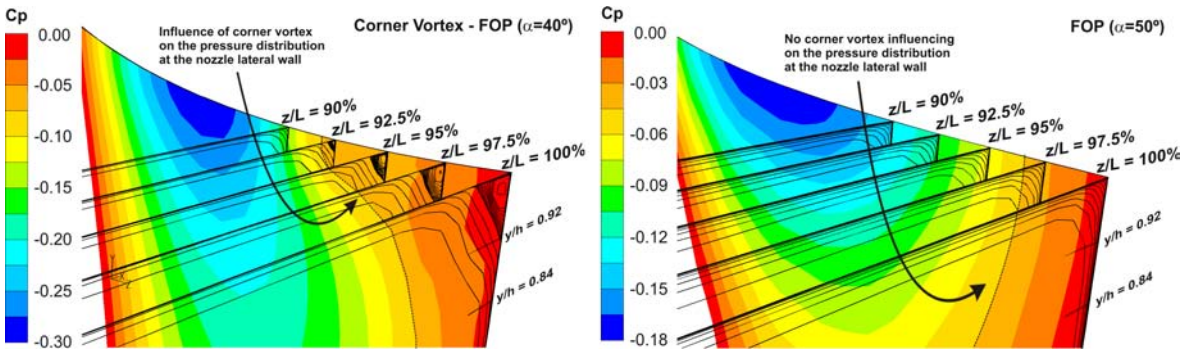

Figure 3.9: Impact of corner vortex on pressure distribution

As the nozzle structure consists of convex surfaces, the possible separation region spans the entire length of the contraction. For that reason is fundamental that the profile leads the flow avoiding adverse pressure gradients which are the essential condition for the separation. Precisely, for testing the avoidance of separation at the nozzle walls, the skin friction coefficient was considered (Figure 3.8). Simulation results show that the LDP and the FOP ($\alpha = 50°$) do not present separation, indicated by the continuously positive skin friction coefficient values over the wall (Sargison et al. (2004)). However, LDP offers more balanced results without drastic increasing gradients of the coefficient. On FOP ($\alpha = 60°$) and FOP ($\alpha = 40°$) there is a region at the wall, near the outlet, that shows a discontinuity of the skin friction coefficient distribution. These areas seem to show corner vortices, which are very common in wind tunnel contractions. In particular, the comparison of pressure distributions on the nozzle lateral wall for the cases with $\alpha = 40°$ and $\alpha = 50°$ reveals the

impact of the corner vortex on the pressure distribution (local negative values of pressure coefficient are more aggressive in the 40° cases leading to the appearance of such vortices), see Figure 3.9. In addition, a visualization of the core of the vortices has been superimposed to illustrate this phenomenon. Note that these structures are not present in the case with 50°.

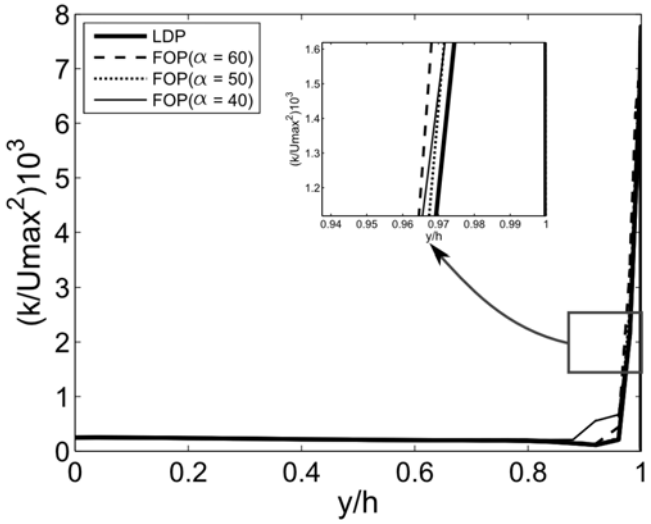

Figure 3.10: Dimensionless turbulent kinetic energy at the outlet on vertical plane

The turbulence generated in the air flow is also an important factor to be considered. The dimensionless turbulent kinetic energy profiles have been analysed at the outlet on the vertical plane (Figure 3.10). As expected, the predicted values for FOP ($\alpha = 60°$) and FOP ($\alpha = 40°$) become higher earlier due to the appearance of corner vortices. The LDP and the FOP ($\alpha = 50°$) models produce less turbulence at the outlet, reaching almost the same values. The dimensionless turbulent kinetic energy of both profiles maintains a constant value of $0.22{\times}10^{-3}$ until it is reached 96% of the contraction length. From that point it increases its value to $7.7{\times}10^{-3}$.

As a conclusion, numerical results obtained with the simulation indicate that the logarithmic profile (LDP) and the polynomial profile ($\alpha = 50°$) provide very good results in terms of flow quality for experimental tests. However, the outcomes show that the flow guided by the LDP nozzle is slightly better conditioned. Accordingly, this was the shape chosen for building the nozzle.

3.1.4 Experimental setup

Finally, the nozzle was constructed with a LDP profile and can be seen in Figure 3.11. A sequence of the construction process can be seen in Figure 3.14. The materials used were MDF boards and plywood boards.

Ten pressure taps were installed along the middle section of a side-wall, and another two were put at the inlet and the outlet, respectively. These taps, connected to a pressure transducer, provided the wall static pressure distribution and the dynamic pressure at the nozzle outlet.

Figure 3.11: Wind tunnel contraction constructed

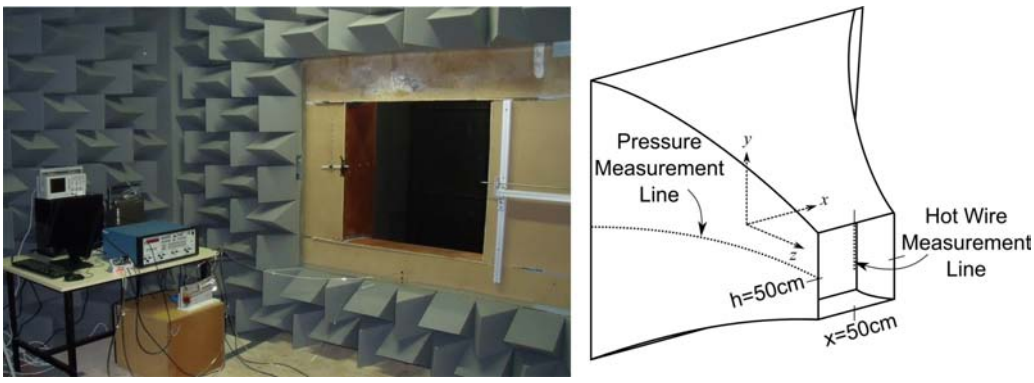

Figure 3.12: Experimental setup for hot-wire measurements

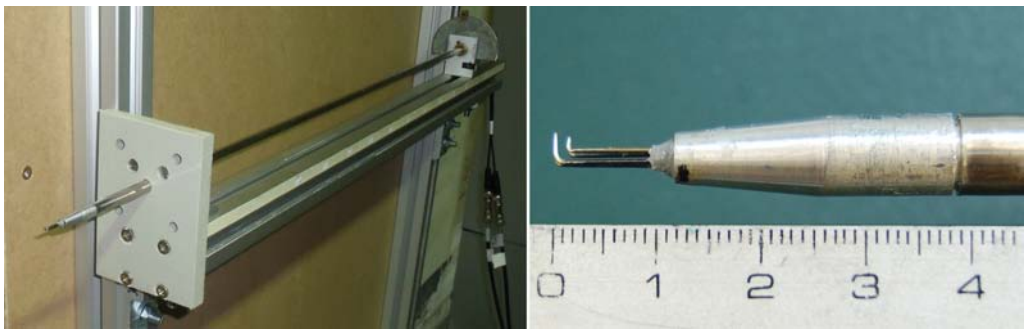

Figure 3.13: Assembly and detail of the X-probe

Figure 3.14: Construction process of the nozzle

The velocity distribution and the turbulence intensity at the outlet of the contraction were measured with a constant temperature X-wire probe made in this laboratory, connected to a TSI IFA 100. The probe had a cut-off frequency of 64 kHz. The IFA 100 outputs were connected to a National Instruments acquisition card that gave the information to a computer. All the aspects of calibration of the probe, capture, record and conversion of measurements were driven by a MATLAB® code, particularly developed for this kind of applications. Some of the Area work on that particular field (use and design of these experimental techniques) is presented in references Blanco-Marigorta et al. (1998); Fernández et al. (2007b,a). Figure 3.12 shows the experimental setup placed in the test section, inside the wind tunnel. The X-probe was placed at several positions on the centre line,

between the middle point and the top wall (Figure 3.13). Different sampling frequencies were tested and it was observed that 20 kHz was high enough to provide accurate data about the turbulent phenomena of the flow.

3.1.5 Experimental results

The static pressure measured along the middle section of a side-wall was compared with the theoretical static pressure (ideal flow with no losses). The dimensionless parameter C_p was used to normalize the data:

$$Cp = \frac{P - P_\infty}{\frac{1}{2}\rho U_\infty^2} \tag{3.3}$$

where P is the static pressure measured along the wall, P_∞ and U_∞ are is the static pressure and the mean velocity measured at the contraction outlet respectively. Good agreement was found between both distributions all over the curve (see Figure 3.15). The static pressure at the inlet of the nozzle becomes dynamic pressure at the outlet without significant losses.

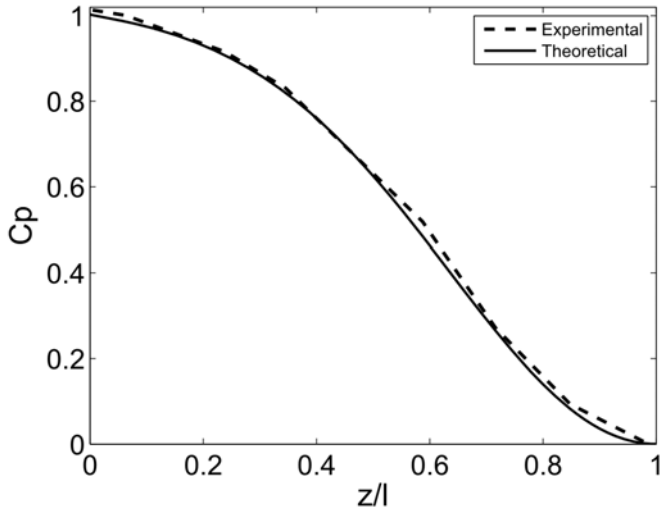

Figure 3.15: Experimental and theoretical pressure coefficient along a side wall

A hot wire probe was positioned at the middle line in vertical plane and was traversed from the centre of the nozzle outlet to the top wall. It was used to perform velocity and turbulence measurements, which provide information about the influence of the walls on the flow.

A first study of the recorded signals showed, as expected, that the reduction of velocity fluctuations was remarkable as the probe approached the centre of the nozzle. This fact revealed, at first sight, the significant reduction of the turbulence level throughout the outlet. A fragment of three signals time spectra, recorded at three particular positions, is depicted in Figure 3.16. There is no significant variation of the flow velocity in signals at $y/h = 0$ and 0.9, in contrast with the data dispersion near the outlet wall ($y/h = 0.99$).

Figure 3.17 compares the power spectral density of the free-stream region ($y/h = 0$) and the viscous region ($y/h = 0.99$). A moving average filter (with a windows size of eleven points)

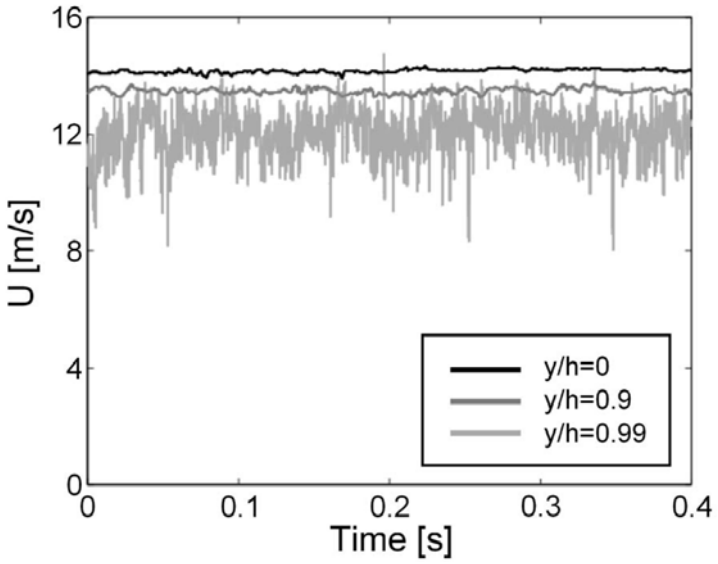

Figure 3.16: Time series of signals recorded at x = 0.5m in vertical plane (y/h = 0, 0.9 and 0.99)

was applied for reducing the signal noise. The PSD level at the viscous region is lower than at the free-stream region throughout all the frequency range, this is mainly related with the lower flow velocity. Both signals show a decay of the PSD with the frequency, greater than the -5/3 exponential decay (Davidson (2004)), which means the flow is still evolving towards a fully-developed state.

Mean velocity values measured at each position and normalized by the maximum velocity are presented in Figure 3.18. It is also showed at the same figure the turbulent intensity level, estimated by

$$TI = \frac{\sqrt{\overline{u'^2}}}{\overline{u}} \tag{3.4}$$

where the overbar denotes the time-averaging value, u is the instantaneous velocity in the outlet at the location of the hot wire, and u' represents the turbulent fluctuation.

Velocity values remain almost constant from the centre of the contraction outlet until y/h = 0.99. The test section flow non-uniformity, based on the difference between the minimum and the maximum nozzle outlet velocity outside the boundary layer (Mathew et al. (2005)), was found to be good (2.3%). The turbulence intensity level estimated is low even at positions near the wall. It is practically constant from the centre to y/h = 0.8, where turbulence intensity roughly reaches 0.6%. From y/h = 0.8 until the last measurement position, the mean TI rises up to 1%. The turbulence intensity was also measured at the centre of the nozzle inlet. At that position the TI was found to be 2.5%, which indicates that the LPD profile chosen reduces significantly the turbulence level coming from the settling chamber. These results indicate that there is no separation of the boundary layer, verifying the numerical ones.

The integral length scale of the largest eddies of the flow was determined by

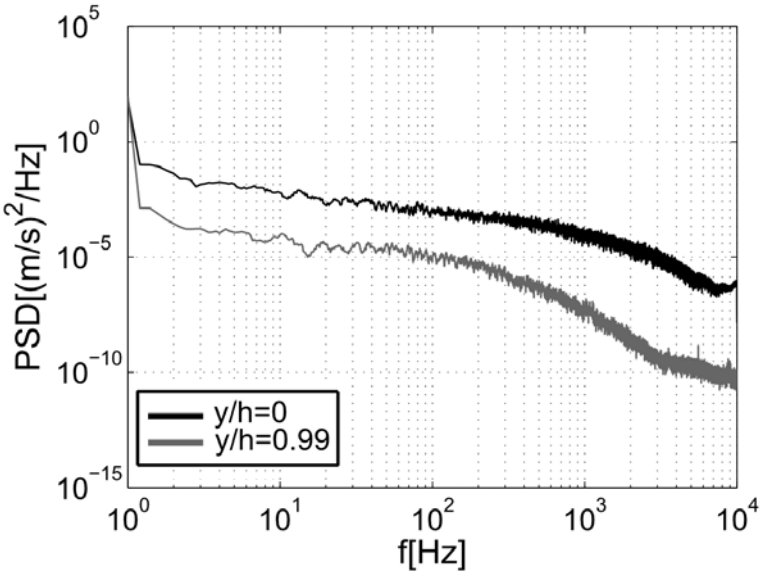

Figure 3.17: Power spectral density at the centre of the nozzle and near the wall

$$L = \overline{U} \int_0^\infty ACF(\tau) d\tau \tag{3.5}$$

$$ACF(\tau) = \frac{\overline{u'(t)u'(t+\tau)}}{\overline{u'^2}} \tag{3.6}$$

where τ is the time lag that is used to construct the ACF (autocorrelation function). This formulation assumes that the average eddy size lies through the correlation of two velocity signals (Taylor's hypothesis). To estimate the integral length scale in (Equation 3.5), it is necessary to evaluate the correlation coefficient (Equation 3.6) of the velocity fluctuations (in time), which theoretically must be defined up to infinity. The area under the correlation gives the value of the integral scale. Because in practice, this is limited, it is necessary to adopt a particular criterion. Following the guidelines of Tropea et al. (2007), three options are suggested: (a) "stop at the first zero crossing, i.e., at the first time separation, τ_{max}, for which the correlation coefficient vanishes. However, in many cases the correlation coefficient starts to exhibit oscillations before this zero is attained" (like in our experiment); (b) "In that case, a second, more-convenient possibility is to define τ_{max} as the value for which the autocorrelation coefficient reaches its first minimum"; and (c) "Another possibility is to estimate the integral scale as the value for which the correlation coefficient attains 1/e of its maximum (equal to 1 for zero separation), i.e., to the value expected if an exponential decay of the correlation coefficient is assumed". In our measurements, we have observed a clear correspondence between the two last limiting criteria: the first minimum is many times coincident with the 1/e limit. On the contrary, if we seek for the crossing with the x-axis, the area under the curve is notably extended and the overall integral value excessively enlarged.

It is evident the high degree of disparity and the inherent uncertainty to define an exact value of the integral length scale. Only an approximate order of magnitude and an overall trend can be given regarding this parameter. Consequently, to provide a reference result,

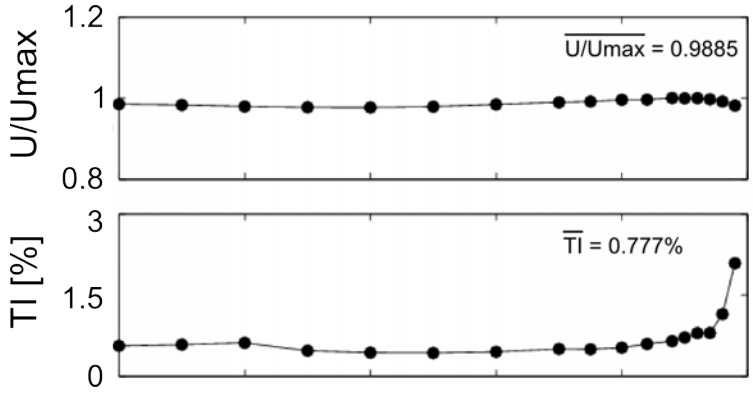

Figure 3.18: Normalized wind speed and turbulent intensity measured at $x = 0.5$m and vertical plane

we have performed a sort of averaging between all the different scales attained with sub-methods (b) and (c), which have been additionally smoothed. In Figure 3.19, the mean value of the distributions and those upper and lower limits representing approximately a 75% confidence level are represented. At the nozzle outlet the integral scale is approximately 50 mm in length in central positions and drops rapidly towards 10 mm close to the end-wall. On the contrary, it is enlarged as we move towards the nozzle inlet along the centre line with typical values in the range of 0.1 to 0.15 m, a fraction of the outlet hydraulic diameter for the nozzle (1 m).

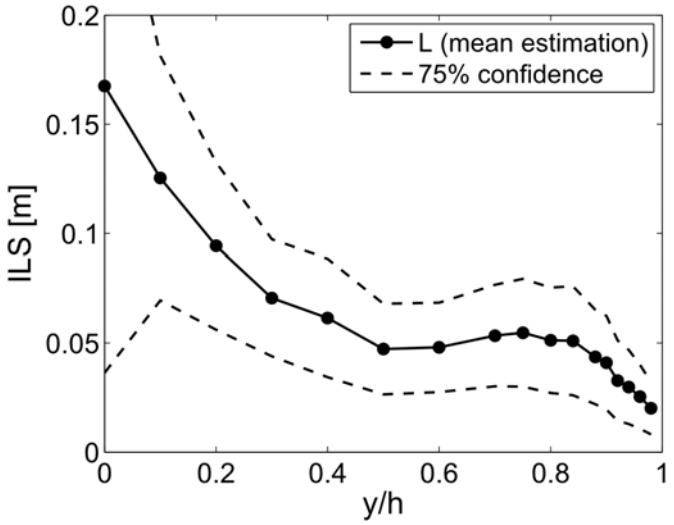

Figure 3.19: Distribution of integral length scale (75% confidence) measured at the centre line

The variation of the turbulence with the wind speed was also studied. For this survey, the X-probe was fixed at the centre of the contraction outlet and measurements were made with twenty different wind speeds. The results are plotted in Figure 3.20. One can note

that the turbulence intensity levels do not differ much. They maintain an approximately constant level of 0.69%.

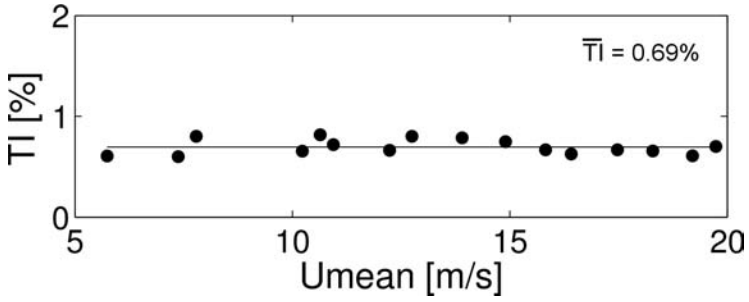

Figure 3.20: Turbulent intensity level for different wind speeds measured at the centre of the nozzle outlet

These outcomes conclude that the novel contraction developed is a good enhancing of the wind tunnel benefits. Thus, it was considered ideal for the design of the PIV wind tunnel.

3.2 Design, construction and characterization of the PIV wind tunnel

The aerodynamic characterization of the elliptic profile using HW and PIV required the construction of a new wind tunnel meeting all the needs. The PIV measurements typically need a closed test section even though the tunnel can be open-loop or close-loop. The components of a closed-test-section wind tunnel and open-loop, from the air inlet to the outlet are: settling chamber, honeycomb, nozzle, test section, diffuser and fan. The settling chamber has the largest cross-section in the facility and contains the honeycomb. The honeycomb with its cells aligned in the flow direction reduces mean or fluctuating variations in transverse velocity, with little effect on streamwise velocity because its pressure drop is small. However, these two elements are not always present in open-loop wind tunnels. The function of the nozzle is threefold: it accelerates the flow, makes the velocity distribution over the cross section of the flow more uniform and reduces the intensity of the turbulence in the airstream. The test section is the part of the tunnel where the tests are conducted. Its characteristics, the magnitude of the air-stream's cross-section and the nature of its boundaries, are decisive for the conception of experiments and the assessment of results. In a closed test section the streamlines are constrained by the walls, and so the local speed in the vicinity of the testing object is raised. The effect of the jet's boundaries become more pronounced the nearer they are to the model, i.e. the larger the blockage ratio. On the other hand, the magnitude of the air-stream's cross section depends on the nozzle features. The diffuser is the gradually-expanding passage following the test section in which the flow speed decreases and pressure rises, the recovery of pressure form kinetic energy reduces the power needed to drive the tunnel. Normally wind tunnels are driven by axial-flow fans which produce a static pressure rise at one point of the circuit to compensate for the total pressure losses in the rest of the circuit.

If the wind tunnel is closed-loop, its outlet is connected to its inlet. Closed circuit tunnels obviously have corners that need guide vanes to deflect the flow without boundary layer

separation. These type of wind tunnels use to require smaller fans, however the facility construction is more expensive.

3.2.1 Open-loop PIV wind tunnel

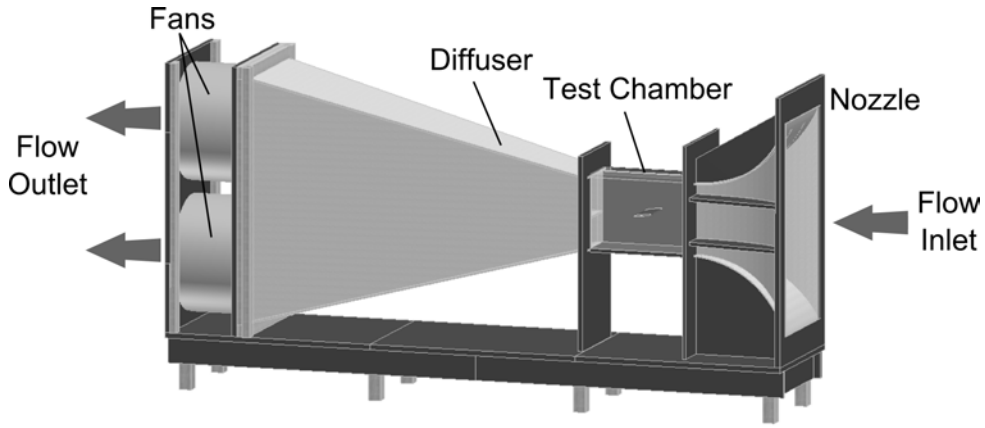

Figure 3.21: Open-loop PIV wind tunnel

A first version of the PIV wind tunnel was constructed with open-loop circuit (see Figure 3.21). This facility, made of plywood and MDF, included two axial fans placed in parallel. The NOVOVENT AXITUB POWER 6-630 P 34-12 fans are driven by an electrical motor with nominal rotation speed of 900 rpm and 0.75 kW.

The rotation speed of the fans can be modified with a variable frequency drive, YASKAWA V1000, in order to obtain a range of flow velocities at the test chamber up to $U_0 \leq 24.5$ m/s (at 50 Hz). The frequency drive used is shown in Figure 3.22.

The test chamber was designed to perform PIV measurements within the tunnel. This meant including two methacrylate walls to ensure optical access and two black walls to prevent laser reflection. The methacrylate walls have an opening and closing system for easy access and cleaning. The size of the test chamber is 0.4 m height ($2H$), 0.2 m width ($2W$) and 0.6 m long ($2L$) as it is depicted in Figure 3.23.

Figure 3.22: Frequency drive

The air was taken directly from the laboratory and accelerated in the nozzle before passing to the test chamber. The nozzle was designed with a contraction ratio of 9:1 using a

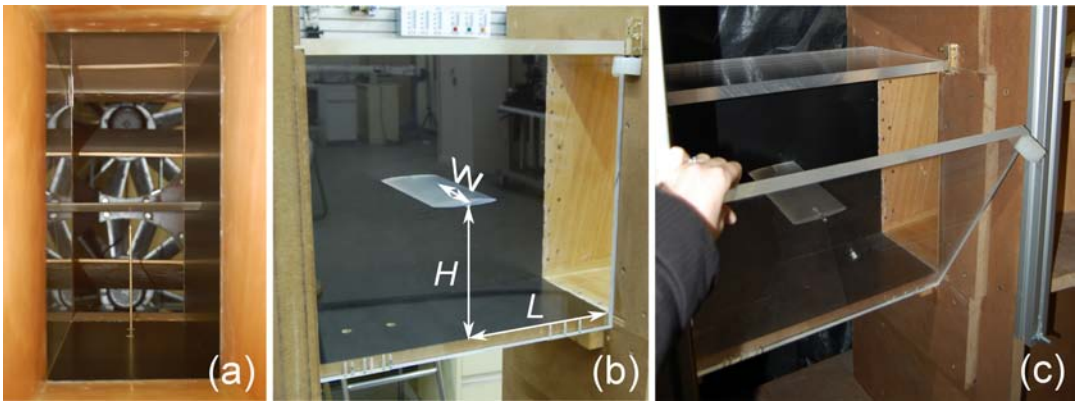

Figure 3.23: (a) Fan view from the test chamber. (b) Test chamber dimensions (c) Test chamber methacrylate walls

logarithmic derivative profile (LDP), which has exhibited good performance in previous work (see Section 3.1). Pictures of the construction and the finished nozzle are depicted in Figure 3.24.

Figure 3.24: (a) Nozzle construction. (b) Finished nozzle

Between the test chamber and the parallel fans is placed an asymmetric straight-walled diffuser. The cross-section of this duct is increased gradually from 0.4×0.2 m^2 to 1.5×0.8 m^2. In order to prevent the detachment of the boundary layer on its walls, three vanes have been placed inside. The divergence angle of every wall is less than 14°.

The free-stream turbulence intensity was measured in the geometrical test chamber using a hot-wire X-probe. Figure 3.25 represents the turbulence intensity as a function of the velocity in the test chamber. A mean level of 1.76% is reached within the operating range as it is marked by the dotted line.

Several attempts were made to perform PIV measurements in the open-loop wind tunnel. However, the desired concentration of tracer particles in the test section was very diffi-

cult to achieve in these conditions. Because the correct seeding is a determinant factor for obtaining optimal data using a PIV device, it was decided to close the wind tunnel constructing a closed-loop facility.

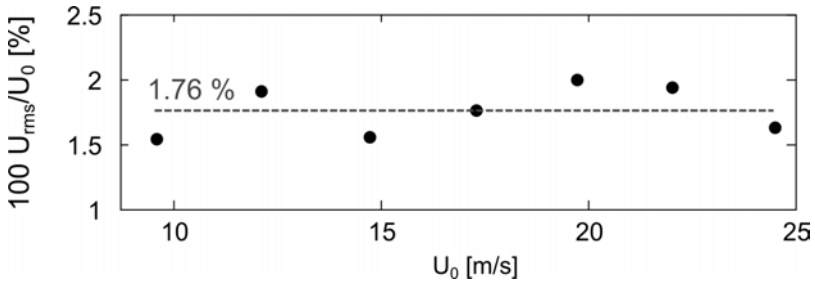

Figure 3.25: Turbulence intensity for different free-stream velocities, U_0, at the centre of the test chamber (open-loop wind tunnel)

3.2.2 Closed-loop PIV wind tunnel

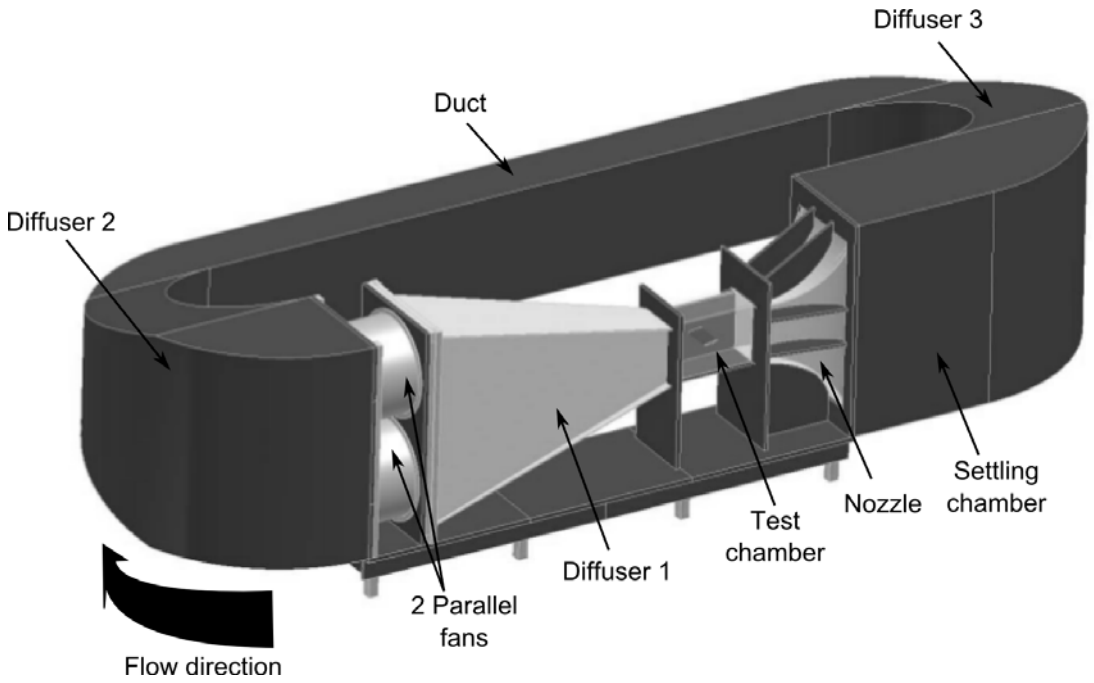

Figure 3.26: Wind tunnel scheme

A scheme of the closed-loop PIV wind tunnel is shown in Figure 3.26. It was necessary to add several elements to close the initially open-loop facility: a settling chamber, two diffusers, a duct and a honeycomb.

The settling chamber was placed before the nozzle. Due to its large cross-sectional area (1.5×0.8 m^2), it reduces the velocity of the air flow before entering the contraction. This element contains the honeycomb. The honeycomb was created with 30×30 mm^2 cells of 150 mm length aligned in the flow direction reducing mean and fluctuating variations in transverse velocity.

Two diffusers were added connecting the fans with the duct and the duct with the settling

chamber respectively, allowing a smooth transition between different cross-sectional areas. They were designed with a curved geometry to reduce the length of the wind tunnel. It was necessary to include vanes to guide the flow and prevent boundary layer separation.

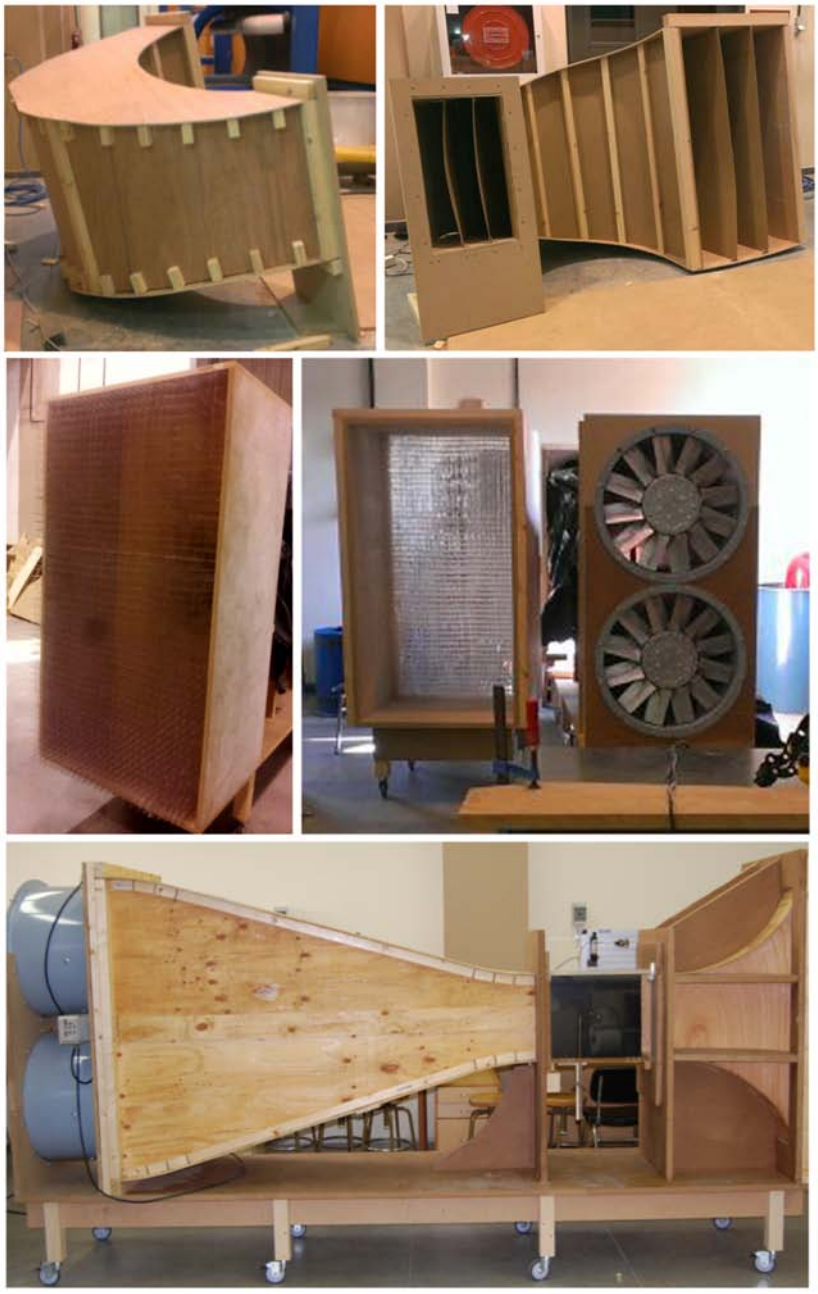

Figure 3.27: Construction process of the PIV wind tunnel

The duct was constructed to join the two diffusers. The length of the duct was already imposed by the span of the previous open-loop wind tunnel and the settling chamber (5 m). Its cross-sectional area was established considering that the air velocity inside should be high enough to prevent a massive deposition of the seeding particles (0.8×0.4 m^2).

Figure 3.27 and 3.28 show the construction process of the PIV wind tunnel and the finished one, respectively.

Figure 3.28: Finished closed-loop PIV wind tunnel

The velocity at the centre of the test chamber was again measured using a hot-wire X-probe. A comparison between velocity signals measured in the open-loop wind tunnel and closed-loop wind tunnel is shown in Figure 3.29. Results showed that the variation of the velocity signal in the open-loop case exhibit a random behaviour with alternation of high and low turbulence levels. On the other hand, the variation of the velocity signal in the closed-loop case is much more uniform.

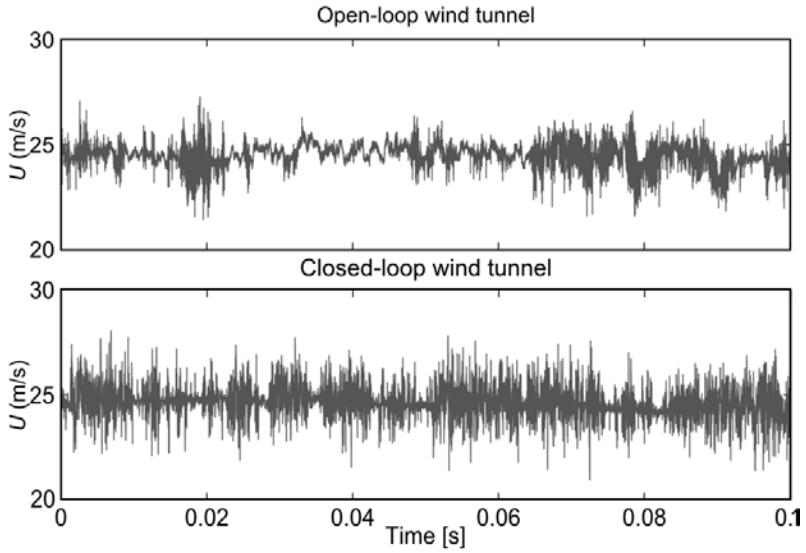

Figure 3.29: Comparison of velocity signals acquired at the test chamber centre of open-loop and closed-loop wind tunnel

The turbulence intensity levels of the closed-loop wind tunnel measured at the centre of the test-section for different flow velocities are plotted in Figure 3.30. The mean turbulence intensity has been increased after closing the wind tunnel, however, it has given more uniformity to the flow. Even though the turbulence levels could be reduced introducing some screens inside the settling chamber (right after the honeycomb) it has been decided to maintain the facility as it was. Since the application of elliptic aerofoils is essentially

focused on turbomachinery, which implies turbulent flows, the absence of screens offers more realistic flow conditions.

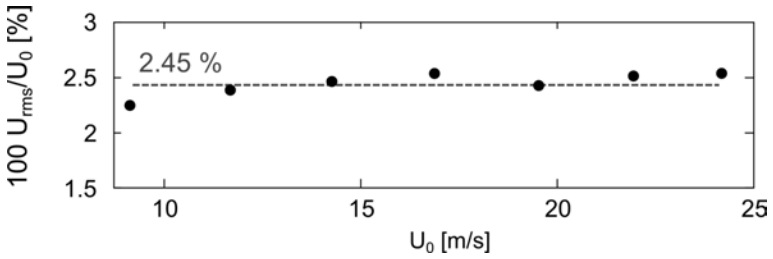

Figure 3.30: Turbulence intensity for different free-stream velocities, U_0, at the centre of the test chamber (closed-loop wind tunnel)

3.3 Elliptic aerofoil

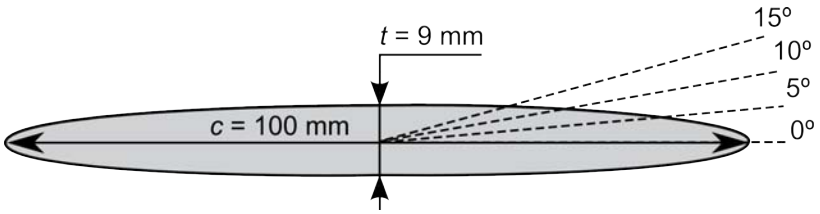

Figure 3.31: Aerofoil scheme

Two methacrylate elliptic aerofoils (Figure 3.31) with a maximum thickness ratio t/c = 0.09 have been used for performing the experiments. The aerofoils have a major axis, chord, of c = 0.1 m and a minor axis, thickness, of t = 0.009 m. The span dimension (b) match the width of the test chamber. Thus, no gap was allowed between the two sides of the profile and the vertical walls of the chamber (see Figure 3.23). The aerofoils were supported at its geometrical centre using two steel rods and the angle of attack was modified manually. The configurations adopted in the present study were $\alpha = 0°$, 5°, 10° and 15°.

The roughness each of aerofoil surface was determined using a roughness tester. The profile average roughness, i.e. the average of the absolute vertical deviations of the roughness profile from the mean line, was R_a = 1.79 µm (Figure 3.32 (c)) and R_a = 0 µm (Figure 3.32 (d)).

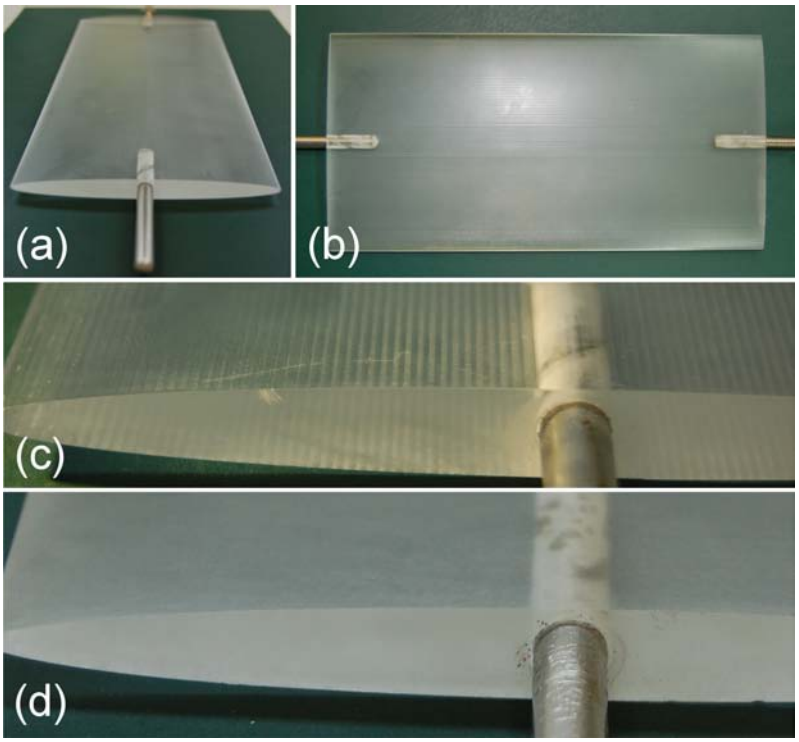

Figure 3.32: Methacrylate elliptic aerofoil. (a) Front view. (b) Side view. (c) Zoom view

3.4 Instrumentation setup

This section explains the different configurations adopted to measure using particle image velocimetry and hot-wire anemometry.

3.4.1 PIV setup

The wind tunnel (1) with the TSI PIV equipment is shown in Figure 3.33. The laser (4) was fixed to a medium-density fibreboard (MDF) structure over the test section (2). Placing the laser in vertical position allowed the light sheet to fall on the upper surface of the aerofoil, perpendicular to the CCD camera (3). The Litron nano laser has a wavelength of 532 nm and a variable frequency between 1 and 15 Hz. Both lenses, the spherical and cylindrical, were attached to the laser body. The camera used is a PowerView™ PIV with very short frame-straddling times. Particles of alumina were introduced into the diffuser, after the test section, using an injector (5). The acquired data was recorded in a computer (6) connected to the synchronizer (7) and the wired remote control device of the laser (8). Insight 3G was the software used for capturing and analysing images.

3.4.1.1 Laser arrangement

It was necessary to set three different laser-camera arrangements to study the flow behaviour around the aerofoil and at its wake. Both laser and camera were moved horizontally a distance of 60 mm each time. This disposition provided an overall image width and height of 310 mm and 117 mm respectively. However the final dimension has been reduced due

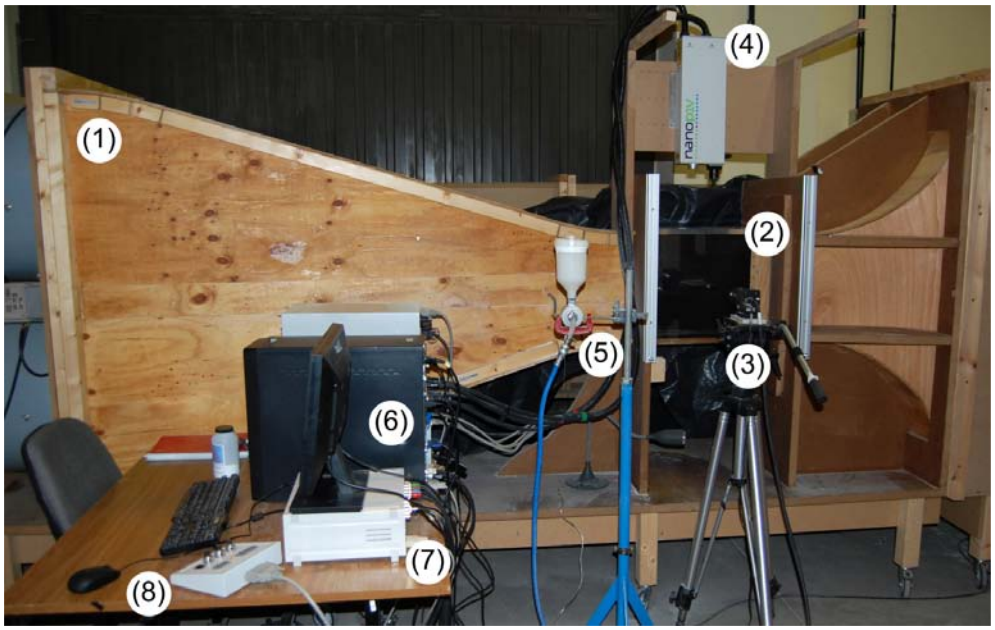

Figure 3.33: PIV experimental setup

to the lack of illumination from the laser sheet in some frame zones. The position of each frame (1 to 3) is indicated in Figure 3.34. There is an overlap of the images to prevent information loss on the vector field.

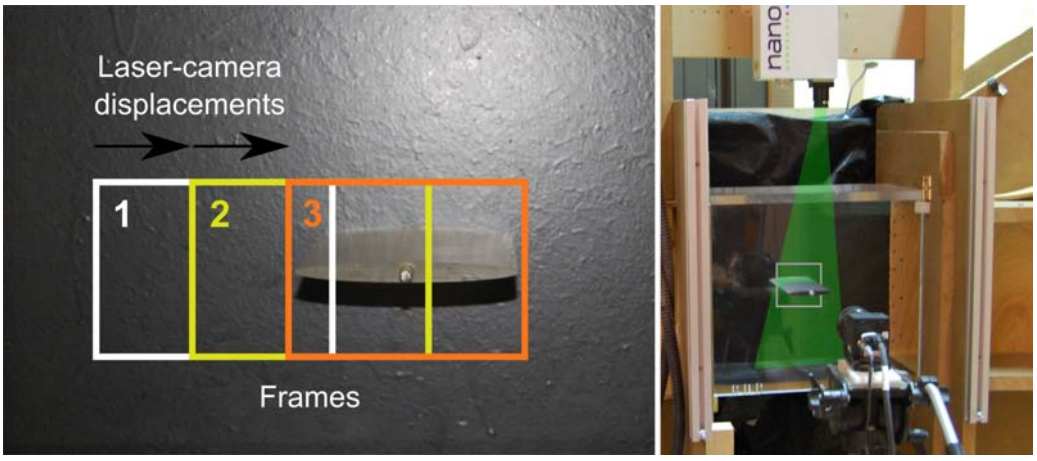

Figure 3.34: Laser sheet arrangement

3.4.1.2 Particles seeding

Three different types of particles were tested in order to determine their suitability: olive oil droplets, water droplets and alumina micro-spheres. Both liquid seeds didn't deliver good snapshots so that the PIV software gave spurious vectors. The concentration of oil droplets was too high and the sizes too small to recognize movement patterns. On the other hand, water droplets didn't scatter enough light to be properly captured by the

CCD camera. Finally, alumina powder was tested and results delivered were optimal.

Based on these outcomes, the tracer particles used for PIV measurements in an air flow were of alumina with a mean diameter of 10 µm. This type of particles has been widely used in literature because of their good optical properties. A Venturi injector was constructed specifically for feeding the wind tunnel (Figure 3.35 (c)). The particles were introduced into a feeding tank connected to the injector through a hole at its bottom. Pressurized air coming from a pipe enters the device, collects the particles and flows through another pipe into the wind tunnel. Injecting particles into the diffuser, right after the test section, make them to travel across the rig before reaching the measurement plane. That ensures a correct distribution in the flow. Because very low velocities are achieved in some areas of the tunnel (1.4 m/s), the heavier particles lay down in the ducts and only the ones that perfectly followed the flow reach the test section.

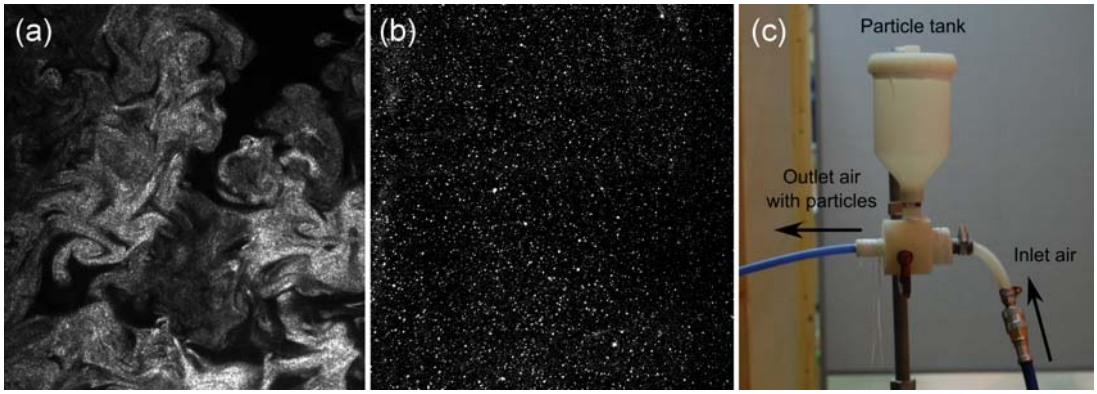

Figure 3.35: (a) Olive oil seeding. (b) Alumina seeding. (c) Particles injector

Although olive oil droplets weren't used for PIV measurements, they became a good alternative to perform flow visualization. Thus, the visualization of the air movement around the aerofoil was accomplished using the same experimental setup as for PIV measurements (Figure 3.33). In this case the Venturi particle seeder was replaced by an oil droplet generator model 9307 of TSI (Figure 3.36) that provides mean droplet sizes of 1 micron for olive oil. The droplets were dragged by the air, following its movement, achieving a high enough concentration to visualize the flow. The laser was used for lighting up the flow and the PowerView™ camera for recording images.

Figure 3.36: Oil droplet generator

3.4.2 Hot-wire anemometry setup

Figure 3.37 shows the experimental setup for hot-wire anemometry measurements. The hot-wire probe (3) was affixed to the lower wall of the test chamber (2) that is part of the PIV wind tunnel (1). The support used for attaching the probe to the test chamber permits movement in vertical axis. A TSI IFA 100 anemometer (4) connected both to the HW probe and to a National Instruments acquisition card that gave the information to a computer (6) was used to perform measurements. Data acquisition and transformation has been done using a MATLAB code developed for these particular applications. The calibration bench (7) has been used previously to each measurement to obtain the Kings law and angular calibration of the hot-wire probe.

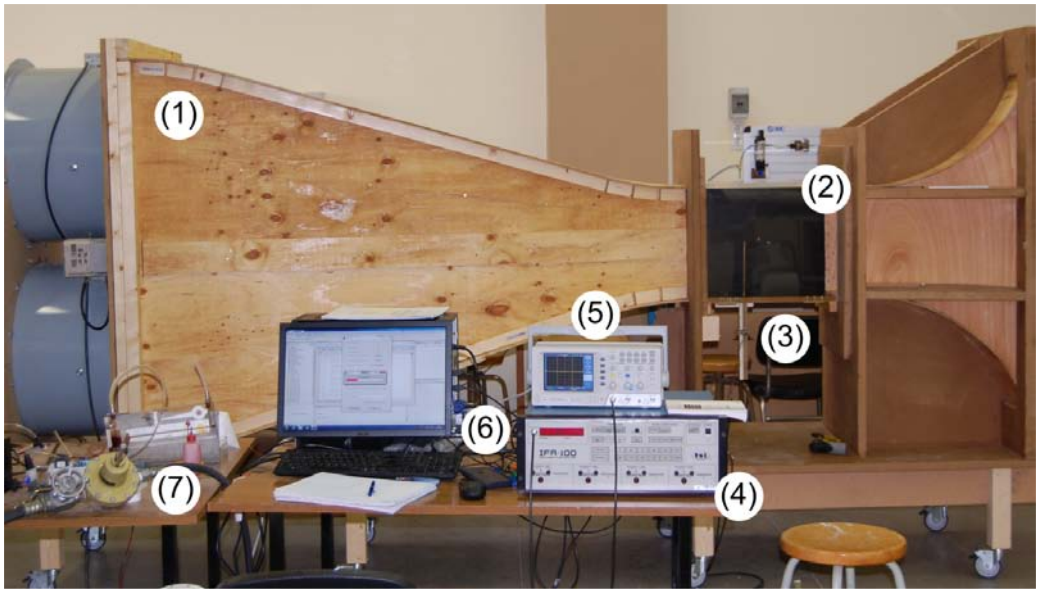

Figure 3.37: HW anemometry experimental setup

3.4.2.1 Hot-wire probe arrangement

The fact that a single hot-wire probe only can acquire data from a certain point in space, imply that many discrete measurements have to be made for characterizing a specific area. In this particular case, the objective was to study the wake behind the aerofoil, which required the definition of a certain downstream area (see Figure 3.38). A great effort has been done to characterize the wake with high resolution. Even though the measuring region was 70 mm height ($y/t = 3.89$) and 70 mm width ($x/c = 0.75$), it led to a high number of measurements. In particular, the probe was placed at more than 1500 different positions (47 vertical $\times$ 8 horizontal $\times$ 4 angles of attack) which requires the same amount of data series to be processed. It must be noted that the origin of the coordinate system was established at the centre of the test chamber and the x, y and z coordinates were defined in the streamwise, normal and span-wise directions respectively. A sampling frequency of 10 kHz was chosen for recording the data during 25 s, which was considered high enough for the phenomena under study.

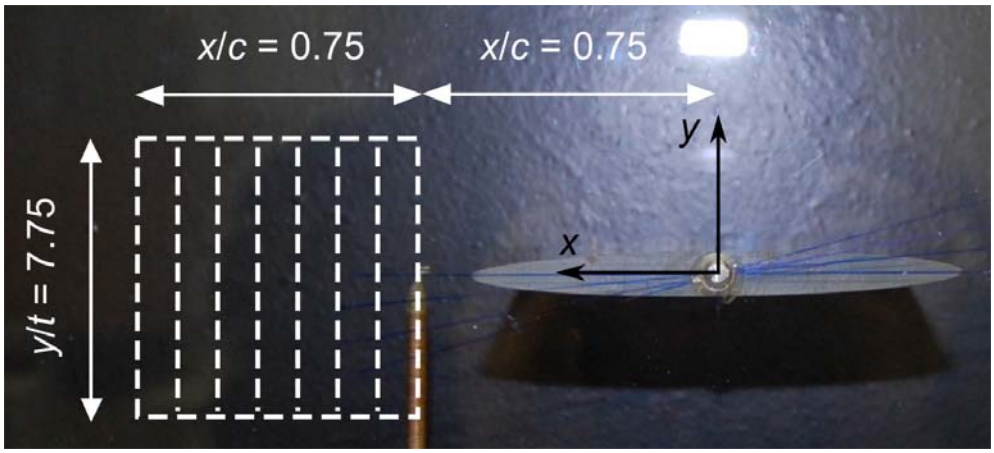

Figure 3.38: HW probe arrangement

CHAPTER 4

PIV measurements and visualization of the flow

The effects of the angle of attack on the flow around a slender elliptical aerofoil with c/t = 0.09 have been studied using Particle Image Velocimetry. Velocity fields comprising the streamwise and the vertical components have been obtained directly from the measurements, whereas another variables have been derived from the velocity field. All the equations used for estimating aerodynamic variables and gaining an insight of the flow behaviour have been listed in this chapter. Contour, vector and streamlines maps were combined to show the flow characteristics in four different experiment configurations. Flow visualization has been also assessed and the structures can be seen to give an in-depth vision of the phenomena.

4.1 Flow analysis

The quantitative flow field measurements taken by using PIV system and the software *Insight 3G* can elucidate significant details about the flow pattern, the behaviour of vortex and turbulent flow structures around the aerofoil. The obtained data was post-processed using *MATLAB*, so another derived variables such as vorticity or turbulent kinetic energy could be calculated. This section describes the procedures and all the variables used to analyse the flow behaviour. Figure 4.1 shows an example of raw image acquired, velocity vectors, streamlines and magnitude obtained after the processing. The results present in this chapter combine streamlines and magnitudes to improve the understanding of the images.

The instantaneous velocity recorded at each interrogation window is composed of a mean component, denoted by overbars, and a fluctuation component, denoted by a prime. These values constitute the basis to the subsequent analysis process.

$$U_n = \sqrt{u_n^2 + v_n^2} \tag{4.1}$$

$$u_n = \overline{u} + u'_n, \quad \overline{u} = \frac{1}{N}\sum_{n=1}^{N} u_n \tag{4.2}$$

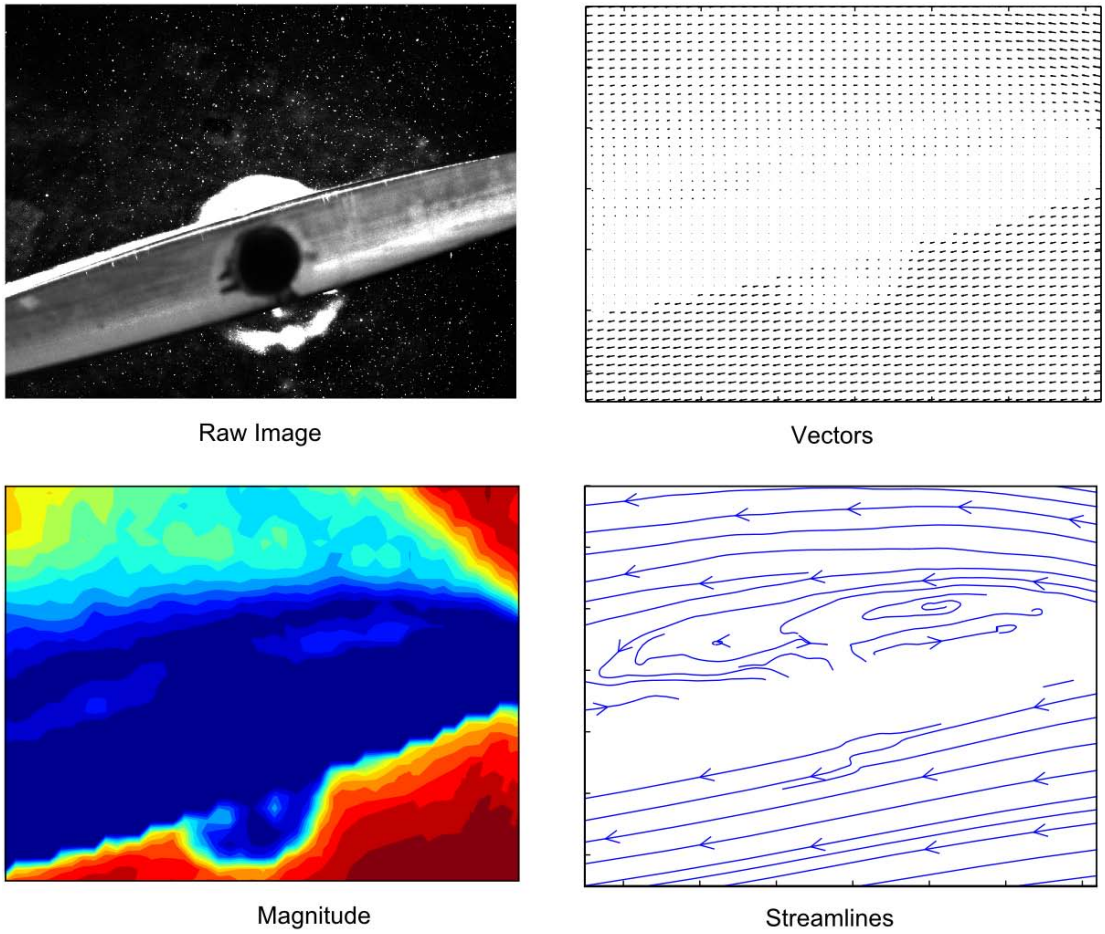

Figure 4.1: Sample of a raw image, flow vectors and streamlines obtained

$$v_n = \overline{v} + v'_n, \quad \overline{v} = \frac{1}{N}\sum_{n=1}^{N} v_n \tag{4.3}$$

where n denotes each snapshot.

The first derived-variable estimated was the turbulent kinetic energy, which is the mean kinetic energy per unit mass associated with eddies in turbulent flow. This magnitude directly represents the "strength" of the turbulence in the flow. It is quantified by the mean of the turbulence normal stresses by,

$$k = \frac{1}{2}\left(\overline{u'^2} + \overline{v'^2}\right) \tag{4.4}$$

where the overbar refers to the spatial average.

The dissipation of the turbulent energy was calculated measuring the gradients of the Reynolds stresses. As the measurements were taken using a two-dimensional PIV system, only two velocity components (u and v) were available. The unknown terms were assumed to be statistically isotropic and thus derivable from the known ones (Sharp et al. (1998)). Therefore, the expression of the turbulent dissipation rate, ε, is formulated as:

$$\varepsilon = \nu \left\{ 2\overline{\left(\frac{\partial u'}{\partial x}\right)^2} + 2\overline{\left(\frac{\partial v'}{\partial y}\right)^2} + 3\overline{\left(\frac{\partial u'}{\partial y}\right)^2} + 3\overline{\left(\frac{\partial v'}{\partial x}\right)^2} + 2\overline{\frac{\partial u'}{\partial y}\frac{\partial v'}{\partial x}} \right\} \tag{4.5}$$

where ν is the kinematic viscosity of the flow.

The vorticity, that account for the rotating motion of the fluid, is calculated using the following equation:

$$\omega = \frac{\partial v}{\partial x} - \frac{\partial u}{\partial y} \tag{4.6}$$

4.2 Velocity field around the aerofoil

The velocity field obtained with the ensemble average of the 300 instantaneous values for a Reynolds number of 80800 is presented in this section. This Reynolds number corresponds to a free-stream velocity of 12.2 m/s. The PIV measurements were performed only at one single velocity because, as it is demonstrated in the following chapter, the normalized velocity profile collapses into one trend when considering the velocity range attainable in the wind tunnel. Results show the classic characteristics expected in the flow passing an aerofoil. Each velocity field was obtained with the overlap of partial frames, as it was explained previously in the Experimental Setup chapter. Unavoidable slight differences in the flow conditions during separate runs led to little results mismatch. Figures in this chapter are composed by the three combined frames. White borders are included in all images to favour their identification. In addition, a black mask has been applied to the aerofoil profile and the circular area at the location of the scratch.

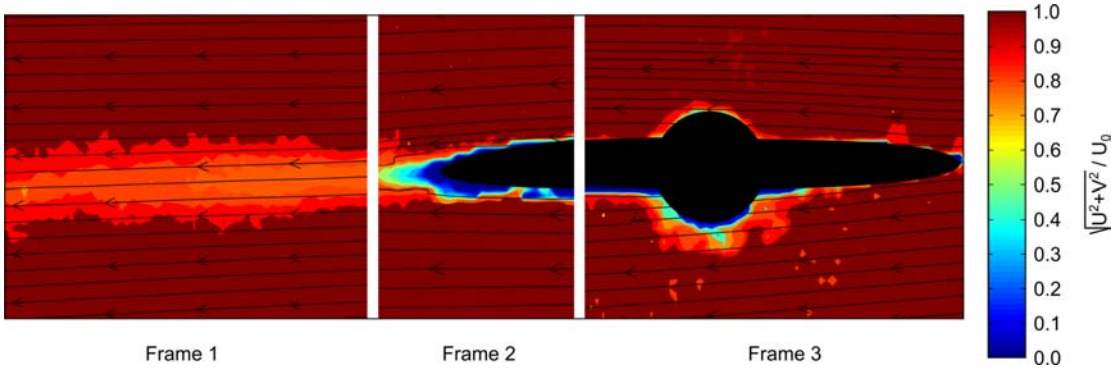

Figure 4.2: Normalized velocity and vectors for 0° angle of attack

The normalized velocity magnitude has been calculated as

$$\frac{U}{U_0} \tag{4.7}$$

where U_0 is the free stream velocity.

Figures 4.2, 4.3, 4.4 and 4.5 show the ensemble-average normalized velocity field for 0° , 5° , 10° and 15° angles of attack respectively. An increase of the angle of attack (α) affects directly the dimension and velocity magnitude of the wake. At 0° the wake behind the

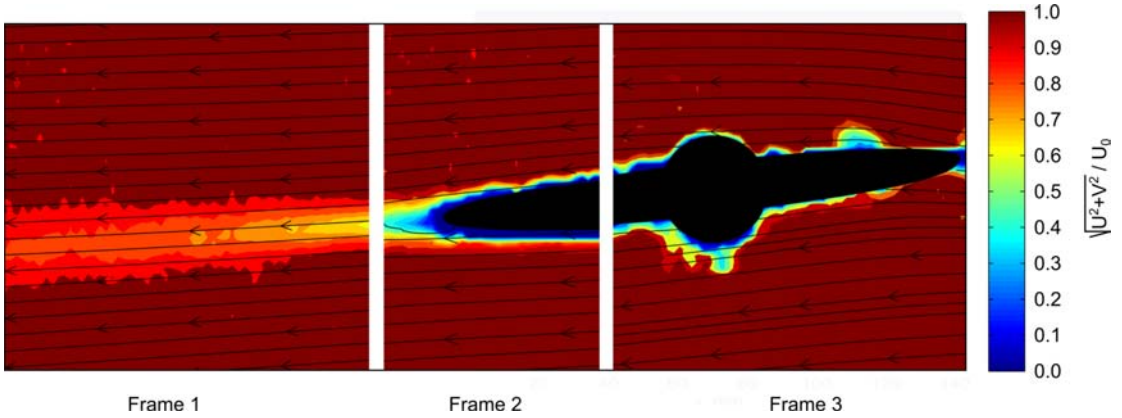

Figure 4.3: Normalized velocity and vectors for 5° angle of attack

aerofoil -zone of reduced velocity- is compact and very similar to the one generated at 5°. This last one exhibits the resultant deflection and has a slightly greater velocity reduction. It has been also observed that the width of the wake is of the same order of magnitude than the aerofoil thickness. Higher angles of attack (10° and 15°) imply wider wakes and lower velocities behind the aerofoil. Moreover, the lower part of the wake remains almost unchanged while the upper part is shifted upwards as α increases. In a quantitative way, the flow deflection does not seem to increase considerably from 5°.

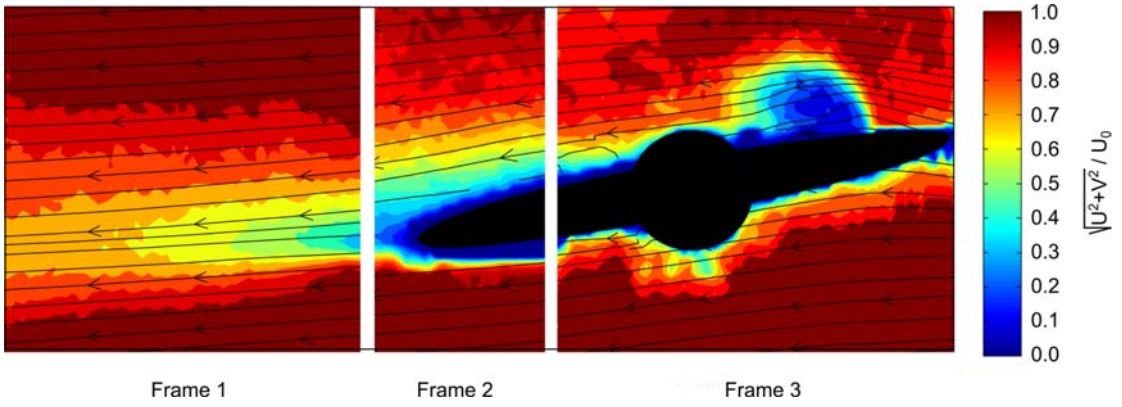

Figure 4.4: Normalized velocity and vectors for 10° angle of attack

The flow over the aerofoil do not exhibit detachment of the boundary layer at 0° and 5°. However, in case of $\alpha = 5°$, a small laminar separation bubble is observed (see Figure 4.3) that starts at an approximate distance from the leading edge of $x/c \approx 0.05$ and disappears at $x/c \approx 0.18$. It must be noted that due to perspective, this distance seems to be further to the leading edge than it really is (see Figure 4.22 for clarification). A correction factor has been applied to x/c in order to overcome this inconvenience. Similar separation bubbles have been reported by other authors (e.g. Huang and Lin (1995) and Mueller and DeLaurier (2003)). This phenomenon observed at Re_c=80800 agrees with the statement of the former authors, that delimit the Reynolds numbers at which the bubble is formed to $1{\times}10^4 < Re_c \leq 5 \times 10^5$. The flow after the bubble remains attached to the upper aerofoil wall until it reaches the trailing edge.

The laminar separation bubble, bigger than the one observed at $\alpha = 5°$, appears also at $\alpha = 10°$. The bubble starts at an approximate distance from the leading edge of $x/c \approx 0.05$

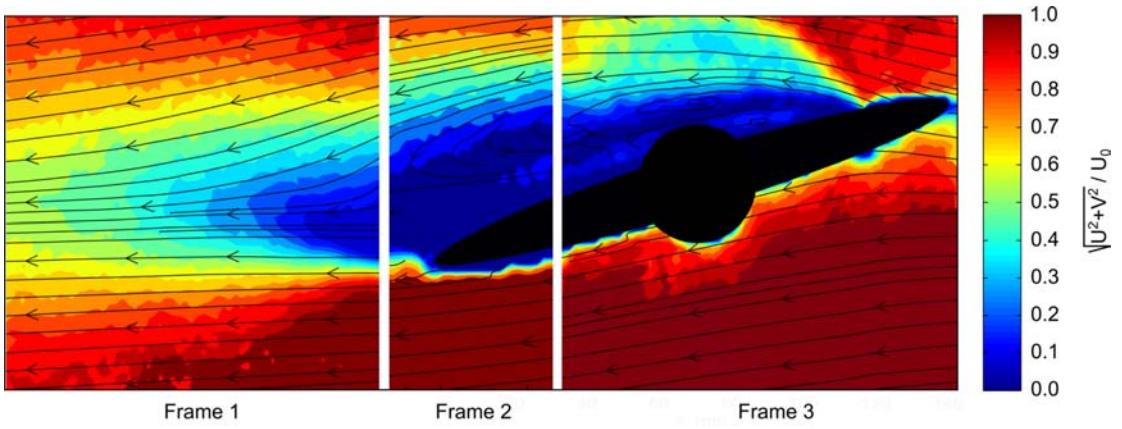

Figure 4.5: Normalized velocity for 15° angle of attack

and disappears at $x/c \approx 0.4$ (see Figure 4.4). However, in this case the fluid is not capable of remaining reattached to the suction surface until the end, and the detachment of the turbulent boundary layer is produced at some point near the middle of the aerofoil leading to the broadening of the wake. For an angle of attack of 15° the separation bubble no longer appears. Instead, the detachment of the boundary layer becomes noticeable at $x/c \approx 0.05$ with a drastic decrease of the flow speed inside the wake.

4.3 Vorticity

The flow ensemble average vorticity and streamlines around the aerofoil have been depicted in Figures 4.3, 4.7, 4.8 and 4.9 at 0° , 5° , 10° and 15° angles of attack respectively. High vorticity values have been found near the aerofoil walls even when all particles were flowing along straight and parallel path-lines -cases at 0° and 5° -. The existence of shear in this areas, i.e. flow velocity variations across streamlines, explains such behaviour.

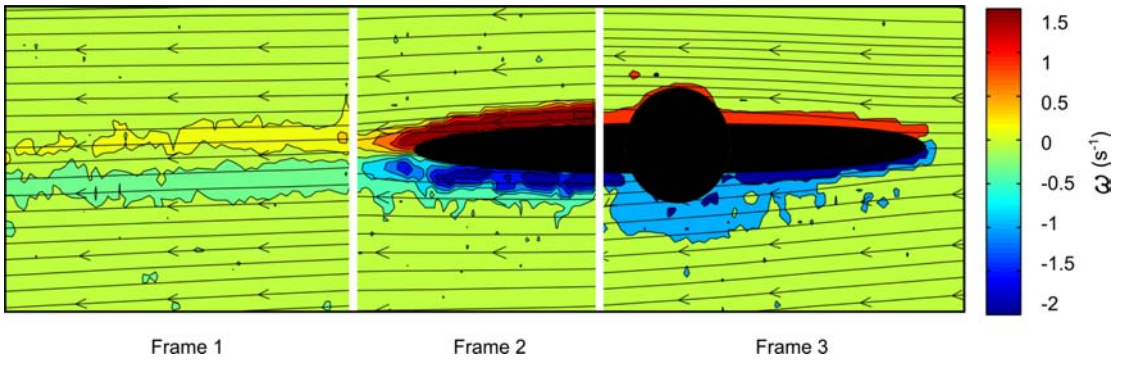

Figure 4.6: Vorticity and streamlines for 0° angle of attack

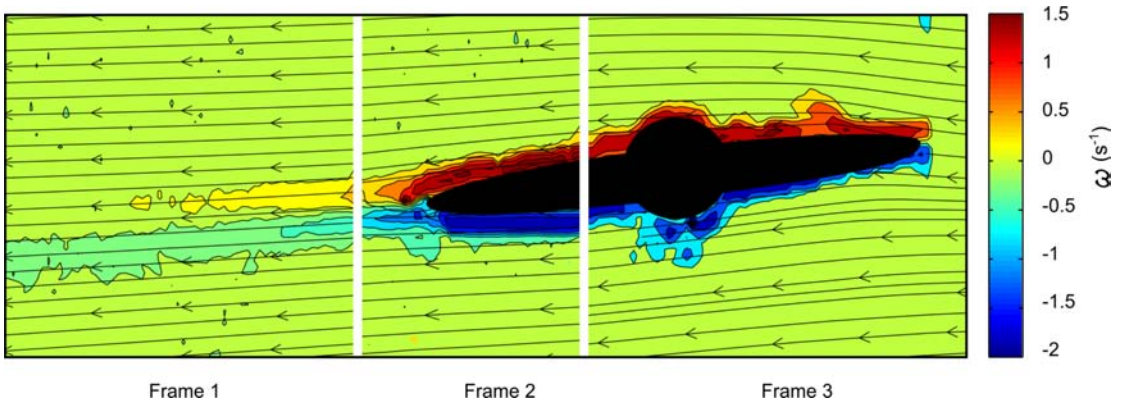

Figure 4.7: Vorticity and streamlines for 5° angle of attack

Positive values of vorticity are gathered in the upper part of the aerofoil and wake, whereas negative values are located in the lower area. A positive vorticity indicates that the flow is turning counter-clockwise and vice versa. Two parallel vorticity regions with different swirling directions have been found downstream of the aerofoil at 0° (Figure 4.6). The flow pattern observed corresponds to the Von Karman vortex street caused by the separation of the flow at the trailing edge. Even though neither in velocity nor in vorticity can be seen individually the Von Karman vortex street, it can be stated that those eddies are produced thanks to the flow visualization (see Section 4.7). These two regions of swirling flow still appear at 5° (see Figure 4.7). However, the positive vortex area on the top seems to dissipate fast, even disappearing at higher angles of attack. The thickness of the negative vorticity region, as well as its magnitude, increase with the angle of attack (see Figures 4.8 and 4.9). This agrees with the stronger flow speed variations in the wake. High positive vorticity values are found at high angles, at the detachment point of the boundary layer, on the upper surface of the aerofoil. The positive vorticity over the aerofoil -associated with the boundary layer- disappears at 15° after the separation point. There is a high-vorticity area related with the shear layer in the frontal zone of the bubble at 10° and in the detached flow at 15°. This vorticity could be attributable to the formation of Kevin-Helmholtz instabilities.

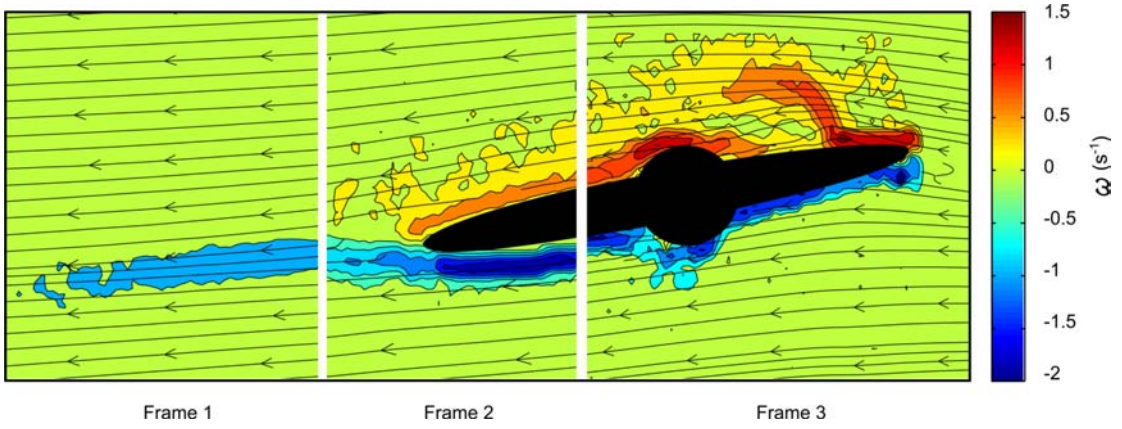

Figure 4.8: Vorticity and steamlines for 10° angle of attack

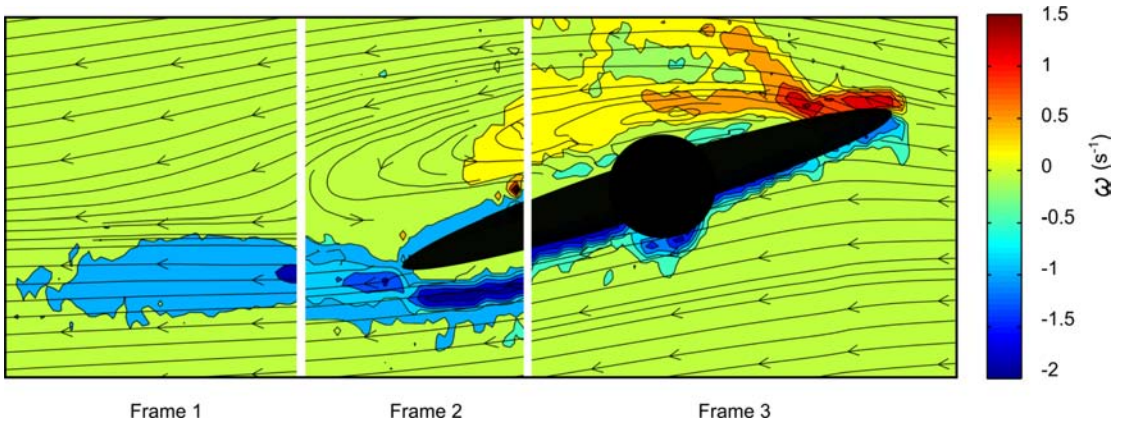

Figure 4.9: Vorticity and streamlines for 15° angle of attack

4.4 Turbulent kinetic energy

In order to analyse the turbulent behaviour of the flow, a quantitative measure of the random unsteady velocity fluctuations has been calculated. The two dimensional turbulent kinetic energy was obtained from the velocity data using Equation 4.4. However, as it has been stated by Spencer and Hollis (2005), the methodology inherent to PIV results in an spatial averaging of the real velocity field into a set of discrete measured velocities. Hence, this filtering produces a reduction of the measured turbulent kinetic energy and the obtained values must be taken only in a relative way and as indicators of the location where the turbulent kinetic energy is more intense.

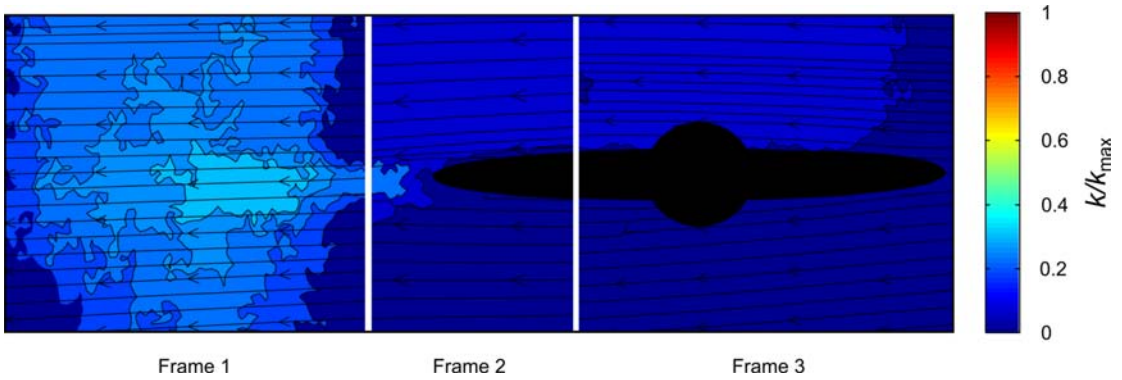

Figure 4.10: Turbulent kinetic energy and streamlines for 0° angle of attack

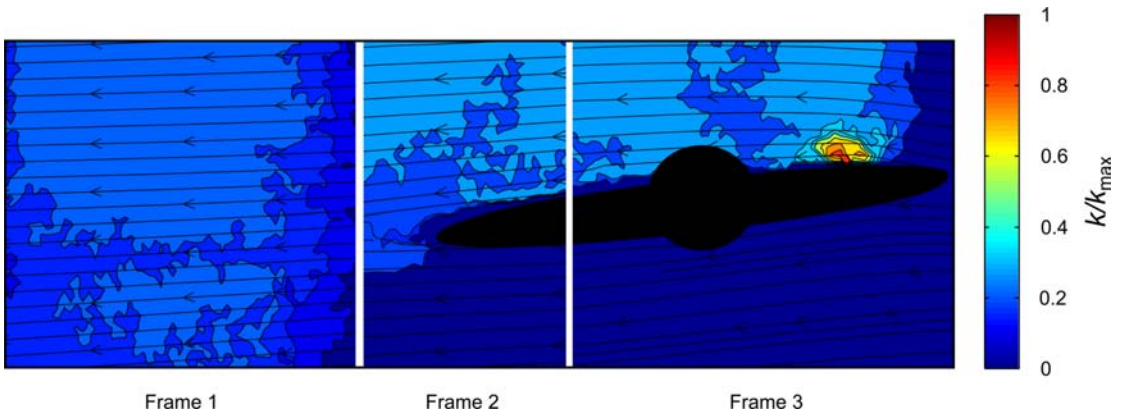

Figure 4.11: Turbulent kinetic energy and streamlines for 5° angle of attack

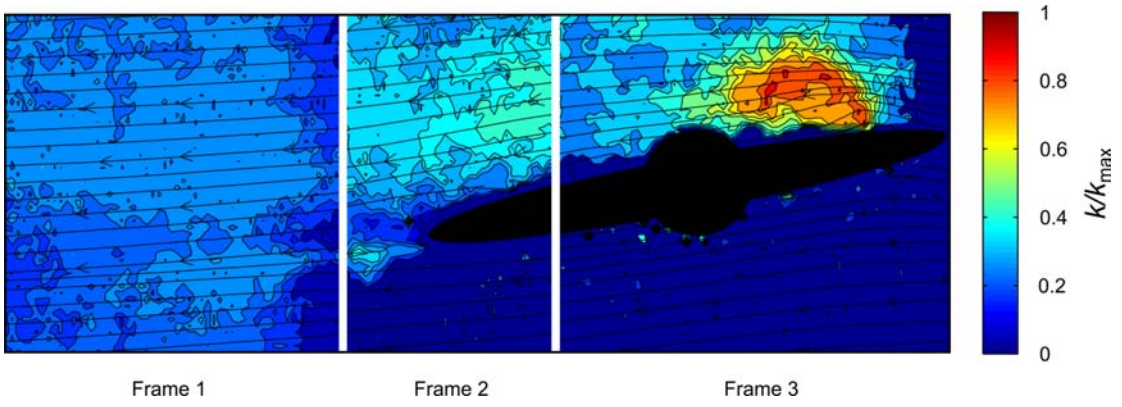

Figure 4.12: Turbulent kinetic energy and streamlines for 10° angle of attack

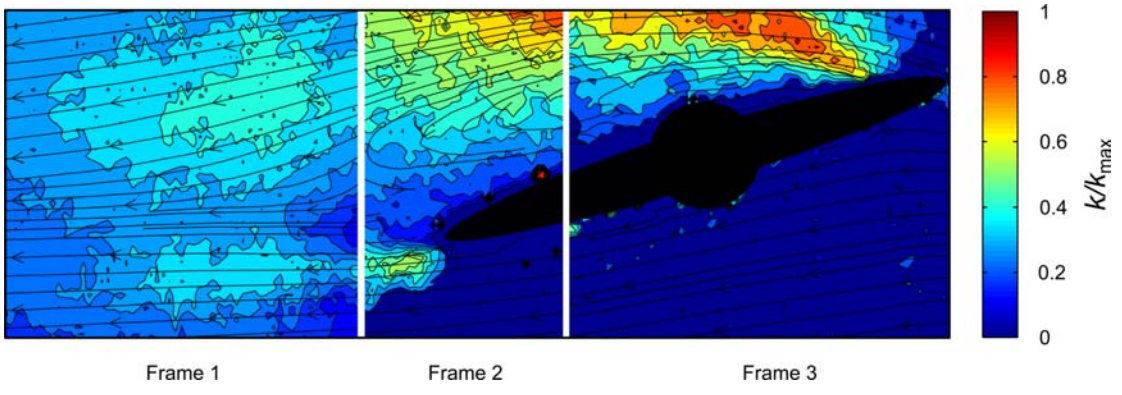

Figure 4.13: Turbulent kinetic energy and streamlines for 15° angle of attack

Figures 4.10, 4.11, 4.12 and 4.13 illustrate the mean normalized turbulent kinetic energy levels as well as the streamlines of the flow for the four studied angles of attack. The value of $k_{max} = 36\ \mathrm{m}^2/\mathrm{s}^2$ used for normalizing corresponds to the highest turbulent kinetic energy estimated, namely at 15°. As it was expected, the levels of the flow field around the aerofoil were found to be relatively low. The regions with the highest levels were found to concentrate at the suction area of the aerofoil. The measured turbulent kinetic energy levels at 0° are significantly small compared to the ones observed at higher angles of attack. At an angle of 5°, the highest values are reached at a fairly small area that matches with the separation bubble reported in section 4.2. The same situation was found at 10°, however the zone with the highest values is larger in this case as the separation bubble extends further downstream. At 15° angle of attack the regions with higher turbulent kinetic energy are along the separation shear layer at the front which could correspond to the shedding path of the unsteady Kelvin-Helmholtz vortex structures.

4.5 Turbulent energy dissipation

It is known that the kinetic energy of turbulence is dissipated by breaking the biggest eddies into smaller ones until it is eventually converted into heat by viscous forces. The turbulent energy dissipation has been estimated considering turbulence as non-homogeneous but statistically isotropic by using Equation 4.5. Figures from 4.14 to 4.17 show the distribution of the normalized mean values of ε for the four studied angles of attack. The value of $\varepsilon_{max} = 4.5 \times 10^3 \mathrm{m}^2/\mathrm{s}^3$ used for normalizing corresponds to the highest turbulent energy dissipation estimated, namely at 15°.

The highest turbulent energy dissipation values are found in regions where the kinetic energy of turbulence was maximum, and decay in the zones where the turbulence is less intense. These areas coincide with the separation bubbles on the upper surface of the aerofoil at 5° and 10°, and with the detached shear layer at 15°.

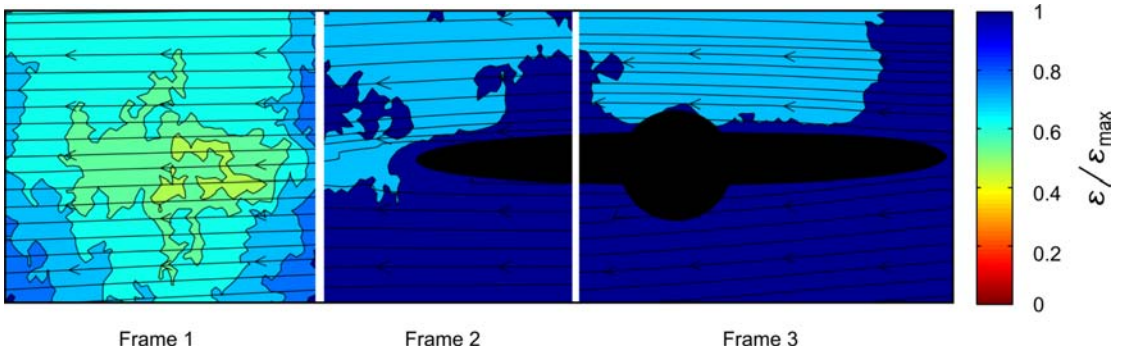

Figure 4.14: Turbulent dissipation rate for 0° angle of attack

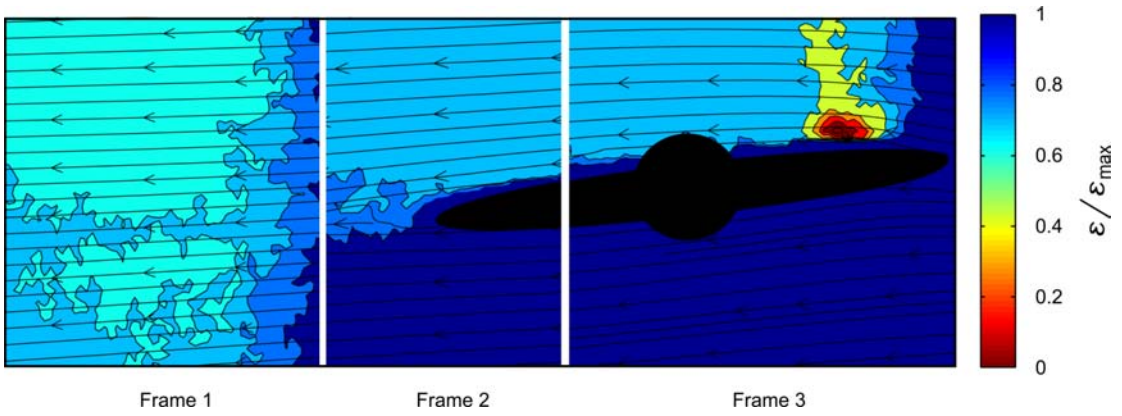

Figure 4.15: Turbulent dissipation rate for 0° angle of attack

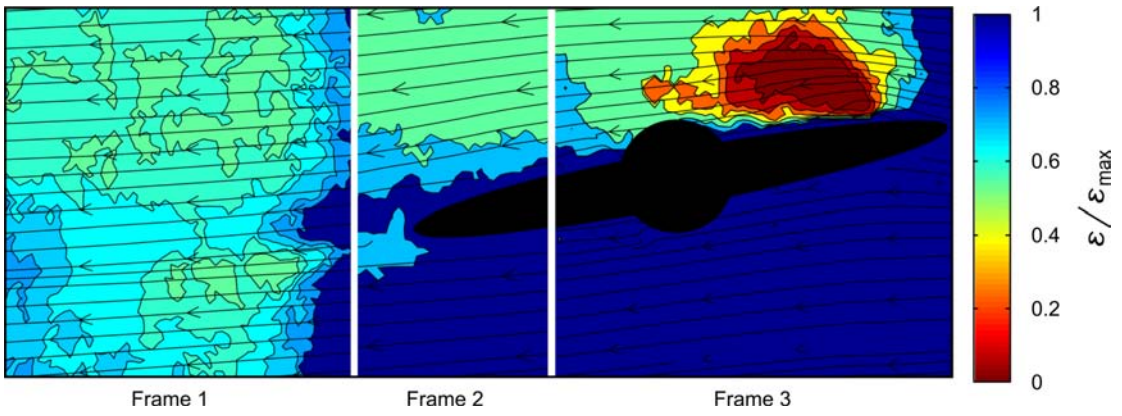

Figure 4.16: Turbulent dissipation rate for 10° angle of attack

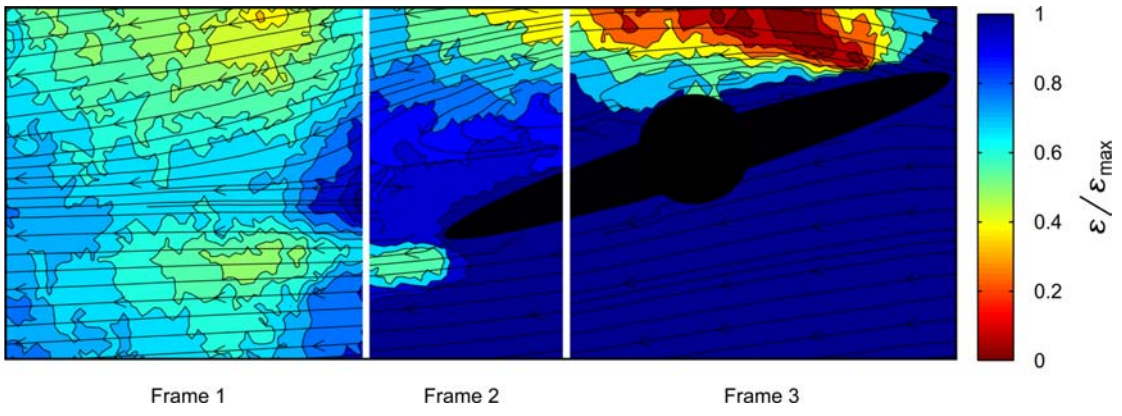

Figure 4.17: Turbulent dissipation rate for 15° angle of attack

4.6 Turbulent length scales

One of the landmarks assessed during the post-processing of the data was to determine the resolution of the measure taken for the calculation of the length scales. That is to say, if the interrogation window size is small enough to adequately obtain the turbulence associated to the small or medium scale vortex. As it has been already commented, the smaller vortex correspond to the Kolmogorov scale and the medium ones to the Taylor microscale. In order to do that, an estimation of this last scale, λ_L, was calculated using the Tennekes and Lumley (1972) relation,

$$\lambda_L = \frac{\overline{u'^2}}{\overline{\left(\frac{\partial u'}{\partial x}\right)^2}} = \left(\frac{\frac{1}{N}\sum_{n=1}^{N} u_n'^2}{\frac{1}{N}\sum_{n=1}^{N}\left(\frac{\partial u_n'}{\partial x}\right)^2} \right) \tag{4.8}$$

The mean value obtained of the Taylor microscale was $\lambda_L = 1.4$ mm which means that, unfortunately, the grid spacing considered (interrogation window size) for the PIV measurements: 2.86 mm, was not big enough to resolve this scale. Hence, neither the Taylor microscale nor the Kolmogorov scale can be correctly determined. However, it is possible to estimate the integral length scale, L, of the turbulence using an statistical quantity, the velocity correlation function, $R_{uu}(x, r)$.

$$R_{uu}(x, r) = \overline{u'(x)u'(x+r)} = \frac{1}{N}\sum_{n=1}^{N} u_n'(x)u_n'(x+r) \tag{4.9}$$

where r is the separation distance between the two correlated points.

The integral length scale can be computed from the two point correlation as the integral of $R_{uu}(x, r)$ over the separation distance, i.e.

$$L = \int_0^\infty \frac{R_{uu}(x, r)}{u_{rms}(x)u_{rms}(x+r)} dr \tag{4.10}$$

where subscript *rms* denotes root-mean-square, which is defined as

$$u_{rms} = \sqrt{\overline{u'^2}} = \sqrt{\frac{1}{N}\sum_{n=1}^{N} u_n'^2} \tag{4.11}$$

When the correlation function is calculated with the steamwise component, u, it is called longitudinal velocity correlation; whereas when is calculated with the vertical component, v, it is called lateral velocity correlation.

The integral length scale, the size of the biggest eddies generated by interaction of the aerofoil with the flow, was calculated on a vertical line at $x/c = 0.75$ downstream of the aerofoil trailing edge. The maximum sizes are found within the wake behind the aerofoil. The estimated values for the four angles of attack are summarized in Table 4.1. The results presented here come from the longitudinal velocity correlation. There is a clear tendency in which the size of the eddies increases with the angle of attack.

Angle of attack	0°	5°	10°	11°
L (mm)	3.6	4.9	11	18

Table 4.1: Maximum integral length scale obtained at $x/c = 0.75$ downstream of the aerofoil trailing edge with PIV

4.7 Flow visualization

In order to increase the understanding of the phenomena, the visualization of the flow passing the aerofoil it has also been undertaken. The PIV equipment -laser, camera, synchronizer and PC- was utilized for this purpose. Olive oil smoke bubbles with diameters of 1 µm have been used as tracer particles because great concentrations can be achieved due to the injection method, and they produce very good contrast between the different flow zones. The images have been taken at a Reynolds number of 80800. The photographs are mainly focused on the suction side and the wake of the aerofoil which are the more problematic areas.

The flow over the suction side of the aerofoil at 0° can be seen in Figure 4.18. It can be perceived a laminar boundary layer all over the upper surface, that remains attached until the aerofoil trailing edge. Although it can not be established in a conclusive way due to the size of the PIV interrogation window, the visualization of the boundary layer in that figure suggest its laminar condition at 0° and the turbulent one at 5° (see Figure 4.19). At 5° there is a laminar boundary layer at the upper surface from the leading edge to approximately $x/c \approx 0.05$, where the bubble appears (see Figure 4.20). Inside the bubble there is a recirculating zone with a reverse flow vortex. At some point in the bubble there is a transition from laminar to turbulent, thus the flow has enough energy to withstand the adverse pressure gradient on the aerofoils surface and reattach. The reattachment point is visible in the image about $x/c \approx 0.18$. Figure 4.21 shows the laminar bubble formed at the suction side of the aerofoil at 10°. The bubble size in this case is much bigger than at 5° and continues further downstream until its reattachment point at $x/c \approx 0.4$. When the angle of attack is increased to 15°, the laminar bubble is no longer created and the detachment point moves forward towards the trailing edge. Figure 4.22 shows the detached flow on the suction area over the aerofoil.

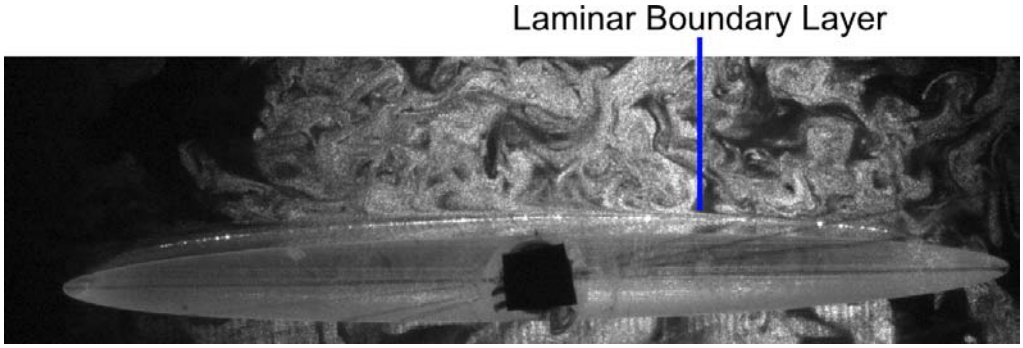

Figure 4.18: Laminar boundary layer at 0°

Representative photographs of the wake at each angle of attack are shown in Figure 4.23. For α =0°, the boundary layer remains attached to the aerofoil surface at all times until it reaches the very end of the trailing edge. The Von Karman vortex street is observed right after the aerofoil. The shedding of swirling vortices is remarkable clear at this angle

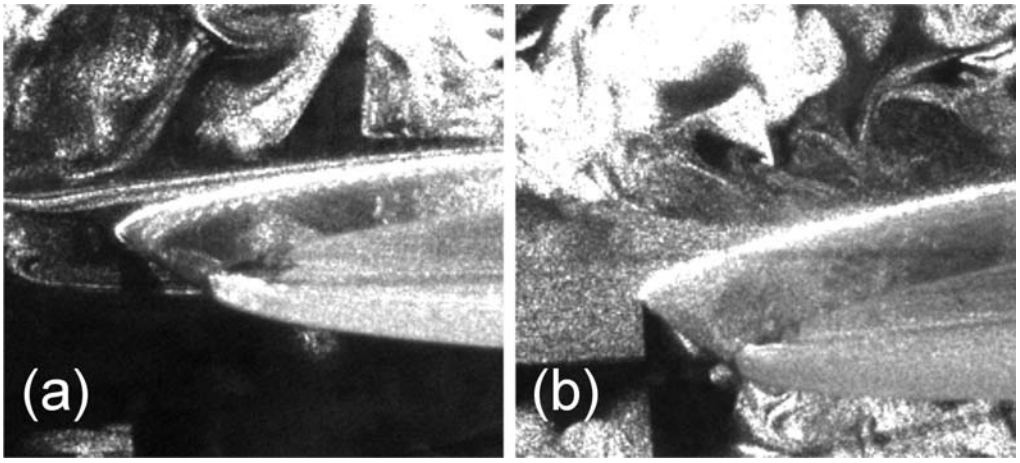

Figure 4.19: (a) Laminar boundary layer at 0°. (b) turbulent boundary layer at 5°

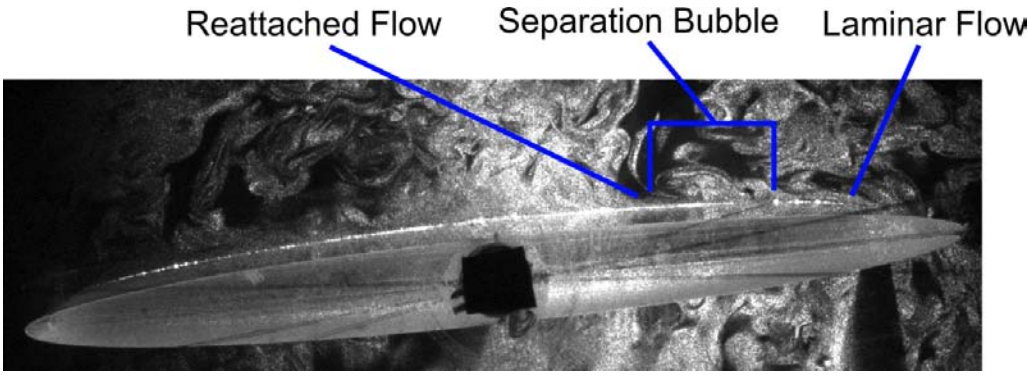

Figure 4.20: Laminar bubble at 5°

of attack. For α =5°, the boundary layer continues attached to the upper surface after the laminar bubble, separating at some point near the rear end of the body. Coherent structures are not so easy to observe at this angle in comparison with the previous one.

The widening of the wake is notable at 10° and especially at 15° caused by the separation of the boundary layer near the leading edge. The visible wake is distinguished by a remarkable smoke diffusivity which contrasts with the inviscid area -brighter in the images- out of the shear layer. The important turbulence intensity that characterizes the wake is responsible of that great diffusivity observed. The roll up of the upper shear layer that possibly corresponds to the Kelvin-Helmholtz vortex structures is also shown in these photographs.

The flow behaviour observed during the visualization agrees with the PIV outcomes described in previous sections.

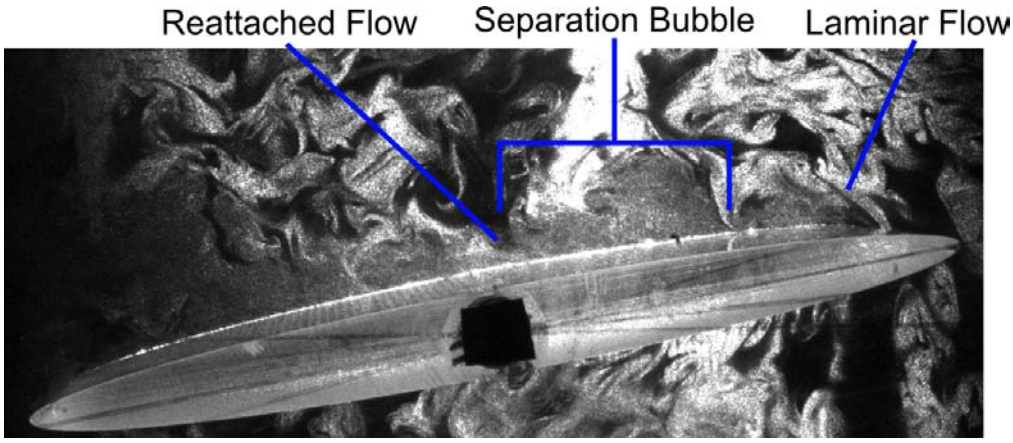

Figure 4.21: Laminar bubble at 10°

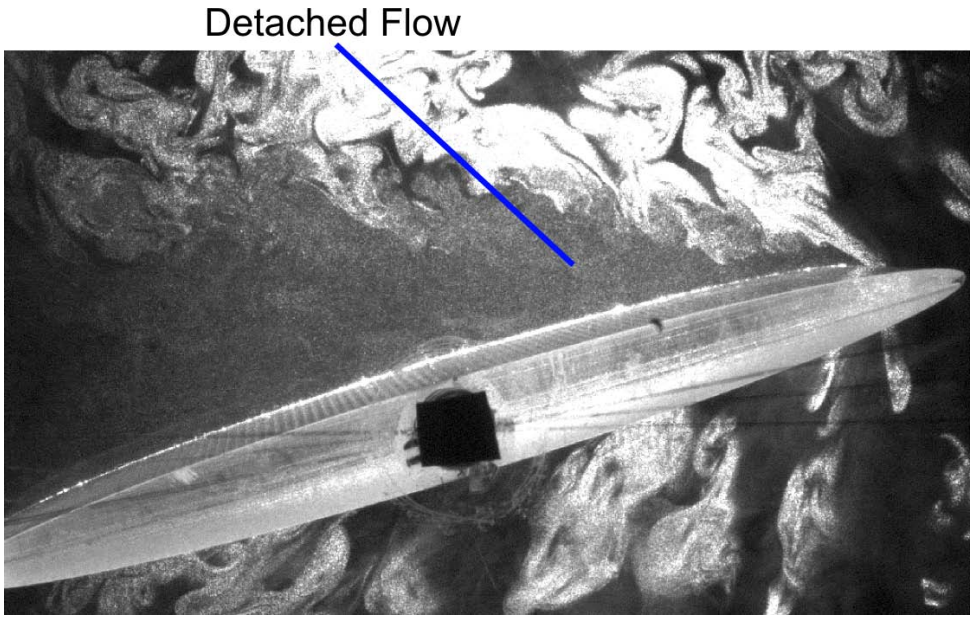

Figure 4.22: Detached flow at 15°

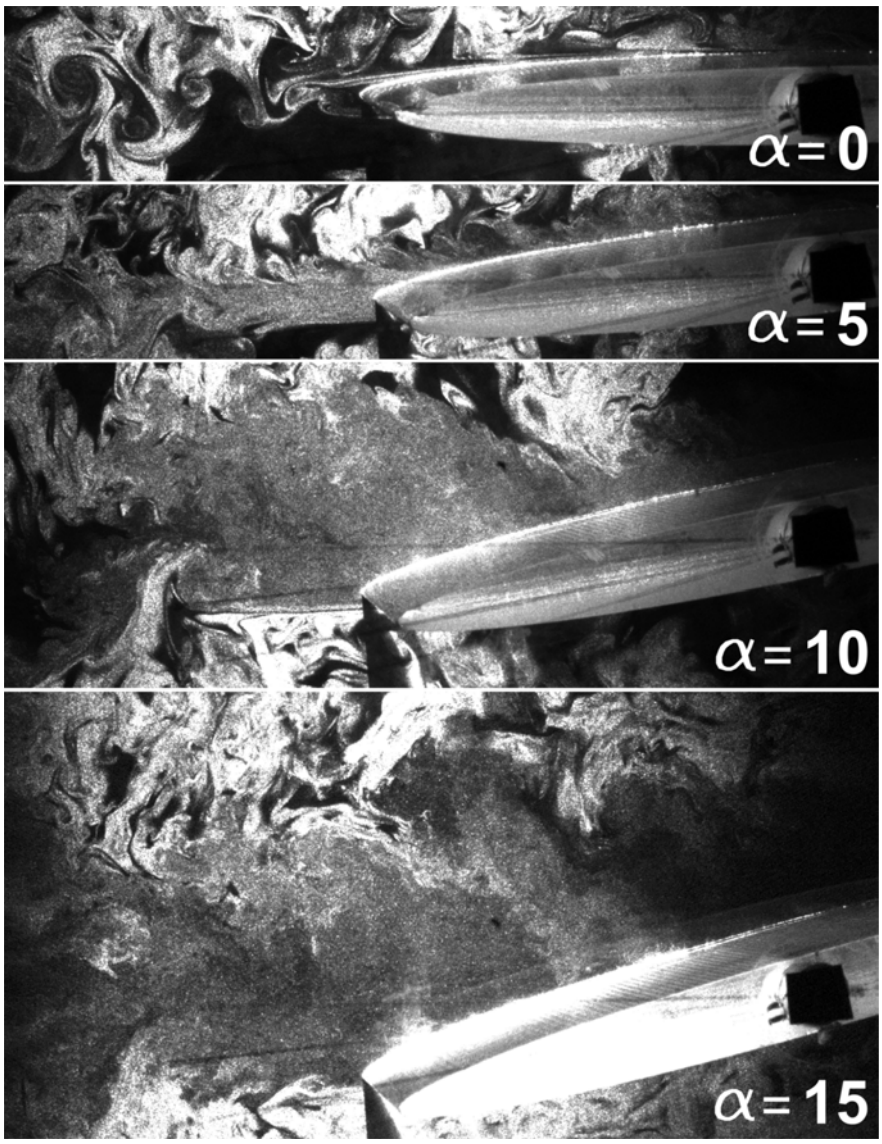

Figure 4.23: Visualization of the wake for different angles of attack and $Re_c = 80800$

CHAPTER 5

HW measurements

More than 2000 measurements have been acquired using hot-wire anemometry in order to gain an insight of the flow behaviour in the wake of the aerofoil. Those measurements have been processed, and results are presented in this chapter. Signals were analysed searching for dominant frequencies shedding light on the processes taking place, and comparative graphs are shown here. Velocity fields, velocity angles and turbulence intensities are depicted as contour maps to give the reader a quantitative and, also, qualitative vision of the acquired data. The study of other variables such as the integral length scales or the drag forces on the aerofoil are assessed as well.

5.1 Flow analysis procedure

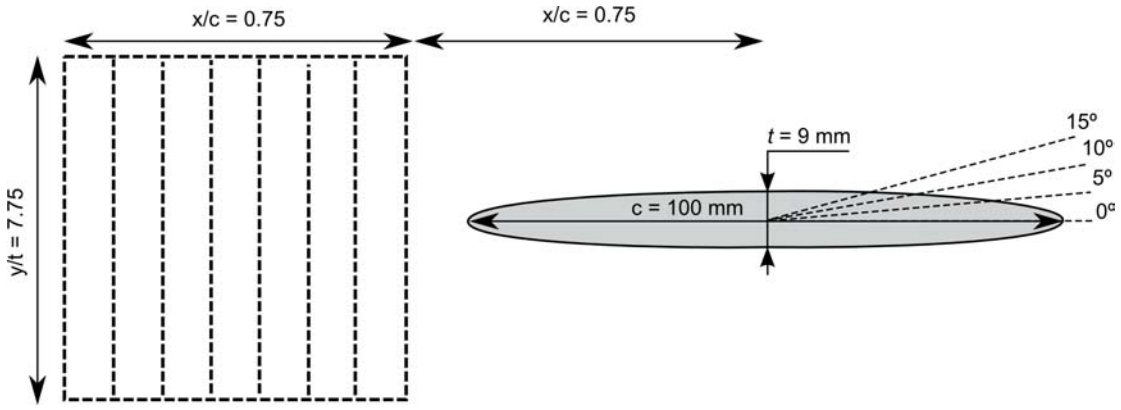

Figure 5.1: Scheme of HW acquisition map

In order to generate measurement maps using hot-wire anemometry it was necessary to process more than 2000 signals. A scheme of the probe measurement positions can be seen in Figure 5.1. A number of 8 measurement points in the horizontal direction (every 10.5 mm) and 47 in the vertical direction (every 1 mm) have been chosen. This difference in spacing is justified by the contrast between velocity variations in both directions. Vertical variations are much stronger than horizontal ones. A sampling frequency of 10 kHz was

chosen for recording the data during 25 s, which represent 250000 sample points for each measurement position. The acquired data was processed using *MATLAB®* codes. These codes, specifically developed for this thesis, were combined with a C++ script to increase its processing speed. Data analysis, both in time and frequency domain, has been performed.

In this section are presented the equations employed to analyse the flow at the wake of the aerofoil.

The instantaneous velocity recorded during a time t is composed of a mean component, denoted by overbar, and a fluctuation component, denoted by a prime.

$$U_n = \sqrt{u_n^2 + v_n^2} \tag{5.1}$$

$$u_n = \overline{u} + u'_n, \quad \overline{u} = \frac{1}{N}\sum_{n=1}^{N} u_n \tag{5.2}$$

$$v_n = \overline{v} + v'_n, \quad \overline{v} = \frac{1}{N}\sum_{n=1}^{N} v_n \tag{5.3}$$

Unlike PIV measurements were N was referred to the 300 snapshots, here N denotes the 250000 values of each signal acquired with a $\Delta t = 10^{-4} s$.

Although the vertical spacing is accurate enough, the horizontal spacing is too big for calculating the vorticity and the turbulent kinetic dissipation. Instead, the turbulent intensity used to quantify turbulence,

$$TI = \frac{\sqrt{\overline{U_n'^2}}}{U_0} \tag{5.4}$$

where U' is the velocity magnitude fluctuations.

$$U_n = \overline{U} + U'_n \tag{5.5}$$

5.2 Reynolds number and aerofoil roughness influence on measurements

The study of the Reynolds number influence on the wake behaviour was performed analysing two different cases, $Re_c = 163300$ and $Re_c = 80800$ at a free-stream velocity of 24.5 m/s and 12.2 m/s respectively. Results showed that although the maximum wake velocity defect increases with the mainstream velocity, due to self-similarity, normalized velocity distributions tend to collapse into a unique trend. This statement is shown in Figure 5.2 where normalized velocity profiles at x/c = 0.75 and 1.75 are plotted. This behaviour is confirmed as well by the work of Farsimadan and Mokhtarzadeh-Dehghan (2010). The flow around the aerofoil would be expected to change at Reynolds numbers higher than 10^5(Lissaman (1983)), however, that effect was not undergone in this case. Thus, it can be supposed that for this particular aerofoil the change is produced at slightly higher Reynolds numbers.

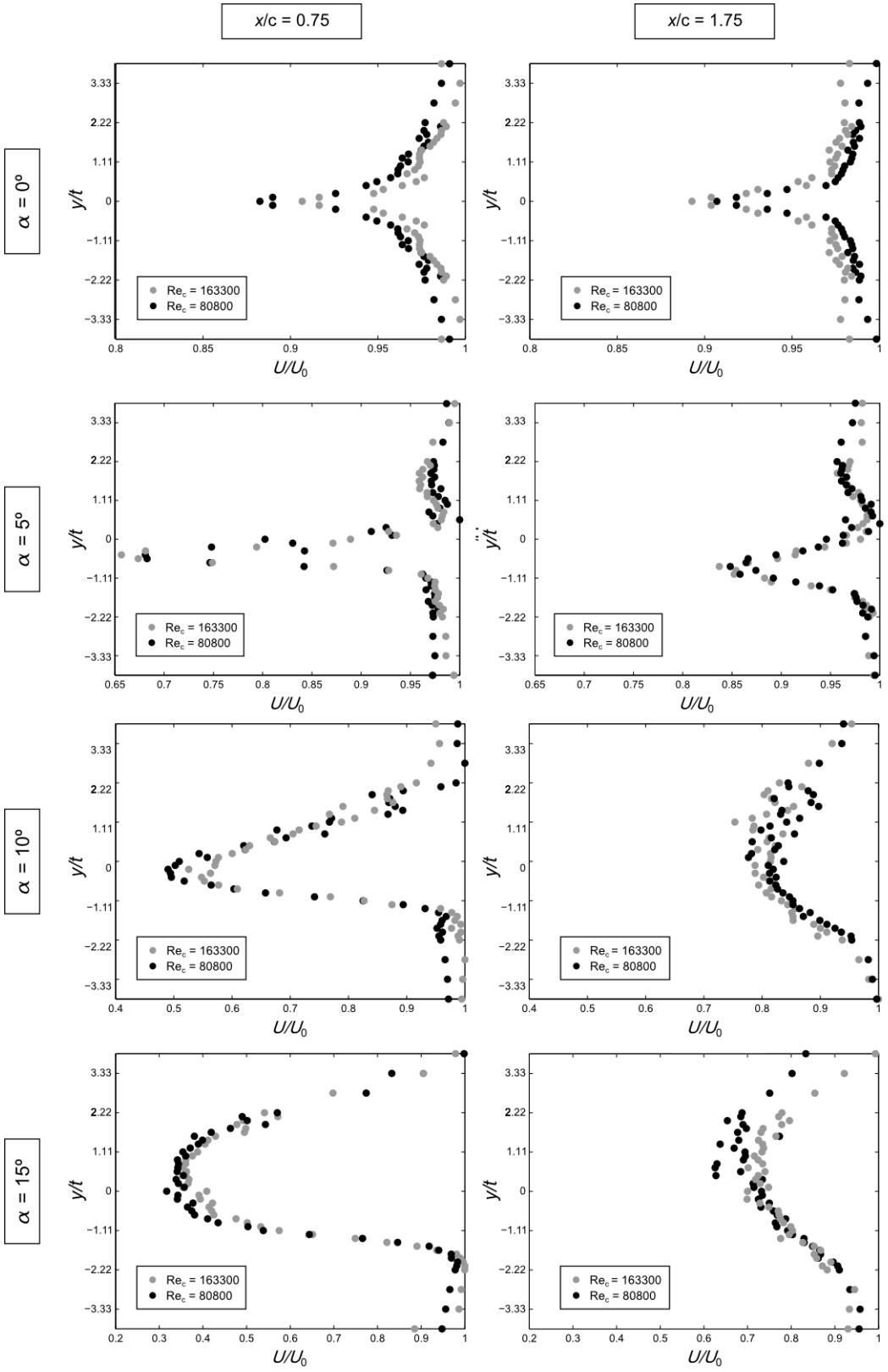

Figure 5.2: Influence of the Reynolds number on the normalized velocity distributions

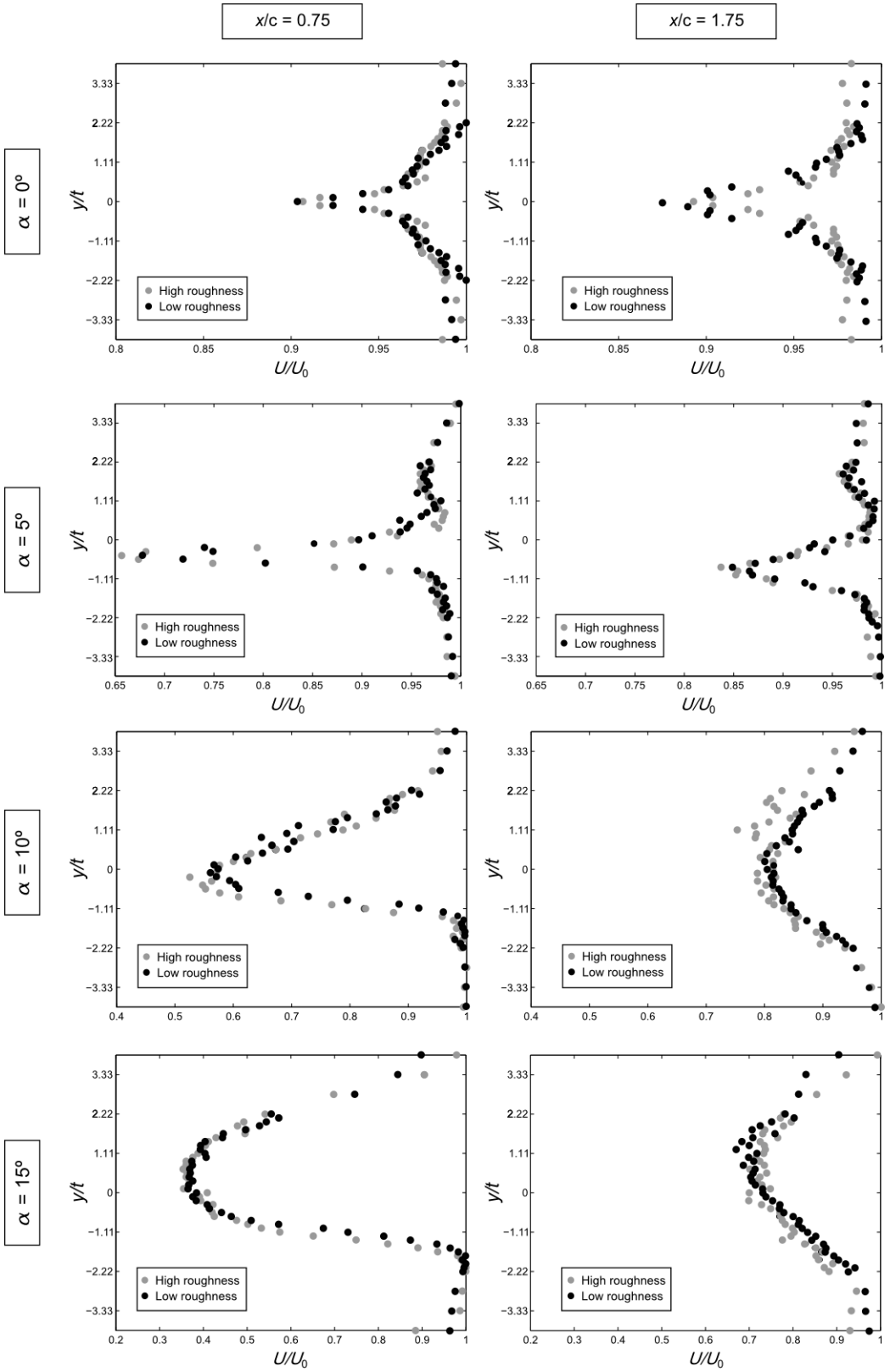

Figure 5.3: Influence of the aerofoil roughness on the normalized velocity distributions

The roughness of the aerofoil surfaces was another analysed variable. Experiments were carried out using two elliptic aerofoils with the same geometry but one with an average roughness of $R_a = 1.79$ µm and another with $R_a = 0$ µm (see Figure 3.32 in Chapter 3). The normalized velocity profiles at x/c = 0.75 and 1.75 are shown in Figure 5.2 for both aerofoils. The normalized distributions collapse again into a unique trend. As with the Reynolds number, it should be expected of the aerofoil behaviour to change if the surface is rough enough due to the upstream displacement of the boundary layer transition (Lissaman). This phenomenon has neither been found during the present research, probably because the roughness has not been high enough to trigger the transition.

As a consequence of these outcomes, the following studies were performed with one aerofoil roughness ($R_a = 1.79$ µm) and one Reynolds number ($Re_c = 80800$).

5.3 Velocity field behind the aerofoil

Distributions of normalized convective velocity, U, for the four studied angles of attack, 0° , 5° , 10° and 15° , are presented in this section. Each velocity field was composed using the 375 measurements obtained at different positions. The normalized velocity magnitude has been calculated taken as a reference the free-stream velocity.

Figures 5.4, 5.3, 5.6 and 5.7 display the normalized wake velocity at $Re_c = 80800$ and the different angles of attack. In these graphs the effect of the angle of attack on the downstream flow becomes evident. As α is increased gradually from 0° to 15°, the wake widens due to the displacement of the detachment point over the suction side of the aerofoil towards the leading edge.

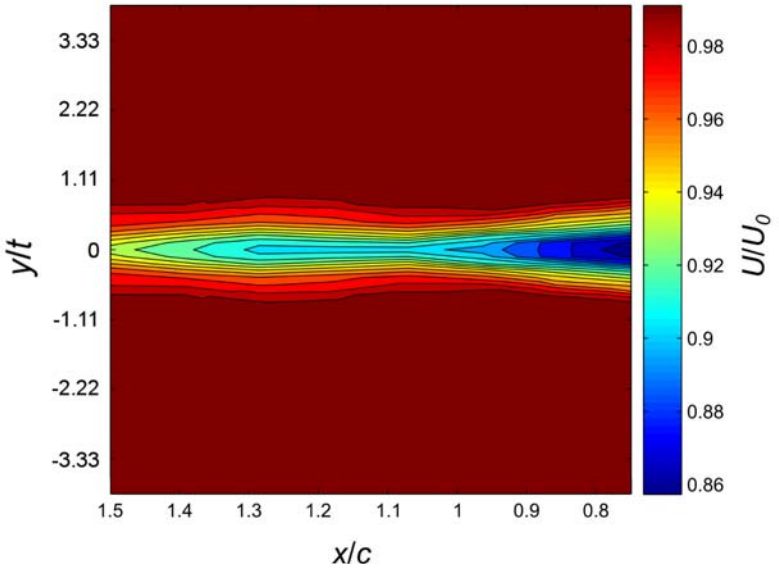

Figure 5.4: Normalized velocity at the wake for 0°

Overall, the flow speed is reduced right after the aerodynamic body. This velocity defect decreases as the distance from the trailing edge is increased, tending to achieve the free-stream value again at a sufficient far location. In addition to the wake area enlargement, the velocity reduction is also affected by the angle of attack in the sense that it rises with

it. Comparing the four figures, a clear tendency can be found for the angle effect on the speed reduction and wake expansion. As the angle of attack is set to higher values, the velocity of the downstream flow decreases, and the difference between the nearest and farthest horizontal position (x/c) speeds progressively increases. Moreover, the width of the wake broadens as α gets higher.

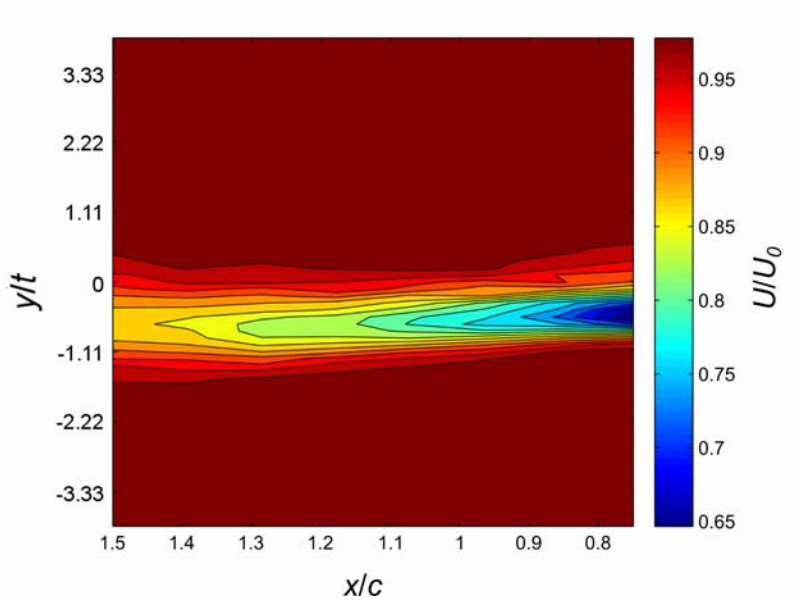

Figure 5.5: Normalized velocity at the wake for 5°

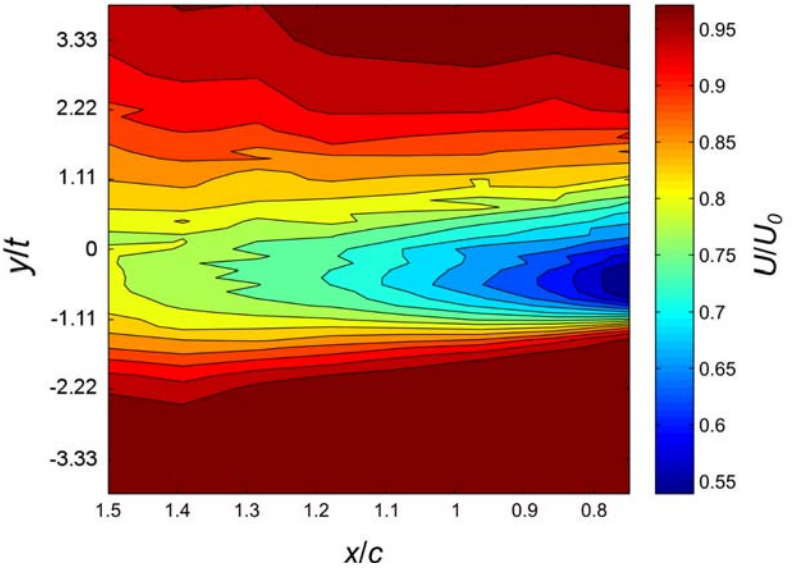

Figure 5.6: Normalized velocity at the wake for 10°

Comparing the flow speed of every case, it is remarkable that its maximum reduction goes from $U = 86\%\ U_0$ ($\alpha = 0°$) to $U = 40\%\ U_0$ ($\alpha = 15°$), always with respect to the free-steam

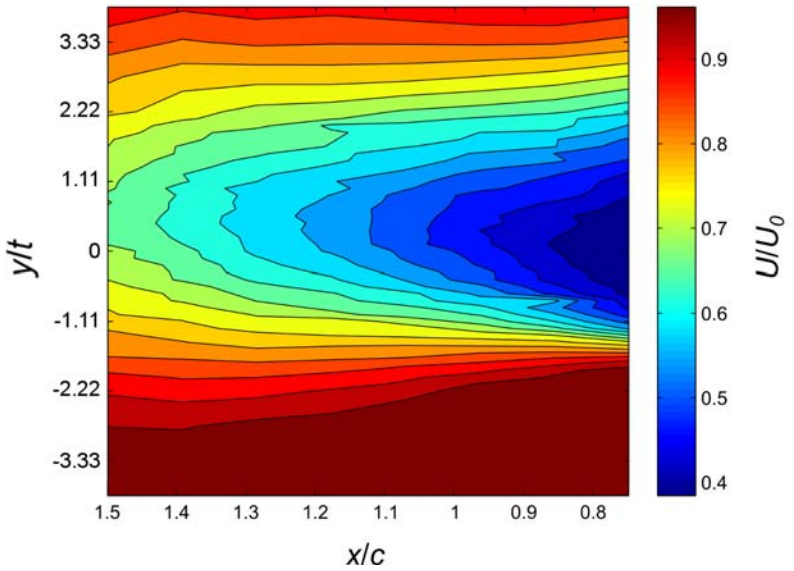

Figure 5.7: Normalized velocity at the wake for 15°

velocity. The effects of that behaviour imply the reduction of the aerodynamic performance of the aerofoil. Although the studied area was not enough to cover all the wake perimeter at 15° , results are representative enough to notice the main changes of its profile. Higher angles imply that the wake expands to the upper region corresponding with the suction side of the aerofoil. This behaviour responds to the boundary layer detachment at a certain position close to the leading edge of the aerofoil.

Due to the fact that HW anemometry is a technique widely used in the Fluid Mechanics research group, the results obtained with it are compared to the PIV ones in order to validate both the new methodology and the acquired data. The distributions of normalized convective velocity of the aerofoil wake as well as its width and orientation seem to be overall in good agreement. Table 5.1 shows a comparison of the minimum velocity results acquired using each technique at two horizontal positions, $x/c = 0.75$ and 1.75. Values obtained with PIV are only slightly lower than the ones of HW at 0°, 5° and 10°, but the difference increase at 15°. The deviation in results mainly at the highest angle of attack may be due the difficulty of the tracer particles to properly follow the flow when the velocities are low and the speed gradient is high. A way to avoid these dissimilarities could be to use even smaller particles that provide lower lag times so they can reach the flow speed faster, although that increments the visualization issues. Regarding the qualitative characteristics of the wake at each angle of attack, no significant differences were found in the results. Both techniques reported a similar shape and widening of the wake as the angle was increased.

x/c	**Angle of attack**	**0°**	**5°**	**10°**	**15°**
0.75	$(U_{min})_{PIV}$	$0.80U_0$	$0.65\ U_0$	$0.50\ U_0$	$0.25\ U_0$
0.75	$(U_{min})_{HW}$	$0.86\ U_0$	$0.65\ U_0$	$0.55\ U_0$	$0.40\ U_0$
1.5	$(U_{min})_{PIV}$	$0.90\ U_0$	$0.85\ U_0$	$0.75\ U_0$	$0.55\ U_0$
1.5	$(U_{min})_{HW}$	$0.93\ U_0$	$0.85\ U_0$	$0.80\ U_0$	$0.70\ U_0$

Table 5.1: Comparison of velocity results obtained with PIV and HW

5.4 Drag forces on the aerofoil

Due to the fact that drag forces are usually much lower than lift forces, it is often difficult to measure them experimentally in an accurate way, so they are calculated using values of the flow variables. In the present research the necessary instrumentation for the direct measuring of the drag and lift there was not available. In addition, specific values of the pressure around the aerofoil were not acquired either. However, the drag forces were determined because it is possible to calculate the integral horizontal forces acting on the aerofoil from their reaction of the flow using the integral momentum conservation, without the need to evaluate the flow quantities at the surface of the body (Anderson (1991)). Figure 5.8 shows a scheme of the approach, where the rotational viscous flow domain in the aerofoil's wake is schematically represented by the shaded region.

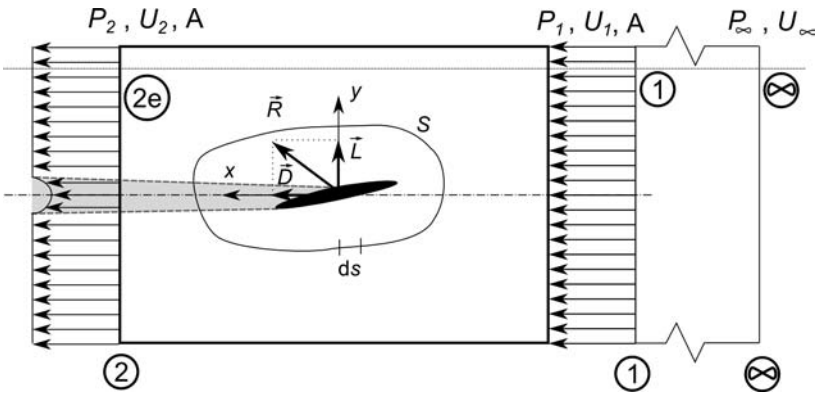

Figure 5.8: Schematic of the control volume approach for integral force determination

Applying the Reynolds transport theorem to the linear momentum in Newton's law, gives the linear-momentum relation for a control volume. This equation relates the resultant aerodynamic horizontal force $\overrightarrow{F_x}$ on the aerofoil to a contour integral around it,

$$\overrightarrow{F_x} = \frac{d}{dt}\left(\int_{cv} \overrightarrow{U}\rho d\vartheta\right) + \int_{cs} \overrightarrow{U}\rho(\overrightarrow{U_r}\cdot\overrightarrow{n})dA \tag{5.6}$$

where cv is an arbitrary integration volume surrounding the aerofoil composed of infinitesimal elements $d\vartheta$, $\overrightarrow{U_r}$ is the relative velocity and $\overrightarrow{n}$ is the outward pointing normal vector. The infinite (∞) location is considered to be at rest and atmospheric pressure. Pressures can be estimated in the region of the flow that behaves as adiabatic and inviscid outside the wake, e.g. the dotted line in Figure 5.8. Assuming a two-dimensional flow field that is steady in the statistical sense, the first term of the equation can be neglected. Figure 5.9 is a sample of the velocity profiles used to determine the forces on the aerofoil. Forces due to wall shear stresses on the surface of the chamber walls were considered as well.

Figure 5.10 shows a comparison between the obtained drag coefficient of the present t/c = 0.09 thickness ratio elliptic aerofoil at Reynolds number of 80800 with results reported by Kwon and Park (2005). These authors investigated the aerodynamic characteristics of a t/c = 0.16 thickness ratio elliptic aerofoil at $Re = 3{\times}10^5$ with and without a boundary-layer transition trip. Even though the compared results do not belong to the exact aerofoil

geometry, they can constitute a reference point to analyse the validity of the calculated data. The C_d obtained at $\alpha = 0°$ and $\alpha = 5°$ are similar to the values that Kwon and Park (2005) gave for a smooth aerofoil at the same angles of attack. At $\alpha = 10°$ the drag has increased and the reached value exceed that for the smooth and the tripped aerofoil. The drag coefficient at 15° is 0.6 quite high due to the stall and was not plotted in the Figure 5.10 to avoid out-scales. Even though there is no data available in this thesis for angles between 10° and 15° the comparison with the results given for the $t/c = 0.16$ thickness ratio elliptic aerofoil suggest that, for the aerofoil studied here, the stall point could be found at an angle of 11 or 12 °.

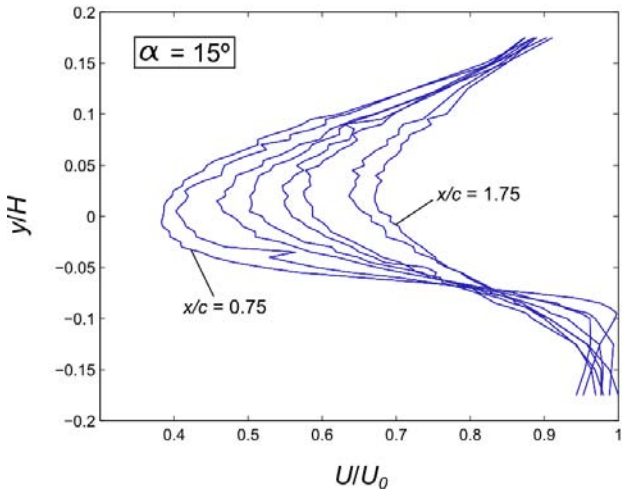

Figure 5.9: Normalized velocity wake profiles for 15°

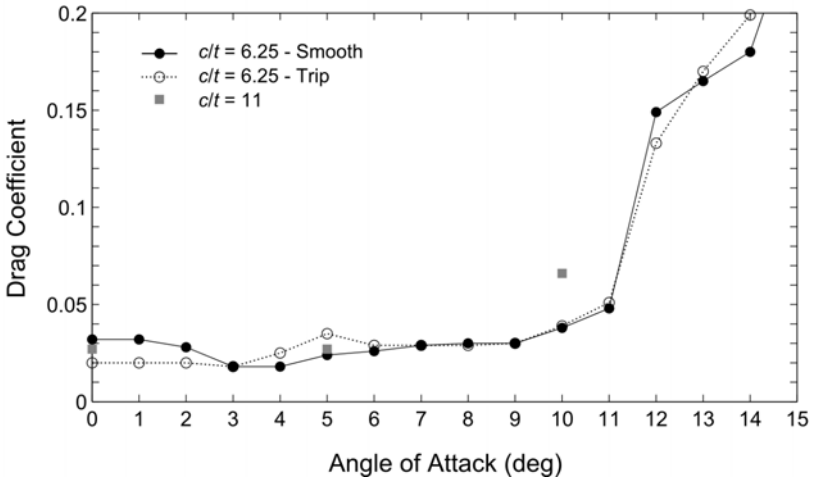

Figure 5.10: Lift and drag coefficient curves comparison with literature

5.5 Velocity angle

The velocity angles have been depicted in Figures 5.11, 5.12, 5.13 and 5.14 to shed light on the flow direction and its possible structures. The increase of the angle of attack produces the increment of the velocity angles. Two zones with opposite signs -the wake and the outside flow- can be differentiated in Figures 5.11 and 5.12, where the wake is so thin that the undisturbed flow is also visible. The upper and lower areas out of the wake have negative and positive angles respectively, while the upper and lower zones inside the wake have positive and negative angles respectively. At this point one must note that it has been considered a positive angle in downwash flow direction (right to left and downwards) and negative in upwash flow direction (right to left and upwards). Thus, the trailing edge redirects the upper flow downwards and the lower flow upwards creating eddies that form the Von Karman vortex street. The phenomena of Von Karman vortex street was visible during the visualization of the flow at $\alpha = 0°$ in Chapter 4 (see Figure 4.21). Both Figures 5.11 and 5.12 for 0° and 5° exhibit similar results. In both cases the angle range spans from -2.5° to 2.5°. On the other hand, the contours of velocity angles for 10° and 15° shown in Figures 5.13 and 5.14 exhibit entirely different structures. On the contrary, two big areas, one in the upper and one in the lower side of the wake with positive and negative angles respectively are observed. These angles distributions correspond to the wake produced by the detachment of the boundary layer at some point in the suction surface of the aerofoil.

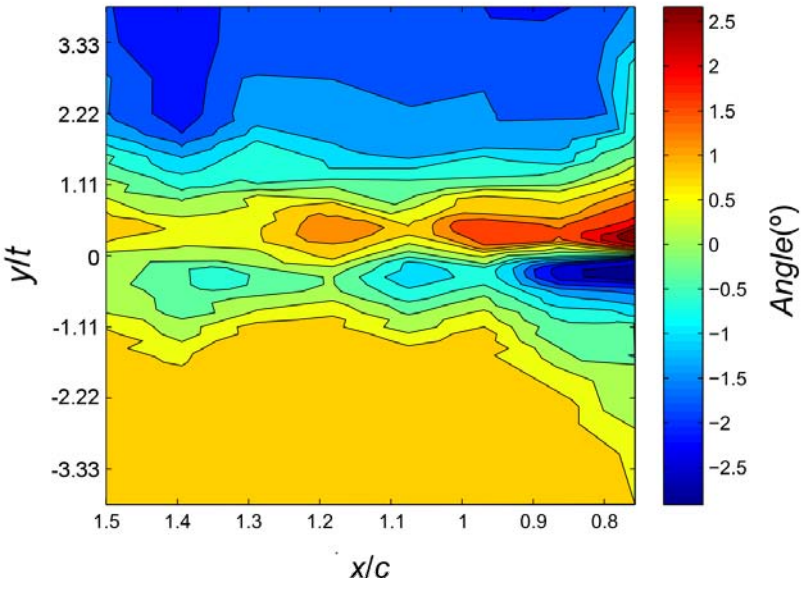

Figure 5.11: Velocity angle at the wake for 0°

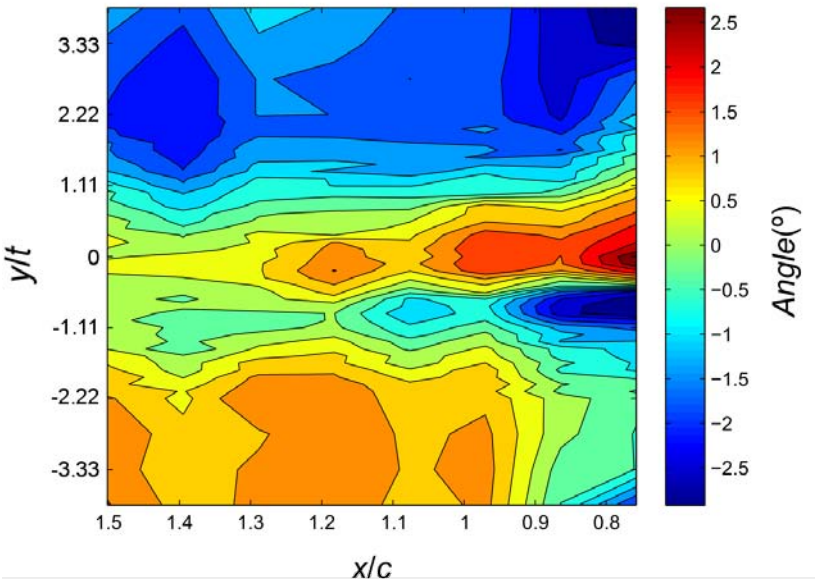

Figure 5.12: Velocity angle at the wake for 5°

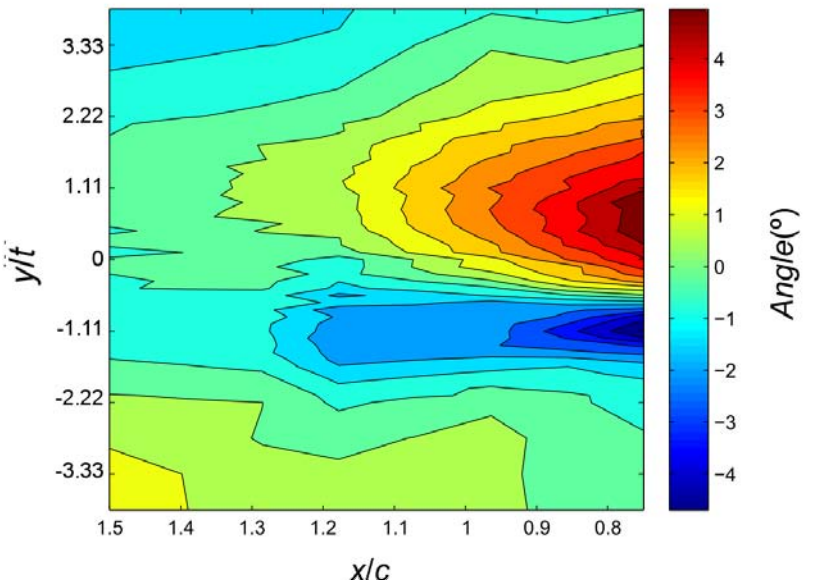

Figure 5.13: Velocity angle at the wake for 10°

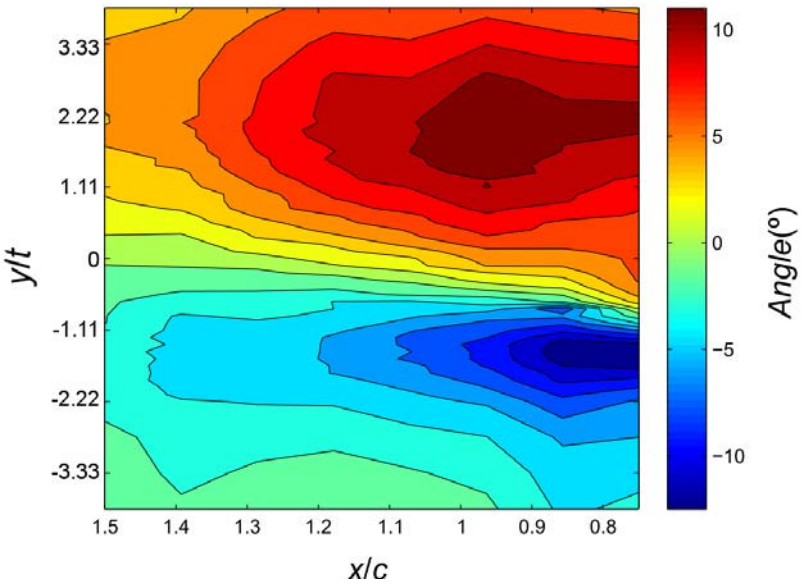

Figure 5.14: Velocity angle at the wake for 15°

5.6 Turbulent intensity

The percentage of turbulent intensity in the aerofoil wake for Re_c= 80800 has been calculated and the obtained maps are presented in Figures 5.15, 5.16, 5.17 and 5.18. At an angle of attack of 0° a clear double peak is shown with a local minimum between both peaks corresponding to the position of maximum velocity defect. This characteristic shape of the turbulent intensity profiles has been reported as well by Farsimadan and Mokhtarzadeh-Dehghan (2010), for a NACA 0012, which reveals the maximum oscillation within the wake shear layer. For higher angles, that double peak is still present; however its symmetry has been lost. The peak located downstream of the pressure side is clearly attenuated in comparison with the upper one. That structure is created by the influence of air flow behaviour on the aerofoil walls: while the boundary layer at the pressure side follows the contour of the body; at the suction side, the detachment takes place affecting the size, shape and magnitude of the turbulence intensity contours. At $\alpha = 15°$ a zone of relatively low turbulent intensity ($TI \approx 17\%$) is observed at the central area of the wake near the trailing edge.

Overall, the increment of the angle of attack results in an increase of the turbulence intensity peak value. There is an augmentation of approximately 12% of the maximum turbulence intensity from $\alpha = 0°$ to 15°. The turbulent intensity levels decrease with the downstream distance (x/c) as they dissipate while moved away from the aerofoil. A widening of the profile can be also noted as a result of the increase of the angle of attack. As it was stated before, the profile doesn't widen symmetrically. The upper region shifts upwards in a greater extent than the lower region of the wake.

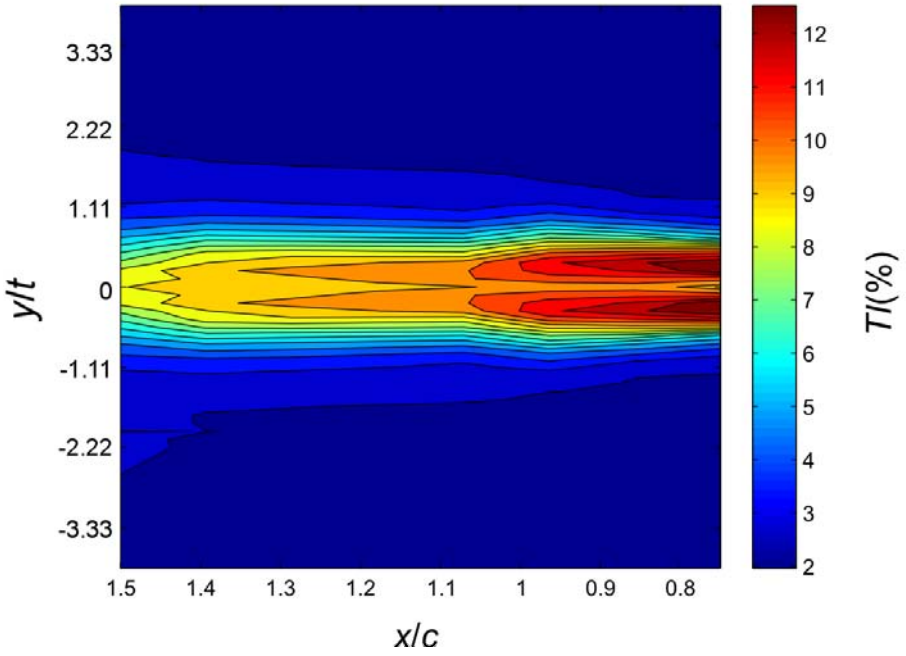

Figure 5.15: Turbulent intensity at the wake for 0°

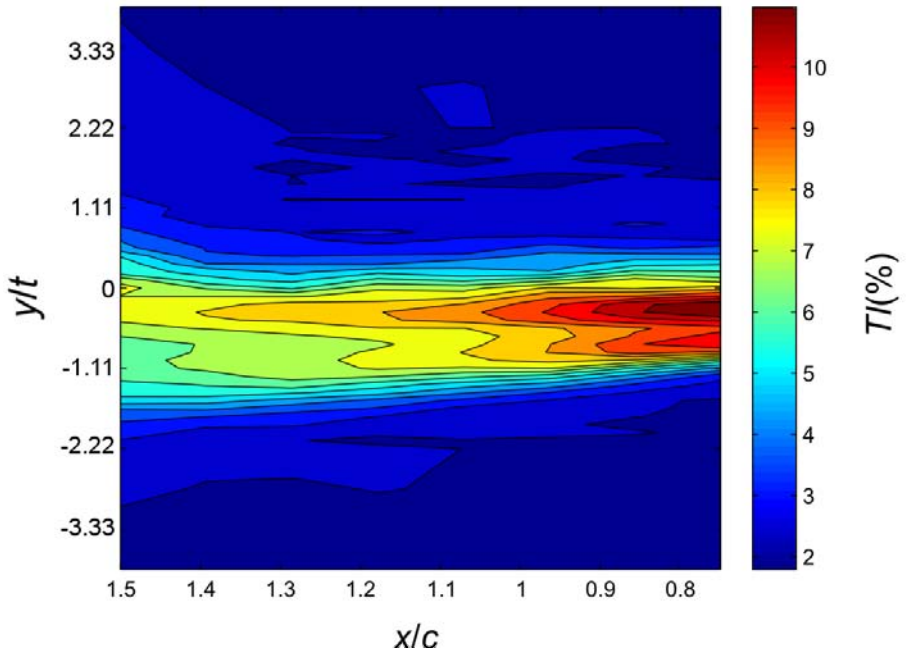

Figure 5.16: Turbulent intensity at the wake for 5°

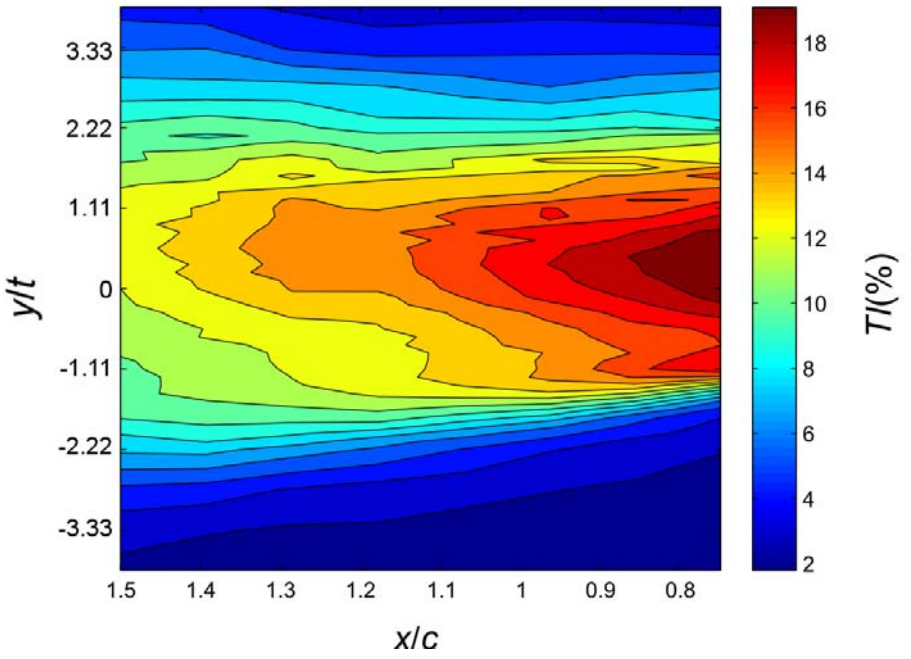

Figure 5.17: Turbulent intensity at the wake for 10°

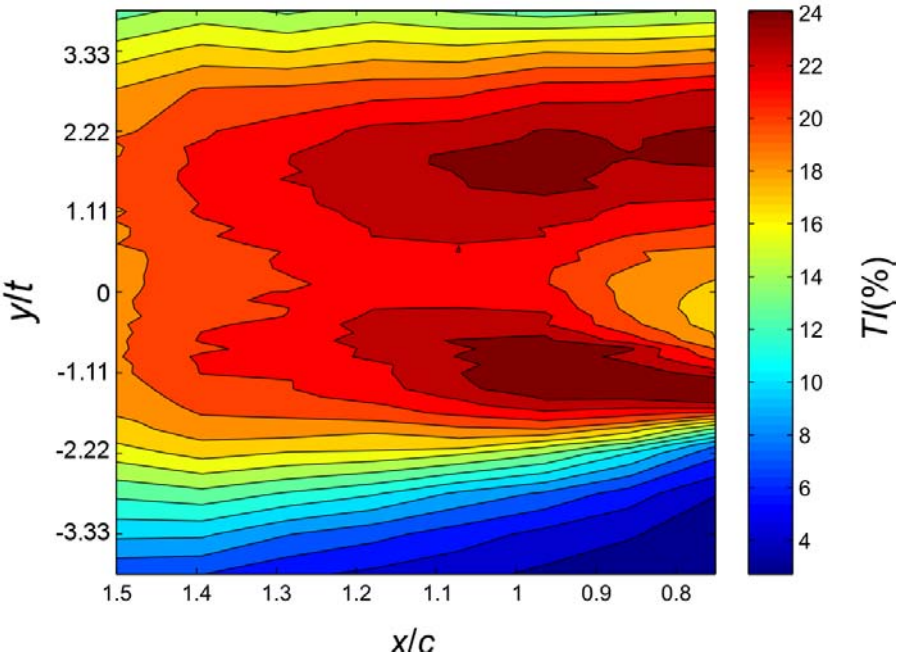

Figure 5.18: Turbulent intensity at the wake for 15°

5.7 Overview of results

In order to facilitate the overview of the data, some quantitative results of the hot-wire measurement campaign are gathered in Table 5.2. Where $\boldsymbol{W_w}$ refers to the wake width.

Angle of attack	**0°**	**5°**	**10°**	**15°**
$\boldsymbol{U_{min}}$ **at** $\boldsymbol{x/c = 0.75}$	0.86 U_0	0.65 U_0	0.55 U_0	0.40 U_0
$\boldsymbol{U_{min}}$**at** $\boldsymbol{x/c = 1.5}$	0.93 U_0	0.85 U_0	0.80 U_0	0.70 U_0
$\boldsymbol{\Delta U_{min}}$ **from** $\boldsymbol{x/c = 0.5}$ **to** $\boldsymbol{1.5}$	0.07 U_0	0.2 U_0	0.25 U_0	0.30 U_0
$\boldsymbol{TI_{max}}$ **at** $\boldsymbol{x/c = 0.75}$	13%	12%	19%	24%
$\boldsymbol{TI_{max}}$**at** $\boldsymbol{x/c = 1.5}$	8%	7%	12%	18%
$\boldsymbol{\Delta TI_{max}}$ **from** $\boldsymbol{x/c = 0.5}$ **to** $\boldsymbol{1.5}$	5%	3%	7%	6%
$\boldsymbol{\alpha_{max}}$ **at** $\boldsymbol{x/c = 0.75}$	±2.5°	±2.5°	±5°	±11°
$\boldsymbol{\alpha_{max}}$**at** $\boldsymbol{x/c = 1.5}$	±0.5°	±0.5°	±0.5°	±5°
$\boldsymbol{\Delta\alpha_{max}}$ **from** $\boldsymbol{x/c = 0.5}$ **to** $\boldsymbol{1.5}$	±2°	±2°	±4.5°	±6°
$\boldsymbol{W_w}$ **at** $\boldsymbol{x/c = 0.75}$	1.1 t	1.7t	4.4 t	>6.6 t
$\boldsymbol{W_w}$ **at** $\boldsymbol{x/c = 1.5}$	1.1 t	2.2t	7.2 t	>7.7 t
$\boldsymbol{\Delta W_w}$ **from** $\boldsymbol{x/c = 0.5}$ **to** $\boldsymbol{1.5}$	0.0 t	0.5t	2.8 t	>1.1 t

Table 5.2: Comparison of angle effects

5.8 Spectra of velocity signals

An analysis of the recorded signals in the frequency domain has been done to look for dominant frequencies. Power spectral densities, *PSD*, of the vertical velocity component (spectra of this component show higher amplitudes) for $\mathrm{Re_c} = 80800$ and $Re_c = 163300$ at 0° , 5° , 10° and 15° angles of attack are shown in Figure 5.21. A characteristic frequency peak is found in all cases studied and its value indicates that there are two phenomena clearly differentiated (one produced at 0° , 5° and another at 10° ,15°). The phenomenon that happens at 0° and 5° seems to be related to the vortex shedding at the trailing edge because the frequency peaks reported are located at the wake and disappear in the free-stream zone. On the other hand, the phenomenon that takes place at 10° and 15° is associated with the abrupt detachment of the boundary layer because no dominant peak is observed within the wake, whereas it is visible at its boundaries. It must be noted that the frequency related to this phenomenon is an order of magnitude smaller than the one of the vortex shedding (0° and 5°). Figure 5.19 shows two images of the flow passing the aerofoil at 15 ° captured at two different instants, that illustrate the oscillations of the detached boundary layer.

The free-stream velocity clearly influences the physics of the phenomenon, increasing the frequency values (see Figures 5.22 and 5.23). Figure 5.20 shows the Strouhal number as a function of the Reynolds number. It must be noted that the characteristic length used for calculating the Strouhal number was the aerofoil thickness when considering 0° and

5°, and the aerofoil chord when considering 10° and 15°. It can be seen that the Strouhal number remains almost constant throughout the considered range of Reynolds numbers with mean values of 0.22 and 0.25 for the lowest and highest angles of attack respectively.

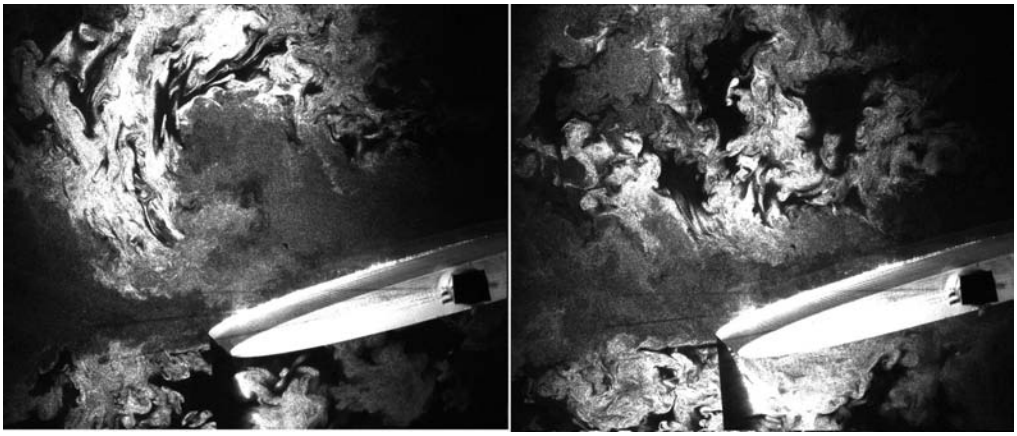

Figure 5.19: Visualization of the detached flow oscillations at 15°

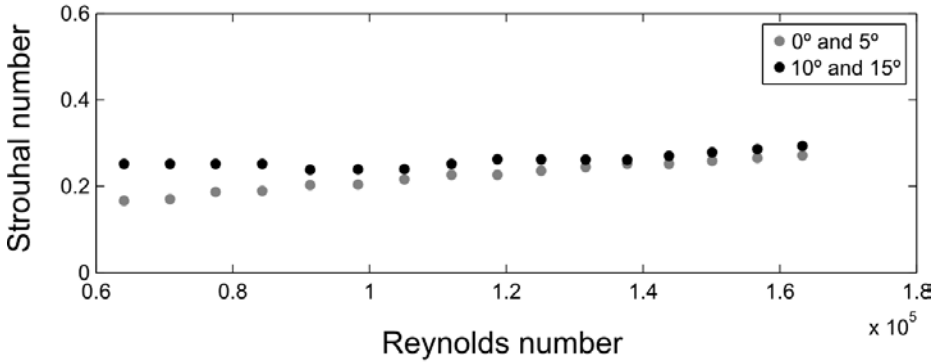

Figure 5.20: Strouhal number as a function of the Reynolds number

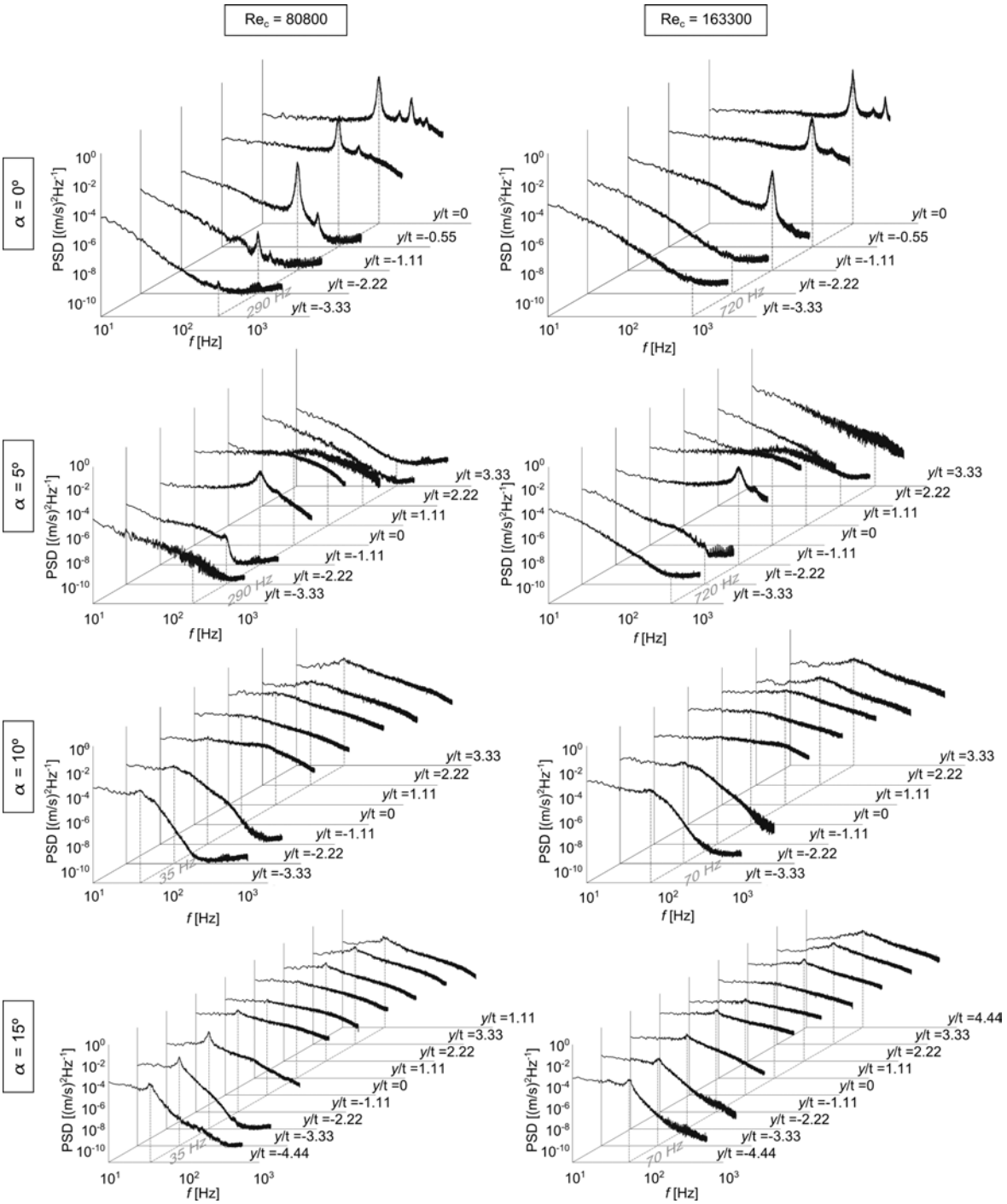

Figure 5.21: PSD of the normal velocity component for 0° , 5° , 10° and 15° measured at different heights and $x/c = 0.75$

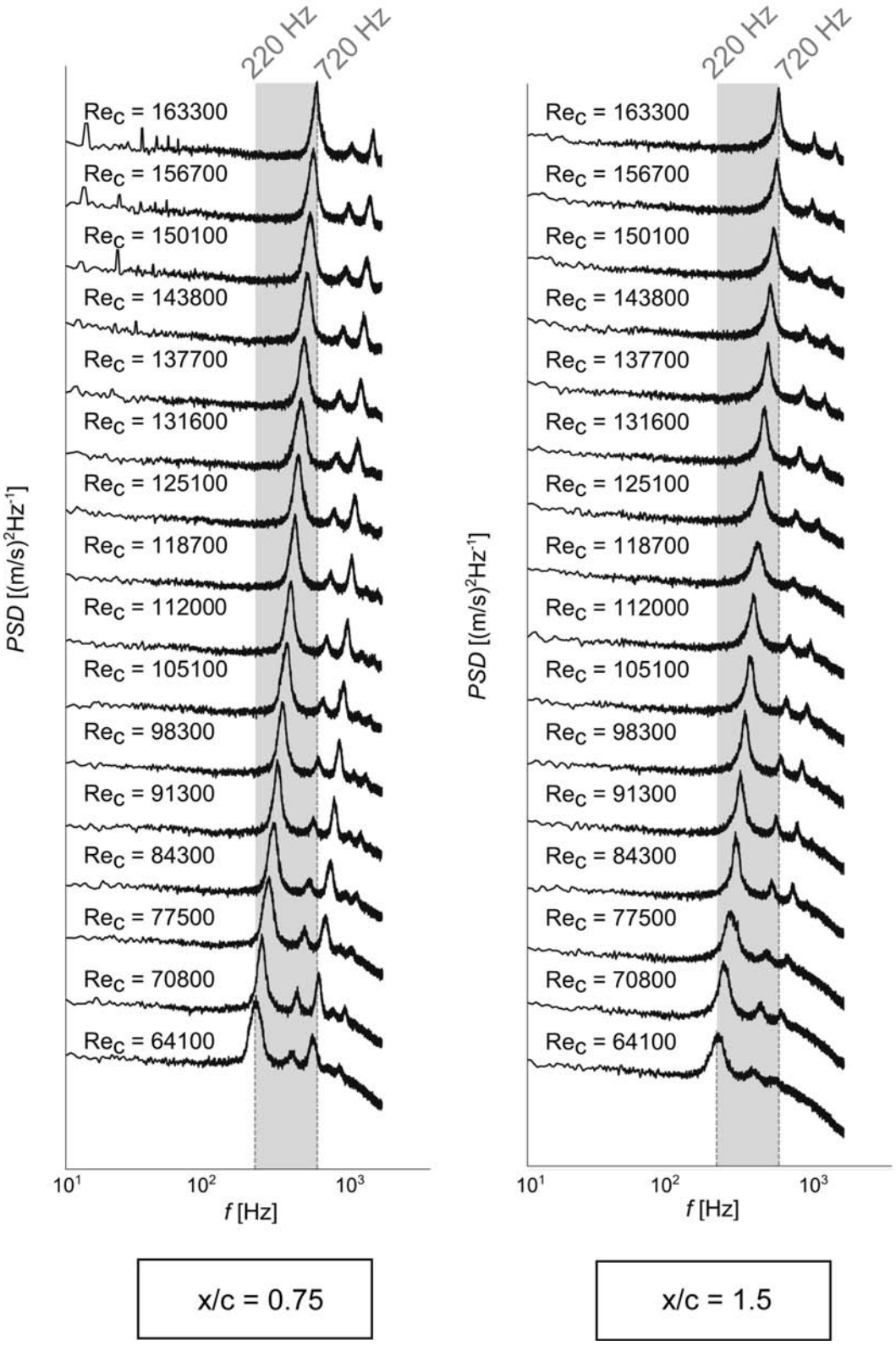

Figure 5.22: PSD of the normal velocity component for $\alpha = 0°$ measured at $y/t = 0$ varying the chord based Re

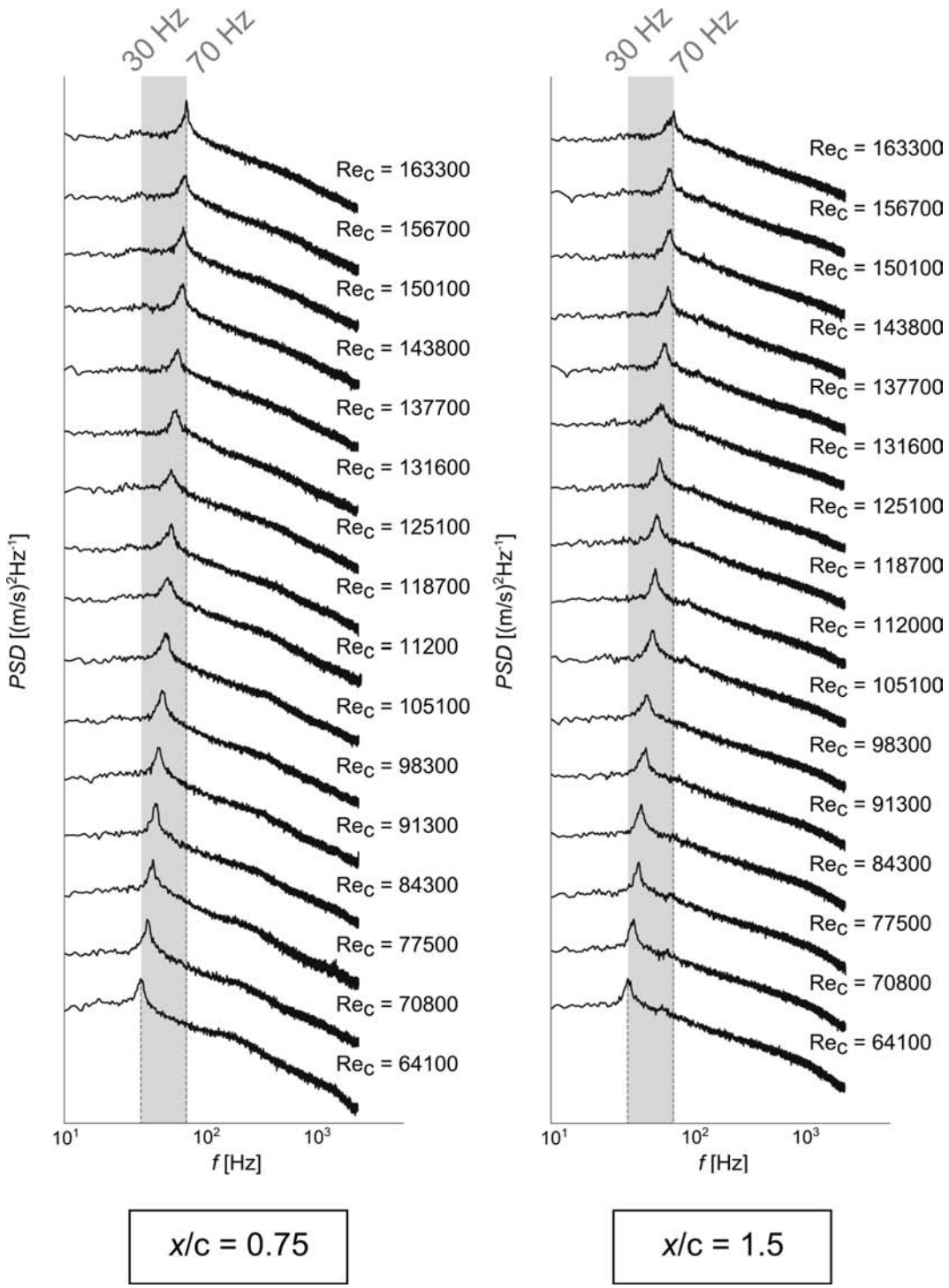

Figure 5.23: PSD of the normal velocity component for $\alpha = 15°$ measured at $y/t = 0$ varying the chord based Re

5.9 Turbulent length scales

In the chapter corresponding to the PIV measurements, the integral length scale was calculated from the two point correlation of $R_{uu}(x, r)$ over the separation distance, see Equation 4.10. This procedure was used because those measurements have good spatial resolution but poor temporal one. With the HW measurements, the spatial resolution is rather low (mainly in the longitudinal direction), but the temporal one is quite good, so an alternative procedure has been employed, using the velocity autocorrelation function the integral length scale, L, of the turbulence was determined analytically using the velocity autocorrelation function, $R_{uu}(\tau)$.

$$R_{uu}(\tau) = \frac{\overline{u'(t)u'(t+\tau)}}{u_{rms}(t)} \tag{5.7}$$

where τ is the time lag used to construct the autocorrelation function and the overbar denote the time-averaging value and the subscript *rms* denotes root-mean-square.

The integral length scale can be computed from the two autocorrelation as the integral of $R_{uu}(\tau)$ over the separation distance, i.e.

$$L = \overline{u} \int_0^\infty R_{uu}(\tau) d\tau \tag{5.8}$$

This formulation assumes that the average eddy size lies through the correlation of two velocity signals (Taylor's hypothesis). To estimate the integral length scale in Equation 5.8, it is necessary to evaluate the correlation coefficient (Equation 5.7) of the velocity fluctuations (in time), which theoretically must be defined up to infinity. In practice, one of the three criteria suggested by Tropea et al. (2007) has been considered. It establishes the possibility of defining τ_{max} as the value for which the autocorrelation coefficient reaches its first minimum. As with the previous procedure, when the correlation function is calculated with the steamwise component, u, it is called longitudinal velocity correlation; whereas when is calculated with the vertical component, v, it is called lateral velocity correlation.

The length of the biggest eddies generated at the vertical line $x/c = 0.75$ is summarized in Table 5.3. The results presented here come from the longitudinal velocity correlation. These values are of the same order of magnitude that the ones obtained using the PIV technique (see Figure 5.24). This confirms that the PIV measurements are capable of perceive the principal characteristics of the turbulence, despite the small differences found in the comparison.

Angle of attack	0°	5°	10°	11°
L (mm)	3.5	4.5	8	22

Table 5.3: Maximum integral length scale obtained at $x/c = 0.75$ with HWA

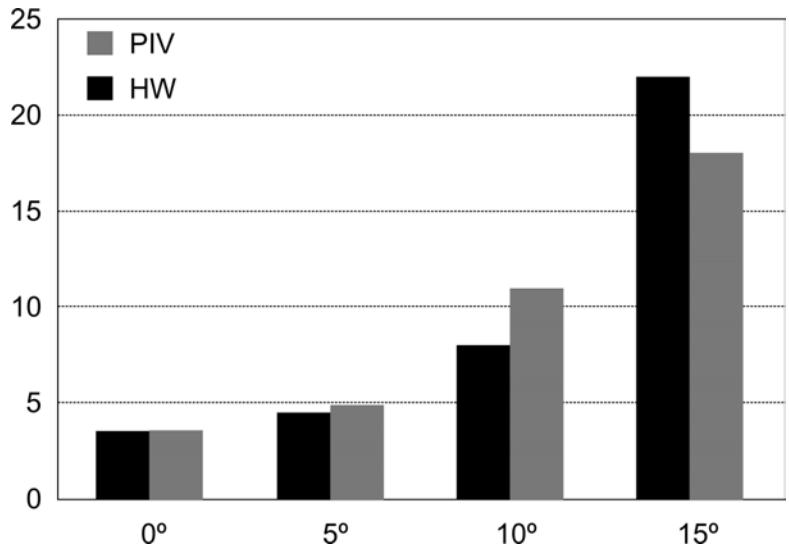

Figure 5.24: Comparison of the length of the biggest eddies obtained with PIV and HW

CHAPTER 6

Conclusions

In this chapter are presented the most significant outcomes and conclusions resulting from the current investigation, with regard to the aerodynamic study of an elliptic aerofoil and facility and instrumentation design and developments required for such purpose.

6.1 Satisfaction of research objectives

The overarching objective of this thesis was to perform a methodological study to characterize the aerodynamics of a low-thickness ($t/c = 0.09$) elliptic aerofoil at low Reynolds numbers with several angles of attack. The outcomes of the study produced baseline data for future aeroacoustic investigations and validation of computational fluid dynamic results.

In order to achieve that main objective, a set of specific tasks that facilitate its progressive accomplishment were defined. These tasks included among others: the design and construction of a low-speed wind tunnel meeting the requirements for performing PIV measurements; the implementation of PIV, a measurement technique never used before at the Fluid Mechanics Area of the University of Oviedo; the manufacture of hot-wire probes for HW anemometry measurement; the development of processing and post-processing codes using MATLAB®; and the experimental analysis of the flow around the elliptic aerofoil utilizing the techniques named before. All these objectives were successfully addressed and the conclusions derived are presented in the following sections.

6.2 Facility and instrumentation development

To perform the aerodynamic analysis of the passing flow around the aerofoil using Particle Image Velocimetry, it was required to design and build a new wind tunnel facility the specific requirements of this technique. The design of the PIV wind tunnel has been described in detail including every element that constitutes it. Special attention has been taken in one of the most important components for guiding the flow, the nozzle. The design, construction and characterization of the contraction have been presented and the improvements obtained with this new proposal were validated before including it in the PIV wind tunnel.

A new wind tunnel contraction profile called logarithmic derivative (LDP) was designed by the author looking for a mathematical equation that was smoother and more gradual than the polynomial equations utilized in the bibliography and employing less parameters as well. This profile was studied and its performance was compared to the ones of another three polynomial profiles (FOP) using the Computational Fluid Dynamics (CFD) package ANSYS FLUENT®. Numerical results showed that the flow velocity of all models remained greater than 99% of the free-stream speed until reaching 96% of the outlet height, thus providing a boundary layer size of 4% of the outlet height. However a detail study of the velocity profiles in the boundary layer area manifested that the LDP exhibited slightly higher velocity values, achieving a better flow uniformity. The boundary layer separation avoidance at the nozzle walls was checked as well, and it was observed that the LDP and the FOP ($\alpha = 50°$) models fulfilled that requirement. The same outcomes were found when analysing the production of less turbulence levels. Overall, numerical results indicated that the logarithmic profile and the polynomial profile ($\alpha = 50°$) provide very good outcomes in terms of flow quality for experimental tests. However, the results show that the flow guided by LDP was slightly better conditioned. Accordingly, this profile was finally employed to construct the nozzle.

To characterize the real performance of the new contraction designed for this thesis, intensive experimental measurements were conducted using pressure transducers and hot-wire anemometry. The longitudinal pressure distribution along the nozzle side-wall revealed an optimal evolution matching perfectly with the theoretical design. Moreover, low levels of turbulence and high flow uniformity were confirmed at the nozzle discharge, with turbulence intensities below 0.7% even without the use of fine screens.

After the design and characterization of the nozzle, a first version of the PIV wind tunnel was built as open-loop circuit. The principal advantages of this design were its reduced dimensions, lower costs and shorter construction process. Nevertheless, after several attempts trying to achieve the required concentration of tracer particles for PIV measurements without success, the necessity of closing the wind tunnel became clear. Thus, the wind tunnel was redesigned with a closed-loop circuit so that particles could be recirculated inside achieving the correct concentration for PIV.

The test chamber of the wind tunnel with both configurations open-loop and closed-loop was characterized using hot-wire anemometry. It was observed that closing the circuit affected the turbulence levels inside the test section, increasing them from 1.76% to 2.45%. However the variation of the velocity signal became much more uniform. It has to be noted that the turbulence levels found in the PIV wind tunnel are higher than the ones in the Acoustic wind tunnel where the nozzle was first developed. Even though they could have been reduced introducing some screens inside the settling chamber right after the honey comb, it was decided not to introduce changes in the facility. The reason behind this decision was that since the application of elliptic aerofoils is essentially focused on turbomachinery, which implies rather high turbulent flows, the absence of screens offered more realistic flow conditions.

The viability of three tracer particles for PIV measurements was studied. The tests performed revealed that both oil and water droplets weren't good enough, giving too many spurious vectors when processing images. In particular, the concentration of olive oil droplets was too high to recognize patterns of movement and water droplets didn't scattered enough light to be properly captured by the camera. Particles of alumina with diameters around 10 µm were tested and demonstrated to be the best option between the three. Also, the measurement uncertainty of the PIV measurement procedure has been analysed,

taking into account the specific particle and optical instrumentation characteristics.

Several tasks of this thesis required the use of another measurement technique: hot-wire anemometry, demanding the manufacture of two different X-wire probes. These tasks were the characterization of the new nozzle design, the PIV wind tunnel or the wake behind the elliptic aerofoil.

Also, from the methodological point of view, several software procedures were developed in both C and Matlab for the analysis of the data. The functions written for the HW measurements focused mainly in increasing the speed of the flow angle and magnitude determination, due to the huge amount of data recorded. The PIV functions concentrated in the computing of derivative magnitudes, as the vorticity or the turbulence parameters.

6.3 Experimental study

With the facility and procedures developed, the effects of the angle of attack on the flow around a slender elliptic aerofoil was studied. This aerofoil has a maximum thickness ratio $t/c = 0.09$, slender than all the ones considered in the literature until now. As it was described before, the experimental campaign comprised particle image velocimetry and hot-wire anemometry. The PIV was used to comprehensive analyse the two-dimensional flow around the aerofoil body. Whereas HW anemometry, due to its operation philosophy, was utilized to study only a section of the downstream wake. Although the area of the considered section was relatively small, up to 1500 measurement positions were employed.

Flow dynamics and statistics were provided thanks to time-resolved PIV technique. Measurement maps were created with the combination of three different snapshots to cover the complete area around the aerofoil. Velocity fields showed the influence of the angle of attack on the dimensions and magnitudes of the wake. The lowest angles exhibit the more compact wakes and the lowest velocity reductions. As the angle was increased, the wake widened and lower velocities were found behind the aerofoil. This enlarging of the wake span was found to be mostly due the upwards shift of the upper shear layer.

The PIV results also offered an insight of the phenomena occurring at the suction surface of the elliptic aerofoil. At 0° the flow was completely attached and the body is covered by a thin boundary layer. When the angle was increased to 5° and 10°, a laminar bubble became noticeable at a distance from the leading edge of approximately $x/c \approx 0.16$. Although the flow behaviour after the bubble differed in the two cases. At 5° the flow continues attached to the surface as a turbulent boundary layer practically up to the trailing edge of the aerofoil. At 10° a detachment of the turbulent boundary layer can be noticed about the middle of the aerofoil, leading to a increased wake. At 15° the flow was observed to be completely detached at a small distance from the leading edge. The detachment and reattachment positions of the laminar bubble, together with the turbulent boundary layer separation, have been compiled to be used as a reference for future numerical simulations.

Turbulent kinetic energy and turbulent energy dissipation data was analysed to shed light on the turbulent phenomena of the flow. As it was expected, the regions with the highest levels of both variables were concentrated at the suction area of the aerofoil, especially in the bubble and the shear layer of the detached flow. Both magnitudes suffered an increase with the angle of attack.

Flow visualization with instantaneous photographs of oil particles illuminated by the laser sheet, was assessed to complete the information given by the PIV technique. The images

show the Von Karman vortex street and the laminar boundary layer on the upper surface of the aerofoil at 0°. In addition, the laminar bubbles formed at intermediate angles of attack and the detachment of the boundary layer at 15° can be also clearly seen.

Complementarity, HW data was also analysed. Normalized velocity maps of a region on the wake of the aerofoil shown the same tendencies than the PIV data. An in depth study of the velocity values compared to the PIV ones revealed that the differences were only significant at 15 °. The deviation in the results at the highest angle of attack may have been due the difficulty of the tracer particles to properly follow the flow when the velocities are low and the speed gradient is high. The solution proposed to avoid these dissimilarities is to use even smaller particles that provide lower velocity lag times. The study of velocity angles showed the existence of coherent structures at lower angles of attack, which agrees with the outcomes derived from the flow visualization.

The HW measurements also provide data to determine the drag force on the aerofoil at the four the angles of attack. Results were compared to the ones published by Kwon and Park (2005) although pertaining to a thicker aerofoil at a higher velocity. The Cd for a t/c = 0.16 thickness ratio elliptic aerofoil at $Re = 3{\times}10^5$ with and without a boundary-layer transition trip. The C_d obtained at $\alpha = 0°$ and $\alpha = 5°$ were similar to the values given for a smooth aerofoil at the same angles of attack. At $\alpha = 10°$ the drag increased and the value exceed those of the bibliography. Comparing the calculated values with the ones published in the cited reference, it was concluded that, for this particular aerofoil, the stall point could be found at an angle of $\alpha = 11°$ or 12°.

Turbulent length scales were obtained using both techniques at a vertical line after the aerofoil -x/c = 0.75-. The maximum sizes at each angle of attack were found within the wake at positions of maximum velocity reduction. A clear tendency was observed in which the size of the eddies increased with the angle. Results obtained with both techniques were in good agreement.

As a final comment, it can be said that the work undertaken during this thesis provides a methodological study that yields the basis for future investigations, as well as a scholar contribution to the knowledge on the aerodynamic characteristics of elliptic aerofoils.

6.4 Future research

As it has been mentioned before, the work accomplished in this thesis has been partly focused on facilitate the study of the dynamic properties of the flow in a PIV aerodynamic tunnel. The second part of this thesis provides the results of the measurements carried out on an elliptic aerofoil. Regarding this matter, it could be possible to carry through investigations in more depth, such as:

- An aerodynamic study with higher flow velocities, looking for the behaviour transition produced at a critical Reynolds number. In addition, this investigation could be completed analysing higher surface roughness or even including trip wires to obtain an equivalent effect.

- A detailed study of the boundary layer over the aerofoil using PIV with much higher magnification factors. It would be very interesting to determine in detail the velocity fields in the transition and the detachment areas.

- Since it have only been considered a single thickness ratio and four angles of attack, in order to obtain a comprehensive data base, it would be necessary to accomplish measurements with other angles of attack and thickness ratios.

Focusing on its practical application, one of the most important aerodynamic data of aerofoils is the variation of the C_l and C_d with the angle of attack. In the experimental research undertaken, the Cd of the elliptic aerofoil has been determined indirectly. However, to obtain adequate values it would be necessary to measure the forces on the profile in a wind tunnel with a precision weighting scale.

Another lines of research that are not directly related with the scope of this thesis, but are important to elliptic profiles and their use in turbomachinery, are proposed here.

- Numerical simulation using CFD techniques. The results obtained in this work can be useful to validate modellizations.
- The study of the cascade behaviour of elliptic profiles for their use in turbomachines of relative high solidity.
- Aeroacoustics studies. The emitted noise is especially important for jet fans and wind turbines applications.

Bibliography

Adeyinka, O. B. and Naterer, G. F. 2005. Experimental uncertainty of measured entropy production with pulsed laser piv and planar laser induced fluorescence. *International Journal of HEat and Mass Transfer 48*, 1450–1461.

Adrian, R. J. 1984. Scattering particle characteristics and their effect on pulsed laser measurements of fluid flow; speckle velocimetry vs particle image velocimetry. *Applied Optics 23,* 11, 1690 – 1691.

Adrian, R. J. 1986. Multi-point optical measurements of simultaneous vectors in unsteady flow: a review. *International Journal of Heat and Fluid Flow 7*, 127–145.

Adrian, R. J. and Yao, C. S. 1985. Pulsed laser technique application to liquid and gaseous flows and the scattering power of seed materials. *Applied Optics 24*, 44–52.

Akbari, M. H. and Price, S. J. 2003. Simulation of dynamic stall for a NACA airfoil using vortex method. *Journal of Fluids and Structures 17*, 855–874.

Alam, M. M., Zhou, Y., YAng, H. X., Guo, H., and Mi, J. 2010. The ultra-low Reynolds number airfoil wake. *Experiments in Fluids 48*, 81–103.

Anderson, J. D. 1991. *Fundamentals of aerodynamics.* McGraw-Hill, New York.

Andrews, G., Bradley, D., and Hundy, G. 1986. Hot wire anemometer calibration for measurements of small gas velocities. *Journal of Heat and Mass Transfer 15,* 10, 1965.

Arbey, H. and Bataille, J. 1983. Noise generated by airfoil profiles placed in a uniform laminar flow. *Journal of Fluid Mechanics 134*, 33–47.

Arena, A. V. and Mueller, T. J. 1980. Laminar separation, transition and turbulent reattachment near the leading edge of airfoils. *AIAA journal 18*, 747–753.

Argüelles, K. M., Fernández, J. M., , Galdo, M., and Blanco, E. 2012. Dual hot wire probes without cross prong-wire interference effects. *XXI Symposium on Measuring Techniques in Turbomachinery.*

Arts, T., Boerrigter, H., Carbonaro, M., Charbonnier, J. M., Degrez, G., Olivari, D., Riethmuller, M. L., and Van den Braembussche, R. A. 2001. *Measurement techniques in fluid dynamics, 2nd Revised Edition.* Von Karman Institute for fluid dynamics.

Aubertine, C. D., Eaton, J. K., and Song, S. 2004. Parameters controlling roughness effects in a separated boundary layer. *International Journal of Heat and Fluid Flow 25*, 444–450.

Baals, D. D. and Corliss, W. R. 1981. *Wind tunnels of NASA*. NASA SP-440, National Aeronautics and Space Administration, Washington (USA).

Badr, H. M., Dennis, S. C. R., and Kocabiyik, S. 2001. Numerical simulation of the unsteady flow over an elliptic cylinder at different orientations. *International Journal for Numerical Methods in Fluids 37*, 905–931.

Baldwin, L. V., Sandborn, V. A., and Laurence, J. C. 1960. Heat transfer from transverse and yawed cylinders in continuum, slip and free molecule airflows. *Journal of Heat Transfer, Transaction of ASME, C82*, 77–86.

Bardera, R. 2005. *Aplicación de PIV a la medida del coeficiente de resistencia aerodinámica*. PhD. Thesis, Universidad Complutense de Madrid.

Barker, D. B. 1997. Measuring fluid velocities with speckle patterns. *Optics Letters 11*, 135–137.

Basset, A. B. 1888. *Treatise on hydrodinamics vol II*. London: Deighton, Bell and Co.

Batill, S. M. and Mueller, T. J. 1981. Visualization of transition in the flow over an airfoil using the smoque wire technique. *AIAA journal 19*, 340–345.

Bell, J. H. and Mehta, R. D. 1988. Contraction design for small low speed wind tunnels. *NASA Contractor Rep. No. NASA-CR-177488*.

Bell, J. H. and Mehta, R. D. 1989. Boundary-layer predictions for small low-speed contractions. *AIAA Journal 27*, 372–374.

Bendat, J. S. and Piersol, A. G. 2000. *Random Data: Analysis and mearurement procedures*. Wiley-Interscience.

Blanco, E., Ballesteros, R., and Santolaria, C. 1996. Hot wire measurements during rotating stall in a variable pitch axial flow fan. *ASME 96-GT-441*.

Blanco-Marigorta, E., Ballesteros-tajadura, R., and Santolaria, C. 1998. Angular range and uncertainty analysis of non-orthogonal crossed hot wire probes. *Journal of FluidsEngineering 120*, 90–94.

Boussinesq, J. 1905. An equation for the phenomena of heat convection and an estimate of the cooling power of fluids. *Journal de Mathematiques 1*, 285–332.

Boussinesq, J. 1914. On the convection of heat from small cylinders in a stream of fluid. *Philosophical Transactions of the Royal Society A 214,* 14, 373–432.

Bracewell, R. N. 1999. *The Fourier transform and its applications, 3rd Edition*. McGraw-Hill Science.

Bradshaw, P. 1971. *An introduction to turbulence and its measurement*. Pergamon Press, New York (USA).

Bradshaw, P. and Pankhurst, R. C. 1964. The desigh of low-speed wind tunnels. *Progress in Aeronautical Sciences 6*, 1–69.

Bradshaw, P. and Wong, F. Y. F. 1972. The reattachment and relaxation of a turbulent shear layer. *Journal of Fluid Mechanics Part 1 52*, 113–35.

Brassard, B. and Ferchichi, M. 2005. Transformation of a polynomial for a contraction wall profile. *Journal of Fluids Engineering 127*, 183–185.

Brooks, T. F. and Hodgson, T. H. 1981. Trailing edge noise prediction from measured surface pressures. *Journal of Sound and Vibration 78*, 69–117.

Brooks, T. F. and Marcolini, M. A. 1985. Scaling of airfoil self-noise using measured flow parameters. *AIAA Journal 23*, 207–213.

Brooks, T. F., Pope, D. S., and Marcolini, M. A. 1989. Airfoil self-noise and prediction. *NASA Reference Publication 1218*.

Bruun, H. H. 1995. *Hot-wire anemometry: principles and signal analysis.* Oxford University Press.

Cambell, G. S. 1957. *Turbulence in the wake of a thin airfoil at low speeds.* Technical memorandum 1427, National Advisory Committee for Aeronautics (NACA), Washington, DC, USA.

Carter, J. and Soria, J. 2001. Piv measurements of turbulent jets. *4th International Symposium on Particle Image Velocimetry*.

Celik, I. B., Ghia, U., Roache, P. J., Freitas, C. J., and Raad, H. C. P. E. 2008. Procedure for estimation and reporting of uncertainty due to discretization in cfd applications. *Journal of Fluids Engineering 130,* 078001, 1–4.

Chang, P. K. 1961. Separation of flow. *Journal of Franklin Institute 272*, 433–448.

Charmichael, B. H. 1981. Low Reynolds number airfoil survey. *NASA CR 165803 1.*

Chou, M. H. and Huang, W. 1996. Numerical study of high-Reynolds-number flow past a bluff object. *International Journal for Numerical Methods in Fluids 23*, 711–732.

Cimbala, J. M. and Krein, M. V. 1990. Effect of freestream conditions on the far wake of a circular cylinder. *AIAA Journal 28,* 8, 1369–1373.

Comte-Bellot, G. 1975. *The hot wire and hot film anemometer: VKI Lecture Series.* Von Karman Institute for fluid dynamics.

Comte-Bellot, G. 1977. Hot-wire and hot-film anemometers. *Measurement of Unsteady Fluid Dynamic Phenomena, Hemisphere Publishing Co.*, 123–162.

Comte-Bellot, G., Charnay, G., and Sabot, J. 1981. Hot-wire and hot-film anemometry and conditional measurements: A report on euremech 132. *Journal of Fluid Mechanics 110*, 115–128.

Crabtree, L. 1959. The formation of regions of separated flow on wing surfaces. *Aeronautical Research Council*, 1–28.

Curle, N. 1955. The influence of solid boundaries upon aerodynamic sound. *Proceedings of the Royal Society A 231*, 504–514.

D'Alessio, S. J. D., Dennis, S. C. R., and Nguyen, P. 1999. Unsteady viscous flow past an impulsively started oscillating and translating elliptic cylinder. *Journal of Engineering Mathematics 35*, 339–357.

Davidson, P. A. 2004. *Turbulence: An Introduction for Scientists and Engineers.* Oxford University Press.

Davies, M. R. and P.O.A.L. 1973. *The hot wire anemometer: VKI Lecture Series.* Von Karman Institute for fluid dynamics.

Devinant, P., Laverne, T., and Hureau, J. 2002. Experimental study of wind-turbine airfoil aerodynamics in high turbulence. *Journal of Wind Engineering and Industrial Aerodynamics 90*, 689–707.

Diwan, S. S. and Ramesh, O. N. 2007. Laminar separation bubbles: Dynamics and control. *Sadhana 32,* 1 and 2, 747–770.

Dodson, M. G. 2005. *An historical and applied aerodynamic study of the Wright Brohers' wind tunnel test program and application to successtul manned flight.* US Naval Academy Technical Report. USNA-334.

Dommelen, L. L. V. and Shen, S. F. 1982. *The genesis of separation.* Numerical and Physical Aspects of Aerodynamic Flows. Springer.

Doolan, J. 2007. Numerical evaluation of contemporary low-speed wind tunnel contraction designs. *Technical Brief. Journal of Fluids Engineering 129*, 1241–1244.

Dryden, H. L. and Kuethe, A. M. 1929. The measurement of fluctuations of air speed by the hot-wire anemometer. *NACA-TR320*.

Dudderar, T. D. and Meynart, R. 1997. Laser speckle photography in a fluid medium. *Nature 270*, 45–47.

Fang, F. 1997. A design method for contractions with square end sections. *ASME Journal of Fluid Engineering 119*, 454–458.

Fang, F., Cheng, J. C., and Hong, Y. T. 2001. Experimental and analytical evaluation of flow in a square-to-square wind tunnel contraction. *Journal of Wind Engineering and Industrial Aerodynamics 89*, 247–262.

Farsimadan, E. and Mokhtarzadeh-Dehghan, M. R. 2010. An experimental study of the turbulence quantities in the boundary layer and near-wake of an airfoil placed at upstream of a 90Âº bend. *Experimental Thermal and Fluid Science 34*, 979–991.

Fernández, J. M., Argüelles, K. M., Santolaria, C., and Blanco, E. 2007a. On the structure of turbulence in a low-speed axial fan with inlet guide vanes. *Experimental Thermal and Fluid Science 32*, 316–331.

Fernández, J. M., Argüelles, K. M., Santolaria, C., and Blanco, E. 2007b. Unsteady flow and wake transport in a low-speed axial fan with inlet guide vanes. *Journal of Fluids Engineering 129*, 1015–1029.

Fink, M. R. 1793. Noise component method for airframe noise. *Journal of Aircraft 16.*

Fink, M. R. 1978. Fine structure of airfoil tone frequency. *95th meeting of the Acoustical Society of America.*

Freitas, C. J. 1993. Journal of fluids engineering editorial. policy statement on the control of numerical accuracy. *Journal of Fluids Engineering 115*, 339–340.

Gaster, M. 1967. The structure and behavior of separation bubbles. *Reports and Memoranda* 3595, 1–9.

Gerontakos, P. and Lee, T. 2005. Near wake behind an airfoil with leading-edge flow control. *Journal of Aircraft 42*, 561–567.

Gerrard, J. H. 1966. The mechanics of the formation region of vortices behind bluff bodies. *Journal of Fluid Mechanics 25,* 2, 401–413.

Goldstein, R. J. 1983. *Fluid Mechanics Measurements.* Hemisphere Publishing Corporation.

Grousson, R. and Mallic, S. 1997. Study of the flow pattern in a fluid by scattered laser light. *Applied Optics 16*, 2334–2336.

H. Huang, D. D. and Gharib, M. 1997. On errors of digital particle image velocimetry. *Measurement Science and Technology 8*, 1427–1440.

Hah, C. and Lakshminarayana, B. 1982. Measurement and prediction of mean velocity and turbulence structure in the near wake of an airfoil. *Journal of Fluid Mechanics 115*, 251–282.

Hallberg, M. P. 2000. Digital piv: Fundamental study including low to moderate high resolution. *Unpublished results*.

Hart, D. P. 2000. Piv error correction. *Experiments in Fluids 29*, 13–22.

Hinsch, K. D. 1993. *Particle Image Velocimetry (PIV). Part A. Application of Particle Image Velocimetry, theory and practice.* DLR.

Hinze, J. O. 1975. *Turbulence.* McGraw-Hill Book Co., New York (USA).

Hoerner, S. F. and Borst, H. V. 1975. *Fluid-Dynamic Lift. Chapter II: Lift characteristics of foil sections.* Hoerner Fluid Dynamics, Vancouver (WA).

Huang, H. 1994. Limitations of and improvements to piv and its application to a backward-facing step flow. *Verlag Köster*.

Huang, R. F. and Lee, H. W. 2000. Turbulence effect on frequency characteristics of unsteady motions in wake of wing. *AIAA Journal 38*, 87–94.

Huang, R. F. and Lin, C. L. 1995. Vortex shedding and shear-layer instability of wing at low-Reynolds numbers. *AIAA Journal 33*, 1398–1403.

Huang, R. F., Wu, J. Y., Jeng, J. H., and Chen, R. C. 2001. Surface flow and vortex shedding of an impuslively started wing. *Journal of Fluid Mechanics 441*, 265–292.

Hucho, W. H. and Sovran, G. 1993. Aerodynamics of road vehicles. *Annual Review of Fluid Mechanics 25*, 485–537.

Jahanmiri, M. 2011. Laminar separation bubble: Its structure, dynamics and control. *Research Report, ISSN 1652-8549*.

Johnson, R. W. 1998. *The handbook of fluid dynamics.* CRC Press.

Jones, B. M. 1938. Unsteady boundary layer for a pitching airfoil at low Reynolds numbers. *Journal of the Royal Aeronautical Society 38*, 747–770.

Keane, R. D. and Adrian, R. J. 1990. Optimization of particle image velocimeters. part i: Double pulsed systems. *Measurement Sciencie and Technology 1,* 11, 1202–1215.

Keane, R. D. and Adrian, R. J. 1992. Theory of cross-correlation analysis of piv images. *Applied Scientific Research 49*, 191–215.

Kim, D. and Chang, J. 2010. Unsteady boundary layer for a pitching airfoil at low Reynolds numbers. *Journal of Mechanical Science and Techology 24*, 429–440.

Kim, J., Kline, S. J., and Johnston, J. P. 1980. Investigation of a reattaching turbulent shear layer: flow over a backward-facing step. *Journal of Fluids Engineering 102,* 9.

Kovasznay, L. S. G. 1950. The hot-wire anemometer in supersonic flows. *Journal of the Aeronautical Sciences 17,* 9, 565–584.

Kovasznay, L. S. G. 1953. Turbulence in supersonic flow. *Journal of the Aeronautical Sciences 20,* 10, 657–674.

Kovasznay, L. S. G. 1959. Turbulence measurements. *Applied Mechanics Reviews 12,* 6, 375–380.

Kwon, K., Park, B., Lee, J., and Park, S. O. 2006. Boundary layer transition measurement over an airfoil by using piv with high magnification. *13th, International symposium on applications of laser techniques to fluid mechanics, Lisbon, Portugal*, 1–8.

Kwon, K. and Park, S. O. 2005. Aerodynamic characteristics of an elliptic airfoil at low Reynolds number. *Journal of Aircraf 42,* 6, 1642–1644.

Larsen, J. W., Nielsen, S. R. K., and Krenk, W. 2007. Dynamic stall model for wind turbine airfoils. *Journal of Fluids and Structures 23*, 959–982.

Laufer, J. 1975. New trends in experimental turbulent research. *Annual Review of Fluid Mechanics 7*, 307–326.

Laufer, J. and Mcclellan, R. 1956. Measurements of heat transfer from fine wires in supersonic flows. *Journal of Fluid Mechanics 1,* 3, 276–289.

Lighthill, M. J. 1952. On sound generated aerodynamically, i: general theory. *Proceedings of the Royal Society A 211*, 564–587.

Lighthill, M. J. 1954. On sound generated aerodynamically, ii: turbulence as a source of sound. *Proceedings of the Royal Society A 222*, 1–32.

Lighthill, M. J. 1963. *Attachment and separation in three-dimensional flows.* Laminar Bound. Layer Theory. Dover, 2nd edition.

Lin, J. and Pauley, L. 1996. Low-Reynolds-number separation on an airfoil. *AIAA Journal 34,* 8, 1570–1577.

Lindgren, B. and Johansson, A. 2002. *Design and Evaluation of a low-speed wind tunnel with expanding corners.* Technical Report, Royal Institute of Technology, Sweden.

Lissaman, P. B. 1983. Low Reynolds numbers airfoils. *Annual Review of Fluid Mechanics 15*, 223–239.

Lomas, C. G. 1986. *Fundamentals of hot-wire anemometry.* Cambridge University Press.

Longhouse, R. E. 1977. Vortex shedding noise of low tip speed axial flow machines. *Journal of Sound and Vibration 53*, 25–46.

Lourenco, L. and Krothapalli, A. 1995. On the accuracy of velocity and vorticity measurements with piv. *Experiments in Fluids 18*, 421–428.

Lowson, M. V. 1993. Aplications of aero-acoustic analysis to wind turbine noise control. *Journal of Wind Engineering 16*, 126–138.

Marchman, J. F. 1987. Aerodynamic testing at low Reynolds numbers. *Jorunal of Aircraft 24*, 107–114.

Marxen, O., Lang, M., Rist, U., and Wagner, W. A. 2003. Combined experimental/numerical study of unsteady phenomena in a laminar separation bubble. *Flow, Turbulence and Combustion 71*, 133–146.

Mathew, J., Bahr, C., Carroll, B., Sheplak, M., and Cattafesta, L. 2005. Design, fabrication, and characterization of an anechoic wind tunnel facility. *11th AIAA/-CEAS Aeroacoustics conference*.

McAlpine, A., Nash, E. C., and Lowson, M. V. 1999. On the generation of discrete frequency tones by the flow around an aerofoil. *Journal of Sound and Vibration 222*, 753–779.

McKenna, S. P. and McGillis, W. R. 2002. Performance of digital image velocimetry processing techniques. *Experiments in Fluids 32*, 106–115.

Mehta, R. D. and Bradshaw, P. 1979. Design rules for small low-speed wind tunnels. *The Aeronautical Journal of the Royal Aeronautical Society 83*, 443–449.

Merzkirch, W. 1987. *Flow Visualization, 2nd Edition.* Academic Press.

Meynart, R. 1992. Digital image processing for speckle flow velocimetry. *Review of Scientific Instruments 53*, 110–111.

Meynart, R. 1993. Instantaneous velocity field measurements in unsteady gas flow by speckle velocimetry. *Applied Optics 22*, 535–540.

Moon-Sang, K. and Sengupta, A. 2005. Unsteady viscous flow over elliptic cylinders at various thickness with different Reynolds numbers. *Journal of Mechanical Science and Technology 19,* 3, 877–886.

Moore, F. K. 1958. *On the separation of the unsteady laminar boundary layer.* Boundary Layer Research. Springer.

Morel, T. 1975. Comprehensive design of axisymmetric wind tunnel contractions. *ASME Journal of Fluid Engineering 97*, 225–233.

Morel, T. 1977. Design of two-dimensional wind tunnel contractions. *ASME Journal of Fluid Engineering 99*, 371–378.

Mueller, T. J. 1985. *Low Reynolds number vehicles.* AGARD-AG-288.

Mueller, T. J. and Batill, S. M. 1982. Experimental studies of separation on a two-dimensional airfoil at low reynolds numbers. *AIAA journal 20*, 457–463.

Mueller, T. J. and DeLaurier, J. D. 2003. Aerodynamics of small vehicles. *Annual Revision of Fluid Mechanics 35*, 89–111.

Nair, M. T. and Sengupta, T. K. Onset of asymmetry: flow past circular and elliptic cylinders. *International Journal for Numerical Methods in Fluids 23,* 12.

Nair, M. T. and Sengupta, T. K. 1997. Unsteady flow past elliptic cylinders. *Journal of Fluids and Structures 11*, 555–595.

Nash, E. C., Lowson, M. V., and McAlpine, A. 1999. A boundary layer instability noise on aerofoils. *Journal of Fluid Mechanics 382*, 27–61.

Nogueira, J., Lecuona, A., and Rodriguez, P. A. 1999. Second-order accurate particle image velocimetry. *Experiments in Fluids 27*, 107–116.

Olivari, D. 1980. Hot-wire techniques: conditional sampling and intermittency. *Von Karman Institute for Fluid Dynamics, Lecture Series - 3, Measurements and Predictions of Complex Turbulent Flows.*

Oro, J. M. F. 2012. *Técnicas numéricas en ingeniería de fluidos.* Editorial Reverté, Barcelona (Spain).

Ota, T., Nishiyama, H., and Taoka, Y. 1987. Flow around an elliptic cylinder in the critical Reynolds number regime. *Journal of Fluids Engineering 109*, 149–155.

Owen, F. K. and Foire, A. W. 1986. Principles and practices of hot-wire anemometers. *Complere Inc., Palo Alto, CA.*

Patel, V. A. 1981. Flow around the impulsively started elliptic cylinder at various angles of attack. *Computers and Fluids 9,* 4, 435–462.

Paterson, R. W., Vogt, P. G., Fink, M. R., and Munch, C. L. 1973. Vortex noise of isolated airfoils. *Journal of Aircraft 10*, 296–302.

Pauley, L. L., Moin, P., and Reynolds, W. C. 1990. The structure of two-dimensional separation. *Journal of Fluid Mechanics 28*, 389–428.

Penaranda, F. E. and Freda, M. S. 1985. *Aeronautical facilities catalogue volume 1.* NASA RP-1132, National Aeronautics and Space Administration, Washington (USA).

Perry, A. E., Chong, M. S., and Lim, T. T. 1982. The vortex-shedding process behind two-dimensional bluff bodies. *Journal of Fluid Mechanics 116*, 77–90.

Pickering, C. D. and Halliwell, N. A. 1984. Speckle photography in fluid flows: signal recovery with two-steps processing. *Applied Optics 23,* 8, 1128–1129.

Pohlen, L. G. and Mueller, T. J. 1984. Boundary layer characteristics of the miley airfoil at low Reynolds numbers. *Journal of Aircraft 21*, 658–664.

Pope, S. B. 2001. *Turbulent Flow.* Cambridge University Press, Cambridge (UK).

Prandt, L. and Tietjens, O. G. 1934. *Fundamentals of hydro and aeromechanics.* Dover Publications.

Prasad, A. and Williamson, C. H. 1997. The instability of the shear layer separating from a bluff body. *Journal of Fluid Mechanics 333*, 375–402.

Prasad, A. K. 2000. Particle image velocimetry. *Current Science 79,* 1, 101–110.

Rae, W. H. and Pope, A. 1984. *Low-speed wind tunnel testing.* John Wiley and Sons, New York (USA).

Raffel, M., Willert, C., Wereley, S., and Kompenhans, J. 2007. *Particle Image Velocimetry, a practical guide.* Springer-Verlag.

Ramaeshan, S. and Ramaswamy, M. A. 2002. A rational method to choose optimum design for two dimensional contractions. *ASME Journal of Fluid Engineering 124*, 554–546.

Richardson, L. F. 1922. *Weather prediction by numerical process.* Cambridge University Press, Cambridge (UK).

Riethmuller, M. L. 2000. *Particle image velocimetry and associated techniques: VKI Lecture series.* Von Karman Institute for fluid dynamics.

Roache, P. J. 2008. Perspective: validation-what does it mean? *Journal of Fluids Engineering 130,* 034503, 1–4.

Roberts, W. B. 1980. Calculation of laminar separation bubbles and their effect on airfoil performance. *AIAA journal 18*, 25–31.

Rose, W. C. and McDaid, W. P. 1976. Turbulence measurement in transonic flow. *Proceedings of the AIAA 9th Aerodynamic Testing Conference, Arlington, Texas.*

Roshko, A. 1954. On the drag and shedding frequency of two-dimensional bluff bodies. *NACA Technical Notes 3169.*

Roshko, A. 1993. Perspectives on bluff body aerodynamics. *Journal of Wind Engineering and Industrial Aerodynamics 49*, 79–100.

Rott, N. 1956. Unsteady viscous flow in the vicinity of a stagnation point. *Quarterly of Applied Mathematics 13*, 444–451.

Rouse, H. and Hassan, M. M. 1949. Cavitation-free inlets and contractions. *Mechanical Engineering 71*, 213–216.

Sandborn, V. A. 1972. *Resistance temperature transducers.* Metrology Press, Fort Collins, Colorado (USA).

Sandborn, V. A. 1974. A review of turbulence measurements in compressible flow. *NASA-TMX-62337.*

Sandham, N. D. 2008. Transitional separation bubbles and unsteady aspects of aerofoil stall. *The Aeronautical Journal 112,* 1133, 395–404.

Sargison, J. E., Walker, G. J., and Rossi, R. 2004. Design and calibration of a wind tunnel with a two dimensional contraction. *Proceedings of the 15th Australasian Fluid Mechanics Conferece 13.*

Sears, W. R. 1956. Some recent developments in airfoil theory. *Journal of Aerospace Sciences 23*, 490–499.

Sharp, K. V., k. C. Kim, and Adrian, R. J. 1998. Dissipation estimation around a rushton turbine using particle image velocimetry. *Proc. 9th Int. Symposoum on Applics. of Laser Techniques of Fluid Mechanics*.

Shubauer, G. B. 1939. Air flow in the boundary layer on an elliptic cylinder. *NACA Rept. 652*.

Simpson, R. L. 1989. Aspects of turbulent boundary layer separation. *Annual Review of Fluid Mechanics 21*, 205–234.

Simpson, R. L. 1996. Aspects of turbulent boundary layer separation. *Progress in Aerospace Sciences 32,* 5, 457–521.

Smol'yakov, A. V. and Tkachenko, V. M. 1983. *The measurement of turbulent fluctuatuins: an introduction of hot-wire anemometry and related transducers.* Springer-Verlag, New York (USA).

Spencer, A. and Hollis, D. 2005. Correcting for sub-grid filtering effects in particle image velocimetry data. *Measurement Science and Technology 16,* 11, 2323–2335.

Stanislas, M., Westerweel, J., and Kompenjans, J. 2003. Particle image velocimetry: Recent improvements. *Proceedings of the EUROPIV 2 workshop held in Zaragoza (Spain), March 31-April 1*.

Strouhal, V. 1878. On one particular way of tone generation (in german). *Annual Review of Physical Chemistry 5*, 216–251.

Strutt, J. W. and Rayleigh, B. 1894. *The theory of sound.* MacMillan and co.

Sturm, H., Dumstorff, G., Busxhe, P., Westermann, D., and Lang, W. 2012. Boundary layer separation and reattachment detection on airfoils by thermal flow sensors. *Sensors 12*, 14292–14306.

Tam, C. K. W. 1974. Discrete tones of isolated airfoils. *Journal of the Acoustical Society of America 55*, 1173–1177.

Tani, I. 1964. Low speed flows involving bubble separation. *Progress in Aerospace Sciences 5*, 70–103.

Tennekes, H. and Lumley, J. L. 1972. *A first course in turbulence.* MIT press, Cambridge.

Tropea, C., Yarin, A. L., and Foss, J. F. 2007. *Measurement of turbulent flows.* Springer.

Unal, M. F. and Rockwell, D. 1988. On vortex shedding from a cylinder. part 1. the initial instability. *Journal of Fluid Mechanics 190*, 491–512.

Vagt, G. H. 1979. Hot-wire probes in low speed flow. *Progress in Aerospace Sciences 18*, 271–323.

Van de Hulst, H. C. 1957. *Light scattering by small particles.* Jogh Wiley & Sons.

Vogt, A., Baumann, P., Gharib, M., and Kompenhans, J. 1996. Investigations of a wing tip vortex in air by means of dpiv. *19th AIAA Advanced Measurement and Ground Testing Techniques*.

Watmuff, J. H. 1999. Evolution of a wave packet into vortex loops in a laminar separation bubble. *Journal of Fluid Mechanics 397*, 119–169.

Werely, S. T. and Meinhart, C. D. 2001. Second-order accurate particle image velocimetry. *Experiments in Fluids 31*, 258–268.

Westerweel, J. 1993. *Digital particle image velocimetry - theory and application*. PhD. Thesis, University Press (Delft).

Westerweel, J., Daribi, D., and Gharib, M. 1997. The effect of discrete window offset on the accuracy of cross-correlation analysis of digital piv recording. *Experiments in Fluids 23*, 20–28.

White, F. M. 1986. *Fluid Mechanics. Boundary-layer flows*. McGraw-Hill, New York (USA).

Willert, E. and Gharib, M. 1991. Digital particle image velocimetry. *Experiments in Fluids 10*, 181–193.

Williams, J. C. 1977. Incompressible boundary-layer separation. *Annual Review in Fluid Mechanics 9*, 113–114.

Williams-Stuber, K. and Gharib, M. 1990. Transition from order to chaos in the wake of an airfoil. *Journal of Fluid Mechanics 213*, 29–97.

Williamson, C. H. K. 1996. Vortex dynamics in the cylinder wake. *Annual Review of Fluid Mechanics 28*, 477–539.

Wolf, T. 1994. Design of a variable contraction for a full-scale automotive wind tunnel. *Journal of Wind Engineering and Industrial Aerodynamics 56*, 1–21.

Wright, S. E. 1976. The acoustic spectrum of axial flow machines. *Journal of Sound and Vibration 45*, 165–223.

Yang, Z., Igarashi, H., Martin, M., and Hu, H. 2008. An experimental investigation on aerodynamic hysteresis ot a low-Reynolds number airfoil. *46th IAA Aerospace Science Meeting and Exhibit, Reno, Nevada*.

Yarusevych, S. 2006. *Investigation of airfoil boundary layer and turbulent wake development at low Reynolds numbers*. PhD. Thesis, University of Toronto (Canada).

Yarusevych, S., Sullivan, P. E., and Kawall, J. G. 2006. Coherent structures in an airfoil boundary layer and wake at low Reynolds numbers. *American Institute of Physics 18*, 1–11.

Zahn, A. F., Smith, R. H., and Louden, F. A. 1929. Forces on elliptic cylinders in uniform air stream. *NACA Rept. 289, NACA TR-315*.

Zhou, Y., Alam, M. M., Yang, H. X., Guo, H., and Wood, D. H. 2011. Fluid forces on a very low Reynolds number airfoil and their prediction. *International Journal of Heat and Fluid Flow 32*, 329–339.

ZIEGLER, M. 1934. The construction of a hot-wire anemometer with linear scale and lwgligible lag. *Proceedings of the Koninklijke Nederlandse Akademie van Wetenschappen 15,* 1.

Appendix I

In this appendix are presented the MATLAB codes developed for acquiring processing and post-processing data with hot-wire anemometry and PIV.

PIV postprocessing

```
%%%%%%%%%%%%%%%%%%%%%%%%%%%%%%%%%%%%%%%%%%%%%%%%%%%%%%%%%%%%%%%%%%%%%%%%%%%%%%%%
% Programa que calcula el campo de velocidad medio a partir de los campos
% obtenidos mediante varias fotografías — PIV postprocesado
% MRL 16/10/2013
%%%%%%%%%%%%%%%%%%%%%%%%%%%%%%%%%%%%%%%%%%%%%%%%%%%%%%%%%%%%%%%%%%%%%%%%%%%%%%%%

clc
close all
clear all

Umed = 12.4;              % Velocidad media del flujo libre en [m/s]

MyPath = ['E:\Mis documentos\...'];
cd (MyPath)               % Accede a la carpeta con el criterio de selección
    de experimentos anterior

Runs = ls(['05_*']);      % Introduce el criterio de selección de
    experimentos
[fr,cr] = size(Runs);


%% Cálculo de la velocidad medida

for Run_no = 1:fr   % Meter un criterio de selección de número de
    fotografías en vez de "fr"

   MyRun = Runs(Run_no,:);
   % Columna 1: x [mm]; Columna 2: y [mm]; Columna 3: U [m/s]; Columna 4:
       V[m/s]
   A = dlmread(MyRun,',' , 1, 0); % Fichero con cabecera de una linea
   %A = dlmread(MyRun,',' , 0, 0); % Fichero sin cabecera
   A(:,5) = [ ];
   [fA,cA] = size(A);

   %% Paso los vectores x, y, U y V a matrices de fm filas y cm columnas de
       cada par de imagenes

   % Determina el número de filas y columnas de las matrices a crear
   cm = 1;
   for i = 2:fA
      if A(i, 2) == A(i-1, 2)
         cm = cm + 1;
      else
         fm = floor(fA / cm);
         % disp(['Dimensiones de la imagen: ' num2str(cm) 'x' num2str(fm)]);
         if cm * fm ~= fA
            error('Dimensiones detectadas incorrectamente (filas * cols ~=
```

```
            total)')
      end
      break;
   end
end

% Crea las matrices de valores x, y, U, V
for ffm = 1:fm
   for ccm = 1:cm
      Mx(ffm,ccm) = A(ccm + cm*(ffm-1),1);
      My(ffm,ccm) = A(ccm + cm*(ffm-1),2);
      Mu(ffm,ccm) = A(ccm + cm*(ffm-1),3);
      Mv(ffm,ccm) = A(ccm + cm*(ffm-1),4);
   end
end


%% Dibuja los vectores velocidad y las líneas de flujo para cada par de
    imágenes

 figure(1)
 quiver(A(:,1), A(:,2), A(:,3), A(:,4), 0.5,'k');
 figure
 streamslice(Mx,My,Mu,Mv, 2);


%% Cálculo del campo medio de velocidades (u, v) (Ensemble Average)

if Run_no == 1
   VelMed = A;
   disp( 'Calculando el campo medio de velocidades')
else
   VelMed(:,3) = VelMed(:,3) + A(:,3);
   VelMed(:,4) = VelMed(:,4) + A(:,4);
   if Run_no == fr
      VelMed(:,3) = VelMed(:,3)/fr; % Media de u, componente x de la
          velocidad
      VelMed(:,4) = VelMed(:,4)/fr; % Media de v, componente y de la
          velocidad
      disp('Finalizado el cálculo del campo medio de velocidades')
   end
end

%% Estudio de la convergencia de un valor cualquiera en función del nº
    de fotos

Conver1(Run_no,1) = Run_no;       % Columna 1 : nº de fotos
Conver1(Run_no,2) = VelMed(3403,3)/Run_no; % Columna 2 : velocidad U en
    un punto
```

```
   if Run_no == fr
      Conver1(Run_no,2) = VelMed(3403,3);
   end

   Conver2(Run_no,1) = Run_no;       % Columna 1 : nº de fotos
   Conver2(Run_no,2) = VelMed(2121,3)/Run_no; % Columna 2 : velocidad U en
       un punto
   if Run_no == fr
      Conver2(Run_no,2) = VelMed(2121,3);
   end

   Conver3(Run_no,1) = Run_no;       % Columna 1 : nº de fotos
   Conver3(Run_no,2) = VelMed(3929,3)/Run_no; % Columna 2 : velocidad U en
       un punto
   if Run_no == fr
      Conver3(Run_no,2) = VelMed(3929,3);
   end
end


%% Paso los vectores x, y, u y v a matrices de fm filas y cm columnas

% Determina el número de filas y columnas de las matrices a crear
cm = 1;
for i = 2:fA
   if A(i, 2) == A(i-1, 2)
      cm = cm + 1;
   else
      fm = floor(fA / cm);
      disp(['Dimensiones de la imagen: ' num2str(cm) 'x' num2str(fm)]);
      if cm * fm ~= fA
         error('Dimensiones detectadas incorrectamente (filas * cols ~=
             total)')
      end
      break;
   end
end

% Crea las matrices de valores x, y, u, v
for ffm = 1:fm
   for ccm = 1:cm
      Mx(ffm,ccm) = VelMed(ccm + cm*(ffm-1),1); % Matriz con la coordenada
          x de cada ventana de interrogacion
      My(ffm,ccm) = VelMed(ccm + cm*(ffm-1),2); % Matriz con la coordenada
          y de cada ventana de interrogacion
      Mu(ffm,ccm) = VelMed(ccm + cm*(ffm-1),3); % Matriz con la velocidad
          u de cada ventana de interrogacion
      Mv(ffm,ccm) = VelMed(ccm + cm*(ffm-1),4); % Matriz con la velocidad
          v de cada ventana de interrogacion
```

```
   end
end


%% Crea una matriz con las filas y columnas de ceros (zona tapada por la
    máscara en el PIV)

 z = 1;
 y = 1;
 for j = 1:ffm
    for k = 1:ccm
       if Mu(j,k) == 0 && Mv(j,k) == 0
          del(z,1) = j; % Columna 1 filas
          del(z,2) = k; % Columna 2 columnas
          z = z+1;
       end
    end
 end


%% Representación de la convergencia de la velocidad en un punto en función
    del número de fotos

figure(3)
plot(Conver1(:,1),abs(Conver1(:,2)),'LineWidth',2,'Color',[0,0,0]); hold on;
plot(Conver2(:,1),abs(Conver2(:,2)),'LineWidth',2,'Color',[0.7,0.7,0.7])
plot(Conver3(:,1),abs(Conver3(:,2)),'LineWidth',2,'Color',[0.5,0.5,0.5])
line([300 300], [0 12],'LineWidth',2,'Color',[0, 0, 0])
title('Velocity convergence as a function of the number of images')
ylabel('\itU average \rm[m/s]')
xlabel('Number of images')
legend('Position 1','Position 2','Position 3', 'Location', 'SouthEast')
axis([0 600 0 12])


%% Representación vectorial del campo medio de velocidades

figure(4)
title('Velocity vectors field')
quiver(VelMed(:,1), VelMed(:,2), VelMed(:,3), VelMed(:,4), 0.5,'k');

figure(5)
title('Flow lines')
streamslice(Mx, My, Mu, Mv, 2);
axis tight


%% Calculo del modulo de la velocidad
```

```
[fMv,cMv] = size(Mu);

for j = 1:cMv
   for i = 1:fMv
      MU(i,j) = sqrt(Mu(i,j)^2 + Mv(i,j)^2);
   end
end


%% Dibuja la gráfica de contornos de velocidades

MU_max = max(max(MU));
figure(6)
contourf (Mx, My, MU/MU_max ,15);
title('Velocity module contours')

%% Dibuja la gráfica de contornos de ángulo

figure(16)
contourf (Mx, My, atan(Mv./Mu) ,15);
title('Velocity angle contours')
caxis([-1.5 1.5])


%% Cálculo de la variacion de velocidad u', v', u'^2, v'^2, (dv'/dx)^2

for Run_no = 1:fr   % Meter un criterio de selección de número de
    fotografías en vez de "fr"

   MyRun = Runs(Run_no,:);
   % Columna 1: x [mm]; Columna 2: y [mm]; Columna 3: U [m/s]; Columna 4:
       V[m/s]
   A = dlmread(MyRun,',' , 1, 0); % Fichero con cabecera de una linea
   %A = dlmread(MyRun,',' , 0, 0); % Fichero sin cabecera
   A(:,5) = [ ];
   [fA,cA] = size(A);


   %% Variacion de las componentes de la velocidad paracada par de imagenes

   for i = 1:fA
      B(:,1) = A(:,3) - VelMed(:,3); % u' = u - u_ensembleaverage
      B(:,2) = A(:,4) - VelMed(:,4); % v' = v - v_ensembleaverage
      B(:,3) = B(:,1).^2;        % (u')^2 = (u - u_ensembleaverage)^2
      B(:,4) = B(:,2).^2;        % (v')^2 = (v - v_ensembleaverage)^2
      B(:,5) = B(:,3) + B(:,4);  % (U')^2 = (sqrt((u')^2+(v')^2))^2
   end
```

```
%% Determina el número de filas y columnas de las matrices a crear

cm = 1;
for i = 2:fA
   if A(i, 2) == A(i-1, 2)
      cm = cm + 1;
   else
      fm = floor(fA / cm);
      %disp(['Dimensiones de la imagen: ' num2str(cm) 'x' num2str(fm)]);
      if cm * fm ~= fA
         error('Dimensiones detectadas incorrectamente (filas * cols ~=
             total)')
      end
      break;
   end
end


%% Crea las matrices de valores u', v' y u'^2, v'^2 de cada par de
    imagenes

for ffm = 1:fm
   for ccm = 1:cm
      MMuvar(ffm,ccm) = B(ccm + cm*(ffm-1),1); % Matriz con la
          variacion de velocidad u' de cada ventana de interrogacion
      MMvvar(ffm,ccm) = B(ccm + cm*(ffm-1),2); % Matriz con la
          variacion de velocidad v' de cada ventana de interrogacion
      MMuvar2(ffm,ccm) = B(ccm + cm*(ffm-1),3); % Matriz con la
          variacion de velocidad u'^2 de cada ventana de interrogacion
      MMvvar2(ffm,ccm) = B(ccm + cm*(ffm-1),4); % Matriz con la
          variacion de velocidad v'^2 de cada ventana de interrogacion
      MMUvar2(ffm,ccm) = B(ccm + cm*(ffm-1),5); % Matriz con la
          variacion de velocidad U' de cada ventana de interrogacion

   end
end


%% Crea una matriz con dos columnas r y Rii (función de correlación de
    velocidad)

dx = (Mx(1,1) - Mx(1,2))*0.001; % Desplazamiento en x(m) de cada
    ventana de interrogación
dy = (My(1,1) - My(2,1))*0.001; % Desplazamiento en y(m) de cada
    ventana de interrogación

% Si el ángulo de ataque es: 0Grad
r = [0 : dx : dx*(63)];    % Vector de separación entre dos puntos
    correlacionados (m)
```

```
c = 1;
for j = 1:fm
   for i = 78:-1:15
      Rii(j,c) = MMuvar(j,78) * MMuvar(j,i);
      c = c+1;
   end
   c = 1;
end

 % Si el ángulo de ataque es: 5Grad
 r = [0 : dx : dx*(63)];    % Vector de separación entre dos puntos
     correlacionados (m)

 c = 1;
 for j = 1:fm
    for i = 78:-1:15
       Rii(j,c) = MMuvar(j,78) * MMuvar(j,i);
       c = c+1;
    end
    c = 1;
 end

 % Si el ángulo de ataque es: 10Grad
 r = [0 : dx : dx*(57)];    % Vector de separación entre dos puntos
     correlacionados (m)

 c = 1;
 for j = 1:fm
    for i = 81:-1:24
       Rii(j,c) = MMuvar(j,81) * MMuvar(j,i);
       c = c+1;
    end
    c = 1;
 end

 % Si el ángulo de ataque es: 15Grad
 r = [0 : dx : dx*(60)];    % Vector de separación entre dos puntos
     correlacionados (m)

 c = 1;
 for j = 1:fm
    for i = 81:-1:21
       Rii(j,c) = MMuvar(j,81) * MMuvar(j,i);
       c = c+1;
    end
    c = 1;
 end
```

```
%% Calcula (dv'/dx)^2, (dv'/dy)^2, (du'/dx)^2 y (du'/dy)^2 de cada par
    de imágenes para poder calcular la tasa de disipacion viscosa más
    adelante

dvvardx2 = zeros(fm,cm);
dvvardy2 = zeros(fm,cm);
duvardx2 = zeros(fm,cm);
duvardy2 = zeros(fm,cm);
duvvardyx = zeros(fm,cm);

for j = 2:cm-1
   for i = 2:fm-1
      if Mu(i+1,j) == 0 || Mu(i-1,j) == 0
         dvvardx2(i,j) = 0;
         duvardx2(i,j) = 0;
         dvvardy2(i,j) = 0;
         duvardy2(i,j) = 0;
         duvvardyx(i,j) = 0;
      else
      dvvardx2(i,j) = ((MMvvar(i,j+1)-MMvvar(i,j-1)) / dx)^2;
      duvardx2(i,j) = ((MMuvar(i,j+1)-MMuvar(i,j-1)) / dx)^2;
      dvvardy2(i,j) = ((MMvvar(i+1,j)-MMvvar(i-1,j)) / dy)^2;
      duvardy2(i,j) = ((MMuvar(i+1,j)-MMuvar(i-1,j)) / dy)^2;
      duvvardyx(i,j) = ((MMuvar(i+1,j)-MMuvar(i-1,j)) / dy) *
          ((MMvvar(i,j+1)-MMvvar(i,j-1)) / dx);
      end
   end
end



%% Cálculo del campo medio de variaciones de velocidad (U', u', v',
    (u')^2, (v')^2, (dv'/dx)^2, u'(x)* u'(x+dx) ) (Ensemble Average)

if Run_no == 1
   Muvar = MMuvar;
   Mvvar = MMvvar;
   Muvar2 = MMuvar2;
   Mvvar2 = MMvvar2;
   MUvar2 = MMUvar2;
   Mdvvardx2 = dvvardx2;
   Mduvardx2 = duvardx2;
   Mdvvardy2 = dvvardy2;
   Mduvardy2 = duvardy2;
   Mduvvardyx = duvvardyx;
   MRii = Rii;
   disp( 'Calculando el campo medio de variaciones de velocidad')
else
```

```
      Muvar = Muvar + MMuvar;
      Mvvar = Mvvar + MMvvar;
      Muvar2 = Muvar2 + MMuvar2;
      Mvvar2 = Mvvar2 + MMvvar2;
      MUvar2 = MUvar2 + MMUvar2;
      Mdvvardx2 = Mdvvardx2 + dvvardx2;
      Mduvardx2 = Mduvardx2 + duvardx2;
      Mdvvardy2 = Mdvvardy2 + dvvardy2;
      Mduvardy2 = Mduvardy2 + duvardy2;
      Mduvvardyx = Mduvvardyx + duvardy2;
      MRii = Rii + MRii;

      if Run_no == fr
         Muvar = Muvar/fr;    % Media de u' (Ensemble average)
         Mvvar = Mvvar/fr;    % Media de v' (Ensemble average)
         Muvar2 = Muvar2/fr;  % Media de (u')^2 (Ensemble average)
         Mvvar2 = Mvvar2/fr;  % Media de (v')^2 (Ensemble average)
         MUvar2 = MUvar2/fr;  % Media de U' (Ensemble average)
         Mdvvardx2 = Mdvvardx2/fr; % Media de (dv'/dx)^2 (Ensemble average)
         Mduvardx2 = Mduvardx2/fr; % Media de (du'/dx)^2 (Ensemble average)
         Mdvvardy2 = Mdvvardy2/fr; % Media de (dv'/dy)^2 (Ensemble average)
         Mduvardy2 = Mduvardy2/fr; % Media de (du'/dy)^2 (Ensemble average)
         Mduvvardyx = Mduvvardyx/fr; % Media de du'/dy * dv'/vx (Ensemble
             average)
         MRii = MRii/fr;      % Media para obtener la función correlación
             de velocidad
         disp('Finalizado el cálculo del campo medio de variaciones de
             velocidad')
      end
   end

end


%% Dibuja la gráfica de contornos de variacion de velocidad

figure(7)
contourf (Mx, My, Muvar ,15);
title('Velocity variation of u contours')

figure(8)
contourf (Mx, My, Mvvar ,15);
title('Velocity variation of v contours')
colorbar
caxis([1 10])


%% Calculo de la Energia Cinetica Turbulenta (Turbulent Kinetic Energy)
```

```
k = 0.5 * (Muvar2 + Mvvar2);


%% Dibuja la gráfica de Energia Cinetica Turbulenta

k_max = max(max(k));
figure(9)
contourf (Mx, My, k ,15);
colorbar
caxis([0 40])
title('Turbulent Kinetic Energy')


%% Calculo de la Intensidad Turbulenta (Turbulent Intensity) TI(U), TI(u),
    TI (v)

TIU = sqrt(MUvar2) ./ MU_max;
TIu = sqrt(Muvar2) ./ MU_max;
TIv = sqrt(Mvvar2) ./ MU_max;
TIU_max = max(max(TIU));


%% Dibuja la gráfica de Intensidad Turbulenta

figure(10)
contourf (Mx, My, TIU ,15);
title('Turbulent Intensity TI(U)')

figure(11)
contourf (Mx, My, TIu ,15);
title('Turbulent Intensity TI(u)')

figure(12)
contourf (Mx, My, TIv ,15);
title('Turbulent Intensity TI(v)')


%% Calculo de la Vorticidad (Vorticity) w = dv/dx - du/dy

w = zeros(fm,cm);
dx = (Mx(1,1) - Mx(1,2))*0.001; % Desplazamiento (m) en x de cada ventana
    de interrogacion
dy = (My(1,1) - My(2,1))*0.001; % Desplazamiento (m) en y de cada ventana
    de interrogacion

for j = 2:cm-1
   for i = 2:fm-1
      if Mu(i+1,j) == 0 || Mu(i-1,j) == 0
         w(i,j) = 0;
```

```
      else
      w(i,j) = ((Mv(i,j+1)-Mv(i,j-1)) / dx) - ((Mu(i+1,j)-Mu(i-1,j)) /
          dy);
      end
   end
end


%% Dibuja la gráfica de Vorticidad

w_max = max(max(w));
figure(13)
contourf (Mx, My, w ,15);
colorbar
caxis([-2 1.5])
title('Vorticity')


%% Tasa de disipacion viscosa

E1 = 15 * 1.48*10^(-5) .* Mdvvardx2; %asumiendo turbulencia homogenea e
    isotropica
E2 = 1.48*10^(-5) .* ((2.*Mduvardx2) + (2.*Mdvvardy2) + (3.*Mduvardy2) +
    (3.*Mdvvardx2) + (2.*Mduvvardyx));




%% Dibuja la gráfica de Tasa de disipacion viscosa

figure(14)
contourf (Mx, My, E1 ,15);
title('Tasa de disipacion viscosa')

figure(15)
contourf (Mx, My, E2 ,15);
title('Tasa de disipacion viscosa')
colorbar
caxis([0 4000])


%% Cálculo de la longitud de escala integral


% Si el ángulo de ataque es: 0Grad
for i = 1:fm
   f(i,:) = MRii(i,:) ./ ((Muvar2(i,78)^0.5) * (Muvar2(i,15)^0.5));
   ILS(i,1) = trapz (r, f(i,:));
end
```

```
% Si el ángulo de ataque es: 5Grad
for i = 1:fm
   f(i,:) = MRii(i,:) ./ ((Muvar2(i,78)^0.5) * (Muvar2(i,15)^0.5));
   ILS(i,1) = trapz (r, f(i,:));
end

% Si el ángulo de ataque es: 0Grad
for i = 1:fm
   f(i,:) = MRii(i,:) ./ ((Muvar2(i,81)^0.5) * (Muvar2(i,24)^0.5));
   ILS(i,1) = trapz (r, f(i,:));
end

% Si el ángulo de ataque es: 15Grad
for i = 1:fm
   f(i,:) = MRii(i,:) ./ ((Muvar2(i,81)^0.5) * (Muvar2(i,21)^0.5));
   ILS(i,1) = trapz (r, f(i,:));
end


%% Cálculo de la longitud de escala de Taylor

TLEt = sqrt(Muvar2 ./ Mduvardx2); % Según Tennekes y Lumley 1972
```

HW postprocessing -time, frequency-

```
%%%%%%%%%%%%%%%%%%%%%%%%%%%%%%%%%%%%%%%%%%%%%%%%%%%%%%%%%%%%%%%%%%%%%%%%%%%%%%%%
% Procesado de los datos de velocidad obtenidos mediante una sonda de hilo
% caliente – Dominio del Tiempo y Dominio de la Frecuencia –
% MRL 04/05/2013
%%%%%%%%%%%%%%%%%%%%%%%%%%%%%%%%%%%%%%%%%%%%%%%%%%%%%%%%%%%%%%%%%%%%%%%%%%%%%%%%

clear all;
close all;

%% Cargar los datos previamente transformados

cd ..
cd Medidas

SR =10000;                    % Frecuencia de adquisición [muestras/s]
H = 200;                      % Altura en mm

Tests = ls('5grad_Variable_Pos2*'); % Introduce el criterio de selección de
    experimentos
[ft,ct] = size(Tests);

for Test_no = 1:ft

   % Accede a las carpetas seleccionados
   Fname = Tests(Test_no,:);
   Fname = strrep(Fname,' ',''); % Elimina los espacios en blanco
   MyPath = [Fname '\DataSet_' Fname];
   cd (MyPath)                % Accede a la carpeta con el criterio de
       selección de experimentos anterior
   disp( [ 'Accediendo a la carpeta: ' Fname])

   Runs = ls('ALR_1306*');       % Lee los archivos con este criterio de
       selección
   [fr,cr] = size(Runs);

   %%Accede a los archivos seleccionados
   for Run_no = 1:fr

      MyRun = Runs(Run_no,:);
      MyRun = strrep(MyRun,' ',''); % Elimina los espacios en blanco
      % Columna 2: Vxy; Columna 3: Ang; Columna 4: Vx; Columna 5: Vy
      [A(:,1),A(:,2),A(:,3),A(:,4),A(:,5)] = textread (MyRun, '%f %f %f %f
          %f' ...
         ,'headerlines',1);      % Lee el archivo

      disp([ 'Procesando ' MyRun ])
      Amed(Run_no,:) = mean(A);  % Calcula la media de cada columna
```

```
[fa,ca] = size(A);          % Número de filas y columnas de la matriz A

%% Extrae la posición de la sonda del nombre del archivo

Ypos = [MyRun(1,18) MyRun(1,19) MyRun(1,20) '.' MyRun(1,21)];

Ypos = str2double(Ypos);    % Convierte el string en un número

if MyRun(1,22) == 'n'
   Ypos = -Ypos;
end

% Cambia las posiciones al criterio habitual de signos (- para "y"
    hacia abajo y + para "y" hacia arriba)
YposAll(Run_no,1) = (-1) * Ypos;

% Extrae la distancia a la pared del nombre del archivo [mm]
DistPared(Run_no) = (-1) * Ypos;

%% Establece el valor de la velocidad de flujo libre que se midió a
    100 mm del centro de la cámara de medida

if MyRun(1,18) == '1'
   UflujoLibre = mean(A(:,2)); % Busca el valor maximo de la velocidad
end

%% Representa la señal de velocidad en el dominio del tiempo

% Crea de la matriz Time Series
% Columna 1: TS_Vxy; Columna 2: TS_Vx; Columna 3: TS_Vy
TS(:,1) = A(:,2);                   % TS de Vxy
TS(:,2) = A(:,4);                   % TS de Vx
TS(:,3) = A(:,5);                   % TS de Vy
t = ((1:length(TS)) ./ SR)';        % Calcula de vector tiempo

figure(1)
plot (t, TS(:,2))
title('Velocity against time')
ylabel('\itv [m/s]')
xlabel('Time [s]')
ylim([-10 40])
xlim([0 12.5])

% Guarda las gráficas en un fichero .tiff dentro de una nueva
% carpeta con el nombre del experimento
[carp arch ext] = fileparts(MyRun);  % Extrae las distintas partes
    del nombre del archivo
mkdir(Fname)                         % Crea una carpeta con el nombre
    del experimento
```

```
cd (Fname)
saveas(gcf, ['TSvy_' arch],'tiffn')
cd ..

%% Cálculo de las características turbulentas del flujo

% Calcula las fluctuaciones de cada variable (columna de la matriz A)
for i = 1:ca
   Fluct(:,i) = A(:,i) - Amed(Run_no,i);
end

% Representa la variación de la velocidad Vy en función del tiempo
figure(2)
plot (t, Fluct(:,4))
title('Velocity fluctuations against time')
ylabel('\itu fluctuations [m/s]')
xlabel('Time [s]')

% Guarda la gráfica en un fichero .fig
cd (Fname)
saveas(gcf, ['TSvx_' arch '.fig'])
cd ..

%% Representa la densidad de potencia espectral de la señal velocidad

% Cálculo del PSD
% Columna 1: PSD_Vxy; Columna 2: PSD_Vx; Columna 3: PSD_Vy
[PSD(:,1), freq] = periodogram(A(:,2), [], length(A(:,5)), SR/2); %
    PSD de Vxy
[PSD(:,2), freq] = periodogram(A(:,4), [], length(A(:,5)), SR/2); %
    PSD de Vx
[PSD(:,3), freq] = periodogram(A(:,5), [], length(A(:,5)), SR/2); %
    PSD de Vy

% Aplicar un filtro de media móvil para suavizar la señal del espectro
% Columna 1: smoothedPSD_Vxy; Columna 3: smoothedPSD_Vx; Columna 4:
    smoothedPSD_Vy
window = 40;                          % Tamaño de la ventana en
    puntos para hacer la media (debe ser impar)
for i = 1:3
   smoothedPSD(:,i) = smooth(PSD(:,i), window);
end

% Representa el PSD de la velocidad Vxy
figure(3)
loglog (freq, smoothedPSD(:,1));
title('Power Spectral Density of the Velocity Signal U')
ylabel('PSD [(m/s)^2/Hz]')
xlabel('Frequency [Hz]')
```

```
xlim ([1E0 1E4])
ylim ([1E-11 1E0])
grid on


% Guarda la gráfica en un fichero .tiff y .fig
cd (Fname)
saveas(gcf, ['PSDvxy_' arch],'tiffn')
cd ..

% Encuentra la frecuencia máxima y la muestra
 smoothedPSD(1:10000) = 0;    % Excluye de la búsqueda los 700
    primeros puntos
 PSDmax = find(smoothedPSD == max(smoothedPSD));
 fmax = freq(PSDmax);
 disp(['Frequency at spectra maximum: ' num2str(fmax) ' Hz (value '
    num2str(smoothedPSD(PSDmax)) ')']);
 plot(fmax, smoothedPSD(PSDmax), '*r')
 text(2E0, 4E-10, ['Maximum at ' num2str(fmax) ' Hz'], 'FontSize',
    12);
 hold off

% Guarda la gráfica en un fichero .tiff
cd (Fname)
saveas(gcf, ['PSDvxy_' arch],'tiffn')
cd ..

% Representa el PSD de la velocidad Vx
figure(4)
loglog (freq, PSD(:,2));
title('Power Spectral Density of the Velocity Signal u')
ylabel('PSD [(m/s)^2/Hz]')
xlabel('Frequency [Hz]')
xlim ([1E0 1E4])
ylim ([1E-11 1E0])
grid on

% Guarda la gráfica en un fichero .tiff y .pdf
cd (Fname)
saveas(gcf, ['PSDvx_' arch],'tiffn')
saveas(gcf, ['PSDvx_' arch '.pdf'],'pdf')
cd ..

% Disminuye la frecuencia de muestreo para disminuir el tamaño de la
    figura
SmoothedPSD(:,3) = downsample(smoothedPSD(:,3),20);
Freq = downsample(freq,20);

% Representa el PSD de la velocidad Vy
```

```
figure(5)
loglog (Freq, SmoothedPSD(:,3));
title('Power Spectral Density of the Velocity Signal v')
ylabel('PSD [(m/s)^2/Hz]')
xlabel('Frequency [Hz]')
xlim ([1E1 1E4])
ylim ([1E-11 1E0])
grid on

% Guarda la gráfica en un fichero .tiff y .eps
cd (Fname)
saveas(gcf, ['PSDvy_' arch],'tiffn')
saveas(gcf, ['PSDvy_' arch '.eps'],'psc2')
cd ..

disp( [ MyRun ' post-procesado' ])

% Representa todas las PSD de la velocidad Vxy (en todas las
    posiciones verticales)
figure(6)
loglog (freq, smoothedPSD(:,1)); hold on
title('Power Spectral Density of the Velocity Signal U')
ylabel('PSD [(m/s)^2/Hz]')
xlabel('Frequency [Hz]')
xlim ([1E0 1E4])
ylim ([1E-11 1E0])
grid on

% Guarda la gráfica 5 en un fichero .tiff
if Run_no == fr
   cd (Fname)
   saveas(figure(4), ['PSDvxAll_' arch],'fig')
   cd ..
end


%% Representa las medias móviles (250 medias de 1000 ptos cada una)

medias = 2500;
j = 1 ;
add = 0;
for i = 1:medias:fa
   for k = i:i+medias-1
      add = add + TS(k,1);
   end
   mmU(j,1) = add/medias;
   j = j+1;
   add = 0;
end
```

```
    varianza (Run_no,1) = var(mmU);

    % Filtro pasabajos
    [b,a] = butter(5,0.1,'low'); % Filtro pasa baja a 0.1 Hz. fad=10000Hz
        --> Fnyq=5000 Hz *0.1 = 500Hz
    Filtro_mmU = filter(b,a,mmU(:,1));

    figure(7)
    plot (1:medias:fa, mmU-Amed(2))
    hold on;
    plot (1:medias:fa,Filtro_mmU-Amed(2),'r')
    title('Moving average of U')
    ylabel('\itMoving average of U [m/s]')
    xlabel('No samples')

    % Guarda la gráfica en un fichero .fig y .tiff
    cd (Fname)
    saveas(gcf, ['MvAvergU_' arch '.fig'])
    saveas(gcf, ['MvAvergU_' arch],'tiffn')
    cd ..


    %% Regresa a la carpeta de origen

    if Run_no == fr
       cd ..
       cd ..
    end

%close all
end

%% Crea una matriz con los datos de posición y varianza y los representa

Flow = [YposAll varianza]; % Crea la matriz

% Obtiene una matriz con el resultado de ordenar la primera columna de
% flow y los índices que indican el orden (ascendente) en que se
% deberian colocar las filas

[r i] = sort (Flow(:,1), 1, 'ascend');
Flow = Flow(i,:);          % Ordena Flow segun los indices i

% Si el 'angulo de calado es 0 grad, los resultados seran simétricos
% respecto al eje horizontal del alabe
if Fname(1,1) == '0'
    [r i] = sort (Flow(:,1), 1, 'descend');
    InvFlow = Flow(i,:);
```

```
      pInvFlow = InvFlow;
      for n = 1:fr
         pInvFlow(n,1) = -InvFlow(n,1);
      end
      pInvFlow(1,:)=[ ];
      Flow = [Flow; pInvFlow];
   end

    mSize = 5;

   if MyRun(1,15) == '0' && MyRun(1,16) == '0'
      marker = '-o';
      colour = 'k';
   elseif MyRun(1,15) == '0' && MyRun(1,16) == '5'
      marker = '-s';
      colour = [0.4,0.4,0.4];
   elseif MyRun(1,15) == '1' && MyRun(1,16) == '0'
      marker = '-^';
      colour = [0.6,0.6,0.6];
   elseif MyRun(1,15) == '1' && MyRun(1,16) == '5'
      marker = '-d';
      colour = [0.8,0.8,0.8];
   end

   figure(8)
   plot (Flow(:,2)/UflujoLibre^2, Flow(:,1)/H, '-o', 'color', colour, ...
      'Linewidth', 1.2, 'MarkerEdgeColor', colour, ...
      'MarkerFaceColor', colour, 'MarkerSize', mSize); hold on
   title('Variance of U for each measurement position')
   xlabel('\itVariance of U/U_{0}^2')
   ylabel('\ity/H')

   figure(9)
   smoothFlow = smooth(Flow(:,1),Flow(:,2),0.25);
   plot (smoothFlow/UflujoLibre^2, Flow(:,1)/H, '-o', 'color', colour, ...
      'Linewidth', 1.2, 'MarkerEdgeColor', colour, ...
      'MarkerFaceColor', colour, 'MarkerSize', mSize); hold on
   title('Variance of U for each measurement position')
   xlabel('\itVariance of U/U_{0}^2')
   ylabel('\ity/H')
end
```

HW postprocessing -turbulence and ILS-

```
%%%%%%%%%%%%%%%%%%%%%%%%%%%%%%%%%%%%%%%%%%%%%%%%%%%%%%%%%%%%%%%%%%%%%%%%%%%%%%%%
% Genera los mapas de variables de velocidad y turbulencia de las medidas
% tomadas con una sonda de hilo caliente. Introducir el criterio de
% selección de experimentos y la velocidad de flujo libre
% MRL 21/05/2013
%%%%%%%%%%%%%%%%%%%%%%%%%%%%%%%%%%%%%%%%%%%%%%%%%%%%%%%%%%%%%%%%%%%%%%%%%%%%%%%%

clear all;
close all;

%% Carga los datos previamente transformados

cd ..
cd Medidas

SR = 10000;                     % Frecuencia de adquisición [muestras/s]
Time = 60;                      % Tiempo de adquisición [s]
Chord = 100;                    % Cuerda del álabe [mm]
H = 200;                        % Semialtura de la cámara de ensayos [mm]


Tests = ls(['5grad_25Hz_Pos1*']); % Introduce el criterio de selección de
    experimentos
[ft,ct] = size(Tests);

for Test_no = 1:ft

   % Accede a la carpeta seleccionada
   Fname = Tests(Test_no,:);
   Fname = strrep(Fname,' ',''); % Elimina los espacios en blanco
   MyPath = [Fname '\DataSet_' Fname];
   cd (MyPath)                  % Accede a la carpeta con el criterio de
       selección de experimentos anterior
   disp( [ 'Accediendo a la carpeta: ' Fname])


   %% Lee los archivos con este criterio de selección

   Runs = ls('ALR_1306*');
   [fr,cr] = size(Runs);

   % Accede a los archivos seleccionados
   for Run_no = 1:fr

      MyRun = Runs(Run_no,:);
      MyRun = strrep(MyRun,' ',''); % Elimina los espacios en blanco
      % Columna 2: V; Columna 3: Ang; Columna 4: Vx; Columna 5: Vy
```

```
[A(:,1),A(:,2),A(:,3),A(:,4),A(:,5)] = textread (MyRun, '%f %f %f %f
    %f' ...
   ,'headerlines',1);      % Lee el archivo
Amed(Run_no,:) = mean(A);  % Calcula la media de cada columna

[fa,ca] = size(A);         % Número de filas y columnas de la matriz A

%% Extrae la posición de la sonda del nombre del archivo

Ypos = [MyRun(1,18) MyRun(1,19) MyRun(1,20) '.' MyRun(1,21)];

Ypos = str2double(Ypos);    % Convierte el string en un número

if MyRun(1,22) == 'n'
   Ypos = -Ypos;
end

% Cambia las posiciones al criterio habitual de signos (- para "y"
% hacia abajo y + para "y" hacia arriba)
YposAll(Run_no,1) = (-1) * Ypos;

% Extrae la distancia a la pared del nombre del archivo [mm]
DistPared = (-1) * Ypos;


%% Calcula la velocidad media y la turbulencia medidas en el test
    MyRun

% Calcula las fluctuaciones de cada variable (columna de la matriz A)
for i = 1:ca
   Fluct(:,i) = A(:,i) - Amed(Run_no,i);
end

Umed(Run_no,1) = mean(A(:,2));      % Media de Vxy
umed(Run_no,1) = mean(A(:,4));      % Media de Vx
vmed(Run_no,1) = mean(A(:,5));      % Media de Vy
AngMed(Run_no,1) = mean(A(:,3));    % Media del ángulo de la velocidad

Ufluc = A(:,2) - Umed(Run_no,1);    % Fluctuaciones de Vxy
ufluc = A(:,4) - umed(Run_no,1);    % Fluctuaciones de Vx
vfluc = A(:,5) - umed(Run_no,1);    % Fluctuaciones de Vy

RMS_U = (mean (Ufluc.^2) )^0.5;     % rms de Vxy
RMS_u = (mean (ufluc.^2) )^0.5;     % rms de Vxy
RMS_v = (mean (vfluc.^2) )^0.5;     % rms de Vxy

TU_U(Run_no,1) = 100 * RMS_U / Umed(Run_no,1); % Intensidad
    turbuluenta de Vxy
TU_u(Run_no,1) = 100 * RMS_u / Umed(Run_no,1); % Intensidad
```

```
        turbuluenta de Vxy
    TU_v(Run_no,1) = 100 * RMS_v / Umed(Run_no,1); % Intensidad
        turbuluenta de Vxy


    U_fluc(Run_no,1) = mean (Ufluc);    % Fluctuaciones medias de Vxy
    u_fluc(Run_no,1) = mean (ufluc);    % Fluctuaciones medias de Vx
    v_fluc(Run_no,1) = mean (vfluc);    % Fluctuaciones medias de Vy


    %% Establece el valor de la velocidad de flujo libre que se midió a
        100 mm del centro de la cámara de medida

    if MyRun(1,18) == '1'
       UmedMax = max(Umed); % Busca el valor maximo de la velocidad
       umedMax = max(umed); % Busca el valor maximo de la velocidad
       vmedMax = max(vmed); % Busca el valor maximo de la velocidad
    end

    disp( [ MyRun ' post-procesado' ])

    %% Calcula la longitud de escala integral por el método del área bajo
        ACF

    %% Accede a la carpeta donde se encuentran las funciones
    cd ..
    cd ..
    cd ..
    cd Matlab_procesamiento

    [DistanciaPared(Run_no,1), L_primcero(Run_no,1), L_minloc(Run_no,1)]
        = funcion_calculo_ILS_AreaACF(Fluct, ...
    DistPared, Amed);

    cd ..
    cd Medidas
    cd (MyPath)

    % Guarda la gráfica en un fichero .fig
    saveas(gcf, ['ACFu_' MyRun '.fig'])

end

%% Crea una matriz con los datos de posición, velocidad, turbulencia y
    ángulo ordenados en
% funcion de la posicion vertical de la sonda

Flow = [YposAll Umed umed vmed TU_U TU_u TU_v AngMed u_fluc v_fluc
    L_primcero L_minloc]; % Crea la matriz
```

```
% Obtiene una matriz con el resultado de ordenar la primera columna de
% flow y los índices que indican el orden (ascendente) en que se
% deberian colocar las filas

[r i] = sort (Flow(:,1), 1, 'ascend');
Flow = Flow(i,:);          % Ordena Flow segun los indices i

% Si el 'angulo de calado es 0 grad, los resultados seran simétricos
% respecto al eje horizontal del alabe
if Fname(1,1) == '0'
   [r i] = sort (Flow(:,1), 1, 'descend');
   InvFlow = Flow(i,:);
   pInvFlow = InvFlow;
   for n = 1:fr
      pInvFlow(n,1) = -InvFlow(n,1);
   end
   pInvFlow(1,:)=[ ];
   Flow = [Flow; pInvFlow];
end

disp([ 'Se han procesado los archivos de la carpeta: ' Fname ])


%% Representa la velocidad media en cada posición de la sonda

mSize = 5;

if MyRun(1,15) == '0' && MyRun(1,16) == '0'
   marker = '-o';
   colour = 'k';
elseif MyRun(1,15) == '0' && MyRun(1,16) == '5'
   marker = '-s';
   colour = [0.4,0.4,0.4];
elseif MyRun(1,15) == '1' && MyRun(1,16) == '0'
   marker = '-^';
   colour = [0.6,0.6,0.6];
elseif MyRun(1,15) == '1' && MyRun(1,16) == '5'
   marker = '-d';
   colour = [0.8,0.8,0.8];
end

figure(1)
plot (Flow(:,2)/UmedMax, Flow(:,1)/H, '-o', 'color', colour, ...
   'Linewidth', 1.2, 'MarkerEdgeColor', colour, ...
   'MarkerFaceColor', colour, 'MarkerSize', mSize); hold on
title('Mean velocity U at each measurement position')
ylabel('\ity/H')
xlabel('\itU/\itU_{0}')
```

```
ylim([-0.175 0.175])
xlim([0.8 1])

figure(2)
plot (Flow(:,3)/umedMax, Flow(:,1)/H, '-o', 'color', colour, ...
   'Linewidth', 1.2, 'MarkerEdgeColor', colour, ...
   'MarkerFaceColor', colour, 'MarkerSize', mSize); hold on
title('Mean velocity u at each measurement position')
ylabel('\ity/H')
xlabel('\itu/\itU_{0}')
ylim([-0.175 0.175])
xlim([0.8 1])

figure(3)
plot (Flow(:,2)/UmedMax, Flow(:,1)/H, marker, 'color', colour, ...
   'Linewidth', 1.2, 'MarkerEdgeColor', colour, ...
   'MarkerFaceColor', colour, 'MarkerSize', mSize); hold on
title('Mean velocity U at each measurement position')
ylabel('\ity/H')
xlabel('\itU/\itU_{0}')
ylim([-0.175 0.175])
xlim([0.2 1])


%% Representa la velocidad media y en cada posición de la sonda

figure(13)

plot (Flow(:,4), Flow(:,1)/H, '-o', 'color', colour, ...
   'Linewidth', 1.2, 'MarkerEdgeColor', colour, ...
   'MarkerFaceColor', colour, 'MarkerSize', mSize); hold on
title('Mean velocity U at each measurement position')
ylabel('\ity/H')
xlabel('\itU/\itU_{0}')
ylim([-0.175 0.175])


%% Representa la turbulencia media en cada posición de la sonda

figure(4)
plot (Flow(:,5), Flow(:,1)/H, '-o', 'color', colour, ...
   'Linewidth', 1.2, 'MarkerEdgeColor', colour, ...
   'MarkerFaceColor', colour, 'MarkerSize', mSize); hold on
title('Turbulent Intensity of U at each measurement position')
ylabel('\ity/H')
xlabel('100 \itU_{rms}/U_{0} \rm[%]')
ylim([-0.175 0.175])
xlim([0 20])
```

```
figure(5)
plot (Flow(:,6), Flow(:,1)/H, '-o', 'color', colour, ...
   'Linewidth', 1.2, 'MarkerEdgeColor', colour, ...
   'MarkerFaceColor', colour, 'MarkerSize', mSize); hold on
title('Turbulent intensity of u at each measurement position')
ylabel('\ity/H')
xlabel('100 \itu_{rms}/U_{0} \rm[%]')
ylim([-0.175 0.175])
xlim([0 20])

figure(7)
plot (Flow(:,5), Flow(:,1)/H, marker, 'color', colour, ...
   'Linewidth', 1.2, 'MarkerEdgeColor', colour, ...
   'MarkerFaceColor', colour, 'MarkerSize', mSize); hold on
title('Turbulent Intensity of U at each measurement position')
ylabel('\ity/H')
xlabel('100 \itU_{rms}/U_{0} \rm[%]')
ylim([-0.175 0.175])
xlim([0 60])

%% Representa las longitudes de escala integral calculadas por la ACF

figure(8)
plot (Flow(:,11), Flow(:,1)/H, marker, 'color', colour, ...
   'Linewidth', 1.2, 'MarkerEdgeColor', colour, ...
   'MarkerFaceColor', colour, 'MarkerSize', mSize); hold on
title('ILS based on the first zero of the ACF calculated at each
   measurement position')
ylabel('\ity/H')
xlabel('\itILS \rm[m]')

figure(9)
plot (Flow(:,12), Flow(:,1)/H, marker, 'color', colour, ...
   'Linewidth', 1.2, 'MarkerEdgeColor', colour, ...
   'MarkerFaceColor', colour, 'MarkerSize', mSize); hold on
title('ILS based on the local minimum of the ACF calculated at each
   measurement position')
ylabel('\ity/H')
xlabel('\itILS \rm[m]')


%% Representa las la vorticidad (du/dy) en cada posición de la sonda

[fF,cF] = size(Flow);

vort(1,1) = 0;
for i = 2:fF
   vort(i,1) = (Flow(i,3) - Flow(i-1,3)) / 1000*(Flow(i,1) -
      Flow(i-1,1));
```

```
    end

    figure(10)
    plot (vort(:,1), Flow(:,1)/H, '-o', 'color', colour, ...
        'Linewidth', 1.2, 'MarkerEdgeColor', colour, ...
        'MarkerFaceColor', colour, 'MarkerSize', mSize); hold on
    title('Vorticity at each measurement position')
    ylabel('\ity/H')
    xlabel('\itvorticity')

    figure(11)
    plot (abs(vort(:,1)), Flow(:,1)/H, '-o', 'color', colour, ...
        'Linewidth', 1.2, 'MarkerEdgeColor', colour, ...
        'MarkerFaceColor', colour, 'MarkerSize', mSize); hold on
    title('Vorticity at each measurement position')
    ylabel('\ity/H')
    xlabel('\it|vorticity|')
end
```

Functions that estimate the ILS with different methods

```
%%%%%%%%%%%%%%%%%%%%%%%%%%%%%%%%%%%%%%%%%%%%%%%%%%%%%%%%%%%%%%%%%%%%%%%%%%%%%%%
% MÉTODO 1: ILS basado en el espectro unidimensional (Pope, 2000 – Cap 6)
% Función que calcula la longitud de escala integral (ILS) en cada
% posición de la sonda a partir de la matriz de fluctuaciones de Vx
% para cada punto (Fluct), la media de la fluctuación de Vx al cuadrado
% (ums), la frecuencia de adquisición (SR), y la distancia a la pared a
% la que se colocó la sonda (DistPared)
% SALIDAS: distancia a la pared (DistPared), Tamaño de los vórtices de
% escala integral (L_M1), vector de frecuencias (Freq), vector de PSD de
% la fluctuación de Vx suavizado (smoothedPSD).
% MRL 05/05/2013
%%%%%%%%%%%%%%%%%%%%%%%%%%%%%%%%%%%%%%%%%%%%%%%%%%%%%%%%%%%%%%%%%%%%%%%%%%%%%%%

function [DistPared, L11, Freq, smoothedPSD] =
    funcion_calculo_ILS_1Despectro(Fluct, ums, SR, DistPared)

   % Calcula la densidad de potencia espectral de la fluctuación de Vx
       (columna 4)
   [PSD(:,1), Freq] = periodogram(Fluct(:,4), [], length(Fluct(:,4)), SR);

   % Aplicar un filtro de media móvil para suavizar la señal del espectro
   window = 11;              % Tamaño de la ventana en puntos para hacer la
       media (debe ser impar)
   smoothedPSD(:,1) = smooth(PSD(:,1), window);

   % Calcula una media en el origen de PSD de la fluctuación de Vx
   media = 0;
   cont = 0;
   for i = 1 : length(Freq)
      if Freq(i) > 0.1 && Freq(i) < 0.2
         media = media + PSD(i);
         cont = cont + 1;
      else
         continue
      end
   end
   E11 = media/cont;

   % Calcula el valor de la ILS, L11 (Pope, 2000 – ec. 6.213)
   L11 = pi*E11/(2*ums);

end
```

```
%%%%%%%%%%%%%%%%%%%%%%%%%%%%%%%%%%%%%%%%%%%%%%%%%%%%%%%%%%%%%%%%%%%%%%%%%%%%
% MÉTODOS 2 y 3: ILS a partir de su definición y basado en
% la microescala de Taylor
% ENTRADAS: Matriz de fluctuaciones (Fluct), media de las
% fluctuaciones de Vx y Vy al cuadrado (ums, vms)y la frecuencia
% de adquisición (SR), viscosidad cinemática (visc)
% SALIDAS: ILS y epsilon por el método 2 y 3 (L_m2, L_m3, epsilon_M2,
% epsilon_M3), Reynolds de las escalas de Taylor e integral (Re_lambda,
% Re_L), tamaños de los vórtices de las escalas de Taylor y Kolmogorov
% (kolmo, taylor).
% MRL 05/05/2013
%%%%%%%%%%%%%%%%%%%%%%%%%%%%%%%%%%%%%%%%%%%%%%%%%%%%%%%%%%%%%%%%%%%%%%%%%%%%

function [epsilon_M02, L_m02, Re_lambda, Re_L, kolmo, taylor, L_m03,
    epsilon_M03, ACF, Lags, Lambda_f] ...
   = funcion_calculo_ILS_Taylor(Fluct, Amed, ums, vms, SR, visc)

   clear K_M02 U_M02
   % Determina la autocorrelación de la fluctuación de Vx
   numlags = 10000;                        % Número de lags (intervalos de
       desplazamiento) usados para constuir la función autocorrelación
   [ACF,Lags,Bounds] = autocorr(Fluct(:,4),numlags);
   ACF = ACF';
   Lags= Lags';

   % Cálculo a partir de una parábola que pasa por los dos primeros puntos
       de la autocorrelación
   Lambda_f = Amed(2)*(1/SR)*(1/(1-ACF(2)))^0.5; % Tamaño de los vórtices
       de la escala de Taylor en sentido longitudinal de flujo
   Lambda_g = (1/2^0.5) * Lambda_f;        % Tamaño de los vórtices de la
       escala de Taylor en sentido transversal de flujo

   % Calcula la energía cinética turbulenta suponiendo v = w
   K_M02 = (0.5 * ums) + vms;
   U_M02 = (2 * K_M02 / 3)^0.5;            % Velocidad caracterísitcas de
       las fluctuaciones

   % Calcula la escala de longitud integral (L) a partir de su definición
   Re_lambda = U_M02 * Lambda_g / visc;    % Re en la escala de Taylor del
       flujo
   epsilon_M02 = 15 * visc * ums^0.5 / Lambda_g^2; % Tasa de disipación
       para un caso homogéneo isotrópico e incompresible
   L_m02 = K_M02^1.5 / epsilon_M02;        % Cálculo del tamaño de longitud
       integral
   Re_L = L_m02 * K_M02^0.5 / visc;        % Re en la escala integral

   kolmo = L_m02 * Re_L^-0.75;             % Tamaño de los vórtices en la
       escala de Kolmogorov
   taylor = Lambda_f;                      % Tamaño de los vórtices en la
```

```
        escala de Taylor

    % Calcula la escala de longitud integral (L) a partir de Re de la
        microescala de taylor (Pope, 2000)
    L_m03 = (3/20) * ((U_M02^2)/visc) * (Lambda_f^2) / (2*(K_M02)^0.5);
    epsilon_M03 = U_M02^3 / L_m03;          % Tasa de disipación que viene
        del concepto de casada de energía turbulenta (Davidson, 2004)

end
```

```
%%%%%%%%%%%%%%%%%%%%%%%%%%%%%%%%%%%%%%%%%%%%%%%%%%%%%%%%%%%%%%%%%%%%%%%%%%%%
% MÉTODO 4: ILS a partir del espectro tridimensional
% ENTRADAS: Matriz de fluctuaciones (Fluct), Enería de las fluctuaciones
% (EnergA), Media de las fluctuaciones de velocidad al cuadrado (ums,
% vms), frecuencia de adquisición (SR), distancia de la sonda a la pared
% (DistPared), viscosidad cinemática (visc), matriz de medias de las
% velocidades (Amed)
% SALIDAS: Distancia de la sonda a la pared (DisPared), longitud de escala
% integral calculada de forma directa (L) y mediante la fórmula 6.260 del
% libro de Pope, 2000
% MRL 05/05/2013
%%%%%%%%%%%%%%%%%%%%%%%%%%%%%%%%%%%%%%%%%%%%%%%%%%%%%%%%%%%%%%%%%%%%%%%%%%%%

function [DistPared, L11, L, K, epsilon] =
    funcion_calculo_ILS_3Despectro(Fluct, EnergA, ...
   ums, vms, SR, DistPared, visc, Amed)

   clear K

   % Calcula la densidad de potencia espectral de la fluctuación de Vx
       (columna 4)
   [PSD(:,1), Freq] = periodogram(Fluct(:,4), [], length(Fluct(:,4)), SR);

   % Aplica un filtro de media móvil para suavizar la señal del espectro
   window = 11;                          % Tamaño de la ventana en puntos
       para hacer la media (debe ser impar)
   smoothedPSD(:,1) = smooth(PSD(:,1), window);

   % Calcula la energía cinética turbulenta, K:
   K_temp = (1/2)*EnergA;                % Calcula la energía cinética
       turbulenta en el dominio del tiempo mediante la integral de la
       variación de Vx
   K = 0.5*ums + vms;

   % Calcula la energía bajo el PSD de una la fluctuación de velocidad Vx
   EnergPSD = trapz(Freq,smoothedPSD); % Calcula la integral de la curva
       PSD mediante la suma de trapecios

   % Calcula la tasa de disipación
   epsilon = 2 * visc * Amed^2 * EnergPSD;

   % Calculamos el valor de la ILS:
   L = K ^ 1.5 / epsilon;                % Forma directa
   L11 = (3*pi / (4*K_temp)) * EnergPSD / Amed; % (Pope, 2000 – 6.260)

end
```

```
%%%%%%%%%%%%%%%%%%%%%%%%%%%%%%%%%%%%%%%%%%%%%%%%%%%%%%%%%%%%%%%%%%%%%%%%%%%%
% MÉTODO 5: ILS a partir del área debajo de la función autocorrelación
% Función que calcula la longitud de escala integral (ILS) en cada
% posición de la sonda.
% ENTRADAS: la matriz de fluctuaciones de Vx para cada punto (Fluct),
% la distancia a la pared a la que se colocó la sonda (DistPared), la
% media de la matriz de datos cargados de cada experimento (Amed)
% SALIDAS: Dintancia a la pared, la ILS calculada con el primer cero, la
% ILS calculada con el mínimo local.
% MRL 05/05/2013
%%%%%%%%%%%%%%%%%%%%%%%%%%%%%%%%%%%%%%%%%%%%%%%%%%%%%%%%%%%%%%%%%%%%%%%%%%%%

function [DistPared, L_primcero, L_minloc] =
    funcion_calculo_ILS_AreaACF(Fluct, ...
 DistPared, Amed)

   % Determina la autocorrelación de la fluctuación de Vx
   numlags = 10000;                        % Número de lags (intervalos de
       desplazamiento) usados para constuir la función autocorrelación
   [ACF,Lags,Bounds] = autocorr(Fluct(:,4),numlags);
   ACF = ACF';
   Lags= Lags';

   % Representa la función autocorrelación
   figure(10)
   plot(Lags, ACF)
   xlabel('Lags');
   ylabel('ACF');
   title('Autocorrelation Function of Vx');


   %% CRITERIO 1 PARA EL CÁLCULO DEL ÁREA BAJO LA ACF:

   % Busca el primer punto donde la autocorrelación se hace cero
   flag = true;
   for n = 1:length(Lags)
      if (ACF(n)< 0) && flag
         limite_primcero = n;     % Lag en el que la correlación se hace
             cero
         flag = false;
         disp( [ 'El primer punto donde la ACF se hace cero está en la
             posición: ' num2str(limite_primcero)])
      end
   end

   % Aplica este límite si la autocorrelación no se hace cero
   if flag == true
      limite_primcero = 10000;
```

```
      disp( [ 'LA ACF no se hace cero. Se impone el mínimo: '
          num2str(limite_primcero)])
   end


   %% CRITERIO 2 PARA EL CÁLCULO DEL ÁREA BAJO LA ACF:

   % Busca el primer mínimo local
   flag = true;
   for n = 1:length(Lags)-1
      if (ACF(n+1) > ACF(n)) && flag
         limite_minloc = n;      % Muestra el límite por pantalla
         flag = false;
         disp( [ 'El primer mínimo local de la ACF está en la posición: '
             num2str(limite_minloc)])
      end
   end

   % Aplica este límite si la autocorrelación no se hace cero
   if flag == true
      limite_minloc = 10000;

      disp( [ 'LA ACF no se hace cero. Se impone el mínimo: '
          num2str(limite_minloc)])
   end


   %% Calcula el área bajo la función autocorrelación y las ILS

   % Áreas
   Area_primcero = trapz (Lags(1:limite_primcero), ACF(1:limite_primcero));
   Area_minloc = trapz (Lags(1:limite_minloc), ACF(1:limite_minloc));

   % Longitudes
   L_primcero = Amed(2) * Area_primcero;
   L_minloc = Amed(2) * Area_minloc;
end
```

Appendix II

In this appendix are presented the published and under review articles related with this thesis

Published articles

- M. Rodríguez Lastra, J. M. Fernández Oro, M. Galdo Vega, E. Blanco Marigorta, C. Santolaria Morros. Novel design and experimental validation of a contraction nozzle for aerodynamic peasurements in a subsonic wind tunnel. *Journal of Wind Engineering and Industrial Aerodynamics* 118 (2013) 35-43.
- J. M. Fernández Oro, K. M. Argüelles, M. Rodríguez Lastra, M. Galdo Vega, B. Pereiras García. Converged statistics for time-resolved measurements in low-speed axial fans using high-frequency response probes. *Experimental Thermal and Fluid Science* 54 (2014) 71-84.
- M. Galdo Vega, M. Rodríguez Lastra, K. M. Argüelles Díaz, J. M. Fernández Oro. Application of deterministic correlations in the analysis of rotor-stator interactions in axial flow fans. *Proceedings of the ASME 2012 Fluids engineering Summer meeting*, FEDSM2012-72450. July 8-12, Rio Grande, Puerto Rico.

Under review articles

- M. Rodríguez Lastra, J. M. Fernández Oro, M. Galdo Vega, E. Blanco Marigorta, C. Santolaria Morros. Influence of intermittency of large-scale turbulence in generation of vortex shedding and shear layer instabilities in a low-thickness elliptic airfoil.
- M. Rodríguez Lastra, M. Galdo Vega, E. Blanco Marigorta, C. Santolaria Morros. PIV measurements on an elliptic airfoil.